Helical phase-based spectroscopy in matter

by

Ashish Jain

A dissertation
presented to the University of Ottawa
in partial fulfillment of the
requirements for the degree of
Doctor of Philosophy
in
Physics

Department of Physics
University of Ottawa
Ontario, Canada, 2024

Examining Committee Membership

The following served on the Examining Committee for this dissertation.

External Examiner: Dr. Maurice O’Sullivan
Senior Director, Optical Systems R/D, Ciena

Supervisor: Dr. Ravi Bhardwaj
Full Professor, Dept. of Physics, University of Ottawa

Internal Member: Dr. Robert Boyd
Canada Research Chair - Full Professor, Dept. of Physics, University of Ottawa

Internal Member: Dr. Karin Hinzer
Vice-Dean, Research, Professor, Faculty of Engineering, University of Ottawa

Internal-External: Dr. Kevin Graham
Professor, Dept. of Physics, Carleton University

Abstract

In the domain of light-matter interaction, a considerable amount of research has been conducted on studying the electric dipole-dominant nonlinear interactions with the fundamental transverse electromagnetic mode of the laser. Moreover, such electric dipole-dominant transitions are often studied using light polarization, associated with spin angular momentum, as an optical probe. In such transition dynamics, the optical phase associated with the wavefront of light is often neglected, as it has been shown to play a minimal role.

In the past two decades, it has been demonstrated that light beams can also possess orbital angular momentum associated with structured phase-fronts, possessing a unique helical twist in space. The realization of such helically phased beams, known as helical beams, has inherently led to the investigation of using the helical phase as a probe to study light-matter interaction instead of polarization. Early studies on exploring the helical phase as a tool to examine matter were not conclusive, as the focus was primarily on dipole-dominant transitions. Recently, theoretical studies based on higher-order multipole moments proposed the existence of helical phase-based differential optical response in matter but only limited to certain symmetries. The experimental evidence of such phase-based differential effects in bulk matter has been elusive, without the use of an intermediary. Our research demonstrates the existence of helical phase-dependent dichroism, differential absorption of left- and right-handed helical beams, in different material phases without any intermediary. Such helical dichroism is intrinsic to all material phases and exists irrespective of their symmetry. We also explore the use of phase in the controlled manipulation of matter. The origin of such phase-dependent effects is explained in terms of proposed nonlinear interaction models.

The primary objective of this dissertation is to demonstrate the observation of :

(i) *Helical phase-based dichroism in liquids.* We investigate the nonlinear absorption of helical light in chiral and achiral molecules in the liquid phase. Chiral interactions are prevalent in nature, as chirality is a fundamental property of many biological molecules. Two non-superimposable mirror images of a chiral molecule, known as enantiomers, have identical physical and chemical properties when analyzed in achiral environments. Such enantiomers can only be discerned in chiral environments or when the probe is chiral in nature. Typically, the chiral structure of the electric field associated with circularly polarized light is utilized as a chiral probe to induce enantioselective transitions. In this work, we demonstrate the use of the helical phase as an alternative chiral probe with efficient chiral sensitivity. By not involving the chirality associated with light polarization, it is shown that enantioselectivity is a phase effect, and the associated chiral signal can be further controlled. In addition, we show the presence of unique phase-based dichroism in achiral molecules with asymmetrical helical beams. The origin of these effects is modeled by considering multipole transition moments in light-matter interactions.

(ii) *Helical phase as a chiral probe to differentiate bio-synthesis relevant amino acids.* We extend the use of the helical phase as a chiral probe to differentiate amino acid powders in a dissolved state, with varying concentrations. Moreover, we show the phase-based dichroism signal to be an order of magnitude higher relative to conventional linear techniques that use polarization as the chiral probe. The chiral response of powdered enantiomers is explained by considering the symmetry structure of the enantiomeric ground states.

(iii) *Intrinsic dichroism in amorphous and crystalline solids with helical light.* We investigate the nonlinear interaction of helical light in amorphous and crystalline solids. Amorphous solids do not possess long-range order due to the disordered arrangement of atoms and are isotropic in nature. The lack of symmetry in an amorphous solid results in the absence of a circular dichroism signal, which is defined as differential absorption of left- and right-circular polarization. In this work, we demonstrate the existence of intrinsic phase-based dichroism in amorphous solids using helical light beams. We show that helical dichroism is responsive to short- to medium-range order present in amorphous solids and is a phase effect. In addition, we demonstrate that helical dichroism is sensitive to the chirality of crystalline solids, and its strength can be tuned using the superposition of helical and Gaussian beams. The origin of intrinsic dichroism is modeled by considering inter-band electron transitions via multiphoton-assisted tunneling.

(iv) *Existence of helical dichroism in achiral plasmonic metasurfaces.* We demonstrate the presence of helical dichroism in achiral and chiral plasmonic metasurfaces. Our results confirm the existence of dichroism in symmetric material geometries. These results were achieved by probing the helicity-dependent linear absorption of linearly polarized asymmetric helical light beams by the plasmonic metasurfaces.

(v) *Spatially controlled nano-structuring.* We examine the effect of the helical phase on surface morphology modifications. Due to the resolution limitation imposed by the light diffraction limit, nanostructuring has been mostly achieved using lithographic techniques based on electron/ion beams. Here, we introduce a novel helical phase-based ablation method demonstrating spatially controlled manipulation of a silicon surface with a sub-wavelength positional precision of 50 nm. This level of control and accuracy paves the way for new possibilities in nano-printing of materials through methods like laser-induced forward transfer.

This dissertation highlights the potentiality of utilizing the helical phase as an alternative chiral probe for examining matter, regardless of its symmetry. The theoretically limitless nature of OAM compared to SAM offers numerous benefits and opens up new possibilities in chiroptical spectroscopy techniques, with potential applications extending up to the pharmaceutical industry. The presence of helical dichroism in amorphous solids provides an alternate approach to determining the short-range order. The design and control of light-matter interactions with helical light introduce new opportunities in the laser processing of materials, ultrafast probing of chiral systems, and nonlinear spectroscopy. The proposed spectroscopy method incorporates the optical phase-based effects, which generally vanish in the electric dipole approximation, by including the electric quadrupole transitions.

Structure of Dissertation

Chapters 1, 2, 6, and 8 of this dissertation follow a monograph format, while Chapters 3, 4, 5, and 7 adopt a dissertation-by-article format, consisting of four peer-reviewed articles. The chapters following the dissertation-by-articles format are preceded by an introduction, key results and advances, and an author contribution section. Theoretical and experimental methods, figures, and references are self-contained within each published article.

Chapter 1 - This chapter outlines the research presented in this dissertation and introduces beams carrying helical phase front. Such helical beams carry finite orbital angular momentum in addition to spin angular momentum. Light modes carrying the helical wavefronts are also discussed, with emphasis on the Laguerre-Gaussian (LG) mode, which is used in our theoretical models discussed in this dissertation. The asymmetrical LG beams solution is also presented. This chapter also discusses various methods to generate such helical beams. However, the emphasis is primarily on the frequently applied device known as the q-plate.

Chapter 2 - This chapter provides comprehensive models for both linear and nonlinear helical light-matter interactions. The multiphoton absorption model within the perturbative regime is presented for chiral and achiral liquids, while the multiphoton-assisted tunneling model in the non-perturbative regime is presented for amorphous and crystalline solids. The latter part of the chapter focuses on the experimental methods employed in the research.

Chapter 3 - This chapter demonstrates the direct observation of helical light as a chiral probe for differentiating chiral molecules. The helical dichroism (HD), defined as the differential absorption of left- and right-helical light, is observed in both chiral and achiral molecules in the liquid phase without the use of any external intermediary. The method explores the helicity-dependent nonlinear propagation of asymmetric helical light beams through the liquid sample. This effect is modeled by considering induced multipole moments, showing that HD arises from the coupling of electric dipoles and quadrupoles.

Chapter 4 - This chapter extends the helical light-based chiroptical detection of enantiopure samples to enantiomeric solutions. The use of the helical wavefront as an efficient chiral probe to differentiate powdered amino acids in the solution phase is demonstrated. The efficiency is shown to be an order of magnitude higher than the conventional linear techniques and comparable to other polarization-based nonlinear techniques.

Chapter 5 - This chapter demonstrates the direct observation of dichroism in amorphous solids with asymmetrical helical beams. Amorphous solids, due to their lack of translational and rotational symmetry, do not typically show circular dichroism, which is the differential absorption of circularly polarized light. However, the existence of intrinsic helical dichroism (HD) in these solids is demonstrated, which could be manipulated by adjusting the beam parameters. Additionally, it is shown that HD in amorphous solids could potentially provide an upper limit for their unique short-range order. HD is also modeled by considering the interband electron transitions via multiphoton-assisted tunneling. The presence of dichroism in both chiral and achiral crystalline solids is also demonstrated.

Chapter 6 - This chapter demonstrates the presence of a dichroism signal in achiral and chiral plasmonic meta-surfaces with helical beams. Achiral structures, due to their symmetry properties, do not exhibit dichroism either with circularly polarized beams or symmetric helical beams. Additionally, efficient chiroptical detection is shown in the case of chiral metasurfaces. This unique effect is explained using asymmetric helical light-matter interactions based on higher-order multipoles.

Chapter 7 - This chapter demonstrates the spatially controlled formation of nanocones on a silicon surface with a sub-wavelength positional precision of 50 nm using helical light beams. The presented technique exploits the superposition of helical and Gaussian beams to actively position the fabricated nanocones in two dimensions.

Chapter 8 - *Conclusion* - This chapter summarizes the key results presented in this dissertation and provides an outlook on the advances made in this dissertation.

Chapter 9 - *Future scope and potential applications* - This chapter provides a comprehensive overview of the potential future expansion of the presented helical phase-based spectroscopy technique. Additionally, three novel potential applications of my research work are proposed.

List of Publications

I contributed to the following peer-reviewed publications.

1. Ashish Jain, Howard Northfield, Ebrahim Karimi, Pierre Berini & Ravi Bhardwaj. Selective and tunable absorption of twisted light in achiral and chiral plasmonic metasurfaces. ***ACS Nano*** **10**, 1021 (2024).
2. Ashish Jain*, Jean-Luc Bégin*, Paul Corkum, Ebrahim Karimi, Thomas Brabec & Ravi Bhardwaj. Intrinsic dichroism in amorphous and crystalline solids with helical light. ***Nature Communication*** **15**, 1350 (2024).
3. Jean-Luc Bégin*, Ashish Jain*, Andrew Parks, Felix Hufnagel, Paul Corkum, Ebrahim Karimi, Thomas Brabec & Ravi Bhardwaj. Nonlinear helical dichroism in chiral and achiral molecules. ***Nature Photonics*** **17**, 82–88 (2023).
4. Ashish Jain*, Jean-Luc Bégin* & Ravi Bhardwaj. Helical dichroism in enantiomeric solutions. ***J. Chem. Phys.***, **159**, 014504 (2023).
5. Ashish Jain, Mitra G. Rahimian & Ravi Bhardwaj. Optimization of Multi-Layer Data Recording and Reading in an Optical Disc. ***Photonics*** **9**, 690 (2022). Only discussed in future scope and potential applications.
6. Mitra G. Rahimian*, Ashish Jain*, Hugo Larocque, Paul Corkum, Ebrahim Karimi, & Ravi Bhardwaj. Spatially controlled nanostructuring of silicon with femtosecond vortex pulses. ***Scientific Reports*** **10**, 12643 (2020)
7. Mariam Alameer, Ashish Jain, Mitra G. Rahimian, Hugo Larocque, Paul Corkum, Ebrahim Karimi, and Ravi Bhardwaj. Mapping complex polarization states of light on a solid. ***Optics Letters*** **43**, 5757 - 5760 (2019). Not a part of this dissertation.

*** Co-first authorship** : Equal contribution research.

Acknowledgements

Let's start from the beginning. I joined the University of Ottawa as a visiting researcher from India. Initially, my research stay was scheduled for three months based on a government scholarship. During this time, I met my supervisor, Professor Ravi Bhardwaj, for the first time. I vividly remember our initial meeting, where he provided a comprehensive overview of the research and gave me a detailed tour of the lab. His support enabled me to extend my stay to a year, and later, I joined as a PhD student.

I would like to express my deepest gratitude to my supervisor for his unwavering support, mentorship, and guidance. It has been a privilege to work with such an exceptional scientist and dedicated mentor. His belief in my research endeavors, invaluable research insights, and the patience with which he engaged with all my ideas, no matter how unconventional, has been indispensable. I am sithe ncerely thankful for his advice and engagement whenever I seek his help with any sort of probdipole-dominantng extended beyond research methods to encopass sociahigher-ordercal aspects of anyengagement. In fact, he continues tphase-basedhow to ask the right questions and the importance of revising my thoughts until I can express them with cphase-basedlso cherish our long discussions on social issues anan d world order.

I could not have foreseen how many brilliant and supportive individuals would be involved in my research endeavors. I would like to express my sincere gratitude to the exceptional scientists and professors with whom I had the privilege to collaborate. I extend my heartfelt thanks to Professor Thomas Brabec for his collaboration, review, and guidance throughout the research. My sincere gratitude goes to Professor Ebrahim Karimi and PhD student Felix Hufnagel for their collaboration and support. I am also grateful to Professor Pierre Berini and research engineer Howard Northfield for their collaboration and insights into the research work. Special thanks to Professor Paul Corkum for his collaboration and valuable insights. I am also deeply thankful to Professor Robert Boyd and Professor Ebrahim Karimi for serving on my comprehensive exam committee and being exceptional teachers. I sincerely enjoyed studying nonlinear optics and electrodynamics under your guidance.

Any research journey is incomplete without the support of a dedicated team, and I was fortunate to have my colleague and friend, Jean-Luc Bégin, by my side. His collaboration, insights, tireless work ethic, and willingness to engage in spirited discussions have equally advanced our collaborative research endeavors and been crucial throughout this journey. Our shared moments of discovery, countless hours spent brainstorming light-matter interaction, and mutual encouragement have not only enriched our research but also made this experience a rewarding and smooth ride. From late-night lab sessions to celebrating our milestones, your commitment and enthusiasm have truly inspired me to work harder and made this experience both productive and enjoyable. Thank you for being an exceptional collaborator and an even better friend. I look forward to many more shared successes and cherished memories together.

I would also like to thank my friend Theng Loo Lim for his constant support, laughter, and our long evening walks, where we discussed all sorts of crazy research ideas and socio-economic

problems. Additionally, I want to express my gratitude to my team member and colleague, Melika Afshar, for bringing many moments of laughter and cheerfulness.

Last but not least, this entire journey would not have been possible without the support of my family. I owe all my research achievements to my parents, Mr. Alok Jain and Mrs. Shweta Jain. Their blessings, love, unwavering support, guidance, and numerous sacrifices have made this possible. My sister, Somya Jain, has been a constant source of support and a life mentor, always being there for me no matter what. I am also grateful to my extended family and the spiritual blessings that have guided me along the way.

Dedicated to

To my parents, Alok Jain and Shweta Jain, without whose unwavering support, life teachings, and numerous sacrifices, I wouldn't have achieved anything. They will forever be my source of inspiration.

To my sister, Somya Jain, for always being there, my mentor and eternal support system.

This dissertation is also dedicated to my late grandfathers, Dr. Jinendra Kumar Jain and Kamal Kumar Jain, whose invaluable teachings on the importance of knowledge, education, and life lessons have shaped the present version of myself.

Table of Contents

List of Figures

Chapter 1

Introduction

Optical spectroscopy is a powerful tool for investigating light-matter interactions, playing a crucial role in various research disciplines and industrial applications. The technique encompasses various methods that are classified based on the property being examined, such as absorption, emission, or scattering of light by a material. Optical spectroscopy provides insights into various material properties, including chemical, electronic, structural, and optical properties.

To understand how optical spectroscopy works, it is essential to consider the interaction between light and matter. The material's response to light can be understood in terms of both microscopic and macroscopic effects. The former involves light-induced electronic transitions in atoms or molecules. In the linear interaction regime, light absorption occurs when the energy of the incident photons matches the energy required to excite electrons from lower to higher energy states. If the photon energies do not correspond to these electronic transitions, light is typically scattered, either elastically (without a change in energy) or inelastically (with a change in energy).

Macroscopically, in the linear regime, the material response is characterized by its refractive index, leading to phenomena such as dispersion, refraction, and absorption (through the imaginary component of the refractive index). An intuitive way to understand the response of a material is by applying a Fourier transform to the electric displacement field (D): $\vec{D}(t) = \varepsilon_0 \int_{-\infty}^{t} \varepsilon\left(t-t'\right) \vec{E}\left(t'\right) dt' \Longleftrightarrow \vec{D}(\omega) = \varepsilon_0 \varepsilon(\omega) \cdot \vec{E}(\omega)$. Here, the convolution of the dielectric constant (ε) with the applied electric field ($\vec{E}$) becomes a multiplication in Fourier space [1]. This transformation explains how a material acts as an impulse response to individual frequencies (through $\varepsilon(\omega) = \int_0^{\infty} \varepsilon(t) e^{-i\omega t} dt$), and therefore the response of a material in terms of dispersion, refraction, and linear absorption of light.

Light-matter interaction differs significantly when the incident light intensity is high enough to induce a nonlinear response. In optical spectroscopy, nonlinear interaction refers to phenomena that occur when the response of a material to an applied optical field depends nonlinearly on the strength of the field. Nonlinear interactions can give rise to a variety of effects, such as multiphoton absorption, high harmonic generation, and four-wave mixing. Even the refractive index acquires a nonlinear component (n_2) via the optical Kerr effect, where the refractive index of the material changes proportionally to the intensity of the light as $n = n_0 + n_2 I$ [2]. These nonlinear effects are extensively used in nonlinear spectroscopic techniques such as pump-probe and two-photon absorption spectroscopy, enabling enhanced spatial resolution, sensitivity, and temporal resolution compared to linear methods [3].

Several properties of light, including polarization, wavelength, intensity, and phase, can be utilized as optical probes to investigate material properties. The applications of these optical probes in various spectroscopic techniques, with a focus on absorption, scattering, and emission processes, are discussed below:

- Emission spectroscopy analyzes the light emitted by atoms or molecules as they transition from higher to lower energy states. The wavelength of the emitted photons corresponds to the energy difference between the discrete energy levels, providing insight into the material's electronic structure. In atoms, these transitions are typically between well-defined electronic energy levels, whereas in molecules, the emitted light may arise from transitions between vibronic states. Fluorescence spectroscopy is one example of emission spectroscopy, where a molecule absorbs light, typically in the ultraviolet or visible range, and then re-emits light at a longer wavelength (lower energy). This shift in energy between absorbed and emitted light is known as the Stokes shift.

  In the nonlinear interaction regime, techniques such as multiphoton fluorescence (MFL) and high harmonic generation (HHG) spectroscopy involve the absorption of two or more photons by a material. MFL spectroscopy involves the absorption of multiple photons, leading to emission at a longer wavelength (lower energy). In contrast, HHG produces photons with frequencies that are integer multiples of the incident photon frequency. [3, 4]. Consequently, emission-based spectroscopic techniques employ various optical probes, including wavelength tunability and emission intensity (to assess emitter concentration and efficiency), along with high temporal resolution in detection systems (for studying excited-state lifetimes)[3].

- Scattering spectroscopy is a technique used to study the interaction between light and matter by analyzing the light that is scattered by the material medium. In this process, light is scattered either elastically or inelastically. In elastic scattering (Rayleigh scattering), the wavelength of the scattered light remains unchanged, as there is no energy exchange between the photons and the material. In contrast, inelastic scattering, such as Raman or Brillouin scattering, involves an energy exchange between the light and the vibrational or acoustic modes of the material, leading to a shift in the wavelength. In the linear interaction regime, Rayleigh, Raman, and Brillouin scattering are widely used to probe the size, structure, and mechanical properties of molecules [2]. In the nonlinear regime, techniques like hyper-Raman scattering allow for the study of vibrational modes that are forbidden in linear Raman scattering due to symmetry constraints, providing deeper insight into molecular dynamics [3].

  In terms of optical probes, several properties of light are utilized by scattering-based spectroscopic techniques. These include the intensity of the scattered light, shifts in the scattered photon energies (revealing the vibrational or electronic states of the material), and the wavelength tunability of the incident light, allowing selective probing of different energy transitions.

- Absorption spectroscopy measures the amount of light absorbed by a material as a function of wavelength. It is primarily used to investigate the chemical and physical properties of atoms and molecules. In the linear regime, absorption spectroscopy is commonly utilized to determine the concentration of particles in a sample, following the Beer-Lambert Law, which relates absorbance to the concentration, path length, and molar absorptivity [2]. In the nonlinear regime, multiphoton absorption spectroscopy is widely used for studying electronic transitions, molecular structures, and optical properties. This nonlinear technique involves the simultaneous absorption of multiple photons, allowing access to the energy states inaccessible through a single-photon absorption. Several properties of light serve as optical probes in absorption spectroscopy, including the intensity of absorbed light (or transmittance), incident photon energies (where absorption at specific photon energies corresponds to electronic, vibrational, or rotational transitions), and temporal properties.

  Circular dichroism (CD) spectroscopy is a form of absorption spectroscopy that utilizes circularly polarized light to study materials exhibiting chirality. Such materials have ‘left-handed’ and ‘right-handed’ forms that are non-superimposable mirror images of each other. Chiral materials exhibit CD, defined as the differential absorption of left- and right-handed circularly polarized light, in both linear and nonlinear interaction regimes. The polarization of light (due to its chiral nature) is utilized as a probe to investigate the structural and optical properties of chiral materials. Thus, a chiral probe is employed to study chiral systems. This technique is particularly valuable in the pharmaceutical industry, where it is used to analyze the stereochemistry, purity, and conformational stability of chiral drugs, providing essential insights into drug efficacy and safety.

Thus far, we have explored how various spectroscopic techniques utilize polarization, wavelength, intensity, and temporal properties of light to probe the physical and chemical characteristics of matter. However, the phase of light can also be analyzed and utilized as a tool to study matter.

- Phase-based spectroscopy encompasses a variety of advanced techniques that analyze changes in the phase of light as it interacts with materials. For example, interferometric spectroscopy can be used to measure changes in the refractive index or thickness of a sample by analyzing phase differences between a reference and a sample beam. In microscopy, phase contrast techniques enhance image contrast by converting phase changes into brightness variations. In a nonlinear regime, techniques like Coherent Anti-Stokes Raman Spectroscopy (CARS) rely on precise phase matching conditions for the growth of the anti-Stokes signal beam, enabling the study of molecular structures and vibrational modes [2]. However, the challenges of accurately controlling and measuring the phase of light, along with the requirement for materials to exhibit low scattering, limit the applicability of these techniques to specialized research environments.

Therefore, a spectroscopic technique that can employ various properties of light, including phase, to examine different states of matter without necessarily requiring highly nonlinear substances or complex experimental setups (e.g., specialized detectors) would provide a valuable addition to the current toolkit.

In this dissertation, a novel *phase-based absorption spectroscopy* is introduced. This technique probes matter using light beams with helical wavefronts. These twisted wavefronts are associated with an orbital angular momentum (OAM) of $\pm l\hbar$ per photon. The handedness of these beams is characterized by the twisting of the wavefront undergoing l intertwined rotations within one wavelength. The chiral nature of the helical wavefront is analogous to the chiral structure of the electric field associated with circularly polarized light. The intensity profile of these beams is defined by a phase singularity (optical vortex) that leads to a null intensity region at the center of the beam. These beams are often referred to as *helical beams* or *optical vortex beams*. Additionally, the central phase singularity of the helical beams can be displaced to generate asymmetric beams. Our technique utilizes these asymmetric beams with the associated helical phase fronts as a *chiral probe* for investigating material properties. This technique is analogous to CD absorption spectroscopy, but instead of using polarization as a chiral probe, it employs the phase of light. The key features of this technique are outlined as follows:

- *Variable absorption*: The absorption of helical light by matter can be enhanced by displacing the phase singularity. This controlled absorption of helical light is observed across various phases of matter, including solids, liquids, gases, and metasurfaces. The underlying principle is applicable in both linear and nonlinear interaction regimes.
- *Differential response of matter*: When the matter is probed with the left- and right-handed asymmetric helical light, differential absorbance is observed. This phenomenon is defined as helical dichroism (HD). In the case of chiral materials, this technique offers an alternative to conventional CD spectroscopy, providing enhanced enantioselectivity due to its tunability and scalability.
- *Tunability and scalability*: The strength of the HD signal can be precisely tuned by displacing the phase singularity and scaled by changing the OAM value. Additionally, the signal strength can be controlled by varying the laser polarization. These unique features are absent in conventional absorption-based spectroscopic techniques.

- *Intrinsic response*: The HD signal is also detected in achiral molecules, metasurfaces, and amorphous solids. This observation challenges the conventional understanding that dichroism does not exist in achiral and amorphous materials. These observations broaden the scope of conventional absorption-based spectroscopy.
- *Ease of application*: This spectroscopy technique is based on transmission measurements and is not constrained by the requirement for materials exhibiting high nonlinearity. Moreover, this technique requires minimal to no sample preparation. As a result, it offers enhanced ease of application compared to several nonlinear spectroscopic methods.
- *Outreach*: Since the absorption of light is the first step in the emission mechanism, the underlying principle can be expanded to other spectroscopic methods. This approach has the potential to improve the signal efficiency of existing techniques, offering notable advantages for industrial applications.

This dissertation also introduces a controlled laser ablation technique with sub-wavelength scale precision. This ablation technique utilizes asymmetrical helical beams to manipulate matter at the sub-wavelength scale and shares similarities with the introduced spectroscopy method. The following section (1.1) discusses helical light beams carrying orbital angular momentum and their origin, as derived from Maxwell's equations.

1.1 Helical light carrying orbital angular momentum

Light, with its dual nature, can be described through both the wave theory and as particles, or 'energy quanta,' known as photons. Maxwell's equations provide a complete framework for understanding light as an electromagnetic wave, demonstrating its capacity to carry both energy and momentum. When light waves interact with matter, energy and momentum are exchanged. The momentum transferred from light to matter can be divided into linear and angular components. Angular momentum itself can be further divided into spin and orbital angular momentum. Spin angular momentum (SAM) is associated with the polarization of light, while orbital angular momentum (OAM) is related to the structure of the wavefronts.

In the plane wave approximation, light exhibits planar wavefronts where the Poynting vector is oriented along the direction of wave propagation. This results in energy transport perpendicular to the wavefronts. However, there is no physical restriction on the structure of wavefronts. A light beam can also carry azimuthally varying or 'helical' wavefronts. Such helical wavefronts undergo l intertwined rotations within one wavelength, which is described by the azimuthal phase factor $e^{il\phi}$ (where ϕ is the azimuthal coordinate)[5, 6, 7]. Due to the phase being undefined at the beam axis, the intensity profile of such helical beams is uniquely identified by the central singularity, leading to an annular profile (see Fig.1.1). Consequently, these beams are also known as optical vortex beams. In contrast to plane waves, the Poynting vector in helically phased beams follows a spiral path, indicating that energy is transported along this spiral trajectory.

In terms of a particle description, the rotation of an electric field (circularly polarized light) can be ascribed to the photons carrying a SAM of $\sigma\hbar$, where $\sigma = \pm 1$ (left- and right-handed circular polarization). For the helical light beams, the azimuthal phase structure is associated with the OAM of $l\hbar$ per photon, where the integer l is theoretically unbound[5, 6, 7]. The helical wavefronts, along with the corresponding intensity, phase, and associated OAM mode, are shown in Fig.1.1. When $l = 0$, the phase structure is trivial, consisting of a series of parallel wavefronts. For $l \geq 1$, the wavefront possesses a helical structure, where the number of intertwined helices is proportional to the magnitude of l, and the sign of l dictates the handedness of the helices.

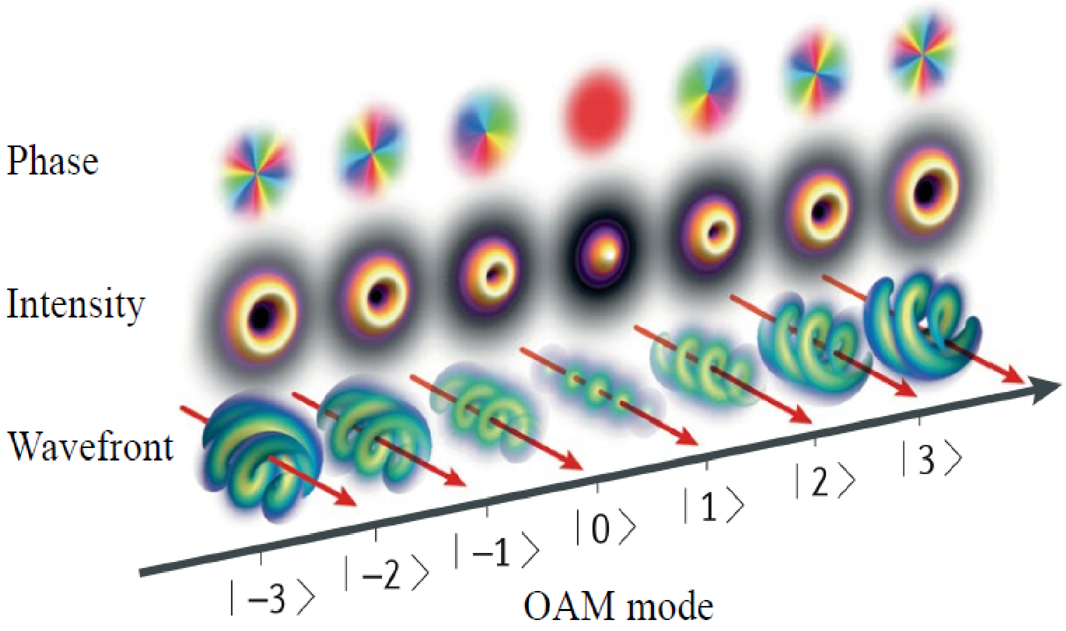

Figure 1.1: **Helical light beams**. The 2D phase profile, intensity pattern, and the twisted wavefront structure of the optical vortex or helical beams. The OAM mode carried by the beam is given beneath the black arrow. The image is reproduced from [8].

1.2 Wave equations - the paraxial approximation

Maxwell's equations constitute a set of relations that govern the behavior and propagation of electromagnetic fields in a material medium. For light propagation in free space, i.e., without sources ($\rho = 0$ and $J = 0$), Maxwell's equations are given by [9]

$$\nabla \cdot \mathbf{E} = 0, \quad \nabla \cdot \mathbf{B} = 0, \quad \nabla \times \mathbf{E} + \frac{\partial \mathbf{B}}{\partial t} = 0, \quad \nabla \times \mathbf{B} - \frac{1}{c^2}\frac{\partial \mathbf{E}}{\partial t} = 0 \tag{1.1}$$

Here $\mathbf{E}$ and $\mathbf{B}$ represent the electric and magnetic fields, respectively, and c represents the speed of light in a vacuum. Taking the curl of the third and fourth equations above and applying the vector identity $\nabla \times \nabla \times \tilde{\mathbf{E}} = \nabla(\nabla \cdot \mathbf{E}) - \nabla^2 \mathbf{E}$, we obtain

$$\left(\nabla^2 - \frac{1}{c^2}\frac{\partial^2}{\partial t^2}\right)\left\{ \begin{array}{c} \mathbf{E} \\ \mathbf{B} \end{array} \right\} = 0 \tag{1.2}$$

The above equation represents the electromagnetic fields propagating in free space. In static cases, fields can be fully determined by the charge and current densities. However, for time-dependent configurations, we can combine the above equations using the vector potential ($\mathbf{A}$) representation. The electric and magnetic fields in terms of the vector potential are given by $\mathbf{E} = -\nabla V - \frac{\partial \mathbf{A}}{\partial t}$ and $\mathbf{B} = \nabla \times \mathbf{A}$, where V is the scalar potential. Substituting these equations into the fourth Maxwell equation, we obtain

$$\nabla \times (\nabla \times \mathbf{A}) = -\mu_0 \epsilon_0 \nabla \left(\frac{\partial V}{\partial t}\right) - \mu_0 \epsilon_0 \frac{\partial^2 \mathbf{A}}{\partial t^2},$$

Using the vector identity mentioned above and rearranging, we obtain

$$\left(\nabla^2 \mathbf{A} - \mu_0 \epsilon_0 \frac{\partial^2 \mathbf{A}}{\partial t^2}\right) - \nabla \left(\nabla \cdot \mathbf{A} + \mu_0 \epsilon_0 \frac{\partial V}{\partial t}\right) = 0 \tag{1.3}$$

Here, ϵ_0 represents the electric permittivity, and μ_0 represents the magnetic permeability of free space, given by $c^2 = \frac{1}{\epsilon_0 \mu_0}$. The above equation does not impose any restrictions on the scalar potential V or the vector potential $\mathbf{A}$. External conditions can be applied to the potentials as long as the resulting electromagnetic fields remain unchanged. Such transformations are generally known as gauge transformations. The Lorentz gauge, ($\nabla \cdot \mathbf{A} = -\mu_0 \epsilon_0 \frac{\partial V}{\partial t}$), is a common choice to simplify the wave equation when describing electromagnetic waves in free space, or when the charge and current densities are well-defined [9]. Therefore, in the Lorentz gauge, vector potential follows a wave equation similar to that of electric and magnetic fields.

$$\nabla^2 \mathbf{A} - \frac{1}{c^2}\frac{\partial^2 \mathbf{A}}{\partial t^2} = 0 \tag{1.4}$$

The above equation can be simplified further by separating the time and spatial dependencies. This can be achieved by approximating the time dependence in the form of sinusoidal waves or in complex form as $\mathbf{A}(\mathbf{r},t) = \mathbf{A}(\mathbf{r})\exp(i\omega t)$ where ω is the angular frequency of the oscillating field. Therefore, the above equation becomes

$$\left(\nabla^2 + k^2\right)\mathbf{A}(\mathrm{r}) = 0 \tag{1.5}$$

Here, k is the wavevector, satisfying $k = \frac{\omega}{c}$. This equation is known as the Helmholtz equation, and a general solution to this differential equation can be expressed in terms of the plane wave solution: $\mathbf{A}(\mathbf{r}) = u_0 e^{-i\mathbf{k}\cdot\mathbf{r}}\hat{n}$, where u_0 is the field amplitude, k is the wavevector in the direction of wave propagation, and the unit vector $\hat{n}$ defines the direction of polarization. Plane waves are mathematical constructs and do not represent physically realizable solutions. The Fourier transform of a plane wave yields a delta function in k-space (Fourier space), which corresponds to a beam with a singular, perfectly defined wave vector and no spread in Fourier space. This reflects the infinite spatial extent and constant amplitude of a plane wave over an infinite volume, which is nonphysical.

Generally, for laser beams, electromagnetic fields spread slowly in the transverse direction and predominantly propagate along a single direction. Consequently, the paraxial approximation can be applied to the Helmholtz equation. In this approximation, the wave is assumed to travel primarily in one direction with only a small angular deviation. In Fourier space (**k**-space), this is reflected in the approximation $k_z = \sqrt{k^2 - k_x^2 - k_y^2}$, simplified as $k\left(1 - \frac{k_x^2+k_y^2}{2k^2}\right)$. This indicates that the **k**-vector is nearly parallel to the z-axis, with $k_z \gg k_x$ and k_y. As a result, a complex-valued amplitude envelope modulates the plane wave traveling in the propagation direction, represented by an exponential factor as

$$\mathbf{A}(\mathbf{r},t) = u(r)e^{-i(kz-\omega t)}\hat{n} \tag{1.6}$$

The paraxial approximation holds under the assumption that the second derivative of the amplitude function u changes gradually with respect to z, i.e. $\left|\frac{\partial^2 u}{\partial z^2}\right| \ll \left|k\frac{\partial u}{\partial z}\right|$ which is also known as the slowly varying amplitude approximation[2]. Substituting Eq.1.6 into Helmolt'z equation 1.5 and neglecting the second derivative term with respect to z from the Laplacian, we get

$$\frac{\partial^2 u}{\partial x^2} + \frac{\partial^2 u}{\partial y^2} - 2ik\frac{\partial u}{\partial z} = 0$$

$$\nabla_T^2 u - 2ik\frac{\partial u}{\partial z} = 0 \tag{1.7}$$

where transverse Laplacian is given as $\nabla_{\mathrm{T}}^2 = \partial^2/\partial x^2 + \partial^2/\partial y^2$.

The solution to the above equation, with the complex amplitude function $\mathbf{u}(r) = u(x,y,z)$, can be calculated in various coordinate systems, such as cylindrical and spherical coordinates.

This leads to the well-known higher-order modes, such as the Laguerre-Gaussian and Bessel modes, in addition to the standard Gaussian mode. These higher-order modes are discussed in subsequent sections.

1.2.1 Helical light carrying linear and angular momentum

This section demonstrates that linearly polarized light can acquire orbital angular momentum (OAM) by introducing an azimuthal phase term in the vector potential. Additionally, beams with a helical wavefront are shown to carry an OAM value of $l\hbar$ per photon. The following derivation is based on the theory published by L. Allen [6].

The spatial component of the vector potential (Eq.1.6) for linearly polarized light along the x-direction can be expressed as

$$\mathbf{A} = u(x, y, z)\exp(\mathrm{i}kz)\hat{\boldsymbol{x}} \tag{1.8}$$

Using the standard identities $\mathbf{E} = -\nabla V - \frac{\partial \mathbf{A}}{\partial t}$ and $\mathbf{B} = \nabla \times \mathbf{A}$, where the scalar potential V is substituted from the Lorentz gauge as $V = \frac{i}{\omega\mu_0\varepsilon_0}\nabla \cdot \mathbf{A}$ [9], the electric and magnetic fields are given as

$$\begin{aligned} \mathbf{E} &= i\omega\left[u\hat{x} + i\frac{\partial u}{k\partial x}\hat{z}\right]e^{ikz} \\ \mathbf{B} &= ik\left[u\hat{y} + i\frac{\partial u}{k\partial y}\hat{z}\right]e^{ikz} \end{aligned} \tag{1.9}$$

From these field equations, the averaged momentum density $\mathbf{g} = \varepsilon_0(\boldsymbol{E} \times \boldsymbol{B})$ can be evaluated. Additionally, the momentum density can be expressed in a gradient form by adding a term $\partial u/\partial z$ of order zero, given by

$$\mathbf{g} = \varepsilon_0\langle\boldsymbol{E} \times \boldsymbol{B}\rangle = \frac{\varepsilon_0}{2}\left[(\boldsymbol{E}^* \times \boldsymbol{B}) + (\boldsymbol{E} \times \boldsymbol{B}^*)\right] = \mathrm{i}\omega\frac{\varepsilon_0}{2}\left(u\nabla u^* - u^*\nabla u\right) + \omega k\varepsilon_0|u|^2\hat{z} \tag{1.10}$$

In the above expression, the amplitude function $u(x, y, z)$ is considered in Cartesian coordinates. However, the expression remains valid when transformed into cylindrical or spherical coordinate systems. Considering the amplitude function in cylindrical coordinates $u(r, \phi, z)$ with an azimuthally varying phase dependence $\exp(\mathrm{i}l\phi)$, given as

$$u(r, \phi, z) = u_0(r, z)\exp(\mathrm{i}l\phi) \tag{1.11}$$

As previously stated, the goal is to demonstrate that the exponential phase term, with explicit l dependence, produces a beam carrying OAM of $l\hbar$ per photon. Substituting the above equation into Eq.(1.10) (with the gradient considered in cylindrical coordinates), the azimuthal (ϕ) component of the momentum density is given by

$$\mathbf{g}_\phi = \varepsilon_0 \langle \boldsymbol{E} \times \boldsymbol{B} \rangle_\phi = \varepsilon_0 \omega l |u|^2 / r \tag{1.12}$$

The angular momentum (j_z) can be readily calculated from the linear momentum density as $j_z = \mathbf{r} \times \mathbf{g}_\phi$, resulting in the magnitude $j_z = \varepsilon_0 \omega l |u|^2$. Also, the energy density (w) can be calculated using $\mathrm{w} = c \cdot \mathbf{g}_z = c \cdot \varepsilon_0 \langle \boldsymbol{E} \times \boldsymbol{B} \rangle_z = \varepsilon_0 \omega^2 |u|^2$. By integrating j_z and w over the beam cross-section, the ratio of angular momentum to energy per unit length can be defined as

$$\frac{L_z}{W} = \frac{\iint r \ \mathrm{d}r \ \mathrm{d}\phi (\boldsymbol{r} \times \langle \boldsymbol{E} \times \boldsymbol{B} \rangle)_z}{c \iint r \ \mathrm{d}r \ \mathrm{d}\phi \langle \boldsymbol{E} \times \boldsymbol{B} \rangle_z} = \frac{\iint r \ \mathrm{d}r \ \mathrm{d}\phi \varepsilon_0 \omega l |u|^2}{\iint r \ \mathrm{d}r \ \mathrm{d}\phi \varepsilon_0 \omega^2 |u|^2} = \frac{\hbar l}{\hbar \omega} \tag{1.13}$$

This result is significant because it demonstrates that a linearly polarized beam with an azimuthal phase dependence of the form $\exp(\mathrm{i} l \phi)$ possesses OAM of $l\hbar$ per photon, independent of the polarization (SAM) of the light. For an elliptically polarized beam, the vector potential in Eq.(1.8) can be written as $\mathbf{A} = (\alpha \hat{\boldsymbol{x}} + \beta \hat{\boldsymbol{y}}) u(x, y, z) \exp(\mathrm{i} k z)$, where α and β are the weights of the electric field in the x- and y-directions. Therefore, for elliptical polarization, the ratio of total angular momentum to energy becomes (using Eq.1.10)

$$\frac{L_z}{W} = \frac{\hbar (l + \sigma)}{\hbar \omega} \tag{1.14}$$

where $\sigma = \mathrm{i} \left(\alpha \beta^* - \alpha^* \beta \right) = \pm 1$ represents right-handed or left-handed circularly polarized light, and 0 for linearly polarized light. This expression shows that the beam consists of photons with an OAM of $l\hbar$ and a SAM of $\sigma\hbar$.

The above results are valid only under the paraxial approximation. For *non-paraxial beams*, the separation of total angular momentum into OAM and SAM components is considered to be nonphysical [10, 11], as it violates gauge invariance. In fact, the results derived by L. Allen et al. for non-paraxial beams [6] show that the ratio of total angular momentum to energy includes an additional correction term compared to the paraxial results in Eq.(1.14). This correction term depends on σ; thus, for circularly polarized beams, it is not possible to separate the total angular momentum into distinct OAM ($l\hbar$) and SAM ($\sigma\hbar$) components. However, for linearly polarized beams ($\sigma = 0$), the correction term vanishes, and the beam possesses only the OAM component, as described by Eq.(1.14). Therefore, in both the paraxial and non-paraxial regimes, linearly polarized light can possess distinct OAM components.

From a historical standpoint, it was also shown that only the *transverse* component of the total angular momentum can be separated into gauge-invariant components of SAM and OAM

[12], which are physically measurable quantities [13], given as

$$\boldsymbol{J}_\perp = \boldsymbol{L}_\perp + \boldsymbol{S}_\perp,$$

where

$$\boldsymbol{S} = \varepsilon_0 \int \boldsymbol{E}_\perp \times \boldsymbol{A}_\perp \mathrm{d}^3\boldsymbol{r}, \quad \boldsymbol{L} = \varepsilon_0 \sum_i \int E^i_\perp (\boldsymbol{r} \times \boldsymbol{\nabla}) A^i_\perp \mathrm{d}^3\boldsymbol{r}. \tag{1.15}$$

In conclusion, irrespective of the theoretical and physical interpretations, a light beam can carry both the OAM and SAM. The following sections provide a more detailed discussion of the SAM and OAM associated with light beams.

1.3 Spin Angular Momentum - The light polarization

For transverse electromagnetic fields, polarization refers to the direction of the electric field vector, which oscillates perpendicular to the direction of propagation. In a plane wave solution to the paraxial wave equation, the resulting wave is linearly polarized in the arbitrary direction $\hat{x}$. Two such waves polarized in orthogonal directions can be expressed as

$$\mathbf{E}_1 = E_1 e^{i\mathbf{k}\cdot\mathbf{z} - i\omega t}\hat{\boldsymbol{x}}$$
$$\mathbf{E}_2 = E_2 e^{i\mathbf{k}\cdot\mathbf{z} - i\omega t}\hat{\boldsymbol{y}}$$

where E_1 and E_2 are complex field amplitudes. The linear combination of these fields results in a homogeneous plane wave, given by

$$\mathbf{E}(\mathbf{z}, t) = (\hat{\boldsymbol{x}} E_1 + \hat{\boldsymbol{y}} E_2)\, e^{i\mathbf{k}\cdot\mathbf{z} - i\omega t}$$

The amplitude and phase relationship between E_1 and E_2 determines the polarization state of the beam. In matrix notation, the above equation can be expanded as

$$\mathbf{E}(\mathbf{z}, t) = E_0 e^{i\mathbf{k}\cdot\mathbf{z} - i\omega t} \begin{bmatrix} \alpha e^{i\phi_x} \\ \beta e^{i\phi_y} \end{bmatrix} = E_0 e^{i\mathbf{k}\cdot\mathbf{z} - i\omega t} e^{i\phi_x} \begin{bmatrix} \alpha \\ \beta e^{i\phi} \end{bmatrix} \tag{1.16}$$

where α and β represent the weighting factors such that $\alpha^2 + \beta^2 = 1$, while ϕ_x and ϕ_y denote the respective phases associated with the x and y components of the electric field. The relative phase difference between two beams is given by $\phi = \phi_y - \phi_x$. For linearly polarized light, both fields have the same phase, such that $\phi = 0$. If the relative phase difference ϕ is between 0 and $\pi/2$, the light is elliptically polarized. For circularly polarized light, the weighting factors have the same magnitude ($\alpha = \beta$) and $\phi = \pm\pi/2$, where $+$ represents left-handed, and $-$ represents right-handed circularly polarized light.

Polarization is often characterized in terms of Dirac notation, which also facilitates linear vector operations. The two sets of linear polarizations, vertical $|V\rangle$ and horizontal $|H\rangle$, form a basis set that fully spans a two-dimensional vector space from which the polarization of light can be determined. Circular polarization can be expressed in this basis as $|L\rangle = \frac{1}{\sqrt{2}}(|H\rangle + i|V\rangle)$ for left circular polarization, and $|R\rangle = \frac{1}{\sqrt{2}}(|H\rangle - i|V\rangle)$ for right circular polarization. Elliptical polarization can also be defined as $\alpha|H\rangle + i\beta|V\rangle$. Another way to represent polarization is through Jones calculus, which is expressed in terms of matrices. The advantage of using the Jones matrix is that every optical element, such as polarizers and phase retarders, can be represented as matrices. Thus, the effect of optical elements on the incident light can be described by matrix multiplication with the Jones vector, allowing for straightforward computation in complex optical setups. For a linear polarization basis, Jones vectors are given by $|H\rangle = \begin{pmatrix} 1 \\ 0 \end{pmatrix}, |V\rangle = \begin{pmatrix} 0 \\ 1 \end{pmatrix}$, for a circular basis as $|L\rangle = \frac{1}{\sqrt{2}}\begin{pmatrix} 1 \\ i \end{pmatrix}, |R\rangle = \frac{1}{\sqrt{2}}\begin{pmatrix} 1 \\ -i \end{pmatrix}$, and $|D\rangle - |A\rangle$ bases representing diagonal and anti-diagonal are given as $|D\rangle = \frac{1}{\sqrt{2}}\begin{pmatrix} 1 \\ 1 \end{pmatrix}, |A\rangle = \frac{1}{\sqrt{2}}\begin{pmatrix} 1 \\ -1 \end{pmatrix}$.

The polarization of light is also associated with the SAM of light. This can be understood through the quantum theory of light, which treats light as composed of energy particles called photons. In a particle physics terminology, photons are bosons with integer spin (specifically, spin-1 gauge bosons); thus, the polarization degree of freedom represents the 'intrinsic' spin of these particles.

Classically, from Eq.(1.15), it can be shown that the SAM is $\pm\hbar$ for circularly polarized light. The SAM of light, in terms of the transverse field components, is expressed as

$$\mathbf{S_{rad}} = \frac{\varepsilon_0}{2i\omega} \int \mathbf{E}^* \times \mathbf{E} d\tau \tag{1.17}$$

The above formula is derived by substituting a monochromatic wave of frequency ω in Eq.(1.15) and applying the relationship $\mathbf{E} = -\nabla V - \frac{\partial \mathbf{A}}{\partial t}$ in the temporal gauge where $V = 0$. In the case of linear polarization, the electric field vector has the form $\mathbf{E} = \frac{E_0}{\sqrt{2}}\hat{x}$, and its complex conjugate remains unchanged as $\mathbf{E}^* = \frac{E_0}{\sqrt{2}}\hat{x}$. Therefore, for linear polarization, $\mathbf{E}^* \times \mathbf{E}$ evaluates to 0, and thus SAM = 0. In the case of circularly polarized light, the electric field is given by $\mathbf{E} = \frac{E_0}{\sqrt{2}}(\hat{x} + i\hat{y})$ (sign convention for left-handed circular polarization), and its complex conjugate is $\mathbf{E}^* = \frac{E_0}{\sqrt{2}}(\hat{x} - i\hat{y})$. Hence, $\mathbf{E}^* \times \mathbf{E}$ evaluates to $i|\mathbf{E}|^2\hat{z}$. From Eq.(1.17), we obtain

$$\mathbf{S_{rad}} = \pm\frac{\varepsilon_0}{2\omega} \int \mathbf{E}^2 \hat{z} d\tau \tag{1.18}$$

where ± represents the handedness of circularly polarized light. Similar to Eq.(1.13), the ratio of SAM to the energy density can be evaluated as

$$\frac{S_z}{W} = \frac{\pm\hbar}{\hbar\omega}$$

This classical description is consistent with the quantization of angular momentum in quantum optics. In the quantum mechanics analogy, the eigenvalue equation for the SAM operator acting on the photon eigenstate $|\psi\rangle$ is given by $\hat{S}_z|\psi\rangle = \sigma\hbar|\psi\rangle$, where σ is ±1 for circularly polarized light.

1.4 Orbital angular momentum - Helical phase front

The orbital angular momentum (OAM) carried by light provides an additional degree of control alongside SAM and is associated with the unique helical wavefront structure. Consequently, such helical beams are often referred to as structured light beams. In terms of a particle description, the helical wavefronts correspond to an OAM of $l\hbar$ per photon. This concept can be further understood using a quantum mechanical analogy. For paraxial beams, the linear momentum was derived in the form $u^*\nabla u - u\nabla u^*$ (Eq.1.10). This expression resembles the probability current expression in quantum mechanics [14], given as

$$\vec{J}[\varphi(\vec{r})] = \frac{\hbar}{2\mu i}\left[\varphi^*\nabla\varphi - \varphi\nabla\varphi^*\right]$$

where φ is the particle wave function, and μ is the mass of the particle. Using the above equation, the eigenvalue of $m_l\hbar$ for the angular momentum operator L_z acting on eigenmode φ can be derived[14]. Similarly, a helicity operator can be defined to act on the eigenmode $\mathbf{u}$, which represents the beam amplitude function in the paraxial equation (Eq.1.10). The eigenvalue equation associated with the helicity operator yields an eigenvalue of $l\hbar$ per photon, given as

$$\hat{L}_z|u\rangle = -\mathrm{i}\hbar\frac{\partial u}{\partial\phi} = l\hbar|u\rangle \tag{1.19}$$

Here, L_z is not a quantum mechanical operator but rather is defined as a helicity operator, which is derived by exploiting an analogy between the paraxial beam treatment and quantum mechanics. Other quantum mechanical properties, such as the orthogonality and normalization of the wave function, can similarly be extended to the beam amplitude function $\mathbf{u}$. It is important to note that the OAM and SAM operators do not behave like true quantum angular momentum operators, as they neither commute nor generate standard orbital rotations[13]. Nonetheless, both OAM and SAM are physically measurable properties of light beams[13].

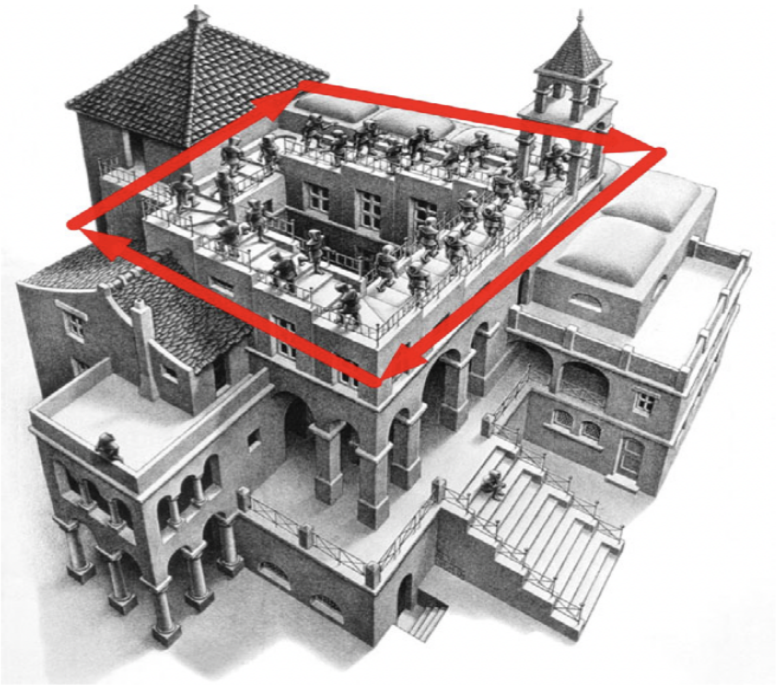

Figure 1.2: **Penrose stair**: The artistic impression for the topological structure of Penrose stairs. The image is reproduced from Shen et al. [15].

The helical wavefront structure of the OAM beams is dependent on the topological charge l. The topological charge arises due to the phase being undefined on the beam axis or around the central spot of a closed loop. The wavefront structure for different l values is shown in Fig.1.1. Physically, the topology of the phase structure can be understood with an analogy of Penrose stairs, shown in Fig.1.2 [15]. In such an artistic illustration, the ascending and descending stairs connect smoothly to their origin after a complete round trip. Even though this is merely an artistic representation and impossible in real space, it can be realized in phase space. The phase ϕ after completing a closed loop from 0 to $2\pi l$ returns to the origin, giving rise to the continuous smooth phase distributions.

1.5 Light modes with helical phase front

Light modes exhibiting helical wavefronts are solutions to the paraxial wave equation and are classified as higher-order electromagnetic modes. Examples of such paraxial solutions include Laguerre-Gaussian beams, Bessel beams, and Hyper-Geometric Gaussian beams. Among these helical light modes, the Laguerre-Gaussian (LG) mode was utilized in the theoretical framework of this research work. The LG mode has been extended to include an asymmetry parameter, resulting in the asymmetric LG mode, and its longitudinal field component has also been derived.

1.5.1 Laguerre-Gaussian Beams

The Laguerre-Gaussian (LG) mode set is one of the solutions to the paraxial wave equation. This higher-order electromagnetic mode forms a complete orthogonal basis in which other paraxial beams can be decomposed. The amplitude of the LG mode is characterized by Laguerre-Gaussian polynomials, as suggested by its name.

The LG mode field amplitude with azimuthal index l and radial index p is given as

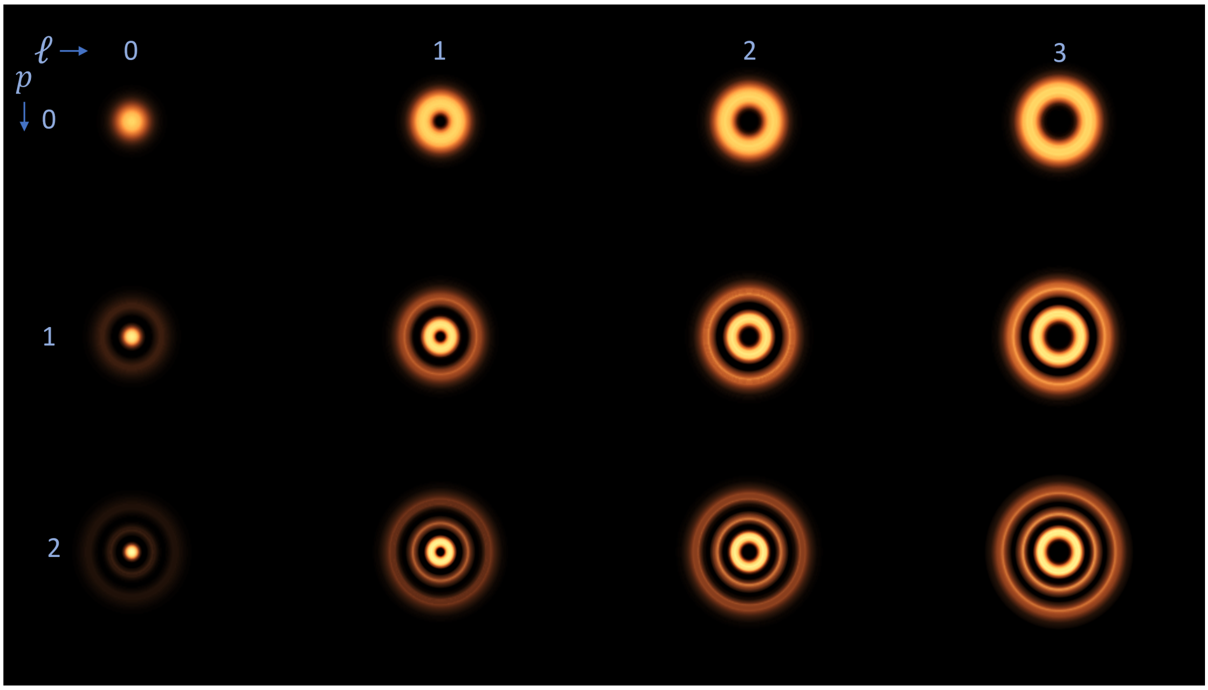

Figure 1.3: **Laguerre-Gaussian beams** with varying azimuthal index l and radial index p. The size of the central singularity increases with the higher OAM value

$$
\begin{aligned}
u(r,\phi,z) = & \frac{E_0}{w(z)} \left(\frac{r\sqrt{2}}{w(z)} \right)^{|l|} \exp\left(-\frac{r^2}{w^2(z)} \right) L_p^{|l|} \left(\frac{2r^2}{w^2(z)} \right) \times \\
& \exp\left(-ik\frac{r^2}{2R(z)} \right) \exp(-il\phi) \exp(i\psi(z))
\end{aligned}
\tag{1.20}
$$

where $w(z)$ is the beam waist as a function of z, given by $w(z) = w_0\sqrt{1+\frac{z^2}{z_R^2}}$, with $z_R = \frac{\pi w_0^2}{\lambda}$

as the Rayleigh range of the beam. Additionally, $R(z) = z\left(1 + \frac{z_R^2}{z^2}\right)$ represents the radius of curvature of the wavefronts, and L_p^l are the generalized Laguerre polynomials, with $L_0^l = 1$. The $\psi(z) = (N+1)\arctan\left(\frac{z}{z_{\mathrm{R}}}\right)$ is the Gouy phase with an additional phase difference of $(2\mathrm{p} + |\ell| + 1)$ in comparison to Gaussian beam, and is acquired as the beam propagates through the focal region. Additionally, E_0 is the normalization constant ($\int_0^{2\pi} d\phi \int_0^{\infty} rdr|u(r,\phi,z)|^2 = 1$), given as

$$E_0 = \sqrt{\frac{2p!}{\pi(p+|l|)!}}$$

here, the index l is the azimuthal phase index yielding OAM of $l\hbar$ per photon, and p characterizes the radial node of the LG mode. The effect of the radial node is that the transverse intensity profile of the beam has p dark nodal rings in addition to the central phase singularity. The intensity profiles of the few LG modes with varying l and p indices are shown in Fig.1.1.

The LG mode profile, described by Eq.(1.20), can also be expressed in Cartesian coordinates. The cartesian coordinate system is often used to describe asymmetric LG modes. The following section provides a detailed discussion of the asymmetrical mode.

1.5.2 Asymmetrical Laguerre-Gaussian beams - beyond paraxial

The intensity cross-section of the LG beam profile is radially symmetric with respect to the optical axis of the beam. An additional parameter, δ, was incorporated to introduce controlled asymmetry. This parameter allows the phase singularity to shift within the beam cross-section, resulting in an asymmetric Laguerre-Gaussian (aLG) beam. Consequently, the wavefront of the originally symmetric LG beam also becomes asymmetric. Figure 1.4 shows the corresponding phase and intensity pattern of the aLG beams.

The motivation for introducing asymmetry in the helical beams stems from the fact that breaking symmetry offers an additional degree of control for investigating the matter. Examples of symmetry violations leading to a deeper insight into physical interactions are well-known in particle physics, such as CPT violation. Similarly, in our research, introducing asymmetry in the beam enabled us to observe intrinsic dichroism in amorphous solids, achiral liquids, and metasurfaces.

The aLG beams were derived following the approach by Cerjan et al. [16], where full-field LG mode solutions were obtained using the angular spectrum method. The paraxial terms were derived from the full field components by neglecting the higher-order terms. The resultant paraxial components consist of a finite longitudinal component. Therefore, this solution was as termed the ‘correction to the paraxial regime.’ The longitudinal component was considered to take into account its linear dependence on l and finite OAM contribution. Recent works have emphasized the crucial role of the longitudinal component in the light-matter interaction. For

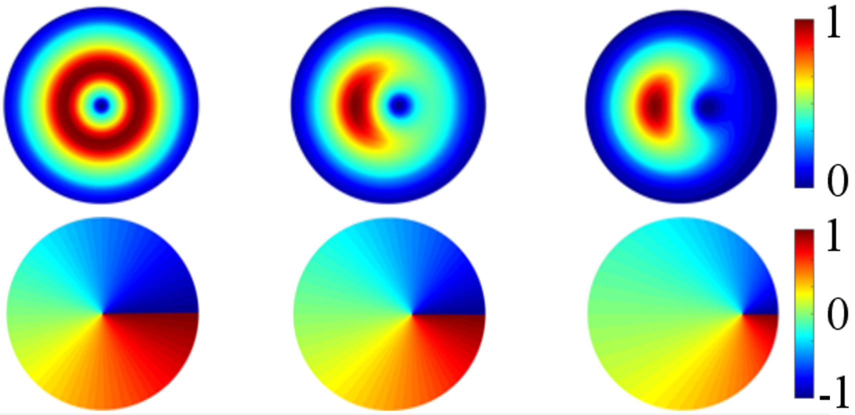

Figure 1.4: **Asymmetrical Laguerre-Gaussian beams.** Simulated intensity profiles of asymmetric OAM beams, along with the 2D phase pattern, obtained at different positions of the singularity.

example, helical light with a finite longitudinal component was used to probe the handedness of chiral nanoparticle aggregates [17]. In addition, the contribution of the longitudinal component becomes consequential when light is tightly focused (with a high NA objective).

The radial amplitude function $u(r, \phi, z)$ (Eq.1.20), at beam waist ($w(z) = w_0$), was transformed to Cartesian coordinates and the l-dependent term was expanded as a complex function with $r^{|l|}\exp(il\phi) = x \pm iy$. The phase singularity was displaced by introducing the asymmetry parameter δ as $x \mp i\eta\delta$ and $y \mp i\zeta\delta$, where η and ζ are parameters that enabled the rotation of the singularity in the x-y plane. The LG mode amplitude (Eq.1.20) in the case of aLG beams can be written as

$$u_o^{\pm}(x, y, z) = E_0 \exp[ikz] \left(\frac{\sqrt{2}\,((x \mp i\eta\delta) \pm i(y \mp i\zeta\delta))}{w_0} \right)^{|l|} \exp\left(-\frac{(x^2 + y^2)}{w_0^2}\right) L_p^{|(l)|}\left(\frac{2\rho^2}{w_0^2}\right) \tag{1.21}$$

To derive the longitudinal (E_z) component, fields with arbitrary polarization were considered and expressed as

$$\mathbf{E}(x, y, z) = (\alpha_z \hat{x} + \beta_z \hat{y})\, u_0(x, y, z) + E_z(x, y, \boldsymbol{z})\hat{\boldsymbol{z}}, \tag{1.22}$$

Applying the first Maxwell's equation ($\nabla \cdot \mathbf{D} = 0$), we get

$$E_z(x, y, z) = \alpha_z \frac{i}{k}\frac{\partial}{\partial x}\left(u_0(x, y, z)\right) + \beta_z \frac{i}{k}\frac{\partial}{\partial y}\left(u_0(x, y, z)\right) \tag{1.23}$$

The longitudinal component E_z can be derived by substituting Eq.(1.21) into the above equation, which is given below (Eq.1.24). However, this longitudinal component is only an approximate solution and is not completely accurate. This is because the full set of paraxial beams is not the exact solution of complete Maxwell's equations, and using the first Maxwell equation in the derivation is itself an approximation. Nonetheless, the resultant field is square-integrable, and the ratio of the total angular momentum flux with the energy flux reproduces results similar to those derived in Eq.(1.14) and matches the original results of L. Allen et al.[5]. The field components of the aLG in the context of paraxial corrections are detailed as follows:

$$\mathbf{E}^{\pm}(x,y,z) = \begin{cases} \alpha u_0^{\pm}(x,y,z) \\ \beta u_0^{\pm}(x,y,z) \\ if\left[(\alpha \pm i\beta)\,\frac{|l| w_0((x\mp i\eta\delta)\mp i(y\mp i\zeta\delta))}{(x\mp i\eta\delta)^2+(y\mp i\zeta\delta)^2} u_0^{\pm}(x,y,z) - \frac{2}{w_0}\left(\alpha(x)+\beta(y)\right) u_0^{\pm}(x,y,z)\right] \end{cases} \tag{1.24}$$

$$\mathbf{B}^{\pm}(x,y,z) = \begin{cases} -\beta \frac{k}{\omega} u_0^{\pm}(x,y,z) \\ \alpha \frac{k}{\omega} u_0^{\pm}(x,y,z) \\ if\frac{k}{\omega}\left[(\alpha \pm i\beta)\,\frac{|l| w_0((y\mp i\zeta\delta)\pm i(x\mp i\eta\delta))}{(x\mp i\eta\delta)^2+(y\mp i\zeta\delta)^2} u_0^{\pm}(x,y,z) - \frac{2}{w_0}\left(\alpha(y)-\beta(x)\right) u_0^{\pm}(x,y,z)\right] \end{cases} \tag{1.25}$$

where k represents the wave vector of the beam, ω is the laser frequency, $f = \lambda/2\pi w_0$, and $\rho = \sqrt{x^2+y^2}$. The $\pm$ represents the handedness or rotational direction of l, i.e., OAM, and p is the radial node. The α and β represents the normalized polarization factors such that $|\alpha|^2 + |\beta|^2 = 1$. The normalization constant E_0 for asymmetric beams was obtained by integrating the intensity overall space (i.e., ∞ to $+\infty$), for $(l = 1)$ it is given as:

$$E_0 = \sqrt{\frac{2k^2 w_0^2}{\pi\left(\alpha^2+\beta^2\right)\left(2w_0^2 + k^2 w_0^4 + 2\left(\zeta^2+\eta^2\right)\delta^2\left(1+k^2 w_0^2\right)\right)}} \tag{1.26}$$

This discussion concludes the theoretical background on the origin of the OAM of light, the paraxial approximation for the helical light modes, and the description of the asymmetric Laguerre-Gaussian mode. The following section discusses various experimental techniques used to generate helical-phased beams.

1.6 Generating helical light beams

Several techniques for generating helical light beams are discussed in this section. In our research, the q-plate device was used to generate the unique asymmetrical helical light beams, which is also discussed in detail.

1.6.1 Diffractive optical elements

The diffractive optical elements can be readily designed to mimic any desired refractive element. Such elements have been a popular choice for producing helical beams. When a Gaussian beam is incident on the "forked diffraction grating", the helically phased beam is produced as the first diffraction order. This unique forked diffraction grating is generated by the interference of a planar wavefront beam, $\psi_1 = e^{ikx}$, with the beam having a helical wavefront $\psi_2 = e^{il\theta}$. The interference of these two beams is directly proportional to the following transfer function [18]:

$$H = |\psi_1 + \psi_2|^2 = \left|e^{ikx} + e^{il\theta}\right|^2 = 2[1 + \cos(kx - l\theta)]$$

Fig.1.5 shows the simulated and experimentally produced interference patterns. The two patterns are in good agreement. The interference pattern is distinctly characterized by a forked structure, which splits proportionally to the l-index of the interfering beam. When such a diffraction grating is illuminated by the Gaussian beam $\psi_G = e^{-r^2/w^2}$, the resulting far-field diffraction pattern can be computed as the Fourier transform of the product $\psi_G H$, where H is the transfer function and ψ_G is the input radial distribution function. Thus, the diffracted beam in the far field is given by

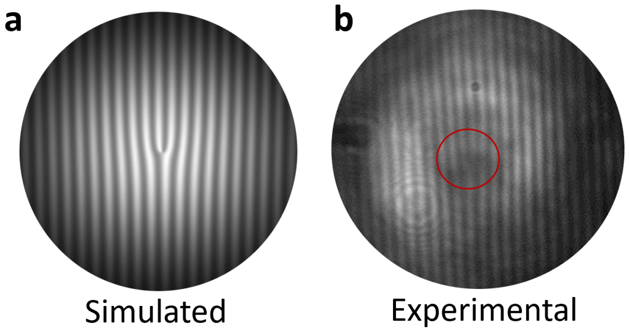

Figure 1.5: **Forked interference pattern** generated upon the superposition of beams with planar and helical wavefronts. **(a)** shows simulated forked grating. For comparison, experimentally obtained superposition is shown in **(b)**, where the red circle highlights the forked part.

$$I = \mathcal{F}\left[\psi_G H\right] = \mathcal{F}\left[e^{-(r/w)^2}\left|e^{ik_x x} + e^{im\theta}\right|^2\right] \tag{1.27}$$

The Fourier transform of $\psi_G H$, representing the diffraction of Gaussian beam by the forked grating structure, is shown in the following Fig.1.6.

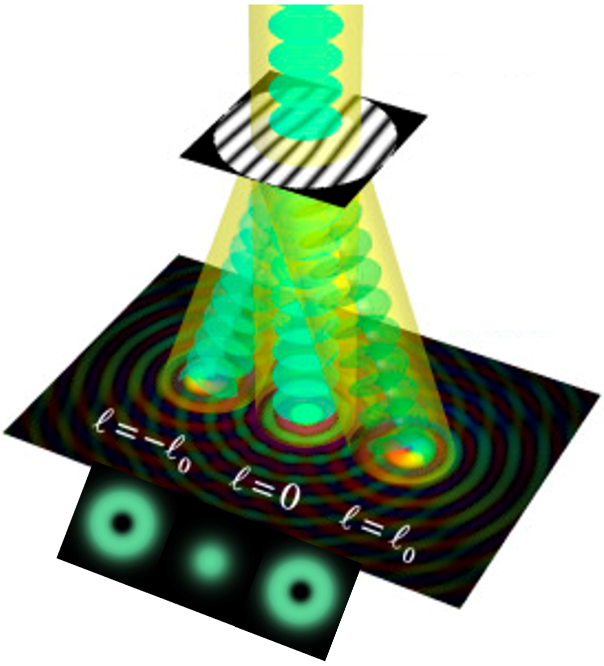

Figure 1.6: **Diffraction via forked rating**. The figure shows the diffraction of incident Gaussian light with a planar wavefront, equivalent to the Fourier transform of $\psi_G H$ (Eq.1.27), resulting in a central Gaussian beam with two adjacent first-order OAM beams ($l = 1$ and $l = -1$) with helical phase fronts. Part of this image is reproduced from Alicia et al.[18]

Here, the diffraction results in a central Gaussian beam (zeroth-order, $n = 0$) and two adjacent first-order helical beams corresponding to opposite handedness of the helical wavefronts, with $l = 1$ and $l = -1$, respectively. Thus, the resulting output effectively forms holograms of the input optical components and, therefore, is often referred to as 'computer-generated holograms' (CGHs). These holograms eliminate the need for costly grating fabrication and can be easily programmed onto pixellated liquid crystal devices such as spatial light modulators (SLMs).

1.6.2 Spiral-phase plate

Helical light modes can also be generated using a refractive optical element, such as a spiral phase plate (SPP). A schematic of the SPP is shown in Fig. 1.7. The SPP resembles a rotating staircase, where the thickness of the dielectric material increases around the azimuthal angle. The height of each dielectric step is given by [19]

$$h = \ell\lambda\theta / \left[2\pi\left(n - n_0\right)\right]$$

where l is the topological charge (OAM of $l\hbar$) of the resultant beam, n_0 is the refractive index of the surrounding medium, n is the refractive index of the dielectric material, λ is the wavelength of the incident beam, and θ is the azimuthal angle. When a light beam with a planar wavefront propagates through the SPP, it acquires an additional phase due to the increasing spiral thickness in the azimuth direction. This azimuth-dependent phase results in a beam with a helical wavefront structure, which is characterized by a topological charge l. SPPs are advantageous for their high conversion efficiency, making them ideal for high-power laser beams. However, they are limited to producing a single mode and require highly precise fabrication.

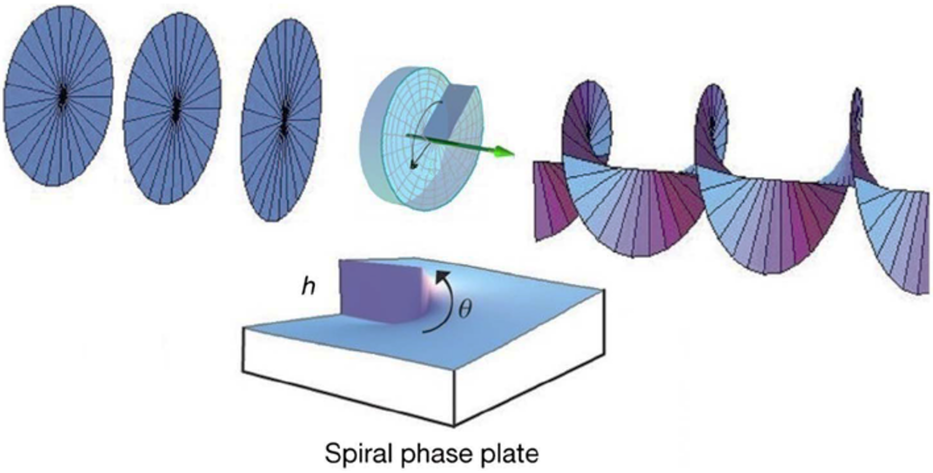

Figure 1.7: **Spiral phase plate(SPP)**. Working principle of an ideal SPP element. An incident optical wavefront undergoes azimuthal phase delay while maintaining the direction of the optical axis. This figure is reproduced from [19].

1.6.3 Q-plate

Several methods for wavefront reshaping using refractive and diffractive optical elements have been discussed. However, the primary focus here is on an optical method that employs the concept of Pancharatnam–Berry (PB) phases to generate helical wavefronts [20, 21]. The PB phase refers to the phase shift that arises when the local polarization state of light traces a closed loop on the Poincaré sphere (a geometric representation of polarization states) [22]. Upon completing the closed loop, the final polarization state differs from the initial state by a phase factor or the PB phase[20, 23, 24]. Optical devices that utilize this principle are known as Q-plates and were first introduced in 2006 [25, 20].

A q-plate is a liquid crystal (LC)-based optical device with a specific azimuthal arrangement of the LC molecular director around a central point. The following section discusses the experimental and technological advantages of a q-plate compared to other methods.

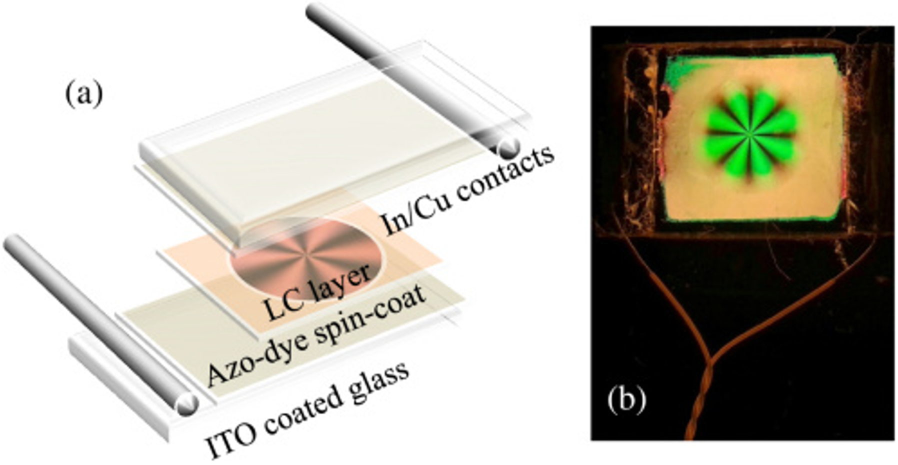

Figure 1.8: **Q-plate** consisting of different optical layers, including liquid crystals, is shown in image (a), and image (b) displays a real device through a crossed-polarizer. The image is reproduced from Rubano et al.[26].

1.6.3.1 Key advantages of Q-plate

Q-plates offer several experimental, technological, and practical advantages over alternative optical devices. In our experiments, helical light beams were generated using the q-plates. The key advantages are as follows[26]

- **Conversion efficiency**: The practical utility of any wavefront-shaping device largely depends on its ability to convert incident light efficiently. With an average conversion efficiency of over $> 97\%$, q-plates are notably efficient for practical applications.
- **Robust optics**: A Q-plate is a portable LC-based optical device that is both compact and stable during continuous use. Its conversion efficiency decreases very slowly over time and requires minimal maintenance.
- **Experimental**: A q-plate offers an advantage over reflective optics by operating in a transmission geometry, which is easier to implement experimentally. Depending on the

application, these devices can be custom-designed for broadband frequencies and ultrafast lasers. Additionally, like any transmission-based optic, the effect of the q-plate on the incident beam can be quantified using the Jones matrix formalism[27].

- **Electrical tuning and superposition**: A q-plate can be electrically tuned to achieve either optimal conversion efficiency or controlled partial OAM conversion. In a transmission geometry, multiple q-plates can be arranged sequentially (cascaded). When coupled with electrical tuning, cascading enables the coherent superposition of SAM and OAM states without the need for complex interferometric setups.
- **Controlled asymmetry**: A Q-plate is a thin LC cell that can easily be mounted on a 2-D translation stage. By calibrating the translation of the stage with the phase singularity, controlled asymmetry can be introduced into the beam profiles. In our research, asymmetrical helical beams were generated using this 2-D translation stage.

1.6.3.2 Structure and working principle of Q-plates

The q-plate comprises a thin LC cell sandwiched between glass plates with azimuthally patterned coatings, as shown in Fig. 1.8a. The orientation of liquid crystals (LCs) is typically characterized by a unit vector **n**, called molecular director, which represents an average local orientation of the anisotropic LCs. Unlike standard LC cells, the molecular director **n** in q-plates is oriented in a specific azimuthal pattern in the cell plane around the central point (origin). Mathematically, the angle between the direction of **n** and the reference axis is expressed in terms of the angle α as

$$\alpha(\phi) = q\phi + \alpha_0.$$

where ϕ is the azimuthal angle, q represents the topological charge, with $l = \pm 2q$ (corresponding to an OAM of $l\hbar$ per photon), and α_0 is the initial angle of the LC director. The physical interpretation of this equation is that for any circular path centered at the origin, the LC director **n** undergoes q complete rotations around itself, where q can be negative depending on the molecular director's rotation direction. Since q is related to the rotation of **n**, it can also take half-integer values. To align the LC molecules along the specific azimuthal pattern, the coating layer of the LC cells is etched accordingly prior to introducing the LCs. The most common method for achieving this etching pattern is through the photo-alignment of dye molecules in the coating layers, which is discussed in the following section.

Another key characteristic of q-plates is their ability to be electrically tuned, enabling precise control over the phase conversion of incident light. This tunability is governed by the parameter δ, which represents the total birefringent phase retardation of the LC film. Typically, the phase retardation of any thin LC film is a function of its thickness. However, the alignment of LC molecular directors can also be modulated by an applied electric field, resulting in controlled phase retardation. This property facilitates the electrical modulation of the q-plate, allowing it to be switched on and off with minimal adjustment to other system parameters.

The effect of a q-plate on the incident beam can be described by the unitary operator $\hat{U}$. When a beam with defined SAM (σ) and topological charge (q) is incident on the q-plate, the portion of the beam is modulated by a factor of $\sin^2(\delta/2)$. This fraction of the beam undergoes a conversion, reversing its SAM and altering its OAM by a factor of $\pm 2q$. The remaining portion of the beam (unconverted photons) retains its initial SAM and OAM states, modulated by a factor of $\cos^2(\delta/2)$. In bra-ket notation, the unitary operator $\hat{U}$ acts on the incident beams with left-handed (SAM $\sigma = +1$) and right-handed (SAM $\sigma = -1$) circular polarization as follows

$$\begin{cases} \hat{U}|L\rangle = \cos(\delta/2)|L\rangle + \mathrm{i}\sin(\delta/2)|R\rangle \mathrm{e}^{+2\mathrm{i}\alpha(\phi)}, \\ \hat{U}|R\rangle = \cos(\delta/2)|R\rangle + \mathrm{i}\sin(\delta/2)|L\rangle \mathrm{e}^{-2\mathrm{i}\alpha(\phi)} \end{cases} \tag{1.28}$$

Optimal conversion of all input photons is achieved when the phase retardation is adjusted to $\delta = \pi$. At this setting, the output acquires a helical phase of $\pm 2\alpha(\phi) = \pm 2\,(q\phi + \alpha_0)$, and all input photons are converted from right- to left-handed circular polarization (and vice versa). Under these conditions, the first term vanishes (see Eq.1.28), enabling full conversion. When a tuned q-plate ($\delta = \pi$) with $q = 1$ is used, the total angular momentum (SAM + OAM) of the photons remains constant, allowing the change in the photon's SAM to be completely transferred to its OAM [20]. Thus, q-plates are often referred to as SAM-to-OAM conversion optics. This process is schematically shown in the Fig.1.9. When a linearly polarized beam is incident on a perfectly tuned q-plate, the output is a superposition of SAM and OAM eigenmodes. This occurs because linear polarization can be decomposed into a combination of $|L\rangle$ and $|R\rangle$ states. Consequently, the output beam is a superposition of $|L\rangle$ and $|R\rangle$ states, each with opposite OAM states, as described by Eq.1.28. Such beams are known as vector vortex beams (VVBs), characterized by non-uniform transverse polarization patterns, which have attracted increasing interest across various research fields[28, 29, 30]. These beams were pivotal for achieving sub-wavelength positional resolution in the phase-based laser ablation method, as discussed in Chapter 7.

The fabrication process of the q-plate is briefly discussed in the following section. For all of our experiments, the q-plates were fabricated and provided to us by our collaborator, Professor Ebrahim Karimi's group.

Q-plate fabrication

This section focuses on the commonly used photo-alignment technique for fabricating q-plates [26]. This technique enables the production of q-plates with both integer and half-integer values of q, although the maximum absolute value of $|q|$ is constrained by experimental protocols and

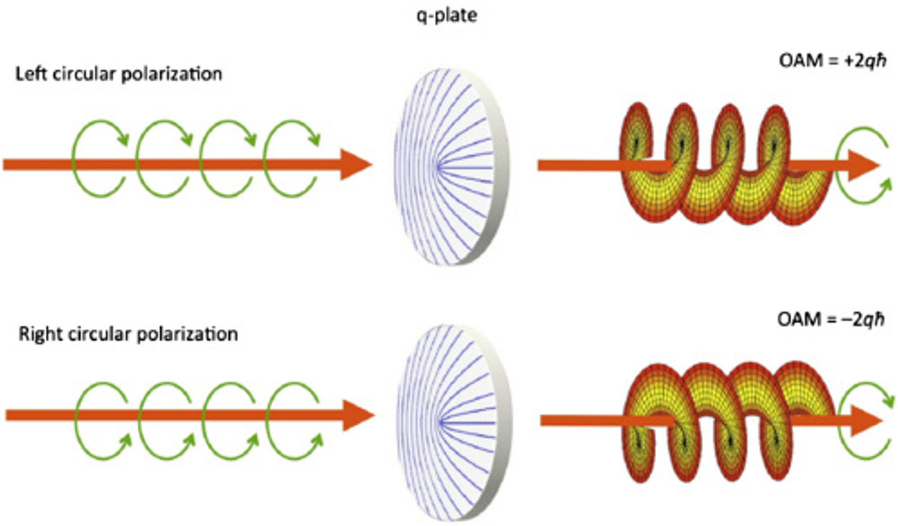

Figure 1.9: **Working principle of the q-plate** This image shows the optimally tuned q-plate ($\delta = \pi$), leading to the full SAM to OAM conversion. This image is reproduced from[26]

technological limitations. A simplified schematic of the photo-alignment process is shown in Fig.1.10.

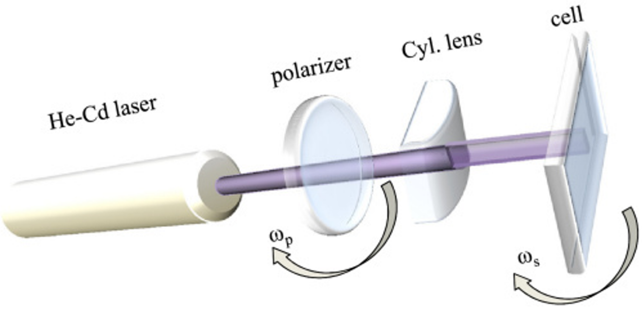

Figure 1.10: **Simplified photo-alignment setup.** The incident light polarization and the liquid crystal cell are both rotated with different angular velocities, as shown. This image is reproduced from[26]

As previously mentioned, the q-plate typically consists of LCs enclosed between glass plates coated with a specific material. In this method, two glass plates coated with indium-tin-oxide (ITO) are used due to ITO's well-known electrical conductivity and transparency. Prior to introducing the LC between these ITO-coated plates, each glass surface is spin-coated with a photosensitive azo dye. The birefringence of the LC cell depends on the cell's thickness; thus, to ensure precise and uniform thickness, dielectric micro-spacers are placed between the glass plates before they are glued together. This process results in an empty LC cell that remains open on two sides.

In the next step, a specific azimuthal pattern is inscribed onto the photosensitive dye by exposing it to near UV light. The alignment of the azo-dye is dependent on the input polarization and tends to reorient perpendicular to the polarization direction. The input laser polarization is precisely controlled using a combination of a half-wave plate and a polarizer. This polarized light is focused through a cylindrical lens to create a line focus, illuminating only a narrow angular section of the empty cell. For detailed patterning, a half-wave plate, a polarizer, and the sample are systematically rotated using motorized mounts that can be remotely controlled. The desired pattern is achieved by adjusting the rotational ratios of these motors. After exposure, LCs are introduced between the plates, which are then sealed on the open sides. Copper wires are attached to the ITO coatings post-sealing, allowing complete control over the birefringent phase retardation δ through external AC voltages, thus enabling the electrical tuning capability of the q-plate.

References

[1] R.N. Bracewell. *The Fourier Transform and Its Applications.* McGraw-Hill Kogakusha, Ltd., Tokyo, second edition edition, 1978.

[2] Robert W. Boyd. *Nonlinear Optics.* Academic Press, Inc., third edition, 2008.

[3] S. Mukamel. *Principles of Nonlinear Optical Spectroscopy.* Oxford Series in Optical and Imaging Sciences. Oxford University Press, 1995.

[4] M. Chergui, M. Beye, S. Mukamel, et al. Progress and prospects in nonlinear extreme-ultraviolet and x-ray optics and spectroscopy. *Nat Rev Phys*, pages 578–596, 2023.

[5] L. Allen, M. W. Beijersbergen, R. J. C. Spreeuw, and J. P. Woerdman. Orbital angular momentum of light and the transformation of laguerre-gaussian laser modes. *Phys. Rev. A*, 45, Jun 1992.

[6] L. Allen, M.J. Padgett, and M. Babiker. Iv the orbital angular momentum of light. volume 39 of *Progress in Optics*, pages 291–372. Elsevier, 1999.

[7] Miles Padgett, Johannes Courtial, and Les Allen. Light's orbital angular momentum. *Physics Today*, 57(5):35–40, 05 2004.

[8] Eliahu Cohen, Hugo Larocque, Frédéric Bouchard, Farshad Nejadsattari, Yuval Gefen, and Ebrahim Karimi. Geometric phase from aharonov-bohm to pancharatnam-berry and beyond. *Nature Reviews Physics*, 1:437–449, 2019.

[9] John David Jackson. *Classical Electrodynamics.* John Wiley & Sons, New York, third edition edition, 1999.

[10] J. M. Jauch and F. Rohrlich. *The Theory of Photons and Electrons: The Relativistic Quantum Field Theory of Charged Particles with Spin One-half.* Springer, 1976.

[11] L. C. Biedenharn and James D. Louck. *Angular Momentum in Quantum Physics: Theory and Application.* Cambridge University Press, 1984.

[12] Claude Cohen-Tannoudji, Jacques Dupont-Roc, and Gilbert Grynberg. *Photons and Atoms: Introduction to Quantum Electrodynamics.* Wiley-Interscience, 1989.

[13] S. J. van Enk and G. Nienhuis. Spin and orbital angular momentum of photons. *Europhysics Letters*, 25:497, 1994.

[14] Jun John Sakurai. *Modern Quantum Mechanics; Rev. Ed.* Addison-Wesley, Reading, MA, 1994.

[15] Yijie Shen, Xuejiao Wang, Zhenwei Xie, Changjun Min, Xing Fu, Qiang Liu, Mali Gong, and Xiaocong Yuan. Optical vortices 30 years on: Oam manipulation from topological charge to multiple singularities. *Light: Science and Applications*, 8:1–29, 2019.

[16] Alexander Cerjan and Charles Cerjan. Orbital angular momentum of laguerre–gaussian beams beyond the paraxial approximation. *Journal of the Optical Society of America A*, 28(11):2253, 2011.

[17] Ward Brullot, Maarten K Vanbel, Tom Swusten, and Thierry Verbiest. Resolving enantiomers using the optical angular momentum of twisted light. *Science Advances*, 2(3):e1501349, 2016.

[18] Alicia V. Carpentier, Humberto Michinel, José R. Salgueiro, and David Olivieri. Making optical vortices with computer-generated holograms. *American Journal of Physics*, 76(10):916–921, 2008.

[19] M. Massari, G. Ruffato, M. Gintoli, F. Ricci, and F. Romanato. Fabrication and characterization of high-quality spiral phase plates for optical applications. *Applied Optics*, 54:4077–4083, 2015.

[20] L. Marrucci, C. Manzo, and D. Paparo. Pancharatnam-berry phase optical elements for wavefront shaping in the visible domain: switchable helical modes generation. *Applied Physics Letters*, 88:221102, 2006.

[21] Julio C. Gutiérrez-Vega. Pancharatnam–berry phase of optical systems. *Optics Letters*, 36:1143–1145, 2011.

[22] Edward Collett. *Field Guide to Polarization.* SPIE Press, 2005.

[23] Thomas F. Jordan. Berry phases for partial cycles. *Physical Review A*, 38:1590, 1988.

[24] David J. Griffiths. *Introduction to Quantum Mechanics.* Cambridge University Press, 2018.

[25] L. Marrucci, C. Manzo, and D. Paparo. Optical spin-to-orbital angular momentum conversion in inhomogeneous anisotropic media. *Physical Review Letters*, 96:163905, 2006.

[26] Andrea Rubano, Filippo Cardano, Bruno Piccirillo, and Lorenzo Marrucci. Q-plate technology: a progress review [invited]. *Journal of the Optical Society of America B*, 36(5):D70–D87, 2019.

[27] Sam Delaney, María M. Sánchez-López, Ignacio Moreno, and Jeffrey A. Davis. Arithmetic with q plates. *Applied Optics*, 56:596–600, 2017.

[28] Kohei Toyoda, Fuyuto Takahashi, Shun Takizawa, Yu Tokizane, Katsuhiko Miyamoto, Ryuji Morita, and Takashige Omatsu. Transfer of light helicity to nanostructures. *Physical Review Letters*, 110:143603–1–143603–5, 2013.

[29] M. G. Rahimian, A. Jain, H. Larocque, P. B. Corkum, E. Karimi, and V. R. Bhardwaj. Spatially controlled nano-structuring of silicon with femtosecond vortex pulses. *Scientific Reports*, 10:1–11, 2020.

[30] Rui Chen, Krishna Agarwal, Colin J. R. Sheppard, and Xudong Chen. Imaging using cylindrical vector beams in a high numerical-aperture microscopy system. *Optics Letters*, 38:3111–3114, 2013.

Chapter 2

Helical light-matter interaction

2.1 Introduction

In the previous chapter, it was established that light waves carry energy and angular momentum, specifically spin angular momentum (SAM) - associated with polarization, and orbital angular momentum (OAM) - associated with the helical wavefront. The interaction of helical beams with matter involves an intrinsic exchange of momentum, a fundamental aspect of light-matter interaction [1]. This momentum transfer gives rise to radiation and gradient forces, resulting in polarization- and phase-dependent effects [2, 3]. In fact, the transfer of SAM to matter, resulting in the generation of mechanical torque, was investigated over 70 years ago [4]. The macroscopic transfer of OAM (and SAM) has also been demonstrated in optical tweezers, where trapped particles initiated rotation according to the total angular momentum of light (SAM+OAM)[1, 5]. These findings also serve as experimental proof that light can carry OAM independent of SAM, in accordance with the theoretical predictions (see Chapter 1).

The influence of SAM in probing electron transitions has been extensively studied, resulting in various effects such as optical rotation (OR) [6], circular dichroism (CD), and photoelectron circular dichroism (PECD). CD refers to circular polarization-dependent differential absorption of light [7], while PECD involves polarization-dependent differential photo-ionization of electrons [8]. In CD, electronic transitions are facilitated by the coupling of electric dipoles and magnetic dipoles [7, 9], whereas in PECD, they are mostly governed by electric dipole-dominant transitions [8, 10]. In all of these techniques, circular polarization (SAM) is utilized as a chiral probe. Chirality is a property of asymmetry, where a system is considered chiral if it cannot be superimposed on its mirror image. Chiral probes are required to investigate materials that lack specific symmetries, such as mirror planes (σ), improper rotations (S_n), and centers of inversion (i). Materials exhibiting these broken symmetries are classified as chiral materials [11]. In contrast, isotropic materials such as symmetric achiral molecules and amorphous solids are indifferent to the handedness of circular polarization and do not exhibit any of the aforementioned phenomena. Thus, both the symmetry of the material and the properties of light govern light-matter interactions, as a chiral probe is needed to investigate the chiral materials.

The twisting wavefront of the helical beams can also serve as a chiral probe to study electron transitions, an alternative to utilizing polarization as a probe. The advantage of using phase is that the associated OAM ($l\hbar$ per photon) is not limited, as the azimuthal index l is theoretically unbounded, while SAM can only take two defined values ($\sigma = \pm 1\hbar$). However, early studies were not successful in demonstrating the efficacy of using a helical phase front as a chiral probe. These studies were mostly limited to the linear absorption regime [12, 13] and focused solely on the coupling of the electric and magnetic dipole transition moments (E1M1 coupling term), inspired by the CD phenomenon. Recently, several theoretical studies concluded that the helical phase-based dichroism can only be observed in chiral molecules [14] and ordered solid-state media [15]. Additionally, they concluded that the combination of both SAM and OAM is required to observe such effects. Experimentally, the helical phase was recently demonstrated as a chiral probe to study powdered chiral molecular media [16], chiral metasurfaces [17], and chiral molecules adsorbed onto the plasmonic nanoparticle aggregates [18]. These materials exhibited helical dichroism (HD), which is defined as differential absorption of left- and right-handed helical light, analogous to CD.

Most of the previous studies were limited to investigating chiral media primarily in the linear absorption regime, often using nanoparticles and explicit chiral geometries as external intermediaries. These studies concluded that the HD vanishes in the case of randomly oriented achiral molecules and amorphous solids. The reason for the vanishing of the HD signal was that these studies focused only on the E1M1 coupling term and employed symmetric helical beams. In addition, due to the isotropic averaging in the randomly orientated molecules, they often neglected the contribution of the coupled electric dipole-quadrupole transition moment (E1E2) to the overall electron transition rate. Therefore, there is a need for a comprehensive helical light-matter interaction model focusing on the role of the OAM of light in investigating different phases of matter. In addition, the proposed model should investigate phase-based electronic transitions in both linear and nonlinear regimes and address the following questions: (1) *Do chiral molecules and chiral crystalline solids exhibit phase-based differential absorption without the use of any external intermediary*? (2) *Can the phase of light be used to study unoriented achiral molecules and amorphous solids*? and (3) *If these effects exist, then in which interaction regime are they observed?*

In this chapter, theoretical models describing the helical light-matter interaction in linear and nonlinear interaction regimes are presented. These models predict that both chiral and achiral molecules exhibit phase-dependent HD effects. Moreover, helical dichroism is not only limited to the molecular case; crystalline and amorphous solids also exhibit phase-dependent preferential absorption. The presence of dichroism in isotropic amorphous solids and unoriented achiral molecules challenges the conventional wisdom, as these materials exhibit no preferential response when studied with polarization as a probe. Furthermore, the simulated outcomes of the discussed models were in qualitative agreement with the experimental results (see Chapters

3 to 7).

The following section discusses different material symmetries in the case of molecules and solids. In Section 2.3, the single photon transition rate is derived considering the multipole transition moments within the framework of time-dependent perturbation theory. The results are verified by deriving the energy absorption rate (which is proportional to the single photon transition rate) via the induced multipoles in Appendix *A*. In Subsection 2.3.1, the origin of CD in chiral systems is discussed, and the origin of the HD in both isotropic achiral and chiral molecules, including enantiomeric solutions, is discussed in Subsection 2.3.2. In Section 2.4, the electronic transitions in the case of a nonlinear regime, including different possible mechanisms (based on the incident energy), are discussed. First, the multiphoton transition rate based on the perturbation theory is derived, followed by the intermediate nonlinear regime between multiphoton and strong field tunneling transitions, defined as multiphoton-assisted tunneling (MPAT). This intermediate regime is responsible for the phenomenon of HD in amorphous solids. The experimental methods and techniques are discussed in Section 2.5.

2.2 Material symmetry in different phases of matter

The response of matter to the applied electromagnetic fields is influenced by the symmetry of the material. Symmetry plays a key role in determining the optical, chemical, electronic, and physical properties of atoms, molecules, and solids. In solids, symmetry is described by the arrangement of atoms or molecules within the crystal lattice, typically classified using space groups. In molecules, symmetry refers to the spatial arrangement of atoms and is described by point groups. Molecules exhibit various symmetry elements, such as rotation axes (C_n), mirror planes (σ), inversion centers (i), and improper rotation axes (S_n). These symmetry elements are essential for determining chemical properties, such as molecular chirality, optical activity, and other properties. The distinction between chiral and achiral molecules is particularly important, as it affects their interactions with electromagnetic fields and other molecules.

Achiral molecules are characterized by their property of being superimposable to their mirror images, which results from the presence of a mirror plane (σ) symmetry element. In addition to mirror symmetry, achiral molecules can also exhibit other symmetry elements, such as an inversion center (i), rotation axes (C_n), and improper rotation axes (S_n). For example, Fig.2.1 shows the achiral methane molecule (CH_4) and its mirror image, which is superimposable with each other. Methane molecules possess six mirror planes, inversion, and several axes of rotational symmetry, including four C_3 axes and three C_2 axes. The C_3 axes allow rotation by 120° degrees (360°/3), and the C_2 axes allow rotation by 180° (360°/2), both of which restore the molecule to a configuration indistinguishable from its original state. It also exhibits improper rotation S_6 axes (60° rotation followed by a reflection through a plane perpendicular to the axis).

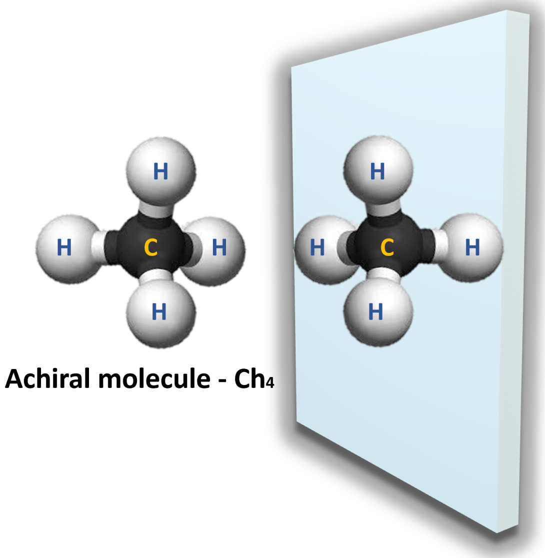

Figure 2.1: **Achiral molecule.** The mirror image of the achiral tetrahedral methane molecule (CH_4) is shown. The molecule is superimposable on its mirror image.

In terms of light-matter interaction, when the polarization of light is used as a probe, these molecules do not exhibit optical activity (no net rotation of the plane of polarization). Thus, they are indifferent to the incident light polarization, and no polarization-based dichroism effects are observed.

Chiral molecules lack the symmetry elements found in achiral molecules, such as mirror planes or centers of inversion. A molecule is considered chiral when it is non-superimposable on its mirror image and does not possess any plane of symmetry. Enantiomers are pairs of molecules that are mirror images of each other but cannot be superimposed, exhibiting opposite chirality (as shown in Fig.2.2). Despite their mirror-image structures, enantiomers have identical physical and chemical properties when analyzed in achiral environments. Such enantiomers can only be discerned in chiral environments or when the probe is chiral in nature. The circular polarization of light serves as a chiral probe to differentiate enantiomers. When illuminated with left- or right-handed circularly polarized light, enantiomer pairs exhibit differential absorption, resulting in circular dichroism (see Sec. 2.3).

Differentiating enantiomers is crucial for applications such as drug development, where a molecule's chirality can significantly influence its biological effectiveness. Enantiomers of a chiral drug may exhibit different biological activities; one enantiomer may be therapeutic, while the other could be inert or even harmful. The thalidomide drug, introduced in the late 1950s, serves as a powerful example of the significance of chirality in pharmaceuticals and its profound implications for drug safety. Thalidomide exists in two enantiomeric forms: R-

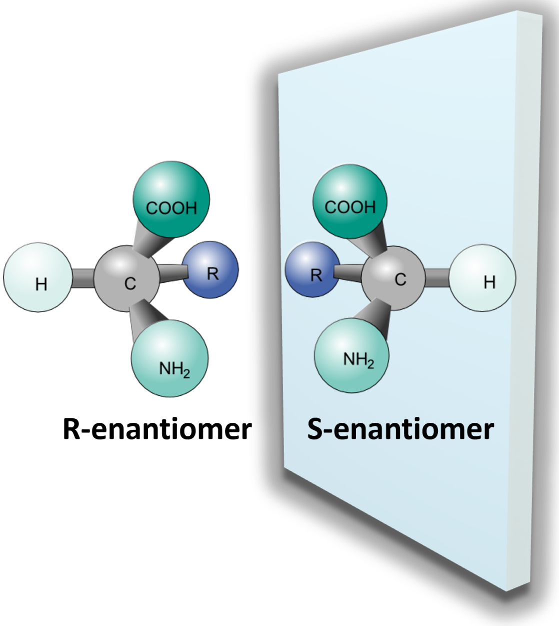

Figure 2.2: **Chiral molecule.** The mirror image of a chiral generic amino acid molecule and the original molecule, which are non-superimposable, are called enantiomers. They are identified by their R- or S- configurations, indicating their handedness

thalidomide, which has effective sedative properties, and S-thalidomide, which is teratogenic and causes developmental abnormalities. Initially marketed as a sedative to treat morning sickness in pregnant women, thalidomide led to one of the most infamous drug disasters in history, resulting in severe birth defects due to the presence of the harmful S-enantiomer.

Mathematically, the parity operator, P, can be used to describe chiral molecules. The parity operator transforms a point $\mathbf{r}$ in space to $-\mathbf{r}$. In quantum mechanics, this operator describes how the spatial configuration of a molecule changes under coordinate inversion, $(x, y, z) \rightarrow (-x, -y, -z)$. The eigenvalues of the parity operator are ± 1, corresponding to even: $\psi_+(x, y, z) = \psi_+(-x, -y, -z)$, and odd: $\psi_-(x, y, z) = -\psi_-(-x, -y, -z)$ wavefunctions, respectively. When the parity operator is applied to a chiral molecule's wavefunction, it produces a wavefunction that corresponds to its mirror image, essentially generating the enantiomer.

$$P\psi_R = \psi_S,$$

Furthermore, in the case of the stationary state solution of the molecular Schrödinger equation, each enantiomer can be associated with symmetric and antisymmetric wavefunctions for their ground energy states. For example, the R-enantiomer can be assigned the symmetric ground state $\Psi_s^g = \frac{1}{\sqrt{2}}(\psi_+^g + \psi_-^g)$, while the antisymmetric $\Psi_{as}^g = \frac{1}{\sqrt{2}}(\psi_+^g - \psi_-^g)$ can be assigned to the S-enantiomer, where Ψ_+ (Ψ_-) is even (odd) under parity. This assignment can be justified as a consequence of slight asymmetry in the molecular potential and is considered a parity violation argument [19, 20]. Applying the parity operator to such states results in

$$P\psi_s^R = P\left(\frac{1}{\sqrt{2}}(\psi_+^g + \psi_-^g)\right) = \frac{1}{\sqrt{2}}(\psi_+^g - \psi_-^g) = \psi_{as}^S \tag{2.1}$$

Therefore, applying the parity operator recovers the opposite-handed enantiomer, demonstrating how both enantiomers are non-superimposable mirror images of each other.

Symmetry in solids

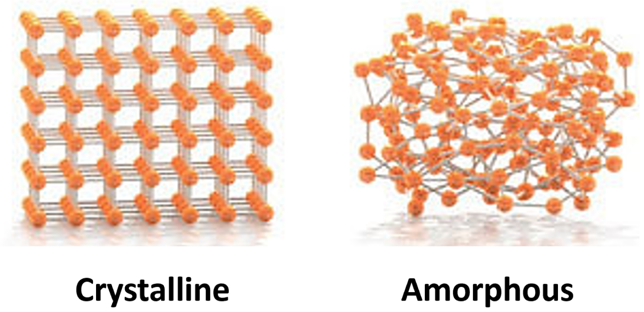

Figure 2.3: 3-Dimensional structure of **(a)** Crystalline solids and **(b)** Amorphous solids . Crystalline solids are uniquely recognized by the presence of long-range order, whereas amorphous solids lack such order.

Solids can be broadly classified into two categories based on the arrangement of atoms or molecules within their crystal lattice: crystalline solids (c-solids) and amorphous solids (a-solids). Figure 2.3 shows the 3-dimensional structure of a c-solid and a-solid.

Crystalline solids are characterized by their highly ordered structures, where atoms, ions, or molecules are arranged in a three-dimensional lattice that repeats over a long-range order. This long-range order gives rise to distinct directional-dependent (or crystal orientation-dependent) physical and electrical properties. Crystalline structures can exhibit several symmetry elements, including rotational axes, mirror planes, and inversion centers. These elements form the basis for classifying materials into one of the 230 distinct space groups, each defining a unique set of symmetry operations. For example, crystals that are non-centrosymmetric (lacking an inversion center) are crucial for applications requiring nonlinear optical properties, such as second-harmonic generation[21].

C-solids can be further divided into chiral and achiral systems. In chiral c-solids, the entire crystal lattice lacks a mirror symmetry or a center of inversion. Therefore, the lattice acts as a chiral center. Consequently, crystals can exhibit chirality even if their constituent molecules are achiral. A common example of a chiral c-solid is quartz, which can be left-handed or right-handed, depending on the direction in which the helical chains of SiO_4 spiral along the c-axis. This is illustrated in Fig.2.4.

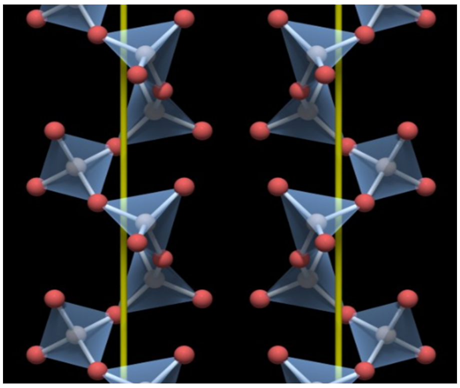

Figure 2.4: **Chiral quartz structure.** 3-dimensional helical chains of SiO_4 tetrahedral spiral forming **(a)** left - **(b)** right- handed quartz structures. Here, red spheres represent the oxygen atoms, and gray represents the silicon atom. This image is reproduced from [22]

Similar to molecules, chiral crystalline solids exhibit differential absorption of circularly polarized light, known as solid-state CD. However, the solid-state CD signal in these materials is often obscured by linear birefringence and macroscopic anisotropies [23]. Consequently, distinguishing chiral crystals requires sophisticated techniques, further complicated by the need for large, high-purity single crystals [24].

Amorphous solids: In contrast to their crystalline counterparts, amorphous solids (a-solids) lack long-range order, with atoms or molecules arranged randomly (see Fig.2.3b). Consequently, a-solids are isotropic, meaning their physical properties are identical in all directions and independent of their orientation. The absence of translational and rotational symmetry also means that amorphous solids do not exhibit differential absorption of polarized light, making them optically indifferent to polarization as a probe. Despite their lack of symmetry in terms of long-range order, a-solids are characterized by the presence of short- and medium-range order, which preserves some degree of ordered structuring at small scales. In the amorphous glass, this short- to medium-range order can extend up to 20 Å [25, 26, 27].

The study of short- and medium-range order in a-solids is an active field of research [28], as such order can result in phenomena typically observed in c-solids and influence other physical properties. In fact, this small-scale order is responsible for the formation of delocalized valence and conduction band energy states. In contrast, the long-range disorder in a-solids leads to the development of band tail states between energy bands. The long-range disorder in amorphous solids also prevents all atoms from satisfying their bonding requirements, resulting in uncoordinated bonds known as dangling bonds. These dangling bonds, which can carry positive or negative charges, give rise to localized tail states that extend into the bandgap from below the conduction band edge and above the valence band edge [29]. Additionally, neutral dangling bonds, along with defects and impurities, contribute to the formation of localized states in the middle of the bandgap [29]. The energy bands in a-solids with band tail states are shown in Fig.2.5.

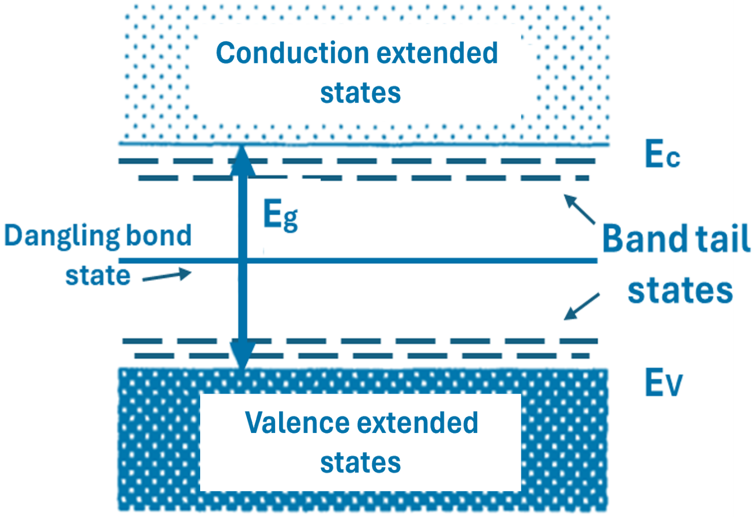

Figure 2.5: **Schematic illustration of energy bands in a-solids**. The bandgap is represented by E_g. Part of this image is reproduced from [29]

In the following section, single-photon absorption facilitated by helical light beams is derived. Additionally, the origin of polarization-based CD and phase-based HD effects is discussed in detail.

2.3 Single-photon absorption - Fermi's Golden Rule

In the linear interaction regime, the electron transition rate due to the single-photon absorption is calculated using quantum-mechanical perturbation theory. Our approach is based on the multiphoton absorption theory presented by R. W. Boyd[21]. Figure 2.6 illustrates the process of single-photon absorption between the ground state $|\mathrm{g}\rangle$ and the excited state $|\mathrm{m}\rangle$.

The time-dependent Schrödinger equation, with the atomic wavefunction $\psi(\mathbf{r}, t)$, is given by[30]

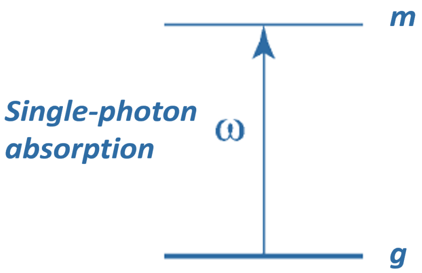

Figure 2.6: **Single-photon absorption** The process of absorption of photons (ω) between the ground state $|\mathrm{g}\rangle$ and the excited state $|\mathrm{m}\rangle$.

$$i\hbar\frac{\partial\psi(\mathbf{r},t)}{\partial t} = \hat{H}\psi(\mathbf{r},t), \tag{2.2}$$

where $\hat{H}$ represents the Hamiltonian operator of the system. Moreover, it can be represented as

$$\hat{H} = \hat{H}_0 + \hat{V}(t). \tag{2.3}$$

where $\hat{H}_0$ is the field-free Hamiltonian for a free atom, and $\hat{V}(t)$ is the interaction Hamiltonian describing the interaction of the atom with the electromagnetic field. The multipolar Hamiltonian in the case of helical light-matter interaction is given as

$$\boxed{\hat{V}(t) = -\mu_\alpha E_\alpha(t) - \frac{1}{3}\theta_{\alpha\beta}\nabla_\alpha E_\beta(t) - m_\alpha B_\alpha(t) - \ldots} \tag{2.4}$$

where μ represents the electric dipole moment, m the magnetic dipole moment, and $\theta_{\alpha\beta}$ the total electric quadrupole moment tensor. In the helical light-matter interaction, the inclusion of multipoles, particularly the quadrupole (which couples with the field gradient), is necessary. Thus, the variation in the field gradients results in a significant quadrupole term, which can have a magnitude comparable to the electric dipole interaction term. The electromagnetic fields in Eq.(2.4) are considered to be monochromatic waves; consequently, the interaction Hamiltonian can be expressed as

$$V(t) = Ve^{-i\omega t} + V^{*}e^{i\omega t} \tag{2.5}$$

where $V = -\mu_\alpha E_\alpha - \frac{1}{3}\theta_{\alpha\beta}\nabla_\alpha E_\beta - m_\alpha B_\alpha - \ldots$, with time dependence written separately.

The solution to the time-dependent Schrödinger equation for the ground state of a free atom (in the absence of an external field) can be explicitly written as

$$\psi_n(\mathbf{r},t) = u_n(\mathbf{r})e^{-i\omega_n t}, \qquad \text{where } \omega_n = E_n/\hbar. \tag{2.6}$$

where energy eigenstates E_n are associated with the eigenvalue equation $\hat{H}_0 u_n(\mathbf{r}) = E_n u_n(\mathbf{r})$. In the presence of a time-dependent multipolar interaction potential $\hat{V}(t)$, Schrodinger equation is given as

$$i\hbar\frac{\partial\psi(\mathbf{r},t)}{\partial t} = \left(\hat{H}_0 + \hat{V}(t)\right)\psi(\mathbf{r},t). \tag{2.7}$$

Since the energy eigenfunction $u_n(\mathbf{r})$ of the free atom span a complete set of basis functions $\hat{H}_0$, the solution to the above equation can be written as a linear combination of these eigenfunctions

$$\psi(\mathbf{r},t) = \sum_l a_l(t)u_l(\mathbf{r})e^{-i\omega_l t}.$$

Substituting the above wavefunction in the Eq.(2.7)

$$\begin{aligned} i\hbar\sum_l \frac{da_l}{dt}u_l(\mathbf{r})e^{-i\omega_l t} + i\hbar\sum_l\left(-i\omega_l\right)a_l(t)u_l(\mathbf{r})e^{-i\omega_l t} \\ = \sum_l a_l(t)E_l u_l(\mathbf{r})e^{-i\omega_l t} + \sum_l a_l(t)\hat{V}u_l(\mathbf{r})e^{-i\omega_l t} \end{aligned}$$

where the second term on the left and the first term on the right are identical since $E_l u_l(\mathbf{r}) = \hbar\omega_l u_l(\mathbf{r})$. The above expression can be further simplified by using the orthogonality condition $\int u_m^*(r)u_l(r)d^3r = \delta_{ml}$ in the above equation

$$i\hbar\frac{da_m}{dt} = \sum_l a_l(t)V_{ml}e^{-i\omega_{lm}t} \tag{2.8}$$

where ω_{lm} represents the difference in frequencies given by $\omega_{lm} = \omega_l - \omega_m$ and V_{ml} is a matrix element of the interaction Hamiltonian, given by

$$V_{ml} \equiv \left\langle u_m|\hat{V}|u_l\right\rangle = \int u_m^*\hat{V}u_l d^3r$$

The matrix form of a Schrödinger's equation is solved using the time-dependent perturbation theory. To facilitate this, a perturbation expansion parameter λ is introduced, and V_{ml} is replaced by λV_{ml} in Eq.(2.8). Additionally, $a_m(t)$ is expanded as a power series in the strength λ of the perturbation, as follows

$$a_m(t) = a_m^{(0)}(t) + \lambda a_m^{(1)}(t) + \lambda^2 a_m^{(2)}(t) + \cdots.$$

Substituting the above expression in Eq.(2.8) and equating both the left and right sides in powers of λ, we get

$$\frac{da_m^{(N)}}{dt} = (i\hbar)^{-1} \sum_l a_l^{(N-1)} V_{ml} e^{-i\omega_{lm} t}, \quad N = 1, 2, 3, \ldots \tag{2.9}$$

In the linear absorption regime, substituting $N = 1$ for single-photon absorption in the above equation. In addition, it is assumed that in the absence of an external electromagnetic field, the atom remains in its ground state ($|g\rangle$), given by $a_g^{(0)}(t) = 1, \quad a_l^{(0)}(t) = 0 \quad \text{for} \quad l \neq g$. Substituting these conditions into Eq.(2.9), we get

$$\frac{da_m^{(1)}}{dt} = -(i\hbar)^{-1} \left[V_{mg} e^{i(\omega_{mg}-\omega)t} + V_{mg}^{*} e^{i(\omega_{mg}+\omega)t} \right] \tag{2.10}$$

where $V = -\mu_\alpha E_\alpha - \frac{1}{3}\theta_{\alpha\beta}\nabla_\alpha E_\beta - m_\alpha B_\alpha$. By integrating the probability amplitude in the equation up to an arbitrary time t, we obtain

$$a_m^{(1)}(t) = \frac{V_{mg}}{\hbar\left(\omega_{mg} - \omega\right)} \left[e^{i(\omega_{mg}-\omega)t} - 1 \right] + \frac{V_{mg}^{*}}{\hbar\left(\omega_{mg} + \omega\right)} \left[e^{i(\omega_{mg}+\omega)t} - 1 \right] \tag{2.11}$$

Here, the first term represents the single-photon absorption, and the second term represents the stimulated emission process. Using the rotating wave approximation (neglecting the second term), the probability $p_m^{(1)}(t)$ that the atom is in the state m after absorbing the single photon at time t is given by

$$p_m^{(1)}(t) = \left| a_m^{(1)}(t) \right|^2 = \frac{\left| V_{mg} \right|^2}{\hbar^2} \left| \frac{e^{i(\omega_{mg}-\omega)t} - 1}{\omega_{mg} - \omega} \right|^2 = \frac{\left| V_{mg} \right|^2}{\hbar^2} \frac{4\sin^2\left[\left(\omega_{mg} - \omega\right) t/2 \right]}{\left(\omega_{mg} - \omega\right)^2} \equiv \frac{\left| V_{mg} \right|^2}{\hbar^2} f(t) \tag{2.12}$$

where $f(t) = \frac{4\sin^2[(\omega_{mg}-\omega)t/2]}{(\omega_{mg}-\omega)^2}$ represents a form of the Sinc function. For large times, i.e., $t \to \infty$, the central peak of the $f(t)$ vs ω curve can be approximated by a delta function. In mathematical terms, this approximation is known as expanding the $\delta(x)$ function as a generalized function (a sequence of functions)[31]. This approximation is written as

$$\lim_{t\to\infty} f(t) = 2\pi t \delta\left(\omega_{mg} - \omega\right)$$

Substituting the above into the probability Eq.(2.12), we get

$$p_m^{(1)}(t) = \frac{\left| V_{mg} \right|^2 t}{\hbar^2} 2\pi \delta\left(\omega_{mg} - \omega\right)$$

In real physical situations, the presence of a delta function in the probability of finding an atom in the excited state is unrealistic. Due to various line-broadening mechanisms, the transition frequency ω_{mg} is not precisely defined. Instead, it is spread over a continuous range (density of states). As a result, the delta function is replaced by the density of states function, or line shape function, $\rho_f\left(\omega_{mg}=\omega\right)$. To account for this substitution, the delta function in the previous equation is replaced by the density of states function. Additionally, the probability $p_m^{(1)}(t)$ is averaged over all possible values of the transition frequency, leading to

$$p_m^{(1)}(t)=\frac{\left|V_{mg}\right|^2 t}{\hbar^2}2\pi\rho_f\left(\omega_{mg}=\omega\right)$$

The transition rate for single-photon absorption in the case of a multipolar interaction Hamiltonian is given by

$$\boxed{R_{mg}^{(n)}=\frac{p_m^{(n)}(t)}{t}=\frac{2\pi}{\hbar^2}|(m|V|g\rangle|^2\rho\left(\omega_{mg}=\omega\right)=\frac{2\pi}{\hbar^2}\left|-\mu_\alpha^{mg}E_\alpha-\frac{1}{3}\theta_{\alpha\beta}^{mg}\nabla_\alpha E_\beta-m_\alpha^{mg}B_\alpha\right|^2\rho\left(\omega_{mg}=\omega\right)} \tag{2.13}$$

This result represents a special case of Fermi's golden rule. The rule is general and can be applied to any quantum system describing the transitions resulting from weak perturbations. Expanding the modulus square in the above equation

$$\begin{aligned}R_{mg}^{(1)}=\tfrac{2\pi}{\hbar^2}&\Big(\left(\mu_\alpha^{mg}E_\alpha\right)\left(\mu_\alpha^{mg}E_\alpha\right)^*+\left(\mu_\alpha^{mg}E_\alpha\right)\left(m_\alpha^{mg}B_\alpha\right)^*+\left(\mu_\alpha^{mg}E_\alpha\right)\left(\tfrac{1}{3}\theta_{\alpha\beta}^{mg}\nabla_\alpha E_\beta\right)^*+\left(m_\alpha^{mg}B_\alpha\right)\left(\mu_\alpha^{mg}E_\alpha\right)^*\\&+\left(m_\alpha^{mg}B_\alpha\right)\left(\tfrac{1}{3}\theta_{\alpha\beta}^{mg}\nabla_\alpha E_\beta\right)^*+\left(m_\alpha^{mg}B_\alpha\right)\left(m_\alpha^{mg}B_\alpha\right)^*+\left(\tfrac{1}{3}\theta_{\alpha\beta}^{mg}\nabla_\alpha E_\beta\right)\left(\mu_\alpha^{mg}E_\alpha\right)^*+\left(\tfrac{1}{3}\theta_{\alpha\beta}^{mg}\nabla_\alpha E_\beta\right)\left(m_\alpha^{mg}B_\alpha\right)^*\\&+\left(\tfrac{1}{3}\theta_{\alpha\beta}^{mg}\nabla_\alpha E_\beta\right)\left(\tfrac{1}{3}\theta_{\alpha\beta}^{mg}\nabla_\alpha E_\beta\right)^*\Big)\rho\left(\omega_{mg}=\omega\right)\end{aligned}$$

Here the interaction between electric dipoles (μ_α^{mg}) is referred to as E1E1 interaction. Similarly, electric dipole–magnetic dipole coupling is termed E1M1, and electric dipole-quadrupole coupling is referred to as E1E2. Neglecting the M1M1, M1M2, and M1E2 terms due to the comparatively smaller magnitude of magnetic dipoles, we obtain

$$\begin{aligned}R_{mg}^{(1)}=\frac{2\pi}{\hbar^2}&\Big[\left|\mu_\alpha^{mg}\right|^2\left|E_\alpha\right|^2+\left|m_\alpha^{mg}\right|^2\left|B_\alpha\right|^2+\left\langle\mu_\alpha^{mg}m_\alpha^{mg^*}\right\rangle_\rho\left(E_\alpha B_\alpha^*\right)+\left\langle m_\alpha^{mg}\mu_\alpha^{mg*}\right\rangle_\rho\left(B_\alpha E_\alpha^*\right)\\&+\frac{1}{3}\Big(\left\langle\theta_{\alpha\beta}^{mg}\mu_\alpha^{mg*}\right\rangle_\rho\left(\nabla_\alpha E_\beta\cdot E_\alpha^*\right)+\left\langle\mu_\alpha^{mg}\theta_{\alpha\beta}^{mg*}\right\rangle\left(E_\alpha(\nabla_\alpha E_\beta)^*\right)\Big)\rho\left(\omega_{mg}=\omega\right)\end{aligned}$$

Here the index ρ is the orientation-dependent weighting factor arising from the anisotropic averaging, which is necessary to take into account the orientation of the multipoles. Taking into consideration the properties of the dipoles, where the electric dipole transition μ is a real quantity ($\mu = \mu^*$), and the magnetic transition dipole m is imaginary ($m = -m^*$) [32], the above equation reduces to

$$\begin{aligned} R^{(1)}_{mg} = \frac{2\pi}{\hbar^2} \Big[&|\mu^{mg}_\alpha|^2 \, |E_\alpha|^2 + |m^{mg}_\alpha|^2 \, |B_\alpha|^2 + \langle \mu^{mg}_\alpha m^{gm}_\alpha \rangle_\rho \left(B_\alpha E^*_\alpha - E_\alpha B^*_\alpha \right) \\ &+ \frac{1}{3} \Big(\left\langle \mu^{mg}_\alpha \theta^{gm}_{\alpha\beta} \right\rangle_\rho \left(\nabla_\alpha E_\beta E^*_\alpha + E_\alpha (\nabla_\alpha E_\beta)^* \right) \Big) \, \rho \left(\omega_{mg} = \omega \right) \end{aligned}$$

In writing the above equation, the response of the quadrupole tensor is approximated as a scalar. Also, the above equation can be written more concisely by using the properties of complex numbers, i.e., $B_\alpha E^*_\alpha - E_\alpha B^*_\alpha = -2i \, \mathrm{Im}\left[E^*_\alpha B_\alpha\right]$ and , $(\nabla_\alpha E_\beta E^*_\alpha + E_\alpha(\nabla_\alpha E_\beta)^*) = 2 \, \mathrm{Re}\left[\nabla_\alpha E_\beta E^*_\alpha\right]$ as

$$\boxed{R^{(1)}_{mg} = \frac{2\pi}{\hbar^2} \left[\underbrace{|\mu^{mg}_\alpha|^2 |E_\alpha|^2}_{\text{E1E1}} + \underbrace{|m^{mg}_\alpha|^2 |B_\alpha|^2}_{\text{M1M1}} + \underbrace{2\langle \mu^{mg}_\alpha m^{gm}_\alpha \rangle_\rho \mathrm{Im}\left[E^*_\alpha B_\alpha\right]}_{\text{E1M1}} + \underbrace{\frac{2}{3} \langle \mu^{mg}_\alpha \theta^{gm}_{\alpha\beta} \rangle_\rho \mathrm{Re}\left[\nabla_\alpha E_\beta E^*_\alpha\right]}_{\text{E1E2}} \right] \rho\left(\omega_{mg} = \omega\right)} \tag{2.14}$$

Here, E1 and M1 are electric and magnetic dipoles, respectively, while E2 represents the electric quadrupoles. This is the central equation of our model describing the single-photon absorption rate in the case of helical light-matter interaction. The E1E2 term contains the field gradient, which gives rise to l dependence (due to the derivative) and becomes a dominant term in the case of the asymmetric beam.

For a single transition, the energy absorbed per unit time (Γ) can be expressed as the product of the energy absorbed per transition and the rate at which these single transitions occur: $\Gamma = \hbar\omega \times R^{(1)}_{mg}$. Therefore, the above transition rate equation can be written in terms of energy absorbed per unit of time (for a single transition) as

$$\Gamma^{(1)}_{mg} = \frac{2\pi\omega}{\hbar} \left[\underbrace{|\mu^{mg}_\alpha|^2 |E_\alpha|^2}_{\text{E1E1}} + \underbrace{|m^{mg}_\alpha|^2 |B_\alpha|^2}_{\text{M1M1}} + \underbrace{2\langle \mu^{mg}_\alpha m^{gm}_\alpha \rangle_\rho \mathrm{Im}\left[E^*_\alpha B_\alpha\right]}_{\text{E1M1}} + \underbrace{\frac{2}{3} \langle \mu^{mg}_\alpha \theta^{gm}_{\alpha\beta} \rangle_\rho \mathrm{Re}\left[\nabla_\alpha E_\beta E^*_\alpha\right]}_{\text{E1E2}} \right] \rho\left(\omega_{mg} = \omega\right) \tag{2.15}$$

This equation is in agreement with the energy absorption rate derived considering the induced multipole moments, as given in Appendix A. Additionally, in the case of one-photon resonance, the density of states can be $\rho_f\left(\omega_{mg} = \omega\right)$ can be approximated by the width of level m [21]. The total energy absorbed for N such transitions over the beam cross-section can be written as

$$W = \int_{-\omega_0}^{\omega_0} N.\Gamma_{mg} dxdy \tag{2.16}$$

The above equation, representing the total energy absorbed, can be explicitly evaluated for the right- and left-handed asymmetrical LG beams. The difference in the absorption of left- and right-handed asymmetrical LG beams is defined as *helical dichroism*. In addition, the E1M1 interaction term is responsible for the conventional CD effect when evaluated for left- and right-circularly polarized light. Each of these effects is discussed in the following sections.

2.3.1 Circular Dichroism - polarization based effect

Circular dichroism is defined as the differential absorption of left- and right-handed circularly polarized light by a chiral medium. This polarization-based effect arises from the dissymmetry in the excitation rates of chiral molecules.

To quantify the effect of polarization as a probe, circularly polarized Gaussian beams can be used. Consequently, using Eq.(2.15) and Eq.(2.16), the differential energy absorbed in the case of CD can be written as:

$$\mathrm{CD} = W^R - W^L = \int_{-\omega_0}^{\omega_0} \left(G'[C^L - C^R] \right) dxdy \tag{2.17}$$

Here, the L and R superscript represents the left- and right-handed circular polarization. The above equation contains the contribution of the E1M1 term, while the contributions of the E1E1, M1M1, and E1E2 terms vanish, as they are identical for both polarization states. The term $G' = \frac{4\pi}{\hbar}.\langle \mu_\alpha^{mg} m_\alpha^{gm} \rangle_\rho$ represents the material response and the parameter $\mathrm{C}^{L,R} = 2\omega \mathrm{Im}\left[\left(E^{L/R} \right)^* \cdot B^{L/R} \right]$ represents a local measure of the degree of circular polarization, known as optical chirality [33]. Therefore, $(C^L - C^R)$ determines the degree of chiral asymmetry in the rate of excitation of a chiral molecule [34]. Optical chirality is often used to describe the phenomenon of circular dichroism in molecules [35, 33].

The CD is an example of *true chirality* [36], as it involves the interaction of chiral molecules with chiral light, a true chiral system. True chirality is exhibited by systems that can be transformed into each other by spatial inversion (parity P) but not by the combination of time reversal (T) and proper spatial rotation. The breaking of PT symmetry in true chiral interactions (chiral light and chiral matter) can give rise to enantioselective effects, such as optical rotation and CD. This can be shown by applying a PT symmetry operation on the optical chirality (C) term (see Eq.2.17) as

$$PT\left\{2\omega\,\mathrm{Im}\left[E^* \cdot B\right]\right\} \rightarrow P\left\{-2\omega\,\mathrm{Im}\left[E \cdot B^*\right]\right\} \rightarrow P\left\{2\omega\,\mathrm{Im}\left[E^* \cdot B\right]\right\} = -2\omega\,\mathrm{Im}\left[E^* \cdot B\right]$$

Thus, CD arises due to the breaking of PT symmetry and is characterized by the presence of a parity-odd time-even pseudoscalar, C.

2.3.2 Helical Dichroism - phase-based effect

Helical dichroism (HD) refers to the helical phase-based differential response of matter. HD can be classified into two types, depending on the chirality of both the matter and the light.

HD (Type I) is evaluated by taking the difference in absorption between the left- and right-helical light for the same material medium. It is a beam-dominated property, and its definition is independent of the material symmetry. In the definition of HD (Type I), the polarization of light remains constant for both the left- and right-helical light. Using Eq.(2.15) and Eq.(2.16) with asymmetric helical beams (Eq.1.24), one obtains

$$\mathrm{HD}_\delta(\text{Type I}) = W_\delta^+ - W_\delta^- = \int_{-\omega_0}^{\omega_0} \left(G'[C^+ - C^-] + A''[\Upsilon^+ - \Upsilon^-] \right) dxdy \tag{2.18}$$

where ± represents the left- and right-handed wavefronts, and δ represents the asymmetry parameter (Eq.1.24) associated with q displacement of the singularity. Additionally, $A'' = \frac{4\pi\omega}{3\hbar}\langle \mu_\alpha^{mg}\theta_{\alpha\beta}^{gm}\rangle_\rho$ represents the material response tensor. The coupling term $\Upsilon^\pm = \frac{2\omega}{3}\mathrm{Re}\left[\left(E_\delta^\pm\right)^* \cdot \nabla E_\delta^\pm\right]$ is defined as optical helicity. Analogous to the case of optical chirality (C), optical helicity, Υ, is a quantity describing the handedness of helical light. It contains the gradient of the electric field, which gives rise to the explicit l dependence. Thus, the HD (Type I) signal scales by increasing the l value. Moreover, the HD signal can be tuned and controlled by varying the δ parameter, ellipticity, and the weighted superposition with a Gaussian beam. These unique features are absent in the traditional polarization-based CD method.

Upon qualitative evaluation of the above equation, it is evident that HD (Type I) does not exist for symmetric LG beams. This absence is due to the evaluation of HD as the difference between beams possessing left- and right-handed phase fronts but with identical polarization. Consequently, the difference $G'[C^+ - C^-]$ vanishes. This is because the polarization-dependent $E1M1$ term ($G'C$) changes sign only with the handedness of circular polarization, and its contribution vanishes since the polarization remains unchanged. Additionally, the $E1E2$ term is zero as the averaged field gradient vanishes. However, for asymmetric LG beams, while the $E1M1$ term still vanishes for the same reasons, the $E1E2$ coupling term remains nonzero, leading to the observation of the HD effect.

HD (Type II) is evaluated by taking the difference of absorption between the left- and right-handed chiral molecules for a specific-handed helical light. Its definition involves both the material and the light beam to be chiral entities, hence a true chiral interaction [36]. Using

Eq.(2.15) and Eq.(2.16), one obtains

$$\mathrm{HD}_{\delta}^{\pm}(\text{Type II}) = W_{\delta}^{+} - W_{\delta}^{-} = \int_{-\omega_0}^{\omega_0} \left(C^{\pm}[G'_R - G'_S] + \Upsilon^{\pm}\left[A''_R - A''_S\right] \right) dxdy \tag{2.19}$$

where R and S represent the two enantiomers. HD(Type II) is a material-dominated property where both the E1M1 and E1E2 coupling terms contribute to differential absorption for asymmetric LG beams. For symmetric LG beams, the E1E2 term averages out to zero, but the E1M1 term is non-zero and can contribute to the HD. In the case of asymmetric LG beams, the E1E2 term is responsible for the change in the sign of the HD curves, and the E1M1 term leads to an offset in the HD curves.

The experimental results demonstrating the presence of helical dichroism in liquids, solutions, solids, and metasurfaces are presented in Chapters 3 to 6. The qualitative origins of these observations are discussed in the following sections.

2.3.2.1 Case I: Achiral molecules

As previously discussed, CD absorption spectroscopy is the conventional technique for studying the optical activity and symmetry properties of the molecules. The E1M1 term (including G'), which is responsible for CD in chiral molecules, vanishes for achiral molecules due to the rotational isotropic averaging in the case of randomly oriented molecules. Only for chiral molecules, the E1M1 term survives the isotropic averaging [34]. This is the same reason why early studies on helical light-matter interaction neglected the E1E2 coupling term, as it also vanishes for the randomly oriented molecules. However, if the molecules are preferentially aligned, the quadrupolar interactions contained in the E1E2 term cannot be neglected [37, 34]. This is the case for asymmetric LG beams, where the spatial inhomogeneity in the intensity profile at the interaction region gives rise to the optical dipole force. This force is defined by $\mathbf{F} = \alpha\frac{1}{2}\nabla E^2 + \alpha\frac{d}{dt}(\mathbf{E}\times\mathbf{B})$. The first term represents the gradient force, while the second term corresponds to the scattering force. The scattering force can be neglected when the Poynting vector remains constant over an optical cycle [3].

Figure 2.7 shows the gradient force component F_x, integrated over the cross-section of a linearly polarized beam, as a function of the displaced position of the singularity. Only the dominant component F_x is plotted, while the F_y component is smaller in magnitude but exhibits similar behavior. The gradient force is zero for symmetric LG beams. As the singularity is displaced, the gradient force increases initially and then decreases toward zero for large displacements, where the beam begins to resemble a Gaussian profile. A net non-zero force is exerted on the induced dipoles, directing them toward the extrema of the radiation field. This force results in a torque that preferentially aligns the molecular axis parallel to the polarization plane [2, 34]. Such molecular alignment in an asymmetric LG beam leads to a non-zero averaged

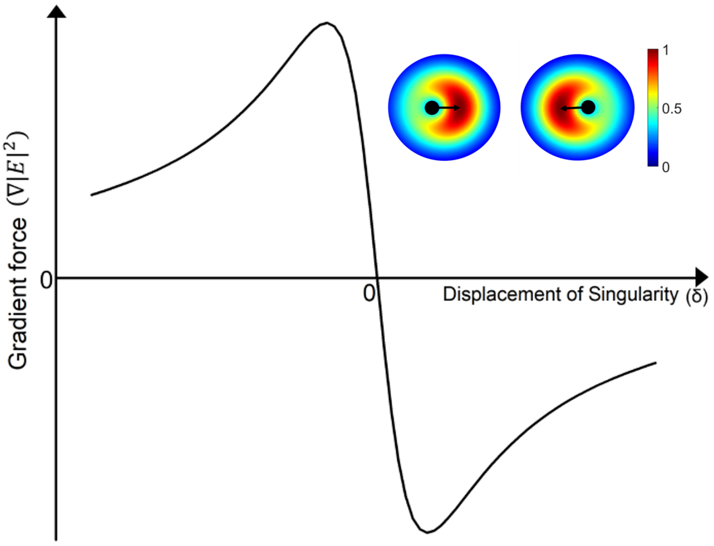

Figure 2.7: **Optical gradient force** as a function of the displaced position of the singularity (δ). The optical gradient force is zero for a symmetric LG beam and is maximum at the position of the displaced singularity. The force converges towards zero for the extreme δ where the beam profile mimics a Gaussian profile. Inset shows the force directed towards the extrema of the field.

$E1E2$ contribution to the HD. Consequently, the HD (Type I) signal is observed only for asymmetric beams (see Chapter 3 for results).

At low laser intensities, the degree of molecular alignment is negligible, and the $E1E2$ term does not contribute to the HD signal. The extent of molecular alignment with an approximately 100-fs laser pulse depends on (1) the laser intensity $\sim 10^{13}\,\mathrm{W/cm^2}$, (2) the molecular polarizability, and (3) temperature and/or solute effects [38, 39, 40]. As the laser intensity increases, even a small degree of molecular alignment in an asymmetric OAM beam becomes sufficient for the $E1E2$ term to become non-zero, contributing to the HD signal. In other words, at sufficiently high laser intensities, a subset of molecules will always have their molecular axes aligned parallel to the electric field, resulting in preferential absorption. For results and further details, refer to the published article and the supplementary file in Chapter 3.

2.3.2.2 Case II: Chiral molecules

In the case of chiral molecules, both the HD (Type I) and HD (Type II) effects are observed. The HD (Type I) effect is analogous to CD, while the HD (Type II) serves as the enantioselectivity signal. For such molecules, the symmetry of the ground state wavefunctions should be incorporated into the derivation of the total transition rate (Eq.2.14). As discussed in Section

2.2, the R-enantiomer can be assigned the symmetric ground state $\Psi_s^g = \frac{1}{\sqrt{2}}\left(\psi_+^g + \psi_-^g\right)$, while the antisymmetric $\Psi_{as}^g = \frac{1}{\sqrt{2}}\left(\psi_+^g - \psi_-^g\right)$ can be assigned to the S-enantiomer, where Ψ_+ (Ψ_-) is even (odd) under parity. Therefore, the symmetry of the wavefunction of individual enantiomers must be considered in the treatment of helical light-matter interactions.

The single photon absorption transition rate, given by Eq.(2.13), can be written as

$$R_{m(s/as)} = \frac{2\pi}{\hbar^2}\left|\left\langle \Psi_m | V | \Psi_{s/as}^g \right\rangle\right|^2 \delta\left(\omega_{m(s/as)} - \omega\right) \tag{2.20}$$

where $\Psi_{s/as}^g$ represents the symmetric/antisymmetric ground state of the enantiomer pair. In the case of ground-state parity violation, the excited states for both enantiomers can be assumed to be a mixed parity state, given by $\psi_m = \frac{1}{\sqrt{2}}\left(\psi_+ + i\beta\psi_-\right)$, where i$\beta$ is a small phase lag factor between the even and odd states [19, 20]. Additionally, considering the interaction Hamiltonian (Eq.2.4) in the form

$$V = -\mu_\alpha E_\alpha - \frac{1}{3}\theta_{\alpha\beta}\nabla_\alpha E_\beta.$$

Here the magnetic dipole term is neglected because it leads to the $E1M1$ coupling term, whose contribution vanishes in the case of HD (Type I) (see Section 2.3.2 for details). The detailed derivation of the single-photon transition rate is given in the article attached in Chapter 4, and the results are discussed here. The enantiomeric transition rates for R- and S- enantiomers can be derived as

$$\begin{aligned} R_{m(as)}^{S,R} = \frac{\pi}{3\hbar^2} \Bigg[&\mp \underbrace{i\beta\left(\langle \psi_+ |\mu_\alpha \ldots \theta_{\alpha\beta}| \psi_- \rangle - \langle \psi_- |\mu_\alpha \ldots \theta_{\alpha\beta}| \psi_+ \rangle\right)}_{\mathscr{C}} \\ &+ \underbrace{\left\langle \psi_+ |\theta_{\alpha\beta}| \psi_+^g \right\rangle \left\langle \psi_-^g |\mu_\alpha| \psi_+ \right\rangle}_{\mathscr{D}} \Bigg] \mathrm{Re}\left[\nabla_\alpha E_\beta E_\alpha^*\right] \rho\left(\omega_{m(as,s)} - \omega\right). \end{aligned} \tag{2.21}$$

where $R_{m(as/s)}^{S/R}$ is the single photon transition rate (initial to final state m) for S- and R-enantiomer and the terms of the form $\langle\psi_-|\mu_\alpha \ldots \theta_{\alpha\beta}|\psi_+\rangle \mathrm{Re}\left[\nabla_\alpha E_\beta E_\alpha^*\right] = \frac{1}{2}\langle\psi_-|\mu_\alpha|\psi_+^g\rangle\ \langle\psi_+^g|\theta_{\alpha\beta}|\psi_+\rangle\left[\nabla_\alpha E_\beta E_\alpha^*\right] + \frac{1}{2}\langle\psi_-|\theta_{\alpha\beta}|\psi_-^g\rangle\langle\psi_-^g|\mu_\alpha|\psi_+\rangle\left[E_\alpha(\nabla_\alpha E_\beta)^*\right]$ is written using the rotational average over the symmetric and antisymmetric parity states. The $\mathcal{C}$ and $\mathcal{D}$ terms represent the mixed electric dipole–quadrupole response tensors (transition moments), coupled with the electric field gradients. The above equations can be concisely written in the form.

$$R_{m(as/s)}^{S/R} = \frac{\pi}{3\hbar^2}\left[\mathcal{D} \mp \mathcal{C}\right] \mathrm{Re}\left[E_\alpha^* \nabla_\alpha E_\beta\right] \rho\left(\omega_{m(as/s)} - \omega\right) \tag{2.22}$$

This expression shows that the transition rate for R-enantiomer is of the form: $\mathcal{D} + \mathcal{C}$ and for S-enantiomer is of the form: $\mathcal{D} - \mathcal{C}$, where $\mathcal{D}$ is bigger than $\mathcal{C}$ since phase lag factor β is small[19]. This difference in the transition rates for the R- and S-enantiomers leads to the observed difference in the magnitude of HD (Type I). The experimental results are given in the article attached in Chapter 4. Also, it is important to note that the analysis presented is only qualitative. A quantitative analysis of HD magnitude would require detailed information about molecular response tensors and wavefunctions.

2.4 Nonlinear interactions

The electron transition mechanism is primarily determined by the intensity of the incident beam and the photon energy relative to the energy gap between the ground and excited states. For intensities exceeding the nonlinear threshold, if the photon energy is lower than the energy gap, absorption is governed by nonlinear processes: either multiphoton absorption or strong-field tunneling at extremely high intensities. The dominant mechanism can be characterized by the Keldysh parameter, which, for solids, is defined as [41, 42]

$$\gamma = \frac{\omega}{e}\left[\frac{mcn\varepsilon_0 E_g}{I}\right]^{1/2}$$

where ω is the laser frequency, I is the incident laser intensity, m and e are the electron's reduced mass and charge, c is the speed of light, n is the refractive index of the material, E_g is the material bandgap, and ε_0 is the permittivity of free space. For atoms, the Keldysh parameter is $\sqrt{2}$ times the above expression, with the bandgap replaced by the ionization potential I_p.

In both solids and molecules, when $\gamma \gtrsim 2$, interband or excited-state transitions are primarily governed by multiphoton processes. Conversely, for $\gamma < 1$, strong-field tunneling dominates [41, 43]. The intermediate regime $1 < \gamma < 2$ involves a combination of both multiphoton absorption and tunneling, with multiphoton-assisted tunneling (MPAT) being the dominant mechanism. However, the other two processes can still be present simultaneously in the intermediate regime [44, 45]. Feynman diagrams provide a unified approach to describing these transition mechanisms in both solids and molecules [21], representing interactions as a sum of time-ordered events and clearly depicting the temporal sequence of processes.

Figure 2.8 shows the Feynman diagram representation of the multiphoton absorption, MPAT, and tunneling transitions in the case of solids. In the multiphoton absorption process, the simultaneous absorption of $(n + 1)$ photons enables the electron to transition to the conduction band (ψ_f^c). The MPAT process is initiated by the absorption of n photons, leading to intermediate or band-tail states, followed by tunneling into the conduction band. In the tunneling regime, the incident field is strong enough to force the electron to tunnel from the valence band (ψ_g^v) to the conduction band. In the case of molecules, the valence band corresponds to the

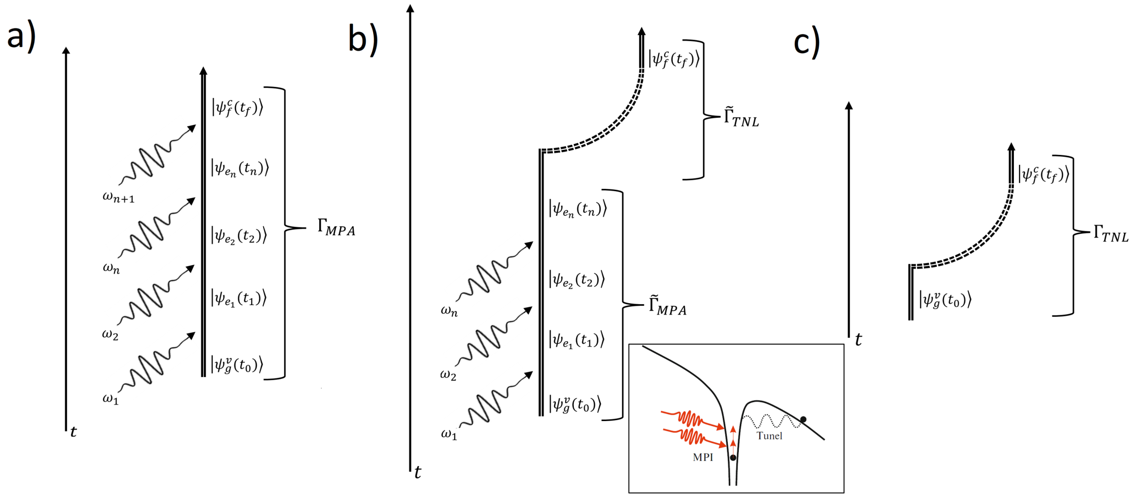

Figure 2.8: **Feynman diagrams** for **a)** multiphoton absorption of $(n+1)\hbar\omega$ to reach the conduction band, **b)** the MPAT process facilitated by absorption of n photons leading to an intermediate state and subsequent tunneling to the conduction band, and **c)** the tunneling transition, where the incident field is strong enough to force the electron to tunnel from the valence band (ψ_g^v) to the conduction band(ψ_f^c).

ground state, while the conduction band is replaced by the continuum. The inset of Fig.2.8b shows the MPAT process in atoms.

Research presented in Chapters 3 to 6 explores the use of helical phase-based spectroscopy in both linear and nonlinear interaction regimes. In the linear regime, plasmonic achiral and chiral metasurfaces exhibited the helical phase-based differential response. Helical dichroism in chiral liquids, achiral liquids, and enantiomeric solutions was observed in the nonlinear multiphoton absorption (MPA) regime. In amorphous solids, the MPAT process was responsible for the observed phase-based dichroism.

The MPA and MPAT processes are briefly discussed in the following sections. *The final results are presented without detailed derivations*, as the comprehensive models can be found in the published articles. These articles, along with their supplementary files, are included in Chapters 3 to 5.

2.4.1 Multiphoton absorption - Perturbation theory

The single-photon transition rate, derived using perturbation theory (Eq.2.13), was extended to the multiphoton transition rate, following the approach by Boyd et al. [21]. The transition rate for the two-photon process, involving the states: g → k → m is given as

$$R_{mg}^{(2)} = 2\pi \left| \sum_{k} \frac{V_{mk} V_{kg}}{\hbar^2 \left(\omega_{kg} - \omega\right)} \right|^2 \rho\left(\omega_{mg} = 2\omega\right) \tag{2.23}$$

$$R_{mg}^{(2)} = 2\pi \left| \sum_{k} \frac{\left(\mu_{\alpha}^{mk} E_{\alpha} + \frac{1}{3}\theta_{\alpha\beta}^{mk} \nabla_{\alpha} E_{\beta} + m_{\alpha}^{mk} B_{\alpha}\right)\left(\mu_{\alpha}^{kg} E_{\alpha} + \frac{1}{3}\theta_{\alpha\beta}^{kg} \nabla_{\alpha} E_{\beta} + m_{\alpha}^{kg} B_{\alpha}\right)}{\hbar^2 \left(\omega_{kg} - \omega\right)} \right|^2 \rho\left(\omega_{mg} = 2\omega\right) \tag{2.24}$$

The two-photon transition rate was obtained by expanding the above equation, neglecting higher-order terms involving $M1$ and $E2$, and applying anisotropic averaging, given by

$$\begin{aligned} R_{mg}^{(2)} = 2\pi \textstyle\sum_k \frac{1}{\hbar^4 \left(\omega_{kg} - \omega\right)^2} & \Big\{ \left|\mu_{\alpha}^{mk} \mu_{\alpha}^{kg}\right|^2 \left|E_{\alpha} E_{\alpha}\right|^2 + 2\left(\left|\mu_{\alpha}^{kg}\right|^2 \left|E_{\alpha}\right|^2 \langle \mu_{\alpha}^{mk} m_{\alpha}^{km} \rangle_{\rho} + \left|\mu_{\alpha}^{mk}\right|^2 \left|E_{\alpha}\right|^2 \langle \mu_{\alpha}^{kg} m_{\alpha}^{gk} \rangle_{\rho}\right) \operatorname{Im}\left[E_{\alpha}^{*} B_{\alpha}\right] \\ & + \tfrac{2}{3}\left(\left|\mu_{\alpha}^{kg}\right|^2 \left|E_{\alpha}\right|^2 \langle \mu_{\alpha}^{mk} \theta_{\alpha\beta}^{km} \rangle_{\rho} + \left|\mu_{\alpha}^{mk}\right|^2 \left|E_{\alpha}\right|^2 \langle \mu_{\alpha}^{kg} \theta_{\alpha\beta}^{gk} \rangle_{\rho}\right) \operatorname{Re}\left[\nabla_{\alpha} E_{\beta} E_{\alpha}^{*}\right] \Big\} \rho\left(\omega_{mg} = 2\omega\right) \end{aligned}$$

The above equation was generalized to the n-photon case, where m represents the final state, and g denotes the ground state, given by

$$\begin{aligned} R_{mg}^{(n)} = 2\pi \rho\left(\omega_{mg} = n\omega\right) & \Bigg[\sum_{p} \sum_{l} \cdots \sum_{r} \sum_{k} \frac{\left|\mu_{\alpha}^{mp} \mu_{\alpha}^{pl} \ldots \mu_{\alpha}^{rk} \mu_{\alpha}^{kg}\right|^2 \left|E_{\alpha}\right|^{2n}}{\hbar^{2n} \left(\omega_{pl} - (n-1)\,\omega\right)^2 \ldots \left(\omega_{rk} - 2\omega\right)^2 \left(\omega_{kg} - \omega\right)^2} \\ & + 2 \sum_{p} \sum_{l} \cdots \sum_{r} \sum_{k} \frac{\left|\mu_{\alpha}^{mp}\right|^2 \left|\mu_{\alpha}^{pl}\right|^2 \ldots \left|\mu_{\alpha}^{rk}\right|^2 \operatorname{Im}\left[\mu_{\alpha}^{kg} m_{\alpha}^{gk}\right] + \left|\mu_{\alpha}^{mp}\right|^2 \left|\mu_{\alpha}^{pl}\right|^2 \ldots \left|\mu_{\alpha}^{kg}\right|^2 \langle \mu_{\alpha}^{rk} m_{\alpha}^{kr} \rangle_{\rho} + \ldots +}{\hbar^{2n} \left(\omega_{pl} - (n-1)\,\omega\right)^2 \ldots \left(\omega_{rk} - 2\omega\right)^2 \left(\omega_{kg} - \omega\right)^2} \\ & \frac{\ldots + \left|\mu_{\alpha}^{mp}\right|^2 \ldots \left|\mu_{\alpha}^{rk}\right|^2 \left|\mu_{\alpha}^{kg}\right|^2 \operatorname{Im}\left[\mu_{\alpha}^{pl} m_{\alpha}^{lp}\right] + \left|\mu_{\alpha}^{pl}\right|^2 \ldots \left|\mu_{\alpha}^{rk}\right|^2 \left|\mu_{\alpha}^{kg}\right|^2 \langle \mu_{\alpha}^{mp} m_{\alpha}^{pm} \rangle_{\rho}}{\hbar^{2n} \left(\omega_{pl} - (n-1)\,\omega\right)^2 \ldots \left(\omega_{rk} - 2\omega\right)^2 \left(\omega_{kg} - \omega\right)^2} \left|E_{\alpha}\right|^{2(n-1)} \operatorname{Im}\left[E_{\alpha}^{*} B_{\alpha}\right] \\ & + \frac{2}{3} \sum_{p} \sum_{l} \cdots \sum_{r} \sum_{k} \frac{\left|\mu_{i}^{mp}\right|^2 \left|\mu_{\alpha}^{pl}\right|^2 \ldots \left|\mu_{\alpha}^{rk}\right|^2 \operatorname{Im}\left[\mu_{\alpha}^{kg} \theta_{\alpha\beta}^{gk}\right] + \left|\mu_{\alpha}^{mp}\right|^2 \left|\mu_{\alpha}^{pl}\right|^2 \ldots \left|\mu_{\alpha}^{kg}\right|^2 \langle \mu_{\alpha}^{rk} \theta_{\alpha\beta}^{kr} \rangle_{\rho} + \ldots +}{\hbar^{2n} \left(\omega_{pl} - (n-1)\,\omega\right)^2 \ldots \left(\omega_{rk} - 2\omega\right)^2 \left(\omega_{kg} - \omega\right)^2} \\ & \frac{\ldots + \left|\mu_{\alpha}^{mp}\right|^2 \ldots \left|\mu_{\alpha}^{rk}\right|^2 \left|\mu_{\alpha}^{kg}\right|^2 \operatorname{Im}\left[\mu_{\alpha}^{pl} \theta_{\alpha\beta}^{lp}\right] + \left|\mu_{\alpha}^{pl}\right|^2 \ldots \left|\mu_{\alpha}^{rk}\right|^2 \left|\mu_{\alpha}^{kg}\right|^2 \langle \mu_{\alpha}^{mp} \theta_{\alpha\beta}^{pm} \rangle_{\rho}}{\hbar^{2n} \left(\omega_{pl} - (n-1)\,\omega\right)^2 \ldots \left(\omega_{rk} - 2\omega\right)^2 \left(\omega_{kg} - \omega\right)^2} \left|E_{\alpha}\right|^{2(n-1)} \operatorname{Re}\left[\nabla_{\alpha} E_{\beta} E_{\alpha}^{*}\right] \Bigg] \end{aligned} \tag{2.25}$$

The above expression for n-photon absorption is obtained by applying the following approximations: 1) The scalar approximation is considered where tensor properties are restricted to a dominant component for oriented molecules; (2) Higher-order terms involving $M1$ and $E2$, such as $M1E2$ and $E2E2$, are neglected; 3) The cross-correlation terms originating from the square of summations (summed over indices) are neglected. The purpose of presenting the above equation is to demonstrate that the $E1E1$, $E1M1$, and $E1E2$ terms responsible for the HD can be expressed in terms of optical chirality (C) and helicity (Υ), similar to the case of single-photon absorption. Consequently, the variation of the HD signal with singularity displacement also extends to multiphoton interactions.

2.4.2 Multiphoton assisted tunneling (MPAT) - Nonperturbative model

In the MPAT process, electron transitions from the valence band (or the ground state in molecules) to intermediate band-tail states (excited states in molecules [44, 45]) by the absorption of a single or multiple photons. This is followed by the subsequent transition to the conduction band (or continuum in molecules) [29] via the tunneling process, as depicted in Fig.2.8. In terms of the Keldysh parameter, the MPAT facilitates the smooth and continuous transition from the dominant multiphoton regime to the ground-state tunneling regime. The MPAT process was first developed for atoms [44, 45], and was extended to the case of solids in our research.

The reason behind using the MPAT transition regime to describe the phase-based dichroism in solids was based on the fact that the HD was observed for a certain range of incident laser intensity. In amorphous fused silica, the HD signal was dominant only within a certain range of laser intensities (2×10^{13} to 8×10^{13} W/cm^2), which corresponds to a Keldysh parameter varying from approximately 2.5 to 1.1. In this intermediate regime, the MPAT process dominated as the primary transition mechanism. Consequently, the multiphoton interaction models developed for molecules could not be directly applied to solids.

The transition amplitude for the MPAT process involving a single-photon absorption (SPA) from the valence band (ψ_v) to an intermediate excited state (ψ_m) and subsequent tunneling to the conduction band (ψ_c) is given by

$$M_{cv} = \sum_m \underbrace{\frac{\langle\psi_m|\,\hat{V}_i\,|\psi_v\rangle}{\hbar(\omega_{mv}-\omega)}}_{M_{SPA}} \underbrace{\frac{i}{\hbar}\int_{t_0}^{t} d\tau\,\langle\psi_c(\tau)|\,\hat{V}_f(\tau)\,|\psi_m(\tau)\rangle\, e^{i(\omega_{mv}-\omega)\tau}}_{M_{TNL}} \tag{2.26}$$

where ω is the laser frequency, $\omega_{mv}=(E_m-E_v)/\hbar$, and E_m and E_v are the energies of the intermediate and valence band states, respectively. In addition, $\hat{V}_i$ and $\hat{V}_f$ are the multiphoton and tunneling interaction Hamiltonians written in a multipole expansion and electric dipole approximation, respectively. The MPAT transition amplitude is a product of two factors: a time-independent single-photon transition amplitude M_{SPA} and a time-dependent excited state tunneling amplitude M_{TNL}. After substituting the valence, intermediate, and conduction band wavefunctions for amorphous solids (see Chapter 5 for details), the total differential transition rate is given as

$$\Delta \mathrm{W} = \mathrm{W}_{\delta}^{+} - \mathrm{W}_{\delta}^{-} = \frac{2\Omega_4 \left(\mu_i^{mv}\theta_{ij}^{vm}\right)}{3\hbar^2 \left(\omega_{mv} - \omega\right)^2} \tilde{\mathrm{W}} \left(\underbrace{\mathrm{Re}\left[\nabla_i E_j^{+} E_i^{+*}\right]}_{\Upsilon^{+}} - \underbrace{\mathrm{Re}\left[\nabla_i E_j^{-} E_i^{-*}\right]}_{\Upsilon^{-}} \right) \tag{2.27}$$

where $\Upsilon^{\pm} = \mathrm{Re}\left[\nabla_i E_j^{\pm} E_i^{\pm *}\right]$ represents the optical helicity, μ_i is the electric dipole moment, θ_{ij} is the electric quadrupole moment, and Ω_4 is the orientation-dependent weighting factor originating from the anisotropic averaging. Also, $\tilde{\mathrm{W}}$ is given by

$$\tilde{\mathrm{W}} = \frac{1}{(2\pi)^4 \hbar} \left(\frac{m_1 \omega p_{\mathrm{cm}}}{m(\eta - 1)!}\right)^2 \left(\frac{eA_0}{2m_1\omega}\right)^{2\eta} \left(\frac{2m^*}{\hbar^2}\right)^{(2\eta+1)/2} \left(\frac{(n\hbar\omega - E_{\mathrm{g}})}{(2\eta - 1)}\right)^{(2\eta-1)/2} \tag{2.28}$$

where m_0 and m_1 are the electron masses in the valence and the conduction bands, $m^{*-1} = m_1^{-1} - m_0^{-1}$ is the total effective electron mass, E_{g} is the bandgap, and A_0 is the magnitude of the vector potential. Also, $n = \eta + 1$ is the total number of photons absorbed for linearly polarized light. The above expression for the total differential transition rate was used to simulate HD (Type I) in amorphous fused silica. The results of the simulation were in qualitative agreement with the experimental data (see Chapter 5). Also, quantitatively, the simulated HD values differed by two orders of magnitude compared to the experimental values. This variation was attributed to the approximate values used for the material response tensors.

2.4.2.1 Dichroism in amorphous solids

For achiral molecules, the torque generated by the dipole force (in the presence of asymmetric light beams) aligns the randomly oriented molecules. Consequently, the electric dipole-quadrupole coupling term (E1E2), which is responsible for the HD effect, survives the isotropic averaging. However, in isotropic amorphous solids, the molecules are fixed in their spatial positions and cannot be aligned by the presence of the dipole force. So, how do amorphous solids exhibit dichroism?

The presence of dichroism in amorphous materials can be explained by the existence of unique short- to medium-range order. During tunneling transitions in atoms, the electron undergoes a spatial displacement given by $\mathbf{x}_0 = I_p/\left(e\mathbf{E}\right)$, where I_p is the ionization potential [42]. The spatial displacement, $\mathbf{x}_0$, is the distance traversed by the electron through the barrier to the tunnel exit. This mechanism of spatial displacement can also be extended to tunneling transitions in solids. In solids, the energy absorbed from the incident laser fields is proportional to the associated injection current, given by $\mathbf{J} = en_0\mathbf{x}_0\dot{\rho}$ [46], where e is the electron charge, n_0 is the electron density in the conduction band, and $\dot{\rho}$ is the injection rate, which is proportional to the transition rate W. Here, $\mathbf{x}_0$ denotes the spatial displacement of electrons after being promoted from the valence band to the conduction band. The current $\mathbf{J}$ is fundamental for maintaining energy conservation, expressed as $\dot{u} = -\mathbf{J}\cdot\mathbf{E}$. In optical tunneling, energy conservation is ensured when this current reflects the spatial displacement of electrons, given by [46]

$$\mathbf{x}_0 = \mathbf{E}E_g/\left(eE^2\right) \tag{2.29}$$

where E_g is the bandgap and $\mathbf{E}$ is the electric field. In amorphous fused silica ($E_g \approx 9eV$[43, 47]), $\mathbf{x}_0$ varies from 6 Å to 18Å corresponding to the range of laser intensities where the HD signal was significant in our experiments. However, this value of electron displacement represents the case of direct tunneling from the valence band to the conduction band. In the MPAT process, there are two contributions to the electron displacement: one from the multiphoton transition to an intermediate band tail (or defect) state, and another from subsequent tunneling to the conduction band. As a result, $\mathbf{x}_0$ in the MPAT process is smaller compared to direct tunneling transitions, which sets the upper limit for the electron displacement [44, 45]. Furthermore, $\mathbf{x}_0$ in the MPAT process is comparable to the short- to medium-range order in amorphous solids (for fused silica, it is less than 20 Å [25, 26, 27]). This restricts isotropic averaging to a more ordered environment, resulting in a finite contribution in amorphous solids, which gives rise to the finite phase-based dichroism. In crystalline solids, the ordered environment always ensures a non-zero HD signal upon isotropic averaging.

This concludes the theoretical discussion on helical light-matter interaction in different material phases.

2.5 Experimental Methods

The phase-based spectroscopy across various material phases was experimentally investigated through the transmission experiments. This section provides a detailed discussion of these experiments. The femtosecond laser system used to perform the transmission measurements is discussed in the following section.

2.5.1 Ti-Sapphire Femtosecond laser

The Ti:Sapphire regenerative amplifier laser system was used in all our experiments. The laser output was centered at 800 nm (bandwidth of ≈ 40 nm), with a minimum pulse duration of 40 femtoseconds (fs), and a maximum pulse energy of 2.5 mJ. The laser system was externally triggered to operate in a gated mode, providing a pulse repetition rate on demand. In its default configuration, the system operated at a 1 kHz repetition rate, corresponding to a continuous wave (CW) mode. This section provides an introductory overview of the operational principles of the Ti:Sapphire femtosecond laser, including both the oscillator and amplifier components.

2.5.1.1 Oscillator

The oscillator generates ultrashort pulses of light with durations ranging from femtoseconds (fs) to several picoseconds. The low-power fs beam from the oscillator serves as a seed laser for the regenerative amplifier, which produces high-power fs pulses. Our fs laser system consisted of a Ti:Sapphire oscillator (Tsunami from Spectra-Physics) producing ∼30 fs pulses at an 80 MHz repetition rate. The oscillator has a wavelength tuning range of 780-820 nm, with an average output power of 400 mW at 800 nm. Figure 2.9 shows the basic layout of the ultrafast Ti:Sapphire oscillator. The configuration of a typical oscillator system includes a Ti:Sapphire rod as the gain medium, along with various optical components such as focusing mirrors, beam splitters, standard mirrors, dispersion control prisms (P_n), a wavelength selection tuning slit, and an Acousto-Optic Modulator (AOM).

Mode-locking

The oscillator utilizes the mode-locking technique to generate ultrashort, coherent light pulses. This is achieved by inducing constructive interference among all the longitudinal modes within the optical cavity. This results in the generation of a single pulse with a sharp peak, repeated at a rate determined by the round-trip time of light within the laser cavity.

Working principle: In a laser cavity, standing waves are formed when the reflected light waves interfere constructively. These standing waves produce a discrete set of longitudinal and transverse modes. Transverse modes are standing wave patterns formed perpendicular to the direction of propagation. These modes determine the spatial distribution of the laser intensity. Longitudinal modes are standing wave patterns formed along the length of the cavity. These modes determine the various frequencies at which the laser can oscillate. These multiple frequencies are separated by the intermodal spacing, which can be derived from the condition of a standing wave:

$$n\lambda = 2L \Rightarrow \quad \Delta\nu = \nu_{n+1} - \nu_n = \frac{(n+1)c}{2L} - \frac{nc}{2L} = \frac{c}{2L} \tag{2.30}$$

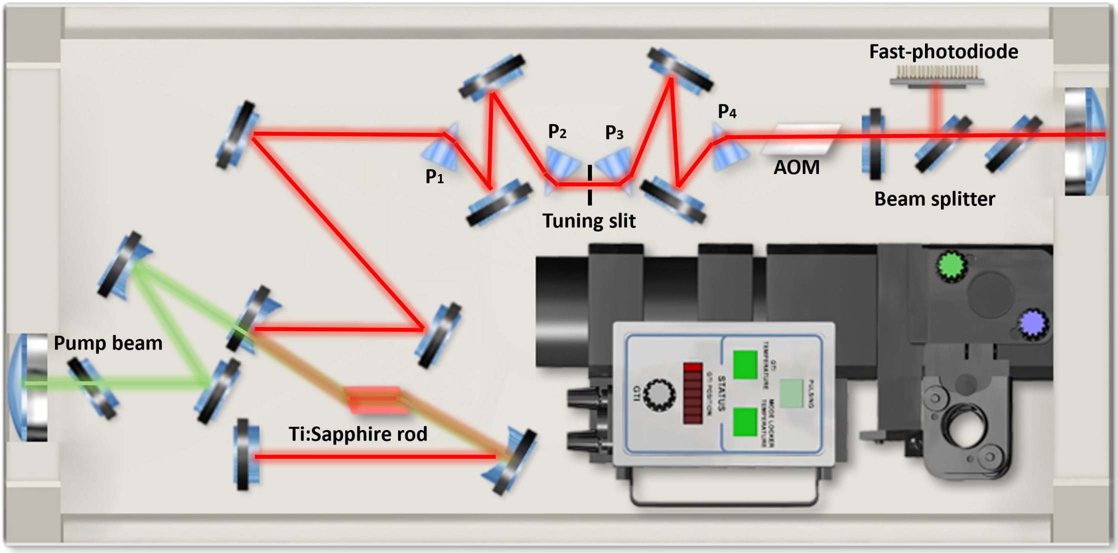

Figure 2.9: **Ti-Sapphire Oscillator.** Schematic of the simplified version of the ultrafast Ti:Sapphire oscillator. Here, P_n represents the dispersion control prisms.

where c is the speed of light, and L is the resonator length. These modes oscillate independently and do not have a fixed phase relationship, causing irregular fluctuations in laser intensity. However, it is possible to maintain a fixed phase relationship between each longitudinal mode, leading to constructive interference, resulting in the generation of a series of ultrashort pulses as the laser output. This is known as mode-locking, and the resulting laser is called a mode-locked laser. The mode-locked pulses are separated by the period $\mathrm{T} = \frac{2\mathrm{L}}{\mathrm{c}}$ which is the round-trip time for a laser beam. This period corresponds to a frequency equal to intermodal spacing $\Delta v = \frac{1}{\mathrm{T}}$. The single pulse's temporal duration, t_p, is given by [48]

$$t_p = \frac{T}{N} = \frac{2L}{cN} = \frac{\lambda_0^2}{2c\delta\lambda}$$

where N is the number of phase-locked modes given by [48] :

$$N = \frac{4L\delta\lambda}{\lambda_0^2}$$

and $\delta\lambda$ is the spectral width (stimulated emission linewidth). Therefore, the broader the spectral width, the shorter the generated pulse. This expression simply illustrates the Heisenberg uncertainty principle $\Delta t\Delta\nu \geq 1/4\pi$ where Δt represents the time uncertainty which may be interpreted as a pulse duration, and $\Delta\nu$ defines the width of the spectral band. The magnitude of this product is dependent on the temporal pulse profile. For Gaussian-shaped pulses, the frequency-bandwidth product is given by $\Delta t_{FWHH} \cdot \Delta\nu_{FWHH} = 0.441$. This is the shortest possible pulse for a given spectral width and describes an ideal, perfectly mode-locked laser with a pulse called the Fourier transform-limited pulse.

But how is mode-locking achieved? In other words, how can adjacent modes be forced to maintain a constant phase relationship?

There are various methods to achieve mode-locking, which can be classified as either 'active' or 'passive.' Active methods generally rely on an external signal to modulate the intracavity light, while passive methods rely on an element within the laser cavity that induces self-modulation of the light. Despite the differences, the principle remains the same: the phases of the longitudinal modes are synchronized to maintain a constant phase relationship, often through mechanisms like optical modulators or saturable absorbers.

- **Active mode-locking**: The resonator losses are modulated periodically to achieve mode-locking. This is achieved by placing a gain medium and an optical loss modulator in the resonant cavity of the laser. When an external signal, with a period matching the cavity round trip time, is applied to the optical modulator, amplitude or phase modulation takes place inside the cavity at a frequency equal to the intermodal separation ($\Delta\omega_q$). This modulation introduces additional radiation components at frequencies $\omega_0 \pm \Delta\omega_q$[48]. When these sidebands overlap with neighboring modes, mode coupling occurs. This coupling forces the modes to share energy and align their phases. This leads to selectively amplifying modes aligned with the modulation frequency and suppressing the rest. Over successive round-trips, this process brings all modes into a synchronized phase. This coupling and synchronization result in a fixed phase relationship between the modes, leading to the generation of ultrashort pulses. An acoustic-optic or electro-optic effect is used to introduce a periodic modulation of the loss in the laser cavity.[48]

  Acousto-Optic Modulators (AOM): When a sound wave propagates through an acousto-optic medium, it produces a periodic variation in the refractive index. This modulation of the refractive index behaves like a moving diffraction grating. Consequently, this interaction modulates the intensity of the incident laser beam at the frequency of the sound wave. By matching the modulation frequency to the frequency difference between the longitudinal modes, AOMs induce mode-locking [48]. The Tsunami Ti:Sapphire oscillator employed in our experiments uses AOM to achieve mode-locking as shown in Fig.2.9.

  Electro-Optic Modulator (EOM): In the case of an EOM, an external electric field changes the refractive index of the electro-optic crystal, modulating the phase or amplitude of the light. By driving the EOM at the frequency equal to the intermodal spacing, light modes interfere constructively, leading to mode-locking[48].

- **Passive mode-locking**: Passive mode-locking is a technique used to generate ultrashort pulses in a laser without the need for external electronic modulation. This is typically achieved using a saturable absorber, a material whose absorption decreases with increasing incident light intensity. Initially, the laser operates with random phase relationships between the longitudinal modes, resulting in fluctuating output intensity. As the intensity inside the cavity increases, the saturable absorber becomes more transparent, allowing high-intensity light to pass through while suppressing low-intensity components. After multiple round trips within the cavity, this process leads to the formation of a stable pulse train and the establishment of mode-locking. Another method is Kerr-lens mode-locking (KLM), which utilizes the intensity-dependent refractive index of a medium to focus the laser beam and induce mode-locking. Passive mode-locking methods are typically used for generating femtosecond laser pulses. [48].

Dispersion control

Within the laser cavity, optical components induce a positive group velocity dispersion (GVD), where shorter wavelengths travel more slowly than longer wavelengths [21]. This difference in propagation speeds results in an undesirable pulse broadening. To counteract this effect, various methods utilizing dispersive materials have been developed to correct and manage the broadening of the pulses.

One effective method for generating stable, short output pulses by compensating for unwanted positive dispersion involves the strategic use of a prism sequence. This technique leverages the unique properties of prisms to achieve a negative GVD within the laser cavity. The working principle of GVD compensation using prisms can be briefly described:

(i) - When a laser pulse enters the first prism, it undergoes spatial dispersion. Typically, the longer (red) wavelengths travel through more of the prism material than the shorter (blue) wavelengths. This differential travel affects the speed of the various frequency components of the pulse, adjusting their relative phases. This process introduces negative group velocity dispersion within the laser cavity, which can compensate for the positive dispersion caused by other optical components.

(ii) - The second prism in the sequence compensates for the angular dispersion introduced by the first prism. This re-collimates the spectral components, although they remain spatially separated. This re-alignment is crucial for reconstituting the pulse into a coherent beam with minimized dispersion effects. Adjusting the position of the prisms alters the group velocity dispersion (GVD) and, consequently, the width of the output pulse. Another pair of prisms after the second prism cancels out the spatial displacement of the spectral components. Thus, the original beam can be recovered using four prisms. Additionally, placing a slit after the second prism acts as a spatial filter, allowing for wavelength tuning as only the desired wavelength is transmitted. The Tsunami Ti-Sapphire laser utilizes four prisms for both dispersion control and wavelength tuning, as shown in Fig.2.9.

2.5.1.2 Laser pulse amplification

When ultrashort laser pulses are amplified, the intensities involved can become extremely high. Such high peak powers can lead to several nonlinear optical effects, such as self-focusing (optical Kerr effect) and two-photon absorption, within the gain medium, which not only limit the achievable amplification but can also damage the medium permanently.

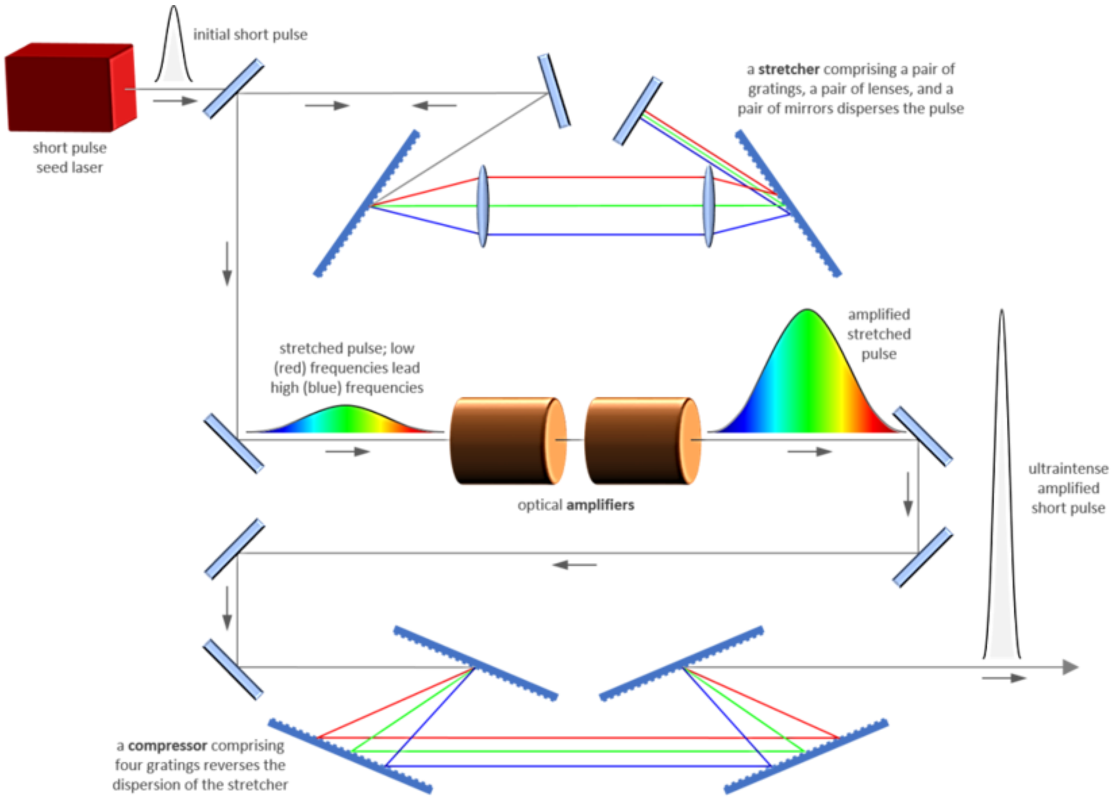

Figure 2.10: **Chirped pulse amplification** Schematic of chirped pulse amplification process. This process consists of pulse stretching, amplification, and compression, leading to the generation of a high-power femtosecond laser pulse. This image is reproduced from [49]

Chirped pulse amplification (CPA) was developed to circumvent this limitation. This technique allows for the amplification of ultrashort pulses to high energies without reaching the damage threshold of the amplifier medium. The term “chirped ” refers to the modification of the pulse such that its instantaneous frequency either increases or decreases linearly with time, resulting in a pulse where different frequencies are spread over different times. The CPA technique is shown in Fig.2.10, where the femtosecond seed pulse from a mode-locked oscillator passes through a grating-based stretcher, an amplifier, and a compressor. The following points explain the working principle of the CPA technique:

- *Stretching the pulse*: The first step in CPA involves stretching the pulse to lower its peak power, thereby avoiding damage to the amplification medium. In our laser system, this is achieved using a pair of gratings. These gratings cause the temporal dispersion of the pulse. Longer wavelengths are made to travel a longer optical path than shorter wavelengths, resulting in a stretched pulse.

- *Amplification*: Once stretched, the pulse's peak power is significantly reduced while the fluence remains unchanged. This allows it to be safely amplified without exceeding the damage threshold of the amplifying medium. In our Ti: Sapphire laser, the regenerative amplification (RA) process is employed.

  In the RA process, the seed pulse is introduced into the amplifier cavity via an electro-optic modulator. In our laser, a Pockels cell (electro-optic) is used, which utilizes the voltage-dependent optical properties of the birefringent crystal, leading to a phase shift in the transmitted light. The Pockels cell precisely controls the timing of the pulse entering and exiting the amplifier. Once inside the amplifier cavity, the pulse is trapped. The Pockels cell, by varying the retardation, ensures that the pulse is reflected back and forth multiple times through the Ti:Sapphire crystal. This crystal is pumped by an external Nd:YAG laser, producing green light at 532 nm, which excites the titanium-doped sapphire to a higher energy state. Each passage through the gain medium increases the energy of the pulse. The pulse remains in the cavity long enough to achieve the desired amplification level. Once the pulse has achieved sufficient energy, the cavity dump phase is activated, i.e., the voltage applied to the Pockels cell is turned off to allow the highly amplified pulse to exit the cavity.

- *Compression*: After amplification, the pulse is compressed to an even shorter duration to achieve the high peak power necessary for practical applications. This is accomplished using another set of gratings, similar to those used for pulse stretching. These gratings are arranged such that they reverse the temporal dispersion imposed by the first set of gratings. The longer wavelengths are sped up, and the shorter wavelengths are slowed down, effectively squeezing the pulse back to a short duration. As a result, a high-power, ultrafast femtosecond laser is produced at the output.

2.5.1.3 Pulse width measurements

A single-shot autocorrelator was used to continuously monitor the pulse duration of the laser at its output. This autocorrelator is sensitive within the range of 30-180 fs. The operation of a single-shot autocorrelator involves splitting the output beam into two separate beams, which are then focused into a nonlinear medium, such as a BBO crystal. As these beams overlap through the BBO crystal, a second harmonic (SH) signal is generated in the forward direction. Single-shot measurements were performed by measuring the spatial profile of the generated second harmonic using a CCD camera. The spatial width of the autocorrelation trace depends on the angle between the split laser pulses. The pulse duration (FWHM - τ_p) was determined from the FWHM Δx of the autocorrelation trace as [50]

$$\tau_\mathrm{p} = k\Delta x \sin(\theta/2)/c$$

where θ is the full angle between the split laser beams incident on the nonlinear medium, and k is a correction factor dependent on the pulse profile (for a Gaussian profile, $k = \sqrt{2}$; for a $sech^2$ profile, $k = 1.3$). The single-shot autocorrelator was controlled using the LabVIEW program.

A single-shot autocorrelator is a version of an intensity correlator as the autocorrelation in time is transformed into a spatial intensity distribution. In a standard intensity autocorrelator, the intensity of the SH signal is dependent on the variation of the time delay between the pulses. The signal is at its maximum when there is a temporal overlap between the two beams and drops off gradually as the temporal mismatch increases. Therefore, the SH signal intensity $A(\tau)$ can be expressed by the following mathematical expression [31]

$$A(\tau) = \int_{-\infty}^{\infty} I_s(t) I_r(t-\tau)dt$$

where I_s is the intensity of one of the beams, and $I_r(t-\tau)$ is the intensity of the delayed pulse. The autocorrelation signal can be calculated considering the incident laser beam intensity as a Gaussian beam. The autocorrelation of the Gaussian pulse, I(t), with itself can be calculated using the above formula as

$$I(t) = \exp\left[-\left(\frac{2\sqrt{\ln 2}t}{\Delta\tau_p^{FWHM}}\right)^2\right], \quad A(\tau) = \exp\left[-\left(\frac{2\sqrt{\ln 2}\tau}{\Delta\tau_A^{FWHM}}\right)^2\right]$$

The above relation shows that the autocorrelation of a Gaussian with itself is a Gaussian pulse but with a different FWHM width. The relation between the FWHM of the incident Gaussian pulse and autocorrelation signal is given as $\Delta\tau_A^{FWHM} = 1.41\Delta\tau_p^{FWHM}$.

Optics in the beam path up to the sample induce a positive GVD, resulting in the broadening of the pulse. So, a negative chirp was introduced (using the laser system) in the experiments to ensure the shortest pulses in the interaction region. This was optimized by measuring the second harmonic generation in a BBO crystal placed at the location of the sample. The pulse duration at the interaction region was about 100 fs.

2.5.1.4 Laser Power and Laser Fluence

The power measurements for most of the experiments presented in this thesis were performed with a power meter with a silicon-based detector (PRONTO-SI, Gentec-eo), capable of measuring average powers between 200 pW to 800 mW with a power calibration uncertainty of ±1.5%

at 800nm. The energy of the individual pulse was determined by dividing the measured average power by the repetition rate of the laser (1kHz).

In all experiments, the incident laser power was measured after the focusing objective to determine the power reaching the target sample. This accounted for all transmission and reflection losses from the optics. Consequently, laser intensity at the focus and laser fluence were calculated using the following

$$I = \frac{P_{\text{peak}}}{A}, \quad F = \frac{E}{A} = \frac{P_{\text{ave}}}{fA} \tag{2.31}$$

where P_{ave} is the measured average laser power, E is the laser pulse energy, A is the effective focal spot area, and, f is the repetition rate (hz). The laser peak power P_{ave} is given by

$$P_{\text{peak}} = \frac{E}{\tau} = \frac{P_{\text{ave}}}{f\tau} = \frac{FA}{\tau}$$

where τ is the pulse duration (fs). The above formula for fluence and intensity is valid only for Gaussian beams. For the same spot size, Laguerre-Gaussian beams (with null intensity region at the center) require higher pulse energies to reach the onset of nonlinear absorption. Also, since the nonlinear threshold fluence is a material property, it remains the same for beams with different l-values. The modified fluence and intensity equations for LG beams are given as [51]:

$$F_l\left[\frac{J}{cm^2}\right] = \frac{2^{(|l|+1)} r^{2|l|} e^{\frac{-2r^2}{w(z)^2}}}{|l|!\pi w\left(z\right)^{2(|l|+1)}} E_l\left[J\right] \qquad I\left[\frac{W}{cm^2}\right] = \frac{2^{(|l|+1)} r^{2|l|} e^{\frac{-2r^2}{w(z)^2}}}{|l|!\pi w\left(z\right)^{2(|l|+1)}} P_l\left[W\right] \tag{2.32}$$

where $l = 0, \pm1, \pm2, \pm3, \ldots$ is the OAM value, r is the radial direction, $w(z)$ is the radius of the beam evaluated at z and E_l is the threshold pulse energy, and P_l is the peak power for different l-values.

The fluence was determined by evaluating the radial parameter r at the maxima of the intensity profile, which occurs when $r_l^2 = w_0^2|l|/2$. For a Gaussian beam ($l = 0$), $r = 0$, while for an OAM beam with $l = 1$, $r_1 = \pm\frac{w_0}{\sqrt{2}}$, and higher-order modes follow similarly. Substituting these values for the radial parameter, we obtained the following expression:

$$\text{For } l = 0 \text{ beam} : F_0\left(r_0\right) = 2\frac{E_0}{\pi w_0^2} \tag{2.33}$$

$$\text{For l} = 1 \text{ beam} : F_1\left(r_1\right) = 2e^{-1}\frac{E_1}{\pi w_0^2} \tag{2.34}$$

2.5.2 Transmission experiments

The helical phase-based differential response (HD) in various material phases was measured using transmission experiments. The transmission of single femtosecond (fs) pulses, each with defined OAM and SAM values, was measured after propagating through the sample. For each successive pulse, the pulse energy was incrementally increased, and the transmitted signal was normalized to the incident pulse. These experiments were conducted in both the linear and nonlinear interaction regimes. The Ti:Sapphire fs laser system, operating in an externally triggered mode (pulse on demand), was utilized for the measurements. The laser triggering was controlled by a digital signal generated via the DAQ USB-6251 (National Instruments).

Figure 2.11 shows the schematic of the optical setup used for the transmission measurements. The linearly polarized Gaussian beam from the laser-amplifier was directed into the transmission setup (entering from the left in Fig.2.11). Prior to the setup, a small portion ($\sim 4\%$) of the beam was reflected towards the single-shot autocorrelator to measure the incident pulse duration. For each successive laser shot, the energy was adjusted using a combination of a cubic polarizer and a half-wave plate (HWP) mounted on a rotation stage (PR50CC, Newport, with a resolution of 0.02°). By rotating the optical axis of the HWP relative to the polarization of the incident light, the laser intensity was varied. Following the energy adjustment, the incident linearly polarized Gaussian beam was converted into a helical light beam. This conversion was achieved using a combination of quarter-wave plates (QWP), a linear polarizer (LP), and a birefringent liquid crystal-based phase plate known as a q-plate (refer to Chapter 1). The effect of these optical components on the incident linearly polarized Gaussian beam can be visualized as follows

$$|V\rangle \longrightarrow \text{QWP}(\pm 45) \xrightarrow[\text{RHC}]{\text{LHC}} \text{Q-plate} \xrightarrow[l-]{l+} \text{QWP}(\mp 45) \xrightarrow{\text{Linear}} \text{QWP}(\theta) \longrightarrow |l, \epsilon\rangle \tag{2.35}$$

The linearly polarized light beam incident on the first QWP generated left-circularly polarized (LCP) or right-circularly polarized (RCP) beams, depending on whether the angle of incidence was 45° or -45° with respect to the horizontal axis. The transmitted circularly polarized beam then propagated through the q-plate with a topological charge q, acquiring OAM ($l\hbar$, where $l = \pm 2q$) and an opposite polarization state (reversed spin angular momentum, SAM). Depending on the conversion efficiency of the q-plate, a portion of the light remained unchanged (refer to Section 1.6.3). The conversion efficiency of the q-plates with $l = 1$ and $l = 3$ was 91 ± 2 %. The second QWP transformed the incident circularly polarized OAM beams into linearly polarized OAM beams, and the unconverted portion of the Gaussian beam also acquired linear polarization. The subsequent linear polarizer removed the undesired portion of the unconverted beam, resulting in the linearly polarized OAM beam with zero SAM. The third QWP was then used to produce the desired ellipticity (ϵ), as described by $|l, \epsilon\rangle$ in Eq. (2.35).

The generated helical beam was incident on a glass plate, which reflected part of the signal onto the avalanche photodiode (APD120A2, Thorlabs), labeled as PD1. An aspheric objective

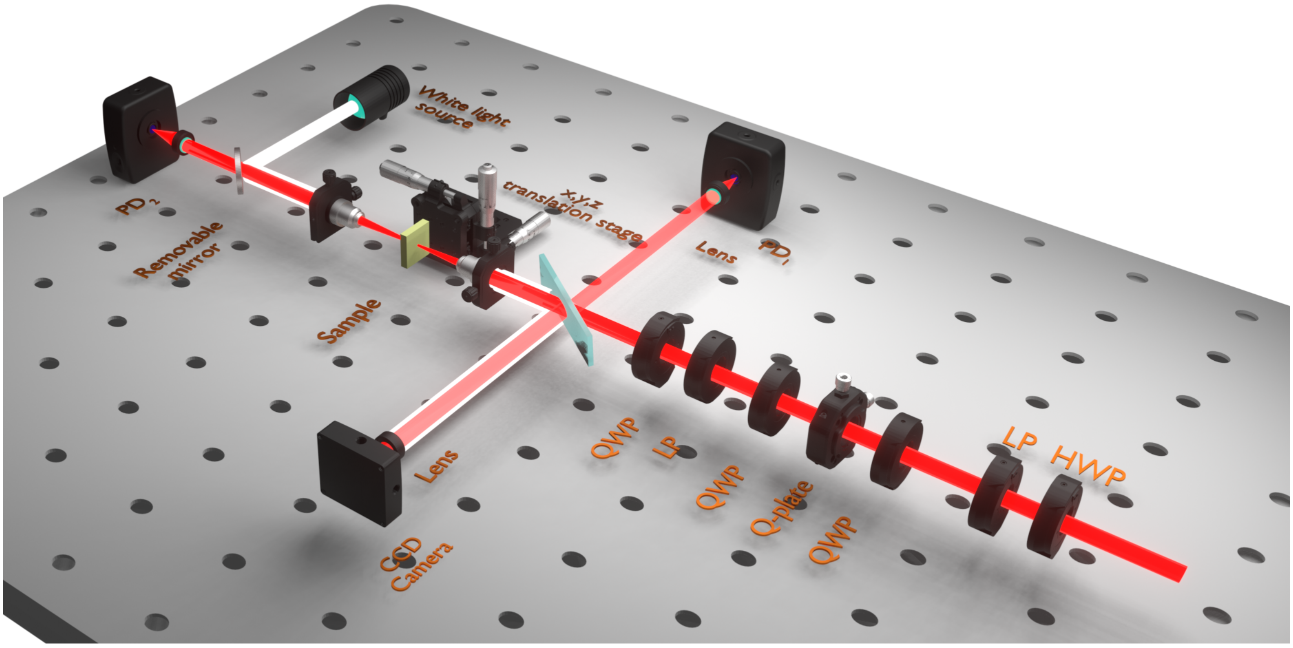

Figure 2.11: **Transmission experiments (a)** The linear polarizer (LP) and half-wave plate (HWP) controlled the incident laser power. The desired OAM and SAM states were generated using a combination of quarter-wave plates (QWPs), a birefringent liquid-crystal phase plate (q-plate), a linear polarizer (LP), and a QWP. Two aspheric lenses (NA=0.3) focused and collimated the incident and transmitted beams. Photodiode PD1 (PD2) monitored the incident (transmitted) light. The charge-coupled device (CCD) camera was used to find the surface of the sample. In the case of experiments with a metasurface, the white light source-based microscopic setup was used to position the incident beam onto the structures of interest on the sample.

lens(Newport, 16 × 11.0 mm EFL) with a numerical aperture (NA) of 0.3 (spot size of 2 ± 0.2 μm) was used to focus the laser pulses into the desired samples. In all experiments, the samples were mounted on three-axis translation stages (XMS50, XMS50, and VP-25XA, Newport), with a resolution of 100 nm along the axial (Z) direction and 50 nm in the lateral (X, Y) dimensions. mounted on a three-axis translation stage. A second aspheric objective with the same NA collected and collimated the transmitted light onto a photodiode (PD2) positioned immediately after the objective. For each laser shot, the transmitted light signal detected by PD2 was normalized to the incoming light signal detected by PD1. This transmittance was plotted as a function of incident pulse energies. The signals from PD1 and PD2 were stretched by an electronic pulse stretcher, digitized, and recorded by a data acquisition card. The control software was written in the LabVIEW software.

The asymmetrical helical beams, central to the helical phase-based spectroscopy, were produced by displacing the singularity (null intensity region) in the OAM beam. This was accomplished by translating the q-plate, which was mounted on x- and y-stages with a step size of $250 \pm 10\mu$m. At the focus, this translation of the q-plate corresponded to a displacement of the singularity with a step size of 300 ± 20 nm relative to the center of the beam. The calibration was achieved by measuring the total translation required to displace the singularity to the periphery of the defocused beam and comparing it to the measured spot size of 2 ± 0.2 μm, obtained through knife-edge measurements.

In experiments with solids (typical dimensions $10 \times 10 \times 1$ mm) and liquid samples contained in a 10 mm thick cuvette, the laser was focused in the middle of the sample. This was achieved by accurately locating the surface of the sample using back-reflected light, which was imaged by a CCD camera (MCE-B013-US, Mightex). During measurements, for each laser shot, the pulse energy was increased by approximately 3 nJ, and the sample was translated by 5μm to irradiate a fresh area. The incident pulse energies were measured before reaching the sample

In the case of the metasurface, the laser was focused on the surface over the desired fabricated nanostructures, and measurements were performed at a fixed spot without translating the sample. The surface of the substrate was determined using a CCD camera, and the incident beam focus was positioned over the desired area using a white-light-based microscopic setup (as shown in Fig. 2.11). Before commencing the experiments, the glass plate positioned in the beam path was tilted at an angle of approximately 20° to avoid Brewster's angle.

Multiple transmission curves were obtained for each sample, which were subsequently averaged and smoothed. The difference in the normalized transmission of left- and right-handed helical light is proportional to the differential absorption, i.e., HD (Type I). These measurements were repeated at different displacements of the singularity (δ), and HD was plotted as a function of displacement. For example, Fig.2.12 shows the transmission curves obtained for left-circularly polarized (LCP) and right-circularly polarized (RCP) Gaussian beams, as well as linearly polarized helical light with $l = \pm 3$ and $\delta = 900$ nm, in the case of an S(-)-camphor diluted solution.

The transmission curves clearly distinguish two absorption regimes: linear and nonlinear absorption. When the incident laser pulse energy is below a specific threshold (≈ 60 nJ for Gaussian and 140 nJ for helical beams), the transmission is 100% and the sample remains transparent. This occurs because linear absorption is absent, as the ionization potential is greater than the incident photon energy of 1.55eV (800 nm). Above the threshold energy, nonlinear multiphoton absorption occurs, leading to a decrease in transmission as the pulse energy increases.

To calibrate the sample and minimize background noise in our setup, transmission measurements were always performed without a sample (in air). These measurements ensured that the photodiodes detected identical signals when changing the helicity of the beam from $+l$ to $-l$. Figure 2.13a shows the transmission curves (ratio of PD_2/PD_1) for the left- (black) and right-handed (red) asymmetrical LG beams through air. The red and black curves overlap within

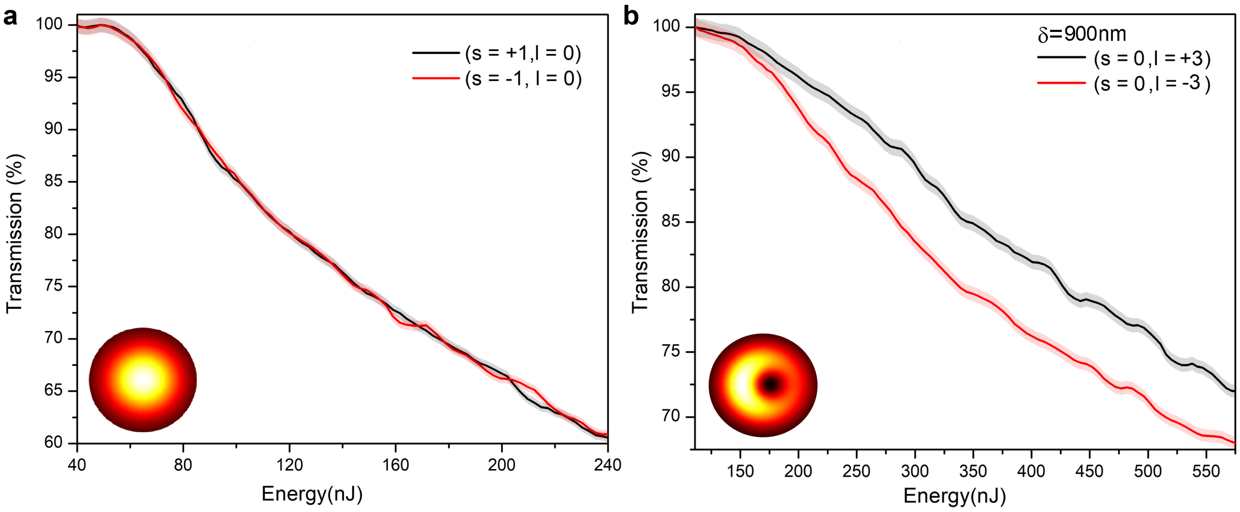

Figure 2.12: Transmission curves for $S(-)$-camphor diluted in chloroform (a) LCP and RCP Gaussian beam ($s = \pm 1$) and (b) linearly polarized helical light $s = 0, l = \pm 3, \delta = 900$nm. The error bands represent the standard error of multiple independent transmission measurements.

0.5% across the entire fluence range. Additionally, Fig.2.13b shows the difference between the PD1 and PD2 signals for linearly polarized $+l$ and $-l$. The signals are centered around zero with a fluctuation of $\pm 0.05V$, and the curves nearly overlap over the entire energy range. Both results demonstrate that no arbitrary signal or noise is introduced by the experimental setup in the observed differential absorption.

Additional checks were performed to ensure that the measured single-shot beam profile, pulse spectrum, and OAM value remained unchanged after transmission through the samples. For further details, refer to the supplementary file attached in Chapter 3.

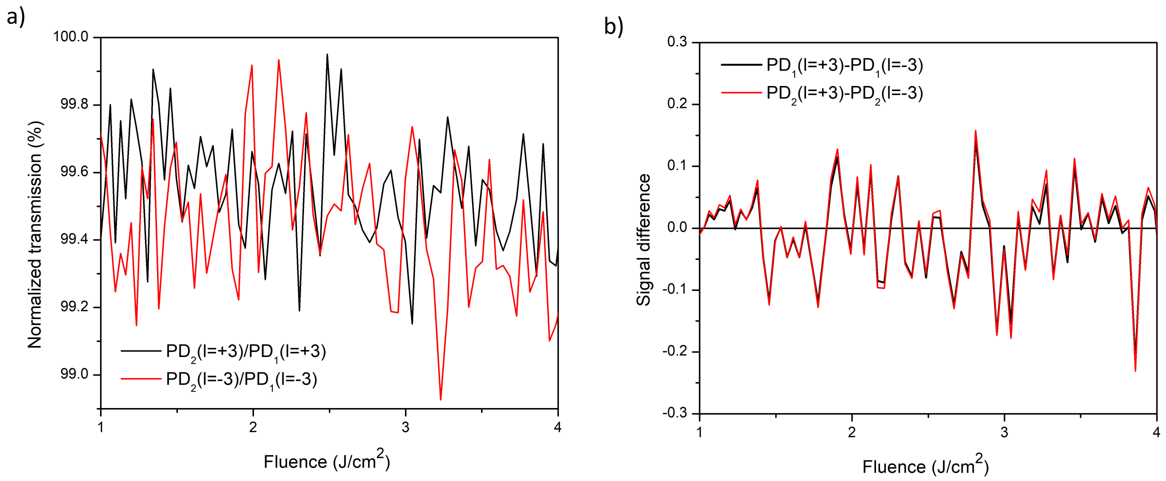

Figure 2.13: Transmission of linearly polarized ($\epsilon = 0.05$) helical light in air for symmetrical OAM beam. **a**) Ratio of PD2 and PD1 signals for $l = +3$ (black) and $l = -3$ (red). **b**) The difference in photodiode signals for the two helicities, PD1 in black and PD2 in red.

References

[1] N. Simpson, K. Dholakia, L. Allen, and M. Padgett. Mechanical equivalence of spin and orbital angular momentum of light: an optical spanner. *Optics Letters*, 22:52–54, 1997.

[2] D. S. Bradshaw and D. L. Andrews. Manipulating particles with light: radiation and gradient forces. *European Journal of Physics*, 38:034008, 2017.

[3] L. Novotny and B. Hecht. *Principles of Nano-Optics*. Cambridge University Press, 2nd edition, 2012.

[4] Richard A. Beth. Mechanical detection and measurement of the angular momentum of light. *Physical Review*, 50:115–125, 1936.

[5] H. He, M.E.J. Friese, N.R. Heckenberg, and H. Rubinsztein-Dunlop. Direct observation of transfer of angular momentum to absorptive particles from a laser beam with a phase singularity. *Physical Review Letters*, 75:826–829, 1995.

[6] Ettore Castiglioni, Sergio Abbate, and Giovanna Longhi. Experimental methods for measuring optical rotatory dispersion: survey and outlook. *Chirality*, 23:711–716, 2011.

[7] Koji Nakanishi, Nina Berova, and Robert W. Woody. *Circular Dichroism: Principles and Applications*. Wiley, 2000.

[8] Maurice H. M. Janssen and Ivan Powis. Detecting chirality in molecules by imaging photoelectron circular dichroism. *Physical Chemistry Chemical Physics*, 16:856–871, 2014.

[9] Ingolf Warnke and Filipp Furche. Circular dichroism: electronic. *WIREs Comput Mol Sci*, 2:150–166, 2012.

[10] Ivan Powis. Photoelectron circular dichroism of the randomly oriented chiral molecules glyceraldehyde and lactic acid. *The Journal of Chemical Physics*, 112:301–310, 2000.

[11] Mark M. Green, R. J. M. Nolte, E. W. Meijer, Scott E. Denmark, and Jay A. Siegel, editors. *Materials-Chirality.* Wiley, 2003.

[12] F. Araoka et al. Interactions of twisted light with chiral molecules: an experimental investigation. *Physical Review A*, 71:055401, 2005.

[13] W. Löffler, D. J. Broer, and J. P. Woerdman. Circular dichroism of cholesteric polymers and the orbital angular momentum of light. *Physical Review A*, 83:065801, 2011.

[14] K. A. Forbes and D. L. Andrews. Spin-orbit interactions and chiroptical effects engaging orbital angular momentum of twisted light in chiral and achiral media. *Physical Review A*, 99:023837, 2019.

[15] K. A. Forbes and D. L. Andrews. Optical orbital angular momentum: twisted light and chirality. *Optical Letters*, 43:435–438, 2018.

[16] J. R. Rouxel et al. Hard x-ray helical dichroism of disordered molecular media. *Nature Photonics*, 16:570–574, 2022.

[17] J. Ni et al. Giant helical dichroism of single chiral nanostructures with photonic orbital angular momentum. *ACS Nano*, 15:2893–2900, 2021.

[18] W. Brullot et al. Resolving enantiomers using the optical angular momentum of twisted light. *Science Advances*, 2:e1501349, 2016.

[19] Georges H. Wagnière. *On Chirality and the Universal Asymmetry: Reflections on Image and Mirror Image.* Wiley-VCH, 2007.

[20] H. B. Tran Tan, D. Xiao, and A. Derevianko. Parity-mixed coupled-cluster formalism for computing parity-violating amplitudes. *Phys. Rev. A*, 105:022803, 2022.

[21] Robert W. Boyd. *Nonlinear Optics.* Academic Press, Inc., third edition, 2008.

[22] Amethyst Galleries' Mineral Gallery. General structure of quartz and silica minerals, 2024.

[23] R. Kuroda, J. J. Novoa, D. Braga, and L. Addadi. *Chirality in Crystals*, page 251. Springer, 2008.

[24] Á. Valentín-Pérez, P. Rosa, E. A. Hillard, and M. Giorgi. Chirality determination in crystals. *Chirality*, 34:163–181, 2021.

[25] S. R. Elliott. Medium-range structural order in covalent amorphous solids. *Nature*, 354:445–452, 1991.

[26] D. L. Price. Intermediate-range order in glasses. *Current Opinion in Solid State and Materials Science*, 1:572–577, 1996.

[27] P. Salmon et al. Topological versus chemical ordering in network glasses at intermediate and extended length scales. *Nature*, 435:75–78, 2005.

[28] S. Lan et al. A medium-range structure motif linking amorphous and crystalline states. *Nature Materials*, 20:1347–1352, 2021.

[29] J. Singh and K. Shimakawa. *Advances in Amorphous Semiconductors.* CRC Press, 1 edition, 2003.

[30] Jun John Sakurai. *Modern Quantum Mechanics; Rev. Ed.* Addison-Wesley, Reading, MA, 1994.

[31] R.N. Bracewell. *The Fourier Transform and Its Applications.* McGraw-Hill Kogakusha, Ltd., Tokyo, second edition edition, 1978.

[32] D. P. Craig and T. Thirunamachandran. *Molecular Quantum Electrodynamics: An Introduction to Radiation Molecule Interactions.* Academic Press Inc., 1984.

[33] Yiqiao Tang and Adam E. Cohen. Enhanced enantioselectivity in excitation of chiral molecules by superchiral light. *Science*, 332:333–336, 2011.

[34] Nan Yang and Adam E. Cohen. Local geometry of electromagnetic fields and its role in molecular multipole transitions. *Journal of Physical Chemistry B*, 115:5304–5311, 2011.

[35] D. Lipkin. Existence of a new conservation law in electromagnetic theory. *J. Math. Phys. (N.Y.)*, 5:696–700, 1964.

[36] Laurence David Barron. True and false chirality and absolute enantioselection. *Rendiconti Lincei. Scienze Fisiche e Naturali*, 24:179–189, 2013.

[37] K. A. Forbes and D. L. Andrews. Orbital angular momentum of twisted light: chirality and optical activity. *J. Phys. Photon.*, 3:022007, 2021.

[38] J. Ohkubo et al. Molecular alignment in a liquid induced by a nonresonant laser field: molecular dynamics simulation. *J. Chem. Phys.*, 120:9123–9132, 2004.

[39] P. W. Dooley et al. Direct imaging of rotation wave-packet dynamics of diatomic molecules. *Phys. Rev. A*, 68:023406, 2003.

[40] S. Fleischer et al. Molecular alignment induced by ultrashort laser pulses and its impact on molecular motion. *Is. J. Chem.*, 52:414–437, 2012.

[41] C.B. Schaffer et al. Laser-induced breakdown and damage in bulk transparent materials induced by tightly focused femtosecond laser pulses. *Meas. Sci. Technol.*, 12:1784, 2002.

[42] L. V. Keldysh. Ionization in the field of a strong electromagnetic wave. *Sov. Phys. JETP*, 20:1307, 1965.

[43] A.Q. Wu et al. Femtosecond laser absorption in fused silica: Numerical and experimental investigation. *Phys. Rev. B*, 72:085128, 2005.

[44] E.E. Serebryannikov and A.M. Zheltikov. Strong-field photoionization as excited-state tunneling. *Phys. Rev. Lett.*, 116:123901, 2016.

[45] M. Klaiber and J. S. Briggs. Crossover from tunneling to multiphoton ionization of atoms. *Phys. Rev. A*, 94:053405, 2016.

[46] P. Jürgens et al. Origin of strong-field-induced low-order harmonic generation in amorphous quartz. *Nat. Phys.*, 16:1035–1039, 2020.

[47] L. Sudrie et al. Femtosecond laser-induced damage and filamentary propagation in fused silica. *Phys. Rev. Lett.*, 89:186601, 2002.

[48] Jean-Claude Diels and Wolfgang Rudolph. *Ultrashort Laser Pulse Phenomena: Fundamentals, Techniques, and Applications on a Femtosecond Time Scale.* Academic Press, Burlington, MA, 2nd edition, 2006.

[49] Plymouth Grating Laboratory. Chirped pulse amplification (cpa), 2024.

[50] K. Sharma, P. A. Naik, P. D. Gupta, and R. A. Ganeev. A second-order autocorrelator for single-shot measurement of femtosecond laser pulse durations. *Sadhana - Acad. Proc. Eng. Sci.*, 26:603–611, 2001.

[51] C. Hnatovsky et al. Materials processing with a tightly focused femtosecond laser vortex pulse. *Opt. Lett.*, 35(20):3417, 2010.

Chapter 3

Nonlinear helicity-dependent light absorption in chiral and achiral molecules

3.1 Introduction

In previous chapters, it was established that the polarization of light associated with spin angular momentum (SAM) can serve as a chiral probe for investigating material chirality. In practical applications, polarization-based techniques like circular dichroism (CD)[1] and optical rotation (OR) [2] are often employed to identify enantiomers and facilitate enantioselective synthesis. In OR, left- and right-handed circularly polarized light travel at different speeds through the enantiomers, resulting in a rotation of the light's polarization. On the other hand, in CD, left-handed and right-handed circularly polarized light are absorbed differently by the enantiomers, leading to a differential absorption of light. As discussed in Chapter 2, CD arises from the relatively weak coupling between electric and magnetic dipole moments, contributing to its low chiral sensitivity, typically in the range of 0.01-1%[3]. The chiral sensitivity of the CD technique can be improved by exploiting local field enhancements in metallic nanostructures[4], using superchiral light[5], or through strong-field techniques with elliptically polarized light[6]. Another recent advancement is photoelectron circular dichroism (PECD), a technique used to study chirality in gases. In PECD, ionizing a chiral molecule leads to an asymmetric ejection of electrons, creating a distribution that differs between enantiomers. This method is significantly more efficient than CD, typically one to two orders of magnitude more sensitive, as it relies solely on electric dipole interactions[7, 8].

One of the significant limitations of the CD technique is that when the chiral signal is inherently weak, it cannot be enhanced without the use of external intermediaries. This limitation has led to the search for alternative chiral probes other than polarization. Light beams carrying orbital angular momentum (OAM) associated with helical wavefronts presented a potential alternative, where the twisted phasefronts could be used as a chiral probe. Such beams are commonly referred to as helical or OAM beams. These beams can carry a theoretically unbounded range of OAM values, $l\hbar$, in contrast to the limited SAM values, offering an advantage over polarization-based techniques.

Earlier studies investigating the use of helical beams to study chirality were inconclusive. Most experiments were conducted under the linear absorption regime[9, 10], while theoretical work primarily focused on the interactions between electric and magnetic dipole transition moments [11]. Recent theoretical studies have proposed that the circularly polarized OAM beams could be employed to probe material chirality by involving higher-order transition moments.[12, 13]. Experimentally, the direct observation of phase-based chiral discrimination has remained elusive [9]. Helical Dichroism (HD), defined as differential absorption of left- and right-helical light (analogous to the CD definition), has only been observed in the presence of intermediaries, such as nanoparticle aggregates (leveraging the local field effects) [14], powdered chiral molecular media[15] (utilizing x-ray diffraction) and chiral metasurfaces [16] (engineered structures. These studies also established that HD vanishes in the case of randomly oriented achiral molecules. Thus, the question naturally arises: *Can the helical wavefronts carried by OAM beams serve as a chiral probe to study both chiral and achiral molecules without the need for external intermediaries?.*

This research demonstrated the direct observation of HD in both chiral and achiral molecules in the liquid phase, without the use of external intermediaries. Our approach was based on probing the helicity-dependent nonlinear absorption of asymmetric helical light beams propagating through the liquid sample. The presence of HD with linearly polarized asymmetric beams confirmed that enantioselectivity was a phase effect. The light-matter interactions were modeled by considering induced multipole moments.

This research was published in the *Nature Photonics* journal (2023), with shared first authorship between my colleague and me, reflecting our equal contributions to the work. The published article and supplementary file are reproduced in this chapter, where the theoretical framework, experimental methods, figures, and references are self-contained within each. The following section presents the key results and advancements.

3.2 Key results and advances

CD measurements were performed in both chiral and achiral molecules by measuring the differential absorption of left- and right-handed circularly polarized light (CPL). As expected, the achiral molecules exhibited no differential response. In the chiral molecules, the CD signal strength was within the noise level of our experimental setup, demonstrating the inherently weak CD at the 800 nm wavelength. In contrast, when the samples were probed with asymmetrical helical light, differential absorption between left- and right-handed asymmetrical light was observed, demonstrating helical dichroism (HD). HD measurements were performed in both chiral and achiral liquids, and the results were plotted as a function of the displacement of the singularity. The results revealed two types of HD: (i) HD (Type I) and (ii) HD (Type II). The key findings can be summarized as follows

- *HD (Type I)*: defined as the differential absorption of left- and right-handed helical light. It is a beam-dominated property, and its definition is independent of material symmetry. The HD (Type I) was observed in both achiral and chiral liquids. The HD signal was zero for symmetric OAM beams and nonzero only with asymmetric OAM beams. This allowed the HD signal to be tuned by varying the displacement of the singularity. Additionally, the HD signal scaled with the OAM value and was further manipulated by adjusting the laser polarization. The results are presented in Fig. 3-5 of the article.
- *HD(Type II)*: defined as the difference of absorption between the left- and right-handed chiral molecules for a specific-handed helical light. It is a material-dominated property, and its definition involves both the material and the light beam to be chiral entities. HD (Type II) demonstrated enantioselectivity in chiral molecules. The HD (Type II) signal was not affected by the displacement of the singularity, although the signal was more stable when the singularity was displaced. The results are presented in Fig.2 and 4 of the article.
- *Theoretical modeling*: The differential absorption of left- and right-handed helical light was simulated using the derived nonlinear interaction model. The electric and magnetic fields were also derived for the asymmetric Laguerre-Gaussian mode. The simulated results, presented in Fig.5 of the published article, were in qualitative agreement with the experimental data. The simulated curve exhibited a similar sinusoidal-shaped differential absorption pattern.

The major advances of this research can be summarized as follows:

1. A novel phase-based chiroptical detection method that utilizes the nonlinear absorption of asymmetric helical light beams in chiral liquids is introduced. The direct observation of helicity-dependent absorption in achiral systems is also demonstrated.

2. The HD signal is precisely tunable by displacing the singularity within an OAM beam and can be scaled according to the OAM value. Additionally, the signal strength can be controlled by varying the laser polarization. These unique features are absent in traditional chiroptical techniques like CD, which rely solely on laser polarization as a chiral probe.

3. HD is a non-resonant technique that does not require tuning of the laser wavelength to specific resonances, the application of external electric and magnetic fields, or special sample preparation.

4. The underlying principle is general and applicable to a large variety of molecules. This work shifts the paradigm of chiroptical detection from using laser polarization to the optical helical phase.

The following section reproduces the author contribution statement from the published article. The published article is attached later.

3.3 Statement of contribution

These authors contributed equally: Ashish Jain and Jean-Luc Bégin.

This project was conceived and designed in collaboration with my colleague Jean-Luc Bégin and my supervisor, Professor Ravi Bhardwaj. It commenced after the completion of my helical light-based laser ablation project (Chapter 7), where the knowledge of helical light beams proved advantageous. My colleague and I built the experimental setup and conducted calibration experiments to minimize background noise. Together, we conducted all the experiments and analyzed the experimental data. The theory of helical light-matter interaction was developed by us, with assistance from PhD student Andrew Parks. Professor Thomas Brabec and my supervisor provided invaluable guidance and worked collaboratively on the theoretical framework. Numerical simulations were performed jointly with my colleague. The q-plates used to generate helical light beams were fabricated by our collaborator, Professor Ebrahim Karimi, and his PhD student Felix Hufnagel. Professors Paul Corkum, Ebrahim Karimi, and Ravi Bhardwaj supervised the project. I prepared the initial draft of the research manuscript with my colleague, Professor Thomas Brabec, and Professor Ravi Bhardwaj. All authors reviewed the manuscript.

nature photonics

Article

https://doi.org/10.1038/s41566-022-01100-0

Nonlinear helical dichroism in chiral and achiral molecules

Received: 10 May 2022

Accepted: 30 September 2022

Jean-Luc Bégin[1,2], Ashish Jain[1,2], Andrew Parks[1], Felix Hufnagel[1], Paul Corkum[1], Ebrahim Karimi[1], Thomas Brabec[1] & Ravi Bhardwaj[1] ✉

Chiral interactions are prevalent in nature, driving a variety of biochemical processes. Discerning the two non-superimposable mirror images of a chiral molecule, known as enantiomers, requires interaction with a chiral reagent with known handedness. Circularly polarized light beams are often used as a chiral reagent. Here we demonstrate efficient chiral sensitivity with linearly polarized helical light beams carrying an orbital angular momentum of $\pm l\hbar$, in which the handedness is defined by the twisted wavefront structure tracing a left- or right-handed corkscrew pattern as it propagates in space. By probing the nonlinear optical response, we show that helicity-dependent nonlinear absorption occurs even in achiral molecules and can be controlled. We model this effect by considering induced multipole moments in light–matter interactions. Design and control of light–matter interactions with helical light may open new opportunities in chiroptical spectroscopy, light-driven molecular machines, optical switching and in situ ultrafast probing of chiral systems and magnetic materials.

Our understanding of light–matter interactions is mainly based on the propagation of homogeneously polarized light and the dominance of the dipole-active transitions between different quantum states of matter. Higher-order multipole effects are often ignored. The strength of dipole transitions is governed by the frequency, intensity and polarization of the incident light. The optical phase, represented by the wavefront of the light beam, plays a minimal role in such transitions. Within the dipole approximation, chiral systems are often studied using circularly polarized light (CPL), in which the dynamical rotation of the electric-field vector around the propagation direction yields an effective spin angular momentum (SAM) $\pm\hbar$, and therefore the handedness.

Two correlated optical techniques are widely used to probe chiral systems based on the propagation of polarized light through a chiral sample: circular dichroism (CD) and optical rotation (OR). In CD, left-CPL and right-CPL are absorbed differently in the two enantiomers, leading to differential absorption[1,2]. In OR, on the other hand, left-CPL and right-CPL travel with unequal velocities in the two enantiomers, leading to polarization rotation[3,4]. The chiral sensitivity of CD is poor, on the order of 0.01–1% (ref. [5]), because it involves coupling of electric and magnetic dipole transitions. CD can be enhanced by employing super chiral light[6], plasmonic structures[7,8] and strong field techniques using elliptically polarized light[9,10]. A distinct gas-phase chiroptical technique that has emerged in recent years is photo-electron circular dichroism (PECD). In PECD, photo-ionization of a chiral molecule results in an asymmetric photo-electron angular distribution for the two enantiomers[11]. PECD is due to pure electric dipole transitions, so its efficiency is one to two orders of magnitude larger than that of CD[5,12].

Light can also carry orbital angular momentum (OAM) of $\pm l\hbar$ associated with dynamical rotation of the wavefront structure[13–15]. The handedness of such helical light beams is defined by the twisting of the wavefront undergoing l intertwined rotations in one wavelength. This additional degree of freedom influences the characteristics of light–matter interactions. The angular distribution[16], time delay[17] and dynamics of photo-electrons[18,19] can be modified during the photo-ionization of atoms and molecules. Also, the OAM of light can be transferred to matter either externally by exerting a torque (as in optical tweezers[20] and Bose–Einstein condensates[21,22]) or internally by rotating the electron distribution and resulting in modified selection rules for transitions that depend on the topological charge l (refs. [23,24]).

---

[1]Department of Physics, University of Ottawa, Ottawa, Ontario, Canada. [2]These authors contributed equally: Jean-Luc Bégin, Ashish Jain.
✉e-mail: ravi.bhardwaj@uottawa.ca

The possibility of no upper bound on the l value, while SAM can assume only two defined values, has generated substantial interest in using helical light beams carrying OAM as a chiral reagent. Early studies on chirality with twisted photons were not promising. Most experiments were performed in the linear absorption regime[25,26], whereas theory focused solely on the coupling of the electric and magnetic dipole transition moments responsible for conventional CD[27]. Helical dichroism (HD), analogous to CD, was demonstrated by exploiting local field effects in molecules adsorbed on nanoparticle aggregates[28], chiral metasurfaces[29] and non-chiral nanostructures[30]. Coupling of the OAM of light with a material's chirality without any intermediary was recently shown to require higher-order transition moments to be engaged along with SAM to observe any chiroptical effects[31,32].

In this Article we introduce a conceptually new form of chiroptical detection technique based on nonlinear absorption of linearly polarized helical light beams in the liquid phase. We first demonstrate enantioselectivity in chiral molecules, directly without any intermediary, by probing the differential absorption between the two enantiomers for a specific helical light—we call this HD(Type II). Second, we show the differential absorption of left- and right-helical light in isotropic achiral and chiral molecules—HD(Type I)—which can be precisely controlled by displacing the singularity present in an OAM beam. Third, we reveal that HD(Type I) is scalable by changing the OAM value and that it can be further controlled by varying the laser polarization. This feature does not exist in polarization-based chiroptical techniques, such as CD. Finally, we show that HD(Type I, II) is a phase effect and does not necessarily require CPL. To understand HD, we model the light–matter interaction by considering multipole expansion. We find that HD arises from coupling of the electric dipole and electric quadrupole terms, and that it can be tuned by changing the laser polarization in addition to the OAM value.

To probe the dichroism, we measured the absorption of loosely focused femtosecond Gaussian and helical light pulses propagating through a liquid sample contained in a cuvette, as shown in Fig. 1a. A q-plate converted incident Gaussian light to an optical vortex beam (OVB) carrying an OAM value that is two times the topological charge, q (refs. [33,34]). Further experimental details are provided in the Methods. Normalized transmission of left- and right-circularly polarized ($s = \pm 1$) helical light ($l = \pm 1$) is shown in Fig. 1b as a function of the peak laser fluence in S(+)-fenchone, $C_{10}H_{16}O$. For each successive laser pulse, the energy was varied using a combination of half-wave plate (HWP) and polarizer, and a fresh sample region was irradiated by translating the cuvette. Each curve in the figure is an average of three independent measurements, and the colour band represents the statistical standard error. At low peak laser fluences, absorption is negligible and all curves overlap. The laser fluence is not sufficient to induce multiphoton transitions. At the onset of multiphoton absorption (~1.4 J cm^{-2}), the transmission starts to decrease monotonically. For a given helicity, transmission is nearly identical for left- and right-CPL, except at fluences greater than ~2.2 J cm^{-2}.

The normalized chiral signal in fenchone, defined as HD (Type II: $\pm l$; $\pm s$) = $2\frac{D(\pm l;\pm s)-L(\pm l;\pm s)}{D(\pm l;\pm s)+L(\pm l;\pm s)}$ (see Methods for notation), is shown in Fig. 1c (solid lines). For a Gaussian beam ($l = 0$), the chiral signal is less than 1% (dashed lines). Overlap of the signal with the error bands represents the sensitivity of our experiment. The chiral signal is enhanced significantly when the helical phase is introduced to the incident beam by switching from a Gaussian beam to an OAM beam. For $l = \pm 1$, HD(Type II) is ~5%. However, SAM associated with light polarization appears to play a minimal role. For a given helicity, the chiral signals for left- and right-CPL nearly overlap with each other within experimental error, similar to the Gaussian beam.

To isolate the role of SAM and OAM, we performed experiments with linearly polarized ($s = 0$) helical ($\pm l$) and Gaussian beams. It is worth noting that multiphoton absorption cross-sections depend on the laser polarization and are typically higher for linear than circular polarization[35–37]. Figure 2a,b shows HD(Type II) in fenchone as a function of peak laser fluence for $l = \pm 1$ and $l = \pm 2$, respectively. The results for limonene ($C_{10}H_{16}$) are shown in Supplementary Section 1. Also shown in Fig. 2a is the differential absorption of two orthogonal linearly polarized Gaussian beams (dashed lines). The chiral signal in fenchone increases with laser fluence, reaching a maximum of ~4–6%, and also increases with the helicity (l value) of the beam (Fig. 2a,b). For $l = 2$, the onset of nonlinear absorption occurs at higher pulse energies. In experiments with different l values, the pulse energies were always varied from below the threshold for the onset of nonlinear absorption to approximately twice the threshold value, as shown in Fig. 1b. This ensured that the nonlinear response regime we investigated remained the same (~10^{13} W cm^{-2}), even though the peak fluence of OAM beams depends on the l value[38] (Supplementary Section 8). Chiral discrimination with linearly polarized helical light beams demonstrates the prominent role of the optical phase associated with the OAM of light.

Generally, differential absorption defined by HD(Type I) = $A(+l, s) - A(-l, s)$ is not expected in isotropic achiral molecules with CPL. This is also true even with helical light[29]. We did not observe any differential absorption of linearly polarized helical light with symmetric OAM beams where the null intensity region is at the centre of the beam. However, when the singularity in the OAM beam is displaced from the centre, achiral molecules with different point group symmetries exhibit dichroism (Fig. 3). The singularity within the focal region of a focused OAM beam can be shifted either by (1) detuning the q-plate, leading to a superposition of the incident Gaussian beam with the converted OAM beam[39], or (2) physically shifting the centre of the q-plate with respect to the incident beam. We used the latter technique, because the former gives rise to a Gaussian component in the transmitted beam. The resultant asymmetric OAM beam introduces an asymmetry in the intensity profile in the focal region, as shown in Fig. 3a. The orientation of the laser polarization is perpendicular to the displacement of the singularity. In the experiment, alignment of the singularity at the centre of the OAM beam can only be defined before the objective, which translates to an uncertainty ~±100 nm at the focus (see Methods for calibration details).

Figure 3b presents the differential absorption of linearly polarized helical light ($l = \pm 1$) in achiral molecules, HD(Type I), with no inversion symmetry—acetone (C_3H_6O), methanol (CH_3OH) and air—for different positions of the singularity in the focused OAM beam. The differential absorption is averaged over a fluence range from the onset of nonlinear absorption (which depends on the ionization potential) in the normalized transmission curve to ~2 J cm^{-2}. In acetone (blue curve) and methanol (red curve), differential absorption exhibits a sinusoidal behaviour, with a change in sign as the singularity traverses the zero position from −1.8 μm to 1.8 μm. The small variation in the zero-crossing point for the two molecules (~100 nm) is due to uncertainty in the position of the singularity. Helicity-dependent absorption does not exist in air (empty cuvette in the experiment) and is independent of the position of the singularity (black curve). This represents the background noise introduced by our experimental set-up (Supplementary Section 5). Helicity-dependent absorption in benzene (C_6H_6), a molecule with inversion symmetry, is shown in Fig. 3c (black curve). The observed behaviour is similar to that of non-centrosymmetric molecules (Fig. 3b), suggesting that the HD signal does not appear to depend on molecular symmetry.

To disentangle the roles of phase and field gradients in an asymmetric OAM beam, we studied the differential absorption of a circularly polarized, non-OAM, annular beam that mimics the profile of a Laguerre–Gaussian (LG) beam with zero OAM value (Supplementary Section 6). Dichroism in R(−)-fenchone (green curve), S(+)-fenchone (red curve) and acetone (blue curve) is independent of the position of the singularity and is less than 1%, within the standard error. Absence of differential absorption confirms that helicity-dependent absorption in achiral molecules is a phase effect and not only due to field gradients.

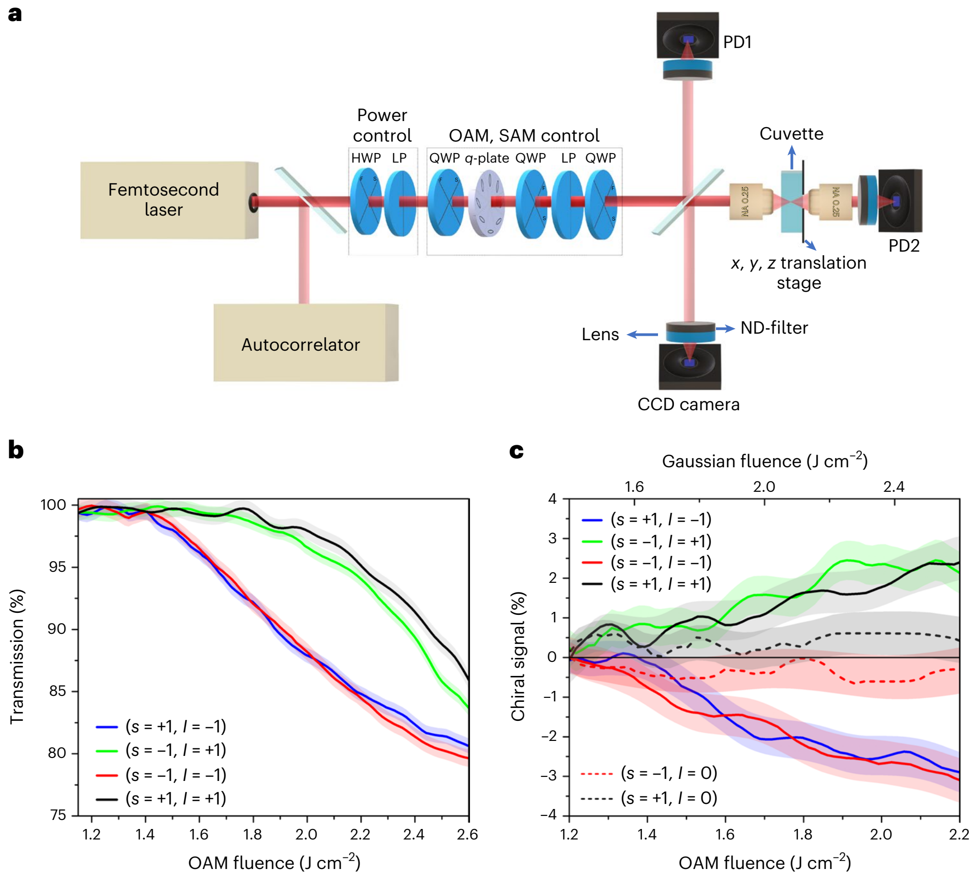

Fig. 1 | Transmission of circularly polarized ($s = \pm1$) femtosecond vortex pulses in fenchone. a, Schematic of the experimental set-up, which consists of a combination of a half-wave plate (HWP) and quarter-wave plates (QWPs), linear polarizer (LP), a birefringent liquid-crystal-based phase plate called a *q*-plate (see Methods for details), photodiodes (PDs), neutral-density (ND) filters and a charged-coupled device (CCD) camera. **b**, Transmission of left- and right-circularly polarized helical light with $l = \pm1$ in *S*(+)-fenchone, as a function of peak laser fluence. **c**, Chiral signal with circularly polarized Gaussian ($l = 0$, dashed lines) and OAM ($l = \pm1$, solid lines) beams in fenchone as a function of peak laser fluence. Each curve in **b** is an average of three independent measurements (sample size) and the colour bands represent the statistical standard error. The colour bands in **c** represent the propagation error of the chiral signal. These experimental results were reproduced multiple times under identical conditions.

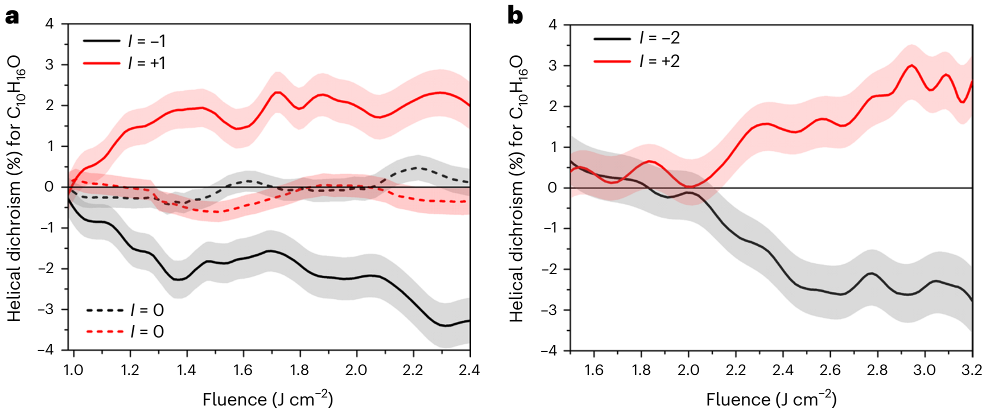

Fig. 2 | Helical dichroism (Type II) in fenchone with linearly polarized light ($s = 0$) as a function of peak laser fluence. a, HD in fenchone for $l = \pm1$ (solid lines) and Gaussian ($l = 0$, dashed lines) beams. The bottom abscissa shows the peak laser fluence for the OAM and Gaussian beams. **b**, HD in fenchone for $l = \pm2$ beams. The colour bands represent the propagation error of the chiral signal for three independent measurements (sample size). These experimental results were reproduced multiple times under identical conditions.

Figure 4a presents the HD(Type I) signal in limonene enantiomers for different positions of the singularity in an OAM beam. The spatial variation of HD(Type I) exhibits the same behaviour as achiral molecules (Fig. 3b,c). The key difference is that with asymmetric OAM beam, the helicity-dependent absorption in the two enantiomers is different, resulting in non-zero chiral signal given by HD(Type II). Figure 4b,c show that the HD(Type II) signal in limonene as a function of peak laser fluence is weakly dependent on the position of the singularity

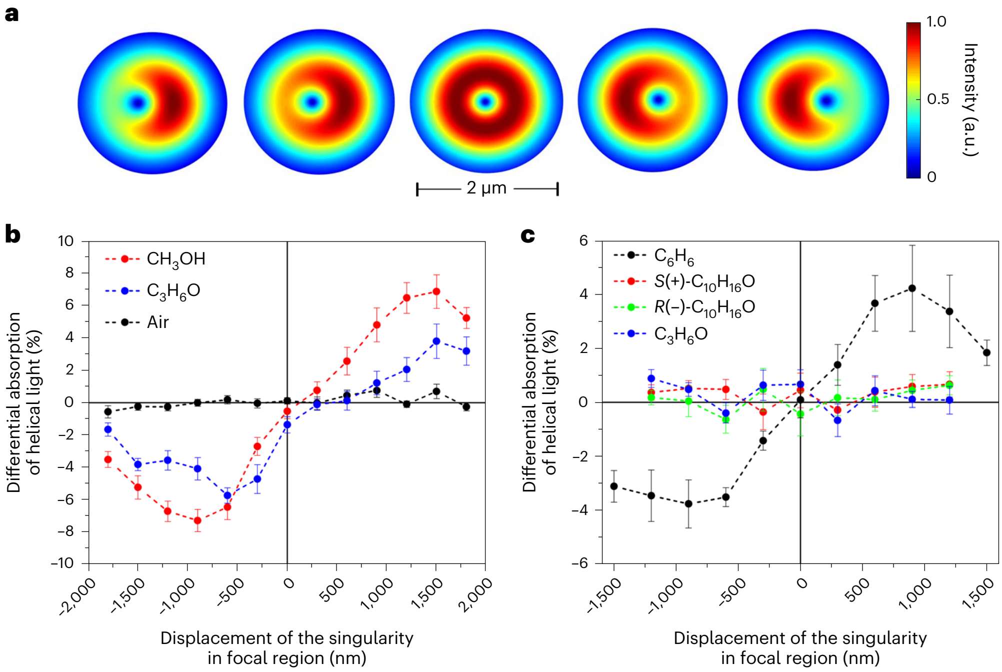

Fig. 3 | Helicity-dependent absorption, HD(Type I), in achiral molecules. **a**, Simulated intensity profiles of asymmetric OAM beams obtained by shifting the position of the *q*-plate with respect to the incident beam. **b**,**c**, Differential absorption of linearly polarized left- and right-helical light ($l = \pm1$) as a function of displacement of the singularity in the focal region. (**b**) Air (black) and achiral molecules with no inversion symmetry (acetone (blue), methanol (red)). (**c**) Benzene (black), an achiral molecule with inversion symmetry. Also shown in **c** is the differential absorption of a circularly polarized non-OAM beam ($l = 0$) with a singularity at the centre in acetone (blue) and *R*(−)- and *S*(+)-fenchone (green and red). The dashed lines connecting the discrete experimental points are for visualization only. The error bars represent the propagation error of the chiral signal for three independent measurements (sample size). These experimental results were reproduced multiple times under identical conditions.

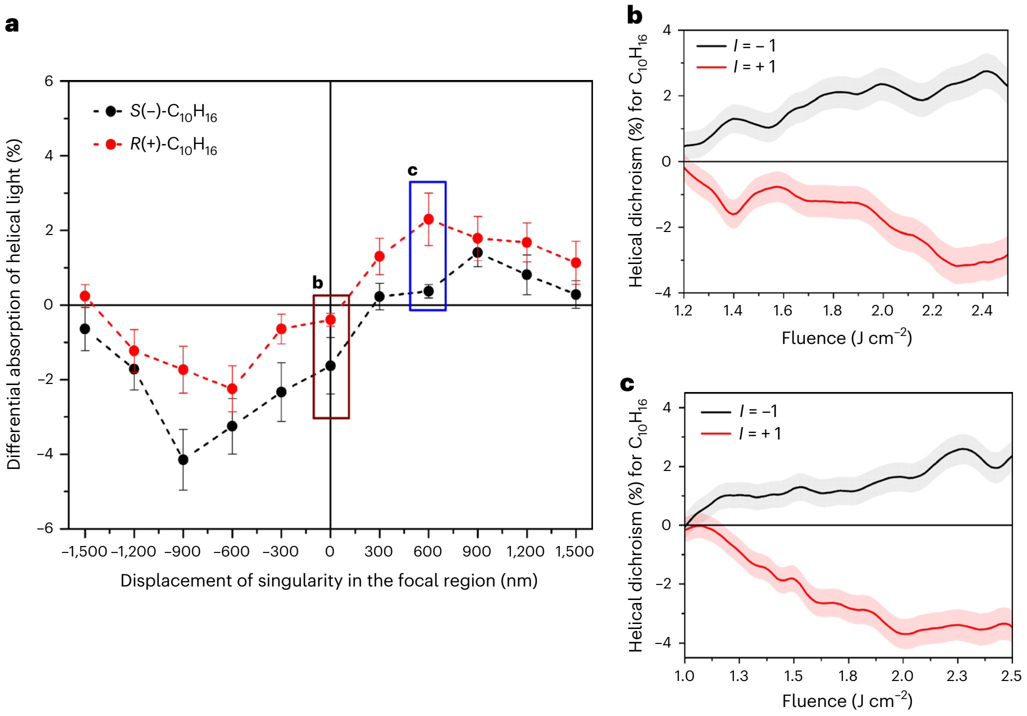

Fig. 4 | Helical dichroism with linearly polarized asymmetric OAM beams ($l = \pm1$) in limonene. **a**, HD(Type I) as a function of the position (or displacement) of the singularity in the OAM beam. **b**,**c**, HD(Type II) as a function of peak laser fluence when the singularity is at the positions marked by the maroon (**b**) and blue (**c**) rectangles in **a**. The error bars and colour bands represent the propagation error of the chiral signal for three independent measurements (sample size).

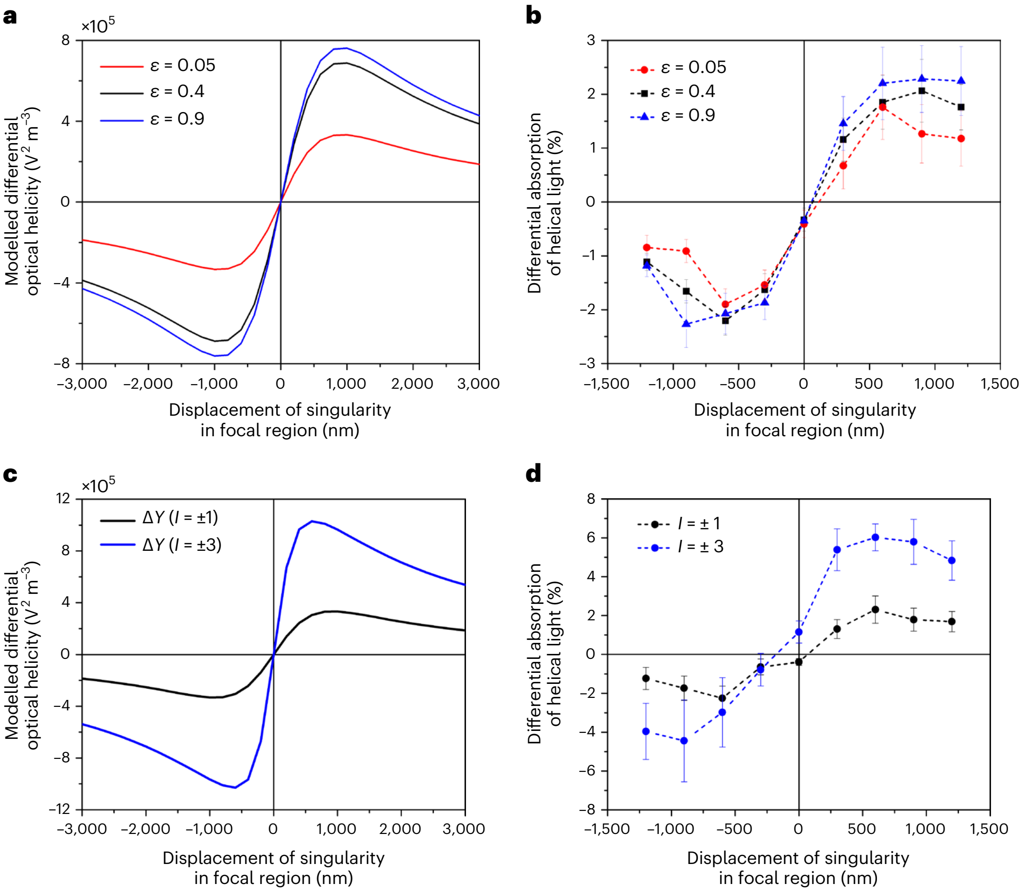

Fig. 5 | Helical dichroism (Type I) with asymmetric OAM beams in R(+)-limonene. Modelled (**a**,**c**) and measured (**b**,**d**) differential absorption as a function of the displacement of singularity for $l = \pm1$ and different ellipticities (**a**,**b**) and for 95% linearly polarized helical light for $l = \pm1, \pm3$ (**c**,**d**). Differential absorption was modelled by the relation $\Delta W \approx A''\Delta\Upsilon$, where $\Delta\Upsilon = \int_{-\omega_0}^{\omega_0}[\Upsilon^+ - \Upsilon^-]\,\mathrm{d}x\mathrm{d}y$ is the differential optical helicity representing the E1E2 coupling term (see main text for details). The error bars represent the propagation error of the chiral signal for three independent measurements (sample size).

within the OAM beam. They were obtained when the singularity is at the positions marked by solid rectangles in Fig. 4a. Similar results were obtained for fenchone (Supplementary Section 1). HD(Type II) signals in limonene (Supplementary Fig. 1) and fenchone (Fig. 2) are of opposite sign (Methods). Although the HD (Type II) signal is not affected by the location of the phase singularity, it is much more stable with an asymmetric OAM beam. The results were also found not to depend on the laser focus position inside the cuvette. The effects of propagation of intense light pulses through the sample were negligible (Supplementary Sections 2 and 4).

To understand the chiral light–matter interaction, we modelled the rate of excitation (Γ) of the molecule using time-averaged induced multipoles (Methods). The coupling terms involving the electric–magnetic dipole (E1M1) and electric dipole–quadrupole (E1E2) moments (equation (8)) are pseudoscalars, so they change sign under improper rotation, contributing to HD(Type I, II) (equations (10) and (11)). HD(Type I) was modelled by evaluating equations (9) and (10), assuming full alignment, using the experimental parameters (equations (12)–(19); $\omega = 2.35 \times 10^{15}$ Hz, $\omega_0 = 2$ μm) and approximating the response tensors G' and A'' with scalars (or pseudoscalar)[40]. The E1M1 term vanishes because we take the difference between left and right-helical beams for the same polarization. Hence, the E1E2 term is the major contributor to the HD(Type I) for asymmetric OAM beams.

Figure 5a depicts the modelled E1E2 term (described in terms of differential optical helicity $\Delta\Upsilon$) for different polarizations, described by ellipticity ε. The magnitude of differential absorption is maximal for circular polarization (ε = 1), decreases with ellipticity and goes to zero for perfect linear polarization (ε = 0). This is in agreement with the experimentally observed sinusoidal behaviour of HD(Type I) for the chiral molecule shown in Fig. 5b and the achiral molecules shown in Fig. 3b,c. The minimum ε value achieved experimentally was 0.05. In the experiments, the displacement of singularity is restricted by the focal spot, whereas the modelling of the E1E2 term does not include such boundary effects. As a result, at the extreme positions of the singularity in the experiment, the intensity profile mimics a symmetric Gaussian, leading to zero gradient force (Supplementary Section 9) and subsequently no differential absorption. However, in the modelling, the intensity profile does not converge to a symmetric Gaussian.

For asymmetric LG beams, the modelled E1E2 term predicts a higher magnitude of differential absorption for higher values of l, as shown in Fig. 5c. Figure 5d shows experimental HD(Type I) for asymmetric LG beams in limonene for two different OAM values of $l = \pm1, \pm3$. The magnitude of HD increases with the l value, in agreement with the modelled E1E2 term, where the limonene response tensor is approximated as a scalar quantity. The E1E2 term is non-zero even for asymmetric non-OAM annular beams. However, because there is no l dependence, HD(Type I) does not exist, as shown in Fig. 3c for the non-OAM, annular beam obtained through Fresnel diffraction.

The contribution of the E1E2 term to the HD signal also depends on the laser fluence. This vanishes at low laser intensity where the degree of molecular alignment is negligible. The extent of molecular alignment with an ~100-fs laser pulse depends on (1) the laser intensity

(~10^{13} W cm^{-2}), (2) the molecular polarizability and (3) the temperature and/or solute effects[41–45]. As the laser intensity increases, any degree of alignment in an asymmetric OAM beam is sufficient for the E1E2 term to be non-zero, and its contribution to the HD signal increases, as observed in the experiments (Figs. 3 and 4).

Our technique affords tunability of OAM-dependent differential absorption in both chiral and achiral systems by (1) changing the ellipticity of the laser polarization (Fig. 5a,b), (2) varying the l value (Fig. 5c,d), (3) superimposing Gaussian and OAM beams to manipulate the field distributions and (4) shifting the singularity. The technique is quite general and can be extended to chiral and achiral transparent solids, plasmonic metasurfaces and gas-phase molecules. The OAM of light offers an additional degree of freedom to control light–matter interactions. This opens new opportunities in next-generation chiroptical spectroscopy, asymmetric catalysis and light-driven molecular machines, where ultrashort light pulses can trigger interconversion of enantiomers for dynamic control of chirality.

A key advantage of using helical light is that the HD signal scales linearly with the l value, as predicted by our qualitative model. In Fig. 5, a linear increase in differential absorption was observed by changing from $l = 1$ to $l = 3$. Our model predicts a linear behaviour until $l \approx 15$, therefore, an increase in differential absorption by a factor of 15 relative to $l = 1$. However, at very high l values, saturation behaviour can be expected, as observed recently in chiral nanostructures[29], due to the increase in the size of the singularity and the finite beam waist determined by the focusing geometry. The enhanced differential absorption with asymmetric OAM beams at higher l values can be utilized in molecular optical switching for digital processing, in which light transmission can be controlled with helicity.

Another unique feature of the scaling behaviour of the HD signal is that it leads to higher chiral sensitivity. In contrast, the sensitivity of current chiroptical techniques that rely on light polarization is predetermined by the nature of the light–matter interaction, which is not scalable. In fenchone, the chiral signal increased from ~4% to ~6% when l was varied from 1 to 2 (Fig. 2). However, the chiral signal in limonene did not show such dependence. Although the l dependence of the chiral signal needs further investigation, the sensitivity of our technique is comparable to PECD and two-photon absorption CD[46].

The demonstrated differential absorption in liquids suggests a degree of control over the ionization of gas-phase molecules when irradiated with an intense helical light beam. In addition to polarization and magnetic field, the OAM of light represents another parameter to control the continuum trajectory of ionized electrons. The OAM of light, together with a transverse magnetic field and longitudinal electric field, generate chiral continuum electrons scalable with the l value. In contrast to single-photon ionization, chiral electron trajectories generated by tunnel ionization have attosecond resolution and can be used to probe chiral dynamics with attosecond precision.

Finally, the chiral motion of free electrons also results in a magnetic field along the laser propagation axis that can be controlled via the optical OAM. The magnetic field will be dominant around the singular part of the beam where the electric field is weak. For OAM single-cycle pulses, the magnetic field can be switched on a timescale of ~1 fs. This opens a potentially new way to in situ, ultrafast probing of magnetic materials.

Online content

Any methods, additional references, Nature Research reporting summaries, source data, extended data, supplementary information, acknowledgements, peer review information; details of author contributions and competing interests; and statements of data and code availability are available at https://doi.org/10.1038/s41566-022-01100-0.

References

1. Caldwell, D. J. & Eyring, H. *The Theory of Optical Activity* (Univ. of Utah, 1971).
2. Nakanishi, K., Berova, N. & Woody, R. *Circular Dichroism: Principles and Applications* (Wiley, 2000).
3. Castiglioni, E., Abbate, S. & Longhi, G. Experimental methods for measuring optical rotatory dispersion: survey and outlook. *Chirality* **23**, 711–716 (2011).
4. Kuball, H.-G. in *Encyclopedia of Analytical Science* 2nd edn (eds Worsfold, P. et al.) 60–79 (Elsevier, 2005).
5. Janssen, M. H. M. & Powis, I. Detecting chirality in molecules by imaging photoelectron circular dichroism. *Phys. Chem. Chem. Phys.* **16**, 856–871 (2014).
6. Tang, Y. & Cohen, A. E. Enhanced enantioselectivity in excitation of chiral molecules by superchiral light. *Science* **332**, 333–336 (2011).
7. Collins, J. T. et al. Chirality and chiroptical effects in metal nanostructures: fundamental and current trends. *Adv. Opt. Matter* **5**, 1700182 (2017).
8. Wang, X. & Tang, Z. Circular dichroism studies on plasmonic nanostructures. *Small* **13**, 1601115 (2017).
9. Cireasa, R. et al. Probing molecular chirality on a sub-femtosecond timescale. *Nat. Phys.* **11**, 654–658 (2015).
10. Bégin, J.-L., Alsaawy, M. & Bhardwaj, R. Chiral discrimination by recollision enhanced femtosecond laser mass spectrometry. *Sci. Rep.* **10**, 14074 (2020).
11. Lux, C. et al. Circular dichroism in the photoelectron angular distributions of camphor and fenchone from multiphoton ionization with femtosecond laser pulses. *Angew. Chem. Int. Ed.* **51**, 5001–5005 (2012).
12. Powis, I. Photoelectron circular dichroism of the randomly oriented chiral molecules glyceraldehyde and lactic acid. *J. Chem. Phys.* **112**, 301 (2000).
13. Allen, L. et al. Orbital angular momentum of light and the transformation of Laguerre-Gaussian laser modes. *Phys. Rev. A* **45**, 8185–8189 (1992).
14. Torres, J. P. & Torner, L. *Twisted Photons: Applications of Light with Orbital Angular Momentum* (Wiley, 2011).
15. Andrews, D. L. & Babiker, M. *The Angular Momentum of Light* (Cambridge Univ. Press, 2013).
16. Surzhykov, A., Seipt, D. & Fritzsche, S. Probing the energy flow in Bessel light beams using atomic photoionization. *Phys. Rev. A* **94**, 033420 (2016).
17. Wätzel, J. & Berakdar, J. Discerning on a sub-optical-wavelength the attosecond time delays in electron emission from magnetic sublevels by optical vortices. *Phys. Rev. A* **94**, 033414 (2016).
18. Picón, A. et al. Transferring orbital and spin angular momenta of light to atoms. *New J. Phys.* **12**, 083053 (2010).
19. Peshkov, A. A., Fritzsche, S. & Surzhykov, A. Ionization of H_2^+ molecular ions by twisted Bessel light. *Phys. Rev. A* **92**, 043415 (2015).
20. Franke-Arnold, S., Allen, L. & Padgett, M. Advances in optical angular momentum. *Laser Photon. Rev.* **2**, 299–313 (2008).
21. Andersen, M. F. et al. Quantized rotation of atoms from photons with orbital angular momentum. *Phys. Rev. Lett.* **97**, 170406 (2006).
22. He, H. et al. Direct observation of transfer of angular momentum to absorptive particles from a laser beam with a phase singularity. *Phys. Rev. Lett.* **75**, 826–829 (1995).
23. Schmiegelow, C. T. et al. Transfer of optical orbital angular momentum to a bound electron. *Nat. Commun.* **7**, 129998 (2016).
24. Picón, A. et al. Photoionization with orbital angular momentum beams. *Opt. Express* **18**, 3660–3671 (2010).

25. Loffler, W., Broer, D. J. & Woerdman, J. P. Circular dichroism of cholesteric polymers and the orbital angular momentum of light. *Phys. Rev. A* **83**, 065801 (2011).
26. Araoka, F. et al. Interactions of twisted light with chiral molecules: an experimetal investigation. *Phys. Rev. A* **71**, 055401 (2005).
27. Andrews, D. L., Romero, L. D. & Babiker, M. On optical vortex interactions with chiral matter. *Opt. Commun.* **237**, 133–139 (2004).
28. Brullot, W. et al. Resolving enantiomers using the optical angular momentum of twisted light. *Sci. Adv.* **2**, 150134 (2016).
29. Ni, J. et al. Giant helical dichroism of single chiral nanostructures with photonic orbital angular momentum. *ACS Nano* **15**, 2893–2900 (2021).
30. Zambrana-Puyalto, X., Vidal, X. & Molina-Terriza, G. Angular momentum-induced circular dichroism in non-chiral nanostructures. *Nat. Commun.* **5**, 4922 (2014).
31. Forbes, K. A. & Andrews, D. L. Spin–orbit interactions and chiroptical effects engaging orbital angular momentum of twisted light in chiral and achiral media. *Phys. Rev. A* **99**, 023837 (2019).
32. Forbes, K. A. & Andrews, D. L. Optical orbital angular momentum: twisted light and chirality. *Opt. Lett.* **43**, 435–438 (2018).
33. Marrucci, L., Manzo, C. & Paparo, D. Optical spin-to-orbital angular momentum conversion in inhomogeneous anisotropic media. *Phys. Rev. Lett.* **96**, 163905 (2006).
34. Hugo, L. et al. Arbitrary optical wavefront shaping via spin-to-orbit coupling. *J. Opt.* **18**, 124002 (2016).
35. Temnov, V. V. et al. Multiphoton ionization in dielectrics: comparison of circular and linear polarization. *Phys. Rev. Lett.* **97**, 237403 (2006).
36. Vivas, M. G. et al. Polarization effect on the two-photon absorption of a chiral compound. *Opt. Express* **20**, 18600–18608 (2012).
37. Gong, S.-H. & Penzkofer, A. Two-photon absorption and two-photon-induced absorption of some organic liquids at 347.15 nm. *Opt. Quantum Electron.* **31**, 269–290 (1999).
38. Oosterbeek, R., Ashforth, S., Bodley, O. & Simpson, M. Measuring the ablation threshold fluence in femtosecond laser micromachining with vortex and Bessel pulses. *Opt. Express* **26**, 34558–34568 (2018).
39. Rahimian, M. G. et al. Spatially controlled nano-structuring of silicon with femtosecond vortex pulses. *Sci. Rep.* **10**, 12643 (2020).
40. Tang, Y. & Cohen, A. E. Optical chirality and its interaction with matter. *Phys. Rev. Lett.* **104**, 163901 (2010).
41. Ohkubo, J. et al. Molecular alignment in a liquid induced by a nonresonant laser field: molecular dynamics simulation. *J. Chem. Phys.* **120**, 9123–9132 (2004).
42. Dooley, P. W. et al. Direct imaging of rotation wave-packet dynamics of diatomic molecules. *Phys. Rev. A* **68**, 023406 (2003).
43. Fleischer, S. et al. Molecular alignment induced by ultrashort laser pulses and its impact on molecular motion. *Is. J. Chem.* **52**, 414–437 (2012).
44. Leibscher, M., Averbukh, I. S. & Rabitz, H. Molecular alignment by trains of short laser pulses. *Phys. Rev. Lett.* **90**, 213001 (2003).
45. Leibscher, M., Averbukh, I. S. & Rabitz, H. Enhanced molecular alignment by short laser pulses. *Phys. Rev. A* **69**, 013402 (2004).
46. Toro, C. et al. Two-photon absorption circular dichroism: a new twist in nonlinear spectroscopy. *Chem. Eur. J.* **16**, 3504–3509 (2010).

Methods

Differential absorption measurements

A Ti:sapphire laser amplifier system, operating in an external trigger mode and producing 45-fs, 800-nm pulses with a maximum pulse energy of 2.5 mJ, was used in the transmission measurements. An aspheric objective lens (numerical aperture (NA) of 0.3) was used to focus the femtosecond pulses into a cuvette (10-mm thick) containing liquid samples of chiral or achiral molecules. A second aspheric objective with the same or higher NA (0.5) collected and collimated the transmitted light onto a photodiode (PD2), positioned immediately after the objective. For every laser shot, the transmitted light signal on PD2 was normalized with the incoming light signal on PD1, reflected off a glass plate positioned in the beam path at an angle of ~20° to avoid Brewster's angle. The signals generated by PD1 and PD2 were stretched by an electronic pulse stretcher, discretized, and recorded by a data acquisition card. A combination of an HWP and a polarizer was used to vary the pulse energy (power control in Fig. 1a). The incident pulse energies were measured before the objective. During the measurement, for every laser shot, the pulse energy was increased by ~3 nJ and the sample was translated by 5 µm to avoid microbubbles. Multiple transmission curves similar to those in Fig. 1a were obtained for each sample, to be averaged and smoothed. The difference in the normalized transmission of left- and right-helical light ($l = \pm1$) is proportional to HD(Type I) (that is, differential absorption). To ensure a shortest pulse in the interaction region, a negative chirp was introduced and optimized by measuring the second harmonic generation in a barium borate crystal placed at the location of the cuvette. A single-shot autocorrelator then continuously monitored the pulse duration. The pulse duration at the interaction region is ~100 fs. Transmission measurements were always performed in an empty cuvette before each experiment to determine and minimize background errors resulting from any discrepancies between the PDs (Supplementary Section 5). In addition, the measured single-shot beam profile, pulse spectrum and OAM value remained unchanged after transmission through the samples (Supplementary Sections 2–4).

Sign dependence of HD in chiral molecules

We used conventional labelling of a chiral molecule by the sign of the direction of rotation of polarized light, dextrorotatory (D; +) and levorotatory (L; −). Chiral molecules are also labelled as (*S*)- and (*R*)- based on their absolute chemical configuration, representing the left- and right-handed isomers. This labelling refers to the spatial orientation of groups at the chiral centre and not to the optical rotation of polarized light. As a result, it is possible for an isomer to be *S*(+), *S*(−), *R*(+) and *R*(−). The sign dependence of the HD signals arises from optical rotation by an enantiomer. HD(Type II) signals in fenchone (Fig. 2) and limonene (Fig. 4b,c) are of opposite signs because they rotate the plane of linear polarization in opposite directions. *R*(+)-limonene and *S*(+)-fenchone rotate the plane of polarization clockwise, and *S*(−)-limonene and *R*(−)-fenchone rotate counterclockwise.

Generation of OAM beams

Light beams carrying orbital and/or spin angular momentum were generated and controlled by an OAM/SAM unit (Fig. 1a) consisting of a combination of a HWP and quarter-wave plates (QWPs), a linear polarizer (LP) and a birefringent liquid-crystal-based phase plate called a *q*-plate[33]. When an incident Gaussian beam propagates through the *q*-plate with a topological charge *q*, it acquires an OAM defined by $l = \pm 2q$, with a phase singularity and hence a null intensity region at the centre of the beam—an optical vortex. The wavefront structure of such beams undergoes *l* intertwined rotations in one wavelength, and the direction of rotation is determined by the sign of the input polarization. The conversion efficiencies of the *q*-plates were 91 ± 2% for $l = 1$, 3 and ~80 ± 2% for $l = 2$. Circularly (linearly) polarized Gaussian beams were produced by a QWP. The ellipticity of CPL at the sample was 97 ± 2%. Circularly (linearly) polarized OAM light $s = \pm1$, $l = \pm1$ ($s = 0$, $l = \pm1$) was generated using a combination of QWP, *q*-plate, QWP, LP and QWP. The ellipticity of circularly (linearly) polarized OAM light reaching the sample was 95 ± 2% (5 ± 2%).

Generation of annular beams and displacement of singularity

An annular light beam with no OAM ($l = 0$) was generated by a circular aperture and exploiting the Fresnel diffraction of the incident Gaussian beam to produce an Airy pattern beam with a null region in the centre of the beam (Supplementary Section 6). A Galilean beam expander and QWP were used to magnify the beam by a factor of four and produce circular polarization. The singularity/null intensity region in the OAM (non-OAM beam) beam was displaced by translating the *q*-plate (circular aperture), mounted on a *x*,*y*-stage, with a step size of 250 ± 40 µm. When focused by the objective, this translated to a displacement step size of 300 ± 20 nm with respect to the centre of the beam. The calibration was achieved by measuring the total translation required to displace the singularity to the periphery of the defocused beam and comparing it to the measured spot size of 2 ± 0.2 µm obtained by knife-edge measurements.

Multipole expansion of the light–matter interaction

We consider a monochromatic electromagnetic field incident on a molecule. The resultant time-harmonic charge and current distributions are described by a multipole expansion. The single-photon rate of excitation of the molecule was expressed in terms of time-averaged induced multipoles.

The induced electric-dipole $\tilde{\mu}$, electric quadrupole $\tilde{\theta}$ and magnetic dipole $\tilde{m}$, are expressed in multipole expansion terms as[47,48]

$$\begin{aligned}\tilde{\mu}_\alpha &= \sum_\beta \tilde{\alpha}_{\alpha\beta}\tilde{E}_\beta + \sum_\beta \tilde{G}_{\alpha\beta}\tilde{B}_\beta + \frac{1}{3}\sum_{\beta\gamma}\tilde{A}_{\alpha\beta\gamma}\tilde{E}_{\beta\gamma};\\ \tilde{\theta}_{\alpha\beta} &= \sum_\gamma \tilde{a}_{\gamma\alpha\beta}\tilde{E}_\gamma;\\ \tilde{m}_\alpha &= \sum_\beta \tilde{\chi}_{\alpha\beta}\tilde{B}_\beta + \sum_\beta \tilde{g}_{\alpha\beta}\tilde{E}_\beta\end{aligned} \tag{1}$$

where the Greek alphabet represents the Cartesian indices. $\tilde{\alpha}_{\alpha\beta}$ is the electric dipole polarizability, $\tilde{\chi}_{\alpha\beta}$ is the magnetic susceptibility, $\tilde{A}_{\alpha\beta\gamma}$ is the electric dipole–quadrupole polarizability, where $\tilde{A}_{\alpha\beta\gamma} = \tilde{a}_{\gamma\alpha\beta}$, and $\tilde{G}_{\alpha\beta}$ is the electric–magnetic dipole polarizability, where $\tilde{G}_{\alpha\beta} = -\tilde{g}_{\alpha\beta}$. The field gradient $\nabla_\beta\tilde{E}_\gamma$ is defined by $\tilde{E}_{\beta\gamma}$ (refs. [47–49]). The complex electric and magnetic fields are defined as $\tilde{E}(t) = \tilde{E}_0 \mathrm{e}^{-i\omega t}$ and $\tilde{B}(t) = \tilde{B}_0 \mathrm{e}^{-i\omega t}$, where $\tilde{E}_0$ and $\tilde{B}_0$ are arbitrary complex vectors and ω is the frequency of the incident light, The terms with tilde are complex quantities $\tilde{\alpha}_{\alpha\beta} = \alpha'_{\alpha\beta} + i\alpha''_{\alpha\beta} = \tilde{\alpha}^*_{\beta\alpha}$, $\tilde{A}_{\alpha\beta\gamma} = A'_{\alpha\beta\gamma} + iA''_{\alpha\beta\gamma} = \tilde{A}_{\gamma\alpha\beta}$ and $\tilde{G}_{\alpha\beta} = G'_{\alpha\beta} + iG''_{\alpha\beta}$.

The dynamic multipole interaction Hamiltonian[47,48] is given by

$$H_{\text{int}} = -\mu_\alpha E_\alpha - \frac{1}{3}\theta_{\alpha\beta}E_{\alpha\beta} - m_\alpha B_\alpha - \ldots \tag{2}$$

The rate of change of the Hamiltonian gives the rate of energy absorption by the induced multipoles[47,48], that is, energy absorbed from the EM fields, expressed in terms of time average:

$$\Gamma = \left\langle \dot{\mu}_\alpha E_\alpha + \dot{m}_\alpha B_\alpha + \frac{1}{3}\dot{\theta}_{\alpha\beta}E_{\alpha\beta} \right\rangle_t \tag{3}$$

where $\dot{\mu}$, $\dot{m}$, $\dot{\theta}$, $E_\alpha = \frac{1}{2}\left(\tilde{E}_\alpha \mathrm{e}^{-i\omega t} + \tilde{E}^*_\alpha \mathrm{e}^{i\omega t}\right)$ and $B_\alpha = \frac{1}{2}\left(\tilde{B}_\alpha \mathrm{e}^{-i\omega t} + \tilde{B}^*_\alpha \mathrm{e}^{i\omega t}\right)$ are real quantities. By considering the component of dipole moment along the electric field direction, we replace β with α (ref. [47]) to get

$$\Gamma_{E1-E1} = \frac{\omega}{4}\alpha''_{\alpha\beta}\left(\tilde{E}^*_\beta\tilde{E}_\alpha + \tilde{E}_\beta\tilde{E}^*_\alpha\right) \to \Gamma_{E1-E1} = \frac{\omega}{2}\alpha''_{\alpha\alpha}\left[\tilde{E}_\alpha\tilde{E}^*_\alpha\right] \tag{4}$$

Magnetic dipole–dipole excitation (M1–M1) is given by

$$\Gamma_{M1-M1} = \frac{\omega}{4}\chi''_{\alpha\beta}\left(\tilde{B}_\beta\tilde{B}^*_\alpha + \tilde{B}^*_\beta\tilde{B}_\alpha\right) \to \Gamma_{M1-M1} = \frac{\omega}{2}\chi''_{\alpha\alpha}\left[\tilde{B}_\alpha\tilde{B}^*_\alpha\right] \tag{5}$$

Electric–magnetic dipole excitation (E1–M1) results in the interaction of the electric field with the electric dipole moment induced by the magnetic field and vice versa. The expression is given by

$$\Gamma_{E1-M1} = \frac{i\omega}{4}\left\langle G'_{\alpha\beta}\right\rangle_{\rho}\left(\tilde{B}_{\beta}\tilde{E}^{*}_{\alpha} - \tilde{E}_{\alpha}\tilde{B}^{*}_{\beta}\right) \rightarrow \Gamma_{E1-M1} = \frac{\omega}{2}\rho G'_{\alpha\alpha}\mathrm{Im}\left[\tilde{E}^{*}_{\alpha}\tilde{B}_{\alpha}\right] \quad (6)$$

To describe the bulk response, the tensor quantity $G'_{\alpha\beta}$ must be averaged over all degrees of molecular orientation. For partial orientation of molecules, due to the laser induced dipole force (see below), we consider anisotropic averaging $\langle G'_{\alpha\beta}\rangle_{\rho} \rightarrow \rho G'_{\alpha\alpha}$ where ρ is an orientation-dependent weighting factor influenced by the degree of molecular alignment[50,51].

Electric dipole–quadrupole excitation (E1–E2) arises from two contributions: (1) the interaction of the electric field with the electric dipole moment induced by the field gradient and (2) the interaction of the field gradient with the quadrupole moment induced by the electric field. The expression is given by

$$\Gamma_{E1-E2} = \frac{\omega}{6}\left\langle A''_{\alpha\beta\gamma}\right\rangle_{\rho}\left[\nabla_{\beta}\tilde{E}_{\gamma}\tilde{E}^{*}_{\alpha} + \tilde{E}_{\alpha}\nabla_{\beta}\tilde{E}^{*}_{\gamma}\right] \rightarrow \Gamma_{E1-E2} = \frac{\omega}{3}\rho A''_{\alpha\alpha\gamma}\mathrm{Re}\left[\tilde{E}^{*}_{\alpha}\nabla_{\alpha}\tilde{E}_{\gamma}\right] \quad (7)$$

We consider anisotropic averaging $\langle A''_{\alpha\beta\gamma}\rangle_{\rho} \rightarrow \rho A''_{\alpha\alpha\gamma}$, where ρ is an orientation-dependent weighting factor influenced by the degree of molecular alignment. For complete alignment ($\rho = 1$), considering the principal molecular axis is oriented along the propagation axis (y), the tensor quantity can be expressed as $\langle A''_{\alpha\beta\gamma}\rangle_{\rho} \rightarrow (A''_{\alpha\alpha\gamma} + A''_{\beta\beta\gamma})$ (ref. [47]). Because the dominant contribution to the dipole moment is along the electric field direction (α), we limit to $A''_{\alpha\alpha\gamma}$. This tensor quantity vanishes for randomly oriented molecules, $\rho = 0$ (isotropic averaging). The higher multipole transitions such as E1M2, E2M1 and E2E2 are ignored because the molecular response tensor for these transitions is very small. The total rate of excitation is a sum of all four absorption rates for an asymmetric LG beam:

$$\Gamma^{\pm}_{\delta} = \frac{\omega}{2}\left\{\underbrace{\alpha''|\tilde{E}^{\pm}_{\delta}|^{2}}_{\text{E1E1}} + \underbrace{\chi''|\tilde{B}^{\pm}_{\delta}|^{2}}_{\text{M1M1}} + \underbrace{\rho G'\mathrm{Im}\left[\left(\tilde{E}^{\pm}_{\delta}\right)^{*}\cdot\tilde{B}^{\pm}_{\delta}\right]}_{\text{E1M1}} + \underbrace{\frac{2}{3}\rho A''\mathrm{Re}\left[\left(\tilde{E}^{\pm}_{\delta}\right)^{*}\cdot\nabla\tilde{E}^{\pm}_{\delta}\right]}_{\text{E1E2}}\right\} \quad (8)$$

The δ is the asymmetrical parameter, $\delta = 0$ for a symmetric LG beam and $\delta \neq 0$ for an asymmetric LG beam. The sign in $\Gamma^{\pm}$ represents the sign of the OAM. The above equation is generalized to multiphoton absorption (Supplementary Section 10). E1 and M1 are the electric and magnetic dipoles, respectively, and E2 is the electric quadrupole. The coupling terms E1M1 and E1E2 are pseudoscalars and change sign under improper rotation. For a specific chiral system, the sign change of these quantities upon reflection would lead to non-zero differential absorption, defined as

$$\Delta W = \int_{-\omega_0}^{\omega_0} \mathrm{HD}\,(\mathrm{Type\ I,\ II})\,\mathrm{d}x\mathrm{d}y \quad (9)$$

and integrated over the beam cross-section. HD(Type I) is defined as the difference between the absorption of left- and right-handed helical light for the same molecule (Figs. 3 and 4a):

$$\mathrm{HD}_{\delta}\,(\mathrm{Type\ I}) = \Gamma^{+}_{\delta} - \Gamma^{-}_{\delta} = G'[C^{+} - C^{-}] + A''\left[\Upsilon^{+} - \Upsilon^{-}\right] \quad (10)$$

HD(Type II) is defined as the difference in absorption between the two enantiomers for a specific helicity and polarization (Figs. 2 and 4b,c):

$$\mathrm{HD}^{\pm}_{\delta}\,(\mathrm{Type\ II}) = \Gamma^{\pm}_{R} - \Gamma^{\pm}_{S} = C^{\pm}\left[G'_{R} - G'_{S}\right] + \Upsilon^{\pm}\left[A''_{R} - A''_{S}\right] \quad (11)$$

where R and S represent the two enantiomers. The parameter $C^{\pm} = 2\omega\mathrm{Im}\left[\left(\tilde{E}^{\pm}_{\delta}\right)^{*}\cdot\tilde{B}^{\pm}_{\delta}\right]$ in equations (3) and (4) is called optical chirality, a local measure of the degree of circular polarization, and we define $\Upsilon^{\pm} = \frac{2\omega}{3}\mathrm{Re}\left[\left(\tilde{E}^{\pm}_{\delta}\right)^{*}\cdot\nabla\tilde{E}^{\pm}_{\delta}\right]$ as optical helicity. Both are time-even psuedoscalars. Optical chirality is often used to describe the phenomenon of CD in molecules[6,47,52] and metasurfaces[29,53,54]. Optical helicity, Υ, is a quantity describing the handedness of helical light. It contains the gradient of the electric field, giving rise to a linear l dependence. The above equations, assuming full molecular alignment, show that the chiral light–matter interaction depends on both molecular transitions (contained in G' and A'') and optical chirality C, and optical helicity, Υ. The contribution of the E1E2 term was modelled in Fig. 5 by considering the optical helicity term Υ (dominant component defined by approximating A'' as a scalar).

The following qualitative behaviour emerges by evaluating equations (9) and (10) for HD(Type I) and equations (9) and (11) for HD (Type II):

- HD(Type I) is a beam-dominated property and does not exist for symmetric LG beams. For asymmetric LG beams, the E1M1 term vanishes (because we take the difference between the left- and right-helical beams for the same polarization) and the E1E2 coupling term is non-zero. For a circularly polarized Gaussian beam, the E1M1 term is non-zero and gives rise to conventional CD.
- HD(Type II) is a material-dominated property where both E1M1 and E1E2 coupling terms contribute to differential absorption for asymmetric LG beams. For symmetric LG beams, the E1E2 term averages out to zero, but the E1M1 term is non-zero and can contribute to HD. E1M1 and E1E2 are of similar magnitudes[47,55]. For asymmetric LG beams with the same polarization but different helicities, the E1E2 term is responsible for the change in the sign of the HD curves. Because the E1M1 term changes sign only with polarization, its finite magnitude leads to an offset in the HD curves (Fig. 4b,c).

The E1E2 coupling term is often ignored because it vanishes for a random orientation of molecules due to rotational isotropic averaging. However, if the molecules are preferentially aligned, the quadrupolar interactions containing A'' cannot be neglected[56]. This is the case for asymmetric LG beams, in which the spatial inhomogeneity in the intensity profile at the interaction region gives rise to an optical dipole force defined by $\mathbf{F} = \alpha\frac{1}{2}\nabla E^{2} + \alpha\frac{\mathrm{d}}{\mathrm{d}t}\left(\mathbf{E}\times\mathbf{B}\right)$, where the first term defines the gradient force and the second term the scattering force, which can be neglected when the Poynting vector remains constant over an optical cycle. A net non-zero force is exerted on the induced dipoles directed towards the extrema of the radiation field (Fig. 3a). The resultant torque preferentially aligns the molecular axis parallel to the polarization plane[57], leading to a non-zero averaged E1E2 contribution to HD. The E1E2 contribution to HD vanishes for symmetric LG beams because the gradient force is zero. The E1M1 term is non-zero even for randomly oriented molecules.

Asymmetric LG beams

We introduced an asymmetry parameter, δ, into the symmetric LG beam to obtain an asymmetric LG beam. We also consider the longitudinal component of the field (E_z) as a correction to the paraxial regime[58,59] to take into account its finite l (OAM) contribution. The importance of the longitudinal component in the light–matter interaction has been recently demonstrated in differentiating nanoparticle aggregates using helical light[28]. When light is focused tightly using a higher-NA objective, the contribution of the longitudinal component becomes significant.

For arbitrary polarization in the paraxial regime, the field components can be written as

$$u^{\pm}_{o}\,(x,y,z) = E_{0}\exp\left[ikz\right]\left(\frac{\sqrt{2}((x\mp i\eta\delta)\pm i(y\mp i\zeta\delta))}{\omega_{0}}\right)^{|l|}\exp\left(-\frac{(x^{2}+y^{2})}{\omega_{0}^{2}}\right)L^{|(l+j)|}_{p-j}\left(\frac{2\rho^{2}}{\omega_{0}^{2}}\right) \quad (12)$$

$$E_x^{\pm}(x,y,z) = \alpha_z u_0^{\pm}(x,y,z) \tag{13}$$

$$E_y^{\pm}(x,y,z) = \beta_z u_0^{\pm}(x,y,z) \tag{14}$$

$$E_z^{\pm}(x,y,z) = if\left[(\alpha_z \pm i\beta_z)\,\frac{|l|\omega_0((x\mp i\eta\delta)\mp i(y\mp i\zeta\delta)}{(x\mp i\eta\delta)^2+(y\mp i\zeta\delta)^2}u_0^{\pm}(x,y,z) - \frac{2}{\omega_0}\left(\alpha_z(x)+\beta_z(y)\right)u_0^{\pm}(x,y,z)\right] \tag{15}$$

$$B_x(x,y,z) = -\beta_z\frac{k}{\omega}u_0^{\pm}(\mathbf{r}), \tag{16}$$

$$B_y(x,y,z) = \alpha_z\frac{k}{\omega}u_0^{\pm}(\mathbf{r}) \tag{17}$$

$$B_z(x,y,z) = if\frac{k}{\omega}\left[(\alpha_z \pm i\beta_z)\,\frac{|l|\omega_0((y\mp i\zeta\delta)\pm i(x\mp i\eta\delta))}{(x\mp i\eta\delta)^2+(y\mp i\zeta\delta)^2}u_0^{\pm}(\mathbf{r}) - \frac{2}{\omega_0}\left(\alpha_z(y)-\beta_z(x)\right)u_0^{\pm}(\mathbf{r})\right] \tag{18}$$

where $f=\lambda/2\pi\omega_0$, $\rho=\sqrt{x^2+y^2}$ and ω_0 is the beam waist. Also, E_0 is the normalization factor obtained by integrating the intensity over all space ($-\infty$ to $+\infty$), and for ($l=1$) it is given as:

$$E_0 = \sqrt{\frac{2k^2\omega_0^2}{\pi\left(\alpha^2+\beta^2\right)\left(2\omega_0^2+k^2\omega_0^4+2\left(\zeta^2+\eta^2\right)\delta^2\left(1+k^2\omega_0^2\right)\right)}} \tag{19}$$

In our case, there is no radial node, hence $p=0$. The ± represents the rotational direction of l. The polarization factors α and β are normalized such that $|\alpha_z|^2+|\beta_z|^2=1$. Displacement of the singularity in the x–y plane can be achieved by varying η and ζ. For generalization, we substituted $\eta=1/4$ and $\zeta=1$, considering the movement of the singularity is slightly displaced from the axial direction experimentally.

Data availability

The minimum dataset necessary to interpret the results can be obtained from the corresponding authors upon reasonable request.

Code availability

The simulation data were obtained by evaluating the equations using standard technical software. The code is available upon reasonable request to the corresponding authors.

References

47. Yang, N. & Cohen, A. E. Local geometry of electromagnetic fields and its role in molecular multipole transitions. *J. Phys. Chem. B* **115**, 5304–5311 (2011).
48. Barron, L. D. *Molecular Light Scattering and Optical Activity* (Cambridge Univ. Press, 2004).
49. Buckingham, A. D. & Dunn, M. B. Optical activity of oriented molecules. *J. Chem. Soc. A* **1971**, 1988–1991 (1971).
50. Andrews, S. S. Using rotational averaging to calculate the bulk response of isotropic and anisotropic samples from molecular parameters. *J. Chem. Educ.* **81**, 877 (2004).
51. Andrews, D. L. & Allcock, P. *Optical Harmonics in Molecular Systems: Quantum Electrodynamical Theory* (Wiley, 2005).
52. Lipkin, D. Existence of a new conservation law in electromagnetic theory. *J. Math. Phys. (N.Y.)* **5**, 696–700 (1964).
53. Wang, Z. et al. A novel chiral metasurface with controllable circular dichroism induced by coupling localized and propagating modes. *Adv. Opt. Mater.* **4**, 883–888 (2016).
54. Guo, Y. et al. Orbital angular momentum dichroism caused by the interaction of electric and magnetic dipole moments and the geometrical asymmetry of chiral metal nanoparticles. *Phys. Rev. A* **102**, 033525 (2020).
55. Loudon, R. *The Quantum Theory of Light* (Oxford Univ. Press, 2003).
56. Forbes, K. A. & Andrews, D. L. Orbital angular momentum of twisted light: chirality and optical activity. *J. Phys. Photon.* **3**, 022007 (2021).
57. Bradshaw, D. S. & Andrews, D. L. Manipulating particles with light: radiation and gradient forces. *Eur. J. Phys.* **38**, 034008 (2017).
58. Cerjan, A. et al. Orbital angular momentum of Laguerre-Gaussian beams beyond the paraxial approximation. *J. Opt. Soc. Am. A* **28**, 2253–2260 (2011).
59. Forbes, K. A. et al. Relevance of longitudinal fields of paraxial optical vortices. *J. Opt.* **23**, 075401 (2021).

Acknowledgements

We acknowledge financial support from the Natural Science and Engineering Council of Canada, Canada Research Chairs and Canadian Foundation for Innovation.

Author contributions

J-L.B., A.J. and R.B. conceived the experiments. J-L.B., A.J. and R.B. designed and planned the experiments. J-L.B. and A.J. conducted the experiments and analysed the results. J-L.B., A.J., A.P., T.B. and R.B. worked on the theory and conducted numerical simulations. F.H. fabricated the *q*-plates, P.C., E.K. and R.B. supervised the project. J-L.B., A.J., T.B. and R.B. prepared the first draft, and all authors reviewed the manuscript.

Competing interests

The authors declare no competing interests.

Additional information

Supplementary information The online version contains supplementary material available at https://doi.org/10.1038/s41566-022-01100-0.

Correspondence and requests for materials should be addressed to Ravi Bhardwaj.

Peer review information *Nature Photonics* thanks David Andrews and the other, anonymous, reviewer(s) for their contribution to the peer review of this work.

nature photonics

Article https://doi.org/10.1038/s41566-022-01100-0

Nonlinear helical dichroism in chiral and achiral molecules

Supplementary materials: Nonlinear helical dichroism in chiral and achiral molecules

Jean-Luc Bégin[1,+], Ashish Jain[1,+], Andrew Parks[1], Felix Hufnagel[1], Paul Corkum[1], Ebrahim Karimi[1], Thomas Brabec[1], and Ravi Bhardwaj[1,*]

[1]Department of Physics, University of Ottawa, Ottawa, ON, K1N 6N5, Canada

Contents

1 HD(Type I, II) in limonene and fenchone

Figures S1 shows HD(Type II) in limonene as a function of fluence for $l = \pm 1$ (Fig.S1a) and ± 3 (Fig.S1b) , respectively for linearly poarized helical light. The chiral signal increases with laser fluence and reaches a maximum of $\sim$ 6-7%. The chiral signals in limonene and fenchone are of opposite signs (black curve and red curves are flipped) because they rotate the plane of linear polarization in opposite directions *(see Methods)*. The chiral signal did not increase with *l*-value in limonene.

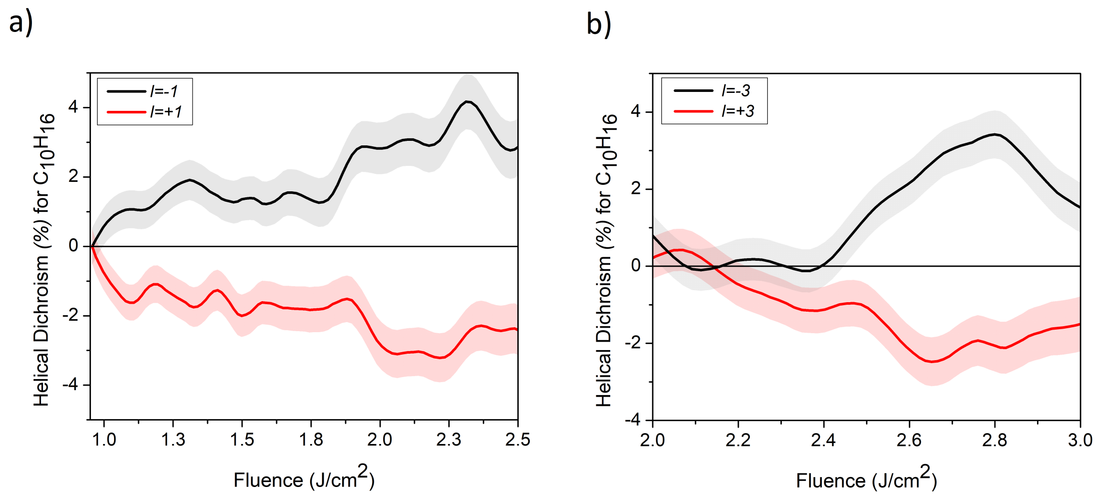

FIG. S 1. HD(Type II) in limonene with linearly polarized light ($s = 0$) as a function of peak laser fluence. **(a)** $l = \pm 1$. **(b)** $l = \pm 3$. The colour bands represent the propagation error of the chiral signal for three independent measurements (sample size).

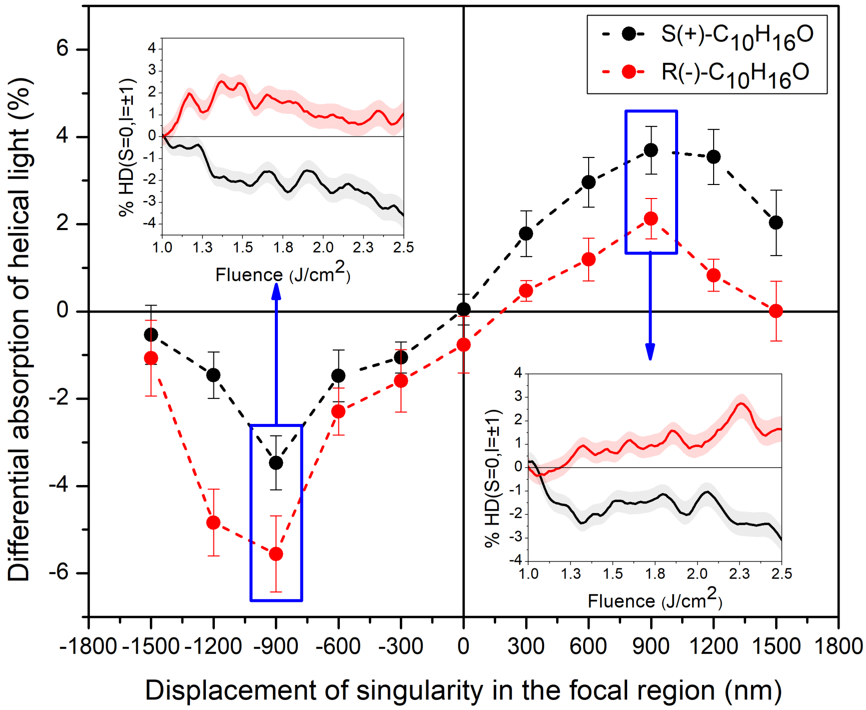

FIG. S 2. Helical dichroism with asymmetric OAM beams in fenchone. Differential absorption of linearly polarized helical light $l = \pm 1$ as a function of the position (or displacement) of the singularity in the OAM beam. The insets show helical dichroism as function of peak laser fluence when the singularity is at the positions marked by solid rectangles. The error bars and colour bands represent the propagation error of the chiral signal for three independent measurements (sample size).

Figure. S2 shows that HD signal in fenchone. The spatial variation of differential absorption, HD(Type I), of linearly polarized helical light in fenchone enantiomers exhibits the same behaviour as achiral molecules (Fig. 3b) as well as limonene enantiomers (Fig. 4). The insets of Fig. S2 represent HD(Type II) as a function of peak laser fluence when the singularity was at the positions marked by solid rectangles.

2 Intensity profile of OAM beams before and after the sample

To ensure that the beam profile is not influenced by nonlinear propagation effects at the interaction region we took single shot images of the beam profile with and without the sample as shown in fig. S3. A pulse energy of 350 nJ for $l = \pm 1$ was chosen because the magnitude helical dichroism (see main article) is largest around that energy region. There was no change in the beam profile after propagating through the sample. This suggests the nonlinear absorption is not influenced by any propagation effects.

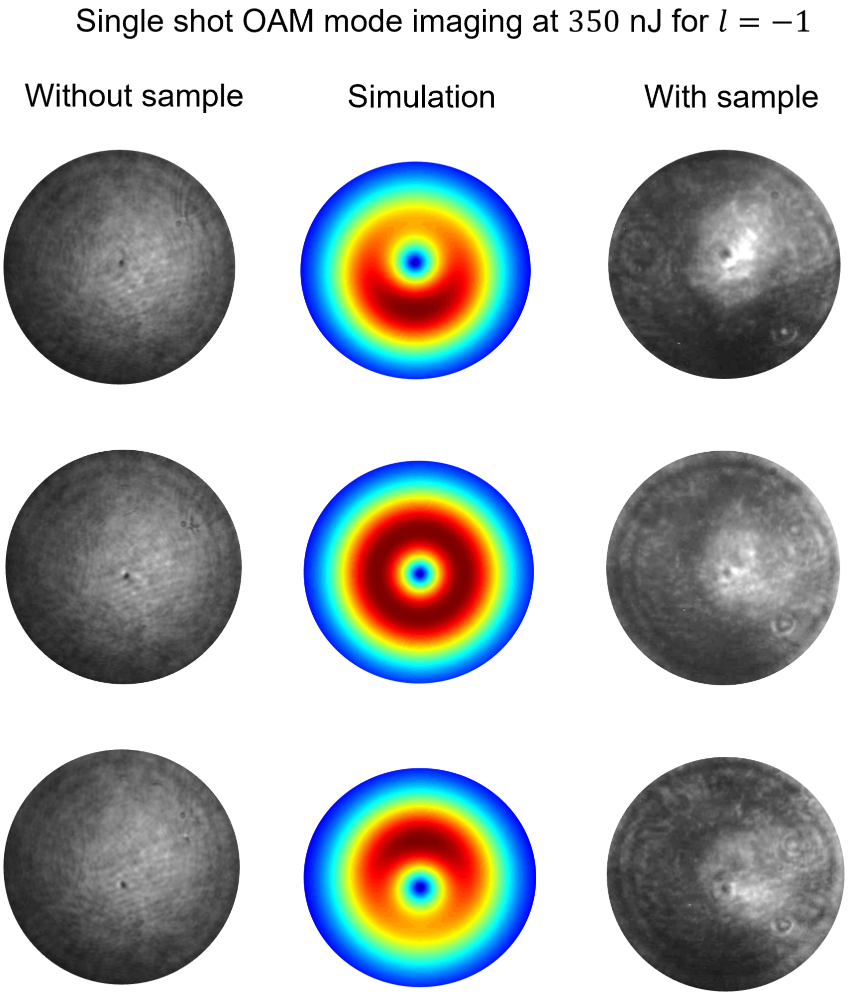

FIG. S 3. Single shot beam profiles of $l = -1$ for a symmetrical LG (center row) and asymmetrical LG (top and bottom rows) beams. The left (right) column shows the beam profiles without(with) the sample. The central column shows the simulated intensity profiles.

3 Measuring the transmitted l value of an OAM beam

To ensure the l value remained unchanged after propagating through the sample, we performed a set of interference experiments involving Gaussian and OAM beams to observe the signature fork patterns. Fig. S4 depicts simulated and measured single-shot fork patterns for $l = -1$ in air (a,b) , $l = +3$ in sample (c,d). Fig. S4 e,f shows the measured patterns for $l = \pm 1$ in the sample. Though the contrast of the interference patterns is poor in the sample due to single-shot measurement, they are in agreement with the expected signature patterns. Results indicate no change in the angular momentum value of the light when propagating through the sample.

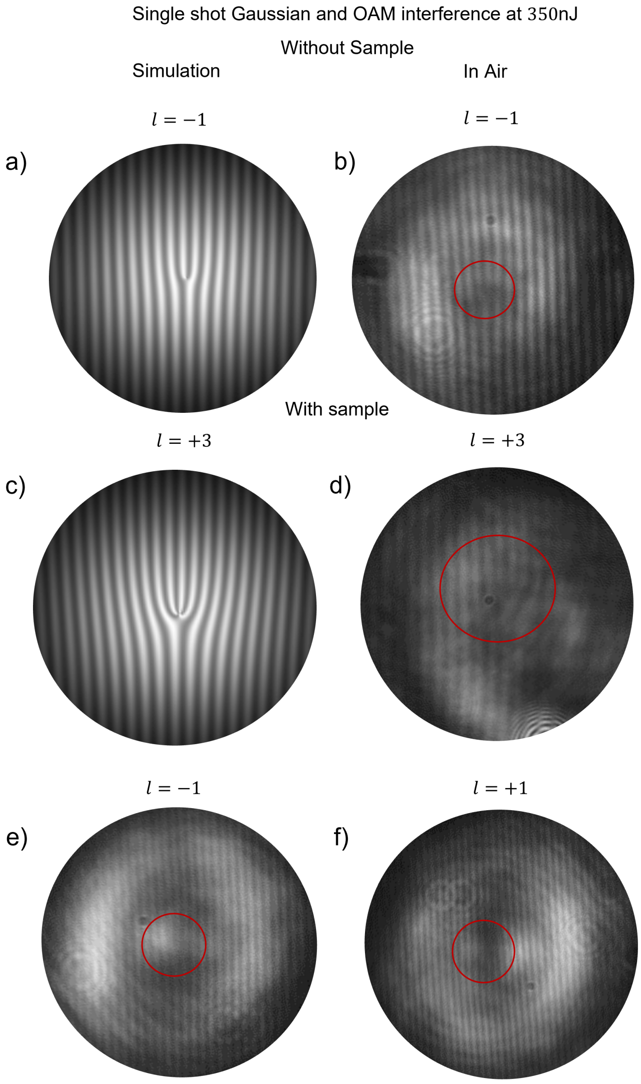

FIG. S 4. Simulated and measured (a,b) two pronged fork pattern for $l=-1$ in air, (c,d) four pronged fork pattern for $l=+3$ in sample. (e,f) measured two pronged fork pattern for $l=\pm 1$ in sample.

4 Single shot transmitted spectrum measurement

Nonlinear affects such as self-phase modulation can influence the propagation of incident light through the sample over the range of pulse energies used in the experiment. Fig. S5 shows set of single-shot spectra (a) of Ti: Sapphire laser used as a reference (black curve), (b) after the power and OAM/SAM control optics (magenta curve) with no sample, and (c) after propagating through (-)-fenchone and (+)-fenchone for linearly polarized helical light, $+l$ (cyan and green curves, respectively) and $-l$ (red and blue curves, respectively). There is no considerable change in the spectral shape after propagating through the sample suggesting nonlinear affects are negligible. Compared to the reference spectrum, the spectrum of light incident on the sample is altered due to numerous optics in the beam path.

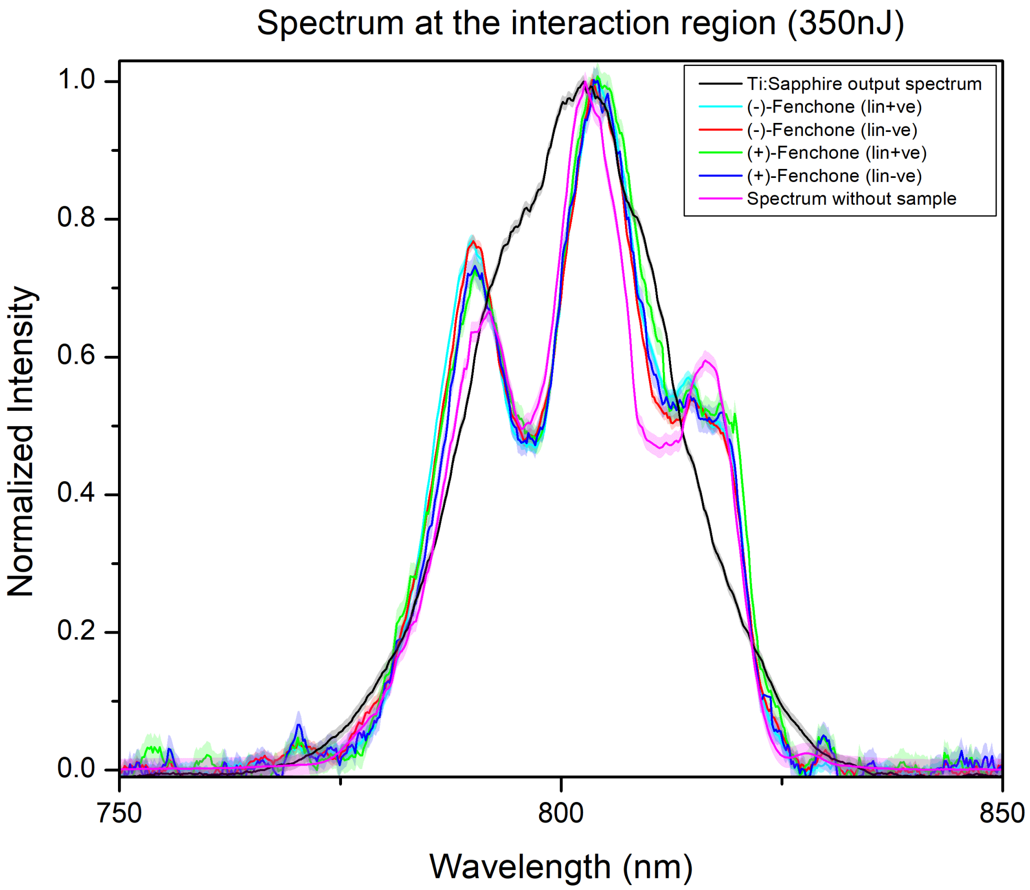

FIG. S 5. Single-shot measurement of transmitted spectra. The reference spectrum (black curve) corresponds to Ti:sapphire laser, spectrum after the power and OAM/SAM contol but with no sample (magenta curve). The cyan (green) and red (blue) curves are the spectrum of linearly polarized $l = +1$ (lin +ve) and $l = -1$ (lin -ve) after propagating through (-)-fenchone ((+)-fenchone).

5 Transmission measurements in air in the absence of sample

In the absence of a sample, transmission measurements conducted in air ensure that the photodiodes detect identical signals when changing the incoming linearly polarized light from $+l$ to $-l$. Fig. S6 a) and b) show transmission of a symmetrical and an asymmetrical LG beams through air. The red (black) curves represent the difference between the PD1 (PD2) signal for linearly polarized $+l$ and $-l$. Both signals are centered about zero with a fluctuation of $\pm 0.05V$. Moreover, the red and black curves nearly overlap over the entire energy range, demonstrating no signal change between PD1 (incident light) and PD2 (transmitted light) as the OAM value changed. This indicates there is no arbitrary signal/noise introduced by the experimental setup to the observed differential absorption in chiral and achiral molecules. Transmission measurements in air were performed before every experimental run and for every position of the displaced singularity.

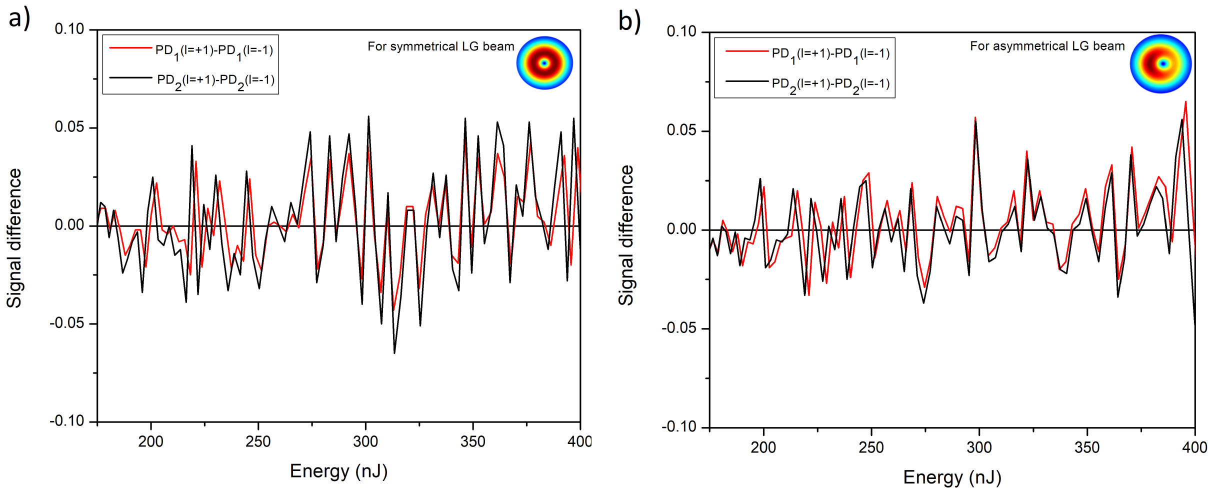

FIG. S 6. Transmission linearly polarized helical light in air (no sample) (a) for a symmetrical and (b) asymmetrical LG beams. The red (black) curve represents the difference between the PD1 signal for $+l$ and $-l$ (PD2 monitoring the transmitted light).

6 Differential absorption with non-OAM beams

Figure S7a shows normalized transmission of a linearly polarized Gaussian beam propagating through left- and right-handed chiral molecule. Both in the linear and the nonlinear regimes, the two curves overlap exhibiting no differential absorption. Similar transmission measurements were conducted for S(-)-limonene with left- and right-circularly polarized annular beam resembling an Airy pattern obtained through Fresnel diffraction (Fig. S7b). In absence of phase, which is responsible for orbital angular momentum, there is no differential absorption in a chiral molecule for a beam with a null intensity at the center. The results remained the same even when the null intensity regions was displaced from the center (fig 3c of the main article). This suggests that differential absorption is not purely due to the field gradient. Helical phase plays a crucial role.

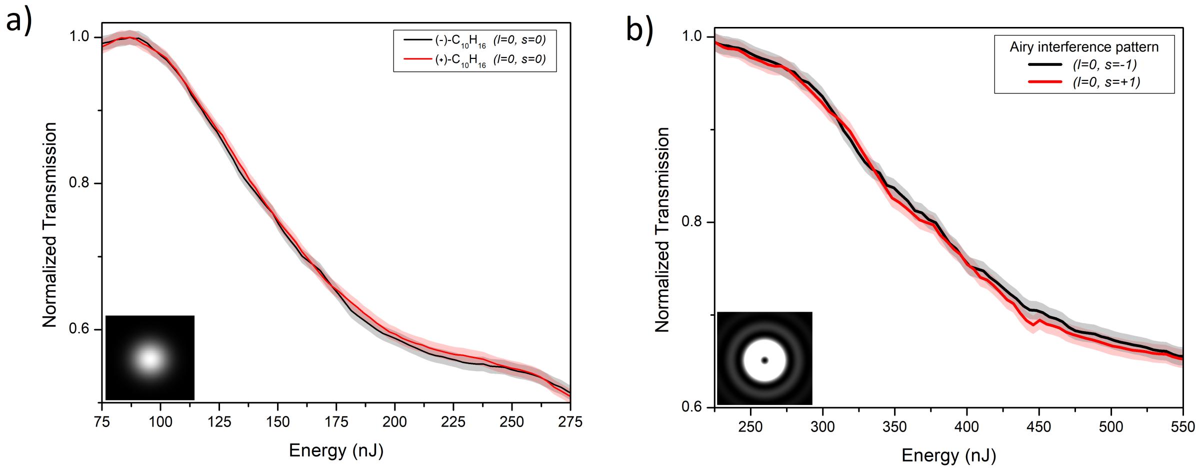

FIG. S 7. (a) Transmission of linearly polarized Gaussian in left- and right-handed limonene. (b) Transmission of left- and right-circularly polarized annular non-OAM beam for S(-)-limonene. Insets show the beam profiles. The colour bands represent the propagation error of the chiral signal for three independent measurements (sample size).

7 Spatial Mapping of singularity

Fig. S8 shows 2D contour map of differential absorption of linearly polarized (ε= 0.09) left and right handed OAM ($l = \pm 1$) for (+)-fenchone, obtained by displacing the singularity in the xy plane. The results presented in Fig.3, 4 (main text) and Fig. S2 are a line scan along one axial direction. The sinusoidal behaviour of differential absorption becomes asymmetric as we displace our singularity off-axis. This behaviour is likely due to the relative angle between the polarization direction and the direction of displacement of the singularity.

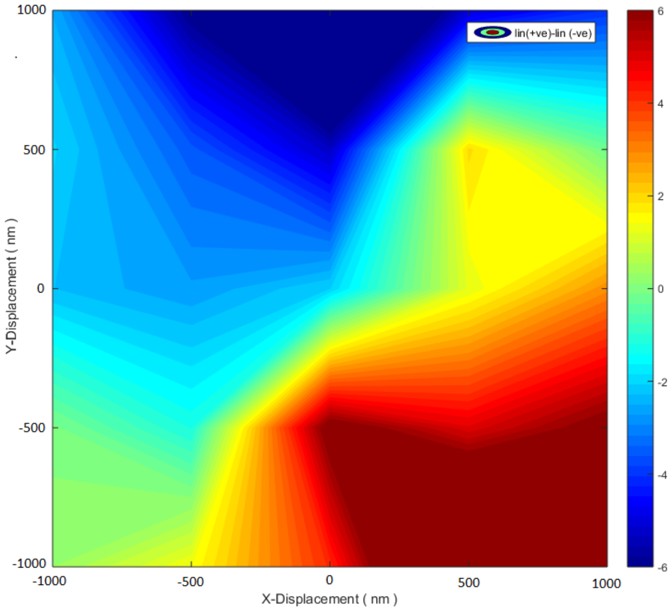

FIG. S 8. Differential absorption of linearly polarized helcial light ($l = \pm 1$) in (+)-fenchone as a function of the displacement of the singularity in the XY-plane.

8 Fluence calculations

In LG beams with increasing l-value, the size of the null intensity region at the center increases. Consequently, for the same spot size higher pulse energies are required to reach the threshold for the onset of nonlinear absorption. This can be seen from the transmission curves shown in Fig. S9 for $l = 1$ (left) and $l = 3$ (right) plotted as a function of laser pulse energy in fenchone.

From the threshold energies, the peak fluence is calculated based on the below equation[1]:

$$F_l\left[\frac{J}{(cm^2)}\right] = \frac{2^{(|l|+1)} r^{2|l|} e^{\frac{-2r^2}{\omega(z)^2}}}{|l|!\pi\omega(z)^{2(|l|+1)}} E_l^{th}\,[J]$$

where $l = 0; \pm 1; \pm 2; \pm 3\ldots$ is the orbital angular momentum value, r is the radial direction, $\omega(z)$ is the radius of a beam evaluated at z=0 and E_l is the threshold pulse energy for different l-values.

For peak fluence, radial parameter r is evaluated at the mamxima of the intensity profile. For Gaussian beam ($l = 0$) maxima occurs at r = 0, for OAM beam with $l = 1$ at $r_{pk} = \pm\frac{w_0}{\sqrt{2}}$ and subsequently for higher order l values at the position of their respective maxima.

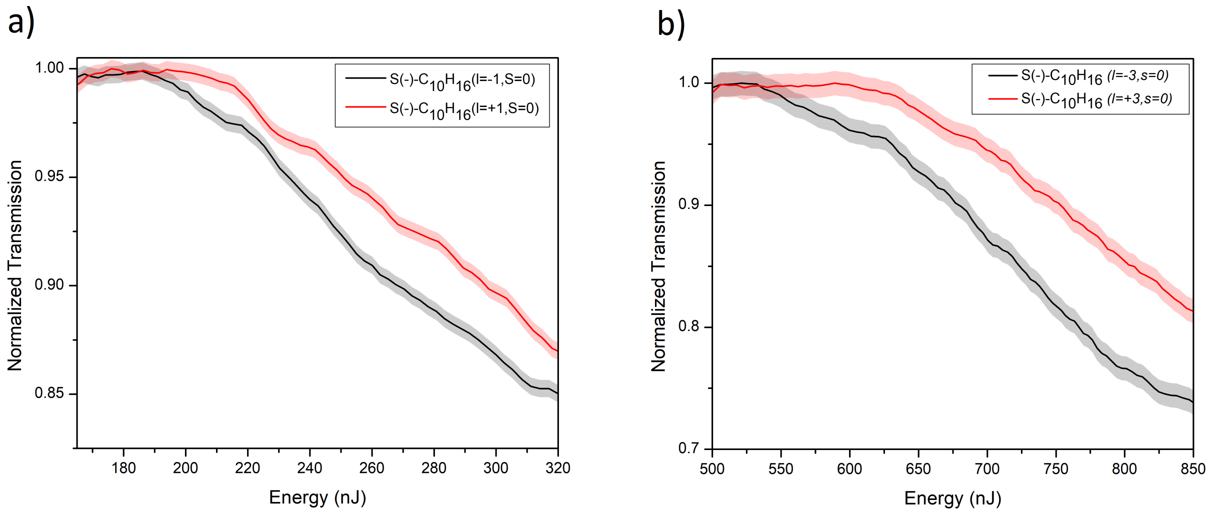

FIG. S 9. Transmission curves of limonene with linearly polarized light ($s = 0$) as a function of pulse energy. **(a)** $l = \pm 1$. **(b)** $l = \pm 3$. The colour bands represent the propagation error of the chiral signal for three independent measurements (sample size).

Substituting the above values for radial parameter, we get

$$\text{For } l = 0 \text{ beam} : F_0\left(r_{pk}\right) = 2\frac{E_0^{th}}{\pi w_0^2}$$

$$\text{For l = 1 beam} : F_1\left(r_{pk}\right) = 2e^{-1}\frac{E_1^{th}}{\pi w_0^2}$$

One can obtain similar equations for higher order OAM beams from which the peak laser fluences were calculated for the presented results.

9 Optical dipole force

Here we show that optical gradient forces are non-zero for asymmetric LG beams. The total force acting on a dipole can be written as[2]

$$\mathbf{F} = (\mu \cdot \nabla)\mathbf{E} + \dot{\mu} \times \mathbf{B} + \dot{\mathbf{r}} \times (\mu \cdot \nabla)\mathbf{B} \tag{1}$$

where μ is the dipole moment. Here first term on the RHS containing the inner product$(\mu \cdot \nabla)$ represents the dipole force due to inhomogeneity in the fields. Second term is the expression of standard Lorentz force and third term represents particle movement in the inhomogeneous magnetic field. The above equation was obtained by assuming dipoles does not change the incident fields. For non relativistic speeds ($\dot{r} << c$), third term can be neglected as it is much smaller in comparison to first two terms. Substituting $\mu = \alpha(\omega)\mathbf{E}(\mathbf{r})$ where α is atomic polarizability, we get,

$$\mathbf{F} = \alpha(\mathbf{E} \cdot \nabla)\mathbf{E} + \alpha(\frac{d\mathbf{E}}{dt} \times \mathbf{B}) \tag{2}$$

Using vector identity $(\mathbf{E} \cdot \nabla)\mathbf{E} = \frac{1}{2}\nabla\left(E^2\right) - \mathbf{E} \times (\nabla \times \mathbf{E})$ and second maxwell equation we get,

$$\mathbf{F} = \alpha\frac{1}{2}\nabla E^2 + \alpha\frac{d}{dt}(\mathbf{E} \times \mathbf{B}). \tag{3}$$

Here, first term defines the gradient force and second term is the scattering force which can be neglected when the poynting vector does not change over an optical cycle. Fig. S10 shows the gradient force component (F$_x$) integrated over the beam

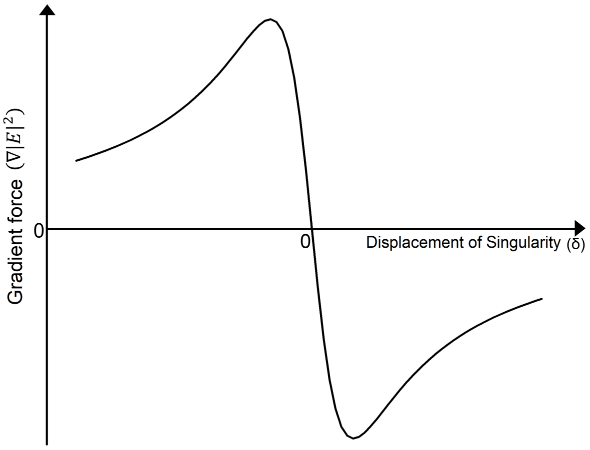

FIG. S 10. Optical gradient force as a function of displaced position of singularities. Optical gradient force is zero for symmetric LG beam and maximum at the position of displaced singularity. Force converges towards zero for the extreme displacement in singularity where beam profile mimics gaussian profile.

cross-section as a function of displaced position of the singularity. For linearly polarized light one of the transverse components will be dominant. The F_y component would be smaller in magnitude however exhibits similar behaviour. The gradient force is zero for the symmetric LG beam for which the singularity is at the center. When the singularity is displaced, the gradient forces initially increases and then decreases to zero for large displacement. A non-zero gradient force would give rise to a torque which preferentially aligns the molecular axis parallel the polarization plane[3]. Such alignment of molecules in an asymmetric LG beams will lead to non-zero averaged E1E2 dipole-quadrupole contribution to HD. Therefore, the HD signal, shown in Fig. 5 of the main text, is zero for symmetric LG beams, increases with the displacement of the singularity reaching a maximum and then decreases when the singularity reaches the beam periphery.

10 Extension of theory to multiphoton case using time-dependent perturbation theory

Using perturbation theory, a generic time-dependent wavefunction

$$|\Psi\rangle = |\Psi\rangle^{(0)} + \sum_m c_m(t)\,|\Psi_m\rangle^{(0)} \tag{4}$$

satisfies the Schrodinger equation

$$(H_0 + \lambda V(t))\,|\Psi\rangle = i\hbar\frac{\partial}{\partial t}|\Psi\rangle \tag{5}$$

where, λ is the perturbation parameter and

$$V(t) = -\mu_\alpha E_\alpha - \frac{1}{3}\theta_{\alpha\beta}\nabla_\alpha E_\beta - m_\alpha B_\alpha - ... \tag{6}$$

is the interaction Hamiltonian[4,5]. The corresponding multipoles and fields are complex quantities. $|\Psi\rangle^{(0)} = |\psi\rangle^{(0)}e^{-iE_n^{(0)}t/\hbar}$ are the stationary states satisfying

$$H_0|\Psi\rangle^{(0)} = i\hbar\frac{\partial}{\partial t}|\Psi\rangle^{(0)} \tag{7}$$

We can expand the time dependent coefficient $c_m(t)$ in powers of perturbation parameter λ.

$$c_m(t) = c_m^{(0)} + \lambda c_m^{(1)}(t) + \lambda^2 c_m^{(2)}(t) + \ldots + \lambda^n c_m^{(n)}(t) \tag{8}$$

where different order coeffecients can be obtained by comparing powers of perturbation parameter λ

$$c_m^{(0)} t(t) = \left(\frac{1}{i\hbar}\right) \int_{-\infty}^{t} dt' \langle m|V(t')|g\rangle e^{i\omega_{mg}t} \tag{9}$$

and nth order is defined as,

$$c_m^{(n)}(t) = \left(\frac{1}{i\hbar}\right)^n \sum_l \int_{-\infty}^{t} dt' \langle m|V(t')|l\rangle c_l^{(n-1)}(t') e^{i\omega_{ml}t'} \tag{10}$$

Now, we calculate the single photon absorption rate and generalize it to multiphoton absorption[6] Considering a interaction Hamiltonian of the form

$$V(t) = Ve^{-i\omega t} + V^* e^{i\omega t} \tag{11}$$

By implementing the rotating wave approximation, we neglected the complex conjugate of the field because we are only considering absorption and ignore the stimulated emission (anti-resonant terms). The probability amplitude can be expressed as

$$p_m^{(n)}(t) = |c_m^{(n)}(t)|^2 \tag{12}$$

and the rate of transition

$$R_{mg}^{(n)} = \frac{p_m^{(n)}(t)}{t} \tag{13}$$

therefore, for single photon we obtain Fermi's golden rule

$$R_{mg}^{(1)} = \frac{2\pi}{\hbar^2} |\langle m|V|g\rangle|^2 \delta(\omega_{mg} - \omega) \tag{14}$$

Single photon transition rate is proportional to absorption cross-section[6] which is proportional to the rate of energy absorption (Γ) derived in the main text. Substituting the interaction Hamiltonian into the rate expression, we get

$$R_{mg}^{(1)} = \frac{2\pi}{\hbar^2} |-\mu_\alpha^{mg} E_\alpha - \frac{1}{3}\theta_{\alpha\beta}^{mg} \nabla_\alpha E_\beta - m_\alpha^{mg} B_\alpha|^2 \delta(\omega_{mg} - \omega) \tag{15}$$

For physical situations, the delta function can be replaced by a lineshape function

$$R_{mg}^{(1)} = \frac{2\pi}{\hbar^2} |-\mu_\alpha^{mg} E_\alpha - \frac{1}{3}\theta_{\alpha\beta}^{mg} \nabla_\alpha E_\beta - m_\alpha^{mg} B_\alpha|^2 \rho(\omega_{mg} = \omega) \tag{16}$$

$$\begin{aligned} R_{mg}^{(1)} = \frac{2\pi}{\hbar^2} \Bigg(& (\mu_\alpha^{mg} E_\alpha)(\mu_\alpha^{mg} E_\alpha)^* + (\mu_\alpha^{mg} E_\alpha)(m_\alpha^{mg} B_\alpha)^* + (\mu_\alpha^{mg} E_\alpha)\left(\frac{1}{3}\theta_{\alpha\beta}^{mg} \nabla_\alpha E_\beta\right)^* + (m_\alpha^{mg} B_\alpha)(\mu_\alpha^{mg} E_\alpha)^* \\ & + (m_\alpha^{mg} B_\alpha)\left(\frac{1}{3}\theta_{\alpha\beta}^{mg} \nabla_\alpha E_\beta\right)^* + (m_\alpha^{mg} B_\alpha)(m_\alpha^{mg} B_\alpha)^* + \left(\frac{1}{3}\theta_{\alpha\beta}^{mg} \nabla_\alpha E_\beta\right)(\mu_\alpha^{mg} E_\alpha)^* + \left(\frac{1}{3}\theta_{\alpha\beta}^{mg} \nabla_\alpha E_\beta\right)(m_\alpha^{mg} B_\alpha)^* \\ & + \left(\frac{1}{3}\theta_{\alpha\beta}^{mg} \nabla_\alpha E_\beta\right)\left(\frac{1}{3}\theta_{\alpha\beta}^{mg} \nabla_\alpha E_\beta\right)^* \Bigg) \rho(\omega_{mg} = \omega) \end{aligned}$$

Ignoring the M1M1, M1E2 and the E2E2 coupling terms and applying the anisotropic averaging, we get

$$\begin{aligned} R_{mg}^{(1)} = \frac{2\pi}{\hbar^2} \big[& |\mu_\alpha^{mg}|^2 |E_\alpha|^2 + |m_\alpha^{mg}|^2 |B_\alpha|^2 + \langle \mu_\alpha^{mg} m_\alpha^{mg*} \rangle_\rho (E_\alpha B_\alpha^*) + \langle m_\alpha^{mg} \mu_\alpha^{mg*} \rangle_\rho (B_\alpha E_\alpha^*) \\ & + \frac{1}{3}\left(\langle \theta_{\alpha\beta}^{mg} \mu_\alpha^{mg*} \rangle_\rho (\nabla_\alpha E_\beta \cdot E_\alpha^*) + \langle \mu_\alpha^{mg} \theta_{\alpha\beta}^{mg*} \rangle \left(E_\alpha \nabla_\alpha E_\beta^*\right) \right) \rho(\omega_{mg} = \omega) \end{aligned}$$

Here ρ is the orientation-dependent weighting factor arising from the anisotropic averaging ($\rho = 0$ for random orientations and $\rho = 1$ for full alignment of molecules). The dipole transition μ is a real quantity , magnetic transition dipole m is imaginary[7]. Approximating the response of the quadrupole tensor as a scalar we can rewrite the above expression as:

$$R_{mg}^{(1)} = \frac{2\pi}{\hbar^2}\left[|\mu_\alpha^{mg}|^2|E_\alpha|^2 + |m_\alpha^{mg}|^2|B_\alpha|^2 + \langle\mu_\alpha^{mg}m_\alpha^{gm}\rangle_\rho\left(B_\alpha E_\alpha^* - E_\alpha B_\alpha^*\right)\right.$$
$$\left. + \frac{1}{3}\left(\langle\mu_\alpha^{mg}\theta_{\alpha\beta}^{gm}\rangle_\rho\left(\nabla_\alpha E_\beta E_\alpha^* + E_\alpha\nabla_\alpha E_\beta^*\right)\right)\right]\rho\left(\omega_{mg} = \omega\right)$$

Since $B_\alpha E_\alpha^* - E_\alpha B_\alpha^* = -2iIm\left[E_\alpha^* B_\alpha\right]$ and, $\left(E_\alpha^*\nabla_\alpha E_\beta + E_\alpha\nabla_\alpha E_\beta^*\right) = 2\mathrm{Re}\left[E_\alpha^*\nabla_\alpha E_\beta\right]$ we can rewrite the above expression as

$$R_{mg}^{(1)} = \frac{2\pi}{\hbar^2}\left[\underbrace{|\mu_\alpha^{mg}|^2|E_\alpha|^2}_{\text{E1E1}} + \underbrace{|m_\alpha^{mg}|^2|B_\alpha|^2}_{\text{M1M1}} + \underbrace{2\langle\mu_\alpha^{mg}m_\alpha^{gm}\rangle_\rho\mathrm{Im}\left[E_\alpha^* B_\alpha\right]}_{\text{E1M1}} + \underbrace{\frac{2}{3}\langle\mu_\alpha^{mg}\theta_{\alpha\beta}^{gm}\rangle_\rho\mathrm{Re}\left[E_\alpha^*\nabla_\alpha E_\beta\right]}_{\text{E1E2}}\right]\rho\left(\omega_{mg} = \omega\right) \tag{17}$$

This is the single photon transition rate and resembles equation (8) of main text. $\mathrm{Im}\left[E_\alpha^* B_\alpha\right]$ and $\mathrm{Re}\left[E_\alpha^*\nabla_\alpha E_\beta\right]$ correspond to optical chirality C and helicity Υ, respectively.

The transition rate for two photon process (transition states: g $\rightarrow k \rightarrow m$) is

$$R_{mg}^{(2)} = 2\pi\left|\sum_k \frac{V_{mk}V_{kg}}{\hbar^2\left(\omega_{kg} - \omega\right)}\right|^2\rho\left(\omega_{mg} = 2\omega\right) \tag{18}$$

$$R_{mg}^{(2)} = 2\pi\left|\sum_k \frac{\left(\mu_\alpha^{mk}E_\alpha + \frac{1}{3}\theta_{\alpha\beta}^{mk}\nabla_\alpha E_\beta + m_\alpha^{mk}B_\alpha\right)\left(\mu_\alpha^{kg}E_\alpha + \frac{1}{3}\theta_{\alpha\beta}^{kg}\nabla_\alpha E_\beta + m_\alpha^{kg}B_\alpha\right)}{\hbar^2\left(\omega_{kg} - \omega\right)}\right|^2\rho\left(\omega_{mg} = 2\omega\right) \tag{19}$$

$$R_{mg}^{(2)} = 2\pi\left|\sum\nolimits_k \frac{\left(\mu_\alpha^{mk}E_\alpha\right)\left(\mu_\alpha^{kg}E_\alpha\right) + \left(m_\alpha^{mk}B_\alpha\right)\left(\mu_\alpha^{kg}E_\alpha\right) + \left(\mu_\alpha^{mk}E_\alpha\right)\left(m_\alpha^{kg}B_\alpha\right) + \left(\frac{1}{3}\theta_{\alpha\beta}^{mk}\nabla_\alpha E_\beta\right)\left(\mu_\alpha^{kg}E_\alpha\right) + \left(\mu_\alpha^{mk}E_\alpha\right)\left(\frac{1}{3}\theta_{\alpha\beta}^{kg}\nabla_\alpha E_\beta\right)}{\hbar^2\left(\omega_{kg} - \omega\right)}\right|^2\rho\left(\omega_{mg} = 2\omega\right) \tag{20}$$

Ignoring the higher order terms involving M1 and E2 we get

$$R_{mg}^{(2)} = 2\pi\sum\nolimits_k \frac{1}{\hbar^4\left(\omega_{kg} - \omega\right)^2}\left\{\left|\mu_\alpha^{mk}E_\alpha\right|^2\left|\mu_\alpha^{kg}E_\alpha\right|^2 + \left|\mu_\alpha^{kg}E_\alpha\right|^2\left[\left(\mu_\alpha^{mk}E_\alpha\right)\left(m_\alpha^{mk}B_\alpha\right)^* + \left(m_\alpha^{mk}B_\alpha\right)\left(\mu_\alpha^{mk}E_\alpha\right)^*\right]\right.$$
$$+\left|\mu_\alpha^{kg}E_\alpha\right|^2\left[\left(\mu_\alpha^{mk}E_\alpha\right)\left(\frac{1}{3}\theta_{\alpha\beta}^{mk}\nabla_\alpha E_\beta\right)^* + \left(\frac{1}{3}\theta_{\alpha\beta}^{mk}\nabla_\alpha E_\beta\right)\left(\mu_\alpha^{mk}E_\alpha\right)^*\right] + \left|\mu_\alpha^{mk}E_\alpha\right|^2\left[\left(\mu_\alpha^{kg}E_\alpha\right)\left(m_\alpha^{kg}B_\alpha\right)^* + \left(m_\alpha^{kg}B_\alpha\right)\left(\mu_\alpha^{kg}E_\alpha\right)^*\right]$$
$$\left.+\left|\mu_\alpha^{mk}E_\alpha\right|^2\left[\left(\mu_\alpha^{kg}E_\alpha\right)\left(\frac{1}{3}\theta_{\alpha\beta}^{kg}\nabla_\alpha E_\beta\right)^* + \left(\frac{1}{3}\theta_{\alpha\beta}^{kg}\nabla_\alpha E_\beta\right)\left(\mu_\alpha^{kg}E_\alpha\right)^*\right]\right\}\rho\left(\omega_{mg} = 2\omega\right)$$

Implementing anisotropic averaging, we get

$$R_{mg}^{(2)} = 2\pi\sum\nolimits_k \frac{1}{\hbar^4\left(\omega_{kg} - \omega\right)^2}\left\{\left|\mu_\alpha^{mk}\mu_\alpha^{kg}\right|^2\left|E_\alpha E_\alpha\right|^2 + \left|\mu_\alpha^{kg}\right|^2\left|E_\alpha\right|^2\left[\langle\mu_\alpha^{mk}m_\alpha^{mk*}\rangle_\rho\left(E_\alpha B_\alpha^*\right) + \langle m_\alpha^{mk}\mu_\alpha^{mk*}\rangle_\rho\left(B_\alpha E_\alpha^*\right)\right]\right.$$
$$+\left|\mu_\alpha^{kg}\right|^2\left|E_\alpha\right|^2\left[\langle\mu_\alpha^{mk}\frac{1}{3}\theta_{\alpha\beta}^{mk*}\rangle_\rho\left(E_\alpha\nabla_\alpha E_\beta^*\right) + \langle\frac{1}{3}\theta_{\alpha\beta}^{mk}\mu_\alpha^{mk*}\rangle_\rho\left(\nabla_\alpha E_\beta E_\alpha^*\right)\right] + \left|\mu_\alpha^{mk}\right|^2\left|E_\alpha\right|^2\left[\langle\mu_\alpha^{kg}m_\alpha^{kg*}\rangle_\rho\left(E_\alpha B_\alpha^*\right) + \langle m_\alpha^{kg}\mu_\alpha^{kg*}\rangle_\rho\left(B_\alpha E_\alpha^*\right)\right]$$
$$\left.+\left|\mu_\alpha^{mk}\right|^2\left|E_\alpha\right|^2\left[\langle\frac{1}{3}\mu_\alpha^{kg}\theta_{\alpha\beta}^{kg*}\rangle_\rho\left(E_\alpha\nabla_\alpha E_\beta^*\right) + \langle\frac{1}{3}\theta_{\alpha\beta}^{kg}\mu_\alpha^{kg*}\rangle_\rho\left(\nabla_\alpha E_\beta E_\alpha^*\right)\right]\right\}\rho\left(\omega_{mg} = 2\omega\right)$$

$$R_{mg}^{(2)} = 2\pi\sum\nolimits_k \frac{1}{\hbar^4\left(\omega_{kg} - \omega\right)^2}\left\{\left|\mu_\alpha^{mk}\mu_\alpha^{kg}\right|^2\left|E_\alpha E_\alpha\right|^2 + 2\left(\left|\mu_\alpha^{kg}\right|^2\left|E_\alpha\right|^2\langle\mu_\alpha^{mk}m_\alpha^{km}\rangle_\rho + \left|\mu_\alpha^{mk}\right|^2\left|E_\alpha\right|^2\langle\mu_\alpha^{kg}m_\alpha^{gk}\rangle_\rho\right)\mathrm{Im}\left[E_\alpha^* B_\alpha\right]\right.$$
$$\left.+\frac{2}{3}\left(\left|\mu_\alpha^{kg}\right|^2\left|E_\alpha\right|^2\langle\mu_\alpha^{mk}\theta_{\alpha\beta}^{km}\rangle_\rho + \left|\mu_\alpha^{mk}\right|^2\left|E_\alpha\right|^2\langle\mu_\alpha^{kg}\theta_{\alpha\beta}^{gk}\rangle_\rho\right)\mathrm{Re}\left[E_\alpha^*\nabla_\alpha E_\beta\right]\right\}\rho\left(\omega_{mg} = 2\omega\right)$$

Generalizing for n-photon case, where m is the final state and g is the ground state state

$$R_{mg}^{(n)} = 2\pi \left[\sum_p \sum_l \cdots \sum_r \sum_k \frac{\left| \mu_\alpha^{mp} \mu_\alpha^{pl} \ldots \mu_\alpha^{rk} \mu_\alpha^{kg} \right|^2 |E_\alpha|^{2n}}{\hbar^{2n} \left(\omega_{pl} - (n-1)\,\omega\right)^2 \ldots (\omega_{rk} - 2\omega)^2 \left(\omega_{kg} - \omega\right)^2} \rho\left(\omega_{mg} = n\omega\right) \right. \tag{21}$$

$$+2 \sum_p \sum_l \cdots \sum_r \sum_k \frac{|\mu_\alpha^{mp}|^2 \left|\mu_\alpha^{pl}\right|^2 \ldots |\mu_\alpha^{rk}|^2 \operatorname{Im}\left[\mu_\alpha^{kg} m_\alpha^{gk}\right] + |\mu_\alpha^{mp}|^2 \left|\mu_\alpha^{pl}\right|^2 \ldots \left|\mu_\alpha^{kg}\right|^2 \langle \mu_\alpha^{rk} m_\alpha^{kr} \rangle_\rho + \ldots +}{\hbar^{2n} \left(\omega_{pl} - (n-1)\,\omega\right)^2 \ldots (\omega_{rk} - 2\omega)^2 \left(\omega_{kg} - \omega\right)^2} \tag{22}$$

$$\frac{\ldots + |\mu_\alpha^{mp}|^2 \ldots |\mu_\alpha^{rk}|^2 \left|\mu_\alpha^{kg}\right|^2 \operatorname{Im}\left[\mu_\alpha^{pl} m_\alpha^{lp}\right] + \left|\mu_\alpha^{pl}\right|^2 \ldots |\mu_\alpha^{rk}|^2 \left|\mu_\alpha^{kg}\right|^2 \langle \mu_\alpha^{mp} m_\alpha^{pm} \rangle_\rho}{\hbar^{2n} \left(\omega_{pl} - (n-1)\,\omega\right)^2 \ldots (\omega_{rk} - 2\omega)^2 \left(\omega_{kg} - \omega\right)^2} |E_\alpha|^{2(n-1)} \operatorname{Im}\left[E_\alpha^* B_\alpha\right] \rho\left(\omega_{mg} = n\omega\right) \tag{23}$$

$$+\frac{2}{3} \sum_p \sum_l \cdots \sum_r \sum_k \frac{|\mu_i^{mp}|^2 \left|\mu_\alpha^{pl}\right|^2 \ldots |\mu_\alpha^{rk}|^2 \operatorname{Im}\left[\mu_\alpha^{kg} \theta_{\alpha\beta}^{gk}\right] + |\mu_\alpha^{mp}|^2 \left|\mu_\alpha^{pl}\right|^2 \ldots \left|\mu_\alpha^{kg}\right|^2 \langle \mu_\alpha^{rk} \theta_{\alpha\beta}^{kr} \rangle_\rho + \ldots +}{\hbar^{2n} \left(\omega_{pl} - (n-1)\,\omega\right)^2 \ldots (\omega_{rk} - 2\omega)^2 \left(\omega_{kg} - \omega\right)^2} \tag{24}$$

$$\left. \frac{\ldots + |\mu_\alpha^{mp}|^2 \ldots |\mu_\alpha^{rk}|^2 \left|\mu_\alpha^{kg}\right|^2 \operatorname{Im}\left[\mu_\alpha^{pl} \theta_{\alpha\beta}^{lp}\right] + \left|\mu_\alpha^{pl}\right|^2 \ldots |\mu_\alpha^{rk}|^2 \left|\mu_\alpha^{kg}\right|^2 \langle \mu_\alpha^{mp} \theta_{\alpha\beta}^{pm} \rangle_\rho}{\hbar^{2n} \left(\omega_{pl} - (n-1)\,\omega\right)^2 \ldots (\omega_{rk} - 2\omega)^2 \left(\omega_{kg} - \omega\right)^2} |E_\alpha|^{2(n-1)} \operatorname{Re}\left[E_\alpha^* \nabla_\alpha E_\beta\right] \rho\left(\omega_{mg} = n\omega\right) \right] \tag{25}$$

Neglecting the higher order cross terms, we therefore obtain similar expressions involving E1E1, E1M1 and E1E2 expressed in terms of optical chirality C and helicity Υ. The above expressions were obtained in a scalar approximation regime where tensor properties are restricted to a dominant component for oriented molecules. However, when the tensor nature of molecular response is considered there will be multitude of cross terms that arise in case of n-photon transitions whose *l*- dependence needs to be investigated further. We considered n-photon transition rates because in our experiments, for example, interaction of Ti:Sapphire femtosecond laser with limonene (I_P = 8.3 ev) is a 6 photon process.

References

1. Oosterbeek, R., Ashforth, S., Bodley, O., & Simpson, M., Measuring the ablation threshold fluence in femtosecond laser micromachining with vortex and Bessel pulses. *Opt. Express* **26**, 34558-34568 (2018).
2. Novotny, L., & Hecht, B., *Principles of Nano-Optics (2nd ed.)* (Cambridge University Press., 2012).
3. Bradshaw, D. S., & Andrews, D. L., Manipulating particles with light: radiation and gradient forces. *Eur. J. Phys.* **38**, 034008 (2017).
4. Jackson, J. D., *Classical Electrodynamics* (International Adaptation, ISBN: 978-1-119-77077-0, 2021).
5. Barron, L.D.,*Molecular Light Scattering and Optical Activity* (Cambridge University Press, Cambridge, England, 2004).
6. Boyd, R.W., *Nonlinear Optics (3rd ed.)* (Academic Press, 2020).
7. Craig, D. P., & Thirunamachandran, T., *Molecular Quantum Electrodynamics: An introduction to radiation molecule interactions* (Academic Press Inc. London, 1984).

References

[1] Koji Nakanishi, Nina Berova, and Robert W. Woody. *Circular Dichroism: Principles and Applications*. Wiley, 2000.

[2] Ettore Castiglioni, Sergio Abbate, and Giovanna Longhi. Experimental methods for measuring optical rotatory dispersion: survey and outlook. *Chirality*, 23:711–716, 2011.

[3] U. J. Meierhenrich, J.-J. Filippi, C. Meinert, J. H. Bredehöft, J.-i. Takahashi, L. Nahon, N. C. Jones, and S. V. Hoffmann. Circular dichroism of amino acids in the vacuum-ultraviolet region. *Angew. Chem., Int. Ed.*, 49:7799, 2010.

[4] J. T. Collins et al. Chirality and chiroptical effects in metal nanostructures: fundamental and current trends. *Adv. Opt. Matter*, 5:1700182, 2017.

[5] Yiqiao Tang and Adam E. Cohen. Enhanced enantioselectivity in excitation of chiral molecules by superchiral light. *Science*, 332:333–336, 2011.

[6] J.-L. Bégin, M. Alsaawy, and R. Bhardwaj. Chiral discrimination by recollision enhanced femtosecond laser mass spectrometry. *Sci. Rep.*, 10:14074, 2020.

[7] Maurice H. M. Janssen and Ivan Powis. Detecting chirality in molecules by imaging photoelectron circular dichroism. *Physical Chemistry Chemical Physics*, 16:856–871, 2014.

[8] Ivan Powis. Photoelectron circular dichroism of the randomly oriented chiral molecules glyceraldehyde and lactic acid. *The Journal of Chemical Physics*, 112:301–310, 2000.

[9] F. Araoka et al. Interactions of twisted light with chiral molecules: an experimental investigation. *Physical Review A*, 71:055401, 2005.

[10] W. Löffler, D. J. Broer, and J. P. Woerdman. Circular dichroism of cholesteric polymers and the orbital angular momentum of light. *Physical Review A*, 83:065801, 2011.

[11] D. L. Andrews, L. D. Romero, and M. Babiker. On optical vortex interactions with chiral matter. *Opt. Commun.*, 237:133–139, 2004.

[12] K. A. Forbes and D. L. Andrews. Optical orbital angular momentum: twisted light and chirality. *Optical Letters*, 43:435–438, 2018.

[13] K. A. Forbes and D. L. Andrews. Spin-orbit interactions and chiroptical effects engaging orbital angular momentum of twisted light in chiral and achiral media. *Physical Review A*, 99:023837, 2019.

[14] W. Brullot et al. Resolving enantiomers using the optical angular momentum of twisted light. *Science Advances*, 2:e1501349, 2016.

[15] J. R. Rouxel et al. Hard x-ray helical dichroism of disordered molecular media. *Nature Photonics*, 16:570–574, 2022.

[16] J. Ni et al. Giant helical dichroism of single chiral nanostructures with photonic orbital angular momentum. *ACS Nano*, 15:2893–2900, 2021.

Chapter 4

Helical dichroism in enantiomeric solutions

4.1 Intoduction

In the previous chapter, chiroptical detection in enantiopure liquids was demonstrated. The strength of the chiral signal was shown to be scalable by varying the l value (OAM) of the beam, as well as tunable by changing the ellipticity and displacing the phase singularity of the beam. These features offered a distinct advantage over conventional CD techniques. However, for a spectroscopy method to be truly comparable to CD spectroscopy, it must be applicable and efficient in the liquid solution phase. The chiral response of an enantiomeric solution is often difficult to observe due to the strong influence of solvent-solute interactions [1]. CD spectroscopy in biologically relevant solutions is crucial for understanding molecular biology and is extensively employed in the pharmaceutical industry for drug-binding research. This raises the question: *Can phase-based spectroscopy be expanded to the solution phase to become relevant for biological applications?*

This work demonstrated the presence of HD in enantiomeric solutions without the need for external intermediaries. The asymmetrical helical beam was utilized as a chiral probe to differentiate enantiopure powders of amino acids and terpenoids dissolved in an achiral solvent at varying concentrations. Theoretically, the chiral response of enantiomers was qualitatively described by incorporating the broken symmetry conditions [2, 3] of the enantiomeric ground states into the helical light-matter interaction model.

This research was published in the *Journal of Chemical Physics* (2023) and was selected as an Editor's Pick (EP in the published title). The first authorship was shared with my colleague due to our equal contributions to the work. The published version of the article is reproduced in this chapter, where the theoretical framework, experimental methods, figures, and references are self-contained. The following section presents the key results and advances.

4.2 Key results and advances

Transmission experiments were performed using enantiopure alanine and camphor powders dissolved in an achiral solvent at varying concentrations. Similar to the case of enantiopure liquids, the transmission curves for left- and right-handed circularly polarized light overlapped within the experimental noise, demonstrating a weak CD signal strength in our setup. Also, the solution exhibited differential absorption when probed with the left- and right-handed asymmetrical helical light. The key results can be summarized as follows:

- *Nonlinear absorption threshold*: Transmission measurements revealed a lower onset of nonlinear absorption for the chiral solutions compared to their respective achiral solvents. This distinctive property made it possible to differentiate the HD signal of chiral molecules with minimal interference from the achiral molecules. This distinction was crucial, as achiral molecules also exhibit helical dichroism.
- *HD (Type I, II)*: The powdered solutions of alanine and camphor exhibited two types of dichroism: HD (Type I) and HD (Type II), similar to the case of enantiopure liquids. The HD (Type I) signal increased with the concentration of the solute. As the concentration approached the solubility limit, the signal exhibited more fluctuations and errors. Additionally, HD (Type I) could be tuned by displacing the phase singularity. HD (Type II), or the chiral signal, did not increase with varying concentrations and reached a maximum of 4%. For comparison, the chiral signal for Gaussian beams reached a relative magnitude of approximately 1%.

The major advances of this research can be summarized as follows:

1. Extended the helical phase-based chiroptical detection spectroscopy to powdered enantiomeric solutions.

2. The differential absorbance of helical light, $\delta A \approx 0.05$ for camphor and alanine solutions, is shown to be an order of magnitude higher compared to conventional resonant linear techniques, such as the CD for alanine ($\delta A \approx 0.0076$). The demonstrated efficiency is of the same order as existing nonlinear techniques, such as $\delta A \approx 0.03$ for alanine with two-photon CD and $\delta A \approx 0.085$ for camphor with PECD.

3. The ability to differentiate enantiomeric solutions using helical light offers an additional advantage for bio-relevant molecules, which are often in powder form. This makes the phase-based spectroscopy technique particularly relevant for industrial applications

The following section reproduces the author's contribution section from the published article. The published version of the article file is attached later.

4.3 Statement of contribution

These authors contributed equally: Ashish Jain and Jean-Luc Bégin.

This project was conceived as an extension of the nonlinear helical dichroism in liquids project and was designed in collaboration with my colleague Jean-Luc Bégin and my supervisor, Professor Ravi Bhardwaj. It commenced following the completion of the nonlinear helical dichroism in chiral and achiral molecules research (Chapter 3), where the developed theoretical model was extended to enantiomers. My colleague and I constructed the experimental setup and conducted calibration experiments to minimize background noise. Together, we performed all the experiments and analyzed the resulting data. The theory of helical dichroism in enantiomers was developed jointly with my colleague and supervisor. All authors contributed to preparing and reviewing the manuscript.

The Journal of Chemical Physics ARTICLE pubs.aip.org/aip/jcp

Helical dichroism in enantiomeric solutions

Cite as: J. Chem. Phys. 159, 014504 (2023); doi: 10.1063/5.0152203
Submitted: 28 March 2023 • Accepted: 12 June 2023 •
Published Online: 5 July 2023

Ashish Jain, Jean-Luc Bégin, and Ravi Bhardwaj[a)]

AFFILIATIONS

Department of Physics, University of Ottawa, Ottawa, Ontario K1N 6N5, Canada

[a)]**Author to whom correspondence should be addressed:** ravi.bhardwaj@uottawa.ca

ABSTRACT

A novel chiroptical sensing technique was recently introduced that utilized the helical phase of the structured light as a chiral reagent instead of polarization of light to differentiate enantiopure chiral liquids. The unique advantage of this non-resonant, nonlinear technique is that the chiral signal can be scaled and tuned. In this paper, we extend this technique to enantiopure powders of alanine and camphor by dissolving them in solvents of varying concentrations. We show the differential absorbance of helical light to be an order of magnitude higher relative to conventional resonant linear techniques and is comparable to nonlinear techniques that use circularly polarized light. The origin of helicity dependent absorption is discussed in terms of induced multipole moments in nonlinear light–matter interaction. These results opens up new opportunities in using helical light as a primary chiral reagent in nonlinear spectroscopic techniques.

INTRODUCTION

Chirality is often investigated by a variety of linear spectroscopic methods, such as Electronic or Vibrational Circular Dichroism (ECD[1,2] or VCD[3]),[4] optical rotatory dispersion,[5] and Raman optical activity.[6] It can also be investigated in the nonlinear absorption regime through two-photon CD[7] and nonlinear optical activity.[8] Most spectroscopic techniques are performed using circularly polarized light as the chiral reagent. The chiroptical response is proportional to the difference between the rate of excitation by right- and left-circularly polarized (RCP and LCP) light. In CD, enantiosensitive transitions in a chiral molecule arise due to the coupling of the electric and magnetic dipole matrix elements (E1M1).[9]

The sensitivity of chiroptical techniques that use polarization of the light as the chiral reagent is limited by the relative size difference between the molecular dimension and the helical pitch of the circularly polarized electromagnetic field. As a result, sensitivity scales inversely with the wavelength of light.[10,11] Thus, linear techniques in the resonant regime, such as VCD, that are performed at infrared wavelengths are often two to three orders of magnitude lower than its counterpart, ECD.[12] Shorter wavelengths, such as x rays, in which the helical pitch is on the same order as the molecular size[13] lead to a greater chiral signal.

Pulsed lasers led to the development of non-resonant, nonlinear chiroptical techniques with enhanced chiral sensitivity due to the intense light fields.[14] Further improvements in efficiency require either to rely exclusively on the electric dipole transitions such as in Photoelectron circular dichroism (PECD) or to redefine a chiral reagent that can increase the chiral signal even with weaker higher order interaction terms. In PECD, ionization of a chiral molecule with circularly polarized light leads to an asymmetry in electron angular distribution.[15,16] PECD has higher efficiency than CD since it relies on electric dipole transitions rather the weaker electric and magnetic dipole coupling term. However, this technique is mostly limited to gas-phase chiral molecules.[17,18]

A conceptually new form of the chiroptical detection technique was recently introduced using the helical phase of the structured light beam as a chiral reagent instead of circular polarization.[19] Such helical light beams, uniquely identified by a phase singularity resulting in a null intensity region in the center, carry an orbital angular momentum of $\pm l\hbar$.[20] Displacing the singularity can induce a chiral sensitive response in bulk liquids due to the multipole interference terms, such as electric–magnetic dipole and electric dipole–quadrupole excitation.[19]

Chiral response with the use of helical light resulted in two types of helical dichroism (HD) signals; HD (Type I) in isotropic chiral and achiral liquids and HD (Type II) in chiral molecules. The former is defined as the differential absorption of left- and right-helical light for the specific enantiomer (analogous to CD), and the latter is differential absorption between the two enantiomers for a specific helicity and polarization of light. HD (Type I) was shown to scale with the l value and tuned by displacing the singularity.[19] HD (Type I and II) was demonstrated in enantiopure liquids, such as limonene and fenchone. However, many chiral systems that have biological significance exist in the powder form, which needs to be dissolved in a solvent.

In this article, we extend the helical dichroism technique from an enantiopure sample to an enantiomeric solution (chiral solute diluted in an achiral solvent). First test case is alanine, an amino-acid used to make proteins, diluted in a water solvent. Second test case is camphor, a terpenoid dissolved in chloroform. Solvents play a crucial role in many biological processes as they can influence the structure and properties of the biomolecules by changing their function and reactivity.[21] Chiral response of an enantiomeric solution is often difficult to observe due to strong influence of solvent–solute interaction.[22] We demonstrate that both enantiomeric solutions exhibit HD (Type I and II) via the differential absorption of left- and right-helical light with an efficiency in absorbance $[\Delta A(\pm l) = \log_{10}\frac{T(-l)}{T(+l)}]$ of $\Delta A \approx 0.05$ for camphor and alanine solution. In comparison, the efficiency of linear CD is $\Delta A \approx 0.0076$ for alanine[23] and $\Delta A \approx 6.5 \times 10^{-6}$ for camphor (VCD).[24] The efficiency of existing nonlinear techniques is $\Delta A \approx 0.03$ for alanine (two-photon CD)[25] and $\Delta A \approx 0.085$ for camphor (PECD).[26]

METHODS

Light can carry Orbital Angular Momentum (OAM) of $\pm l\hbar$ associated with dynamical rotation of the wavefront structure.[20] Such beams are also called helical light beams whose handedness is defined by the twisting of the wavefront undergoing l intertwined rotations in one wavelength, tracing a left- or right-handed corkscrew pattern while propagating in space. In addition, light also carries Spin Angular Momentum (SAM) associated with the dynamical rotation of the electric field vector around the propagation direction, which is often used as a chiral reagent. The polarization of the light is defined as the intrinsic spin degree of freedom. For circularly polarized light, photons carries a spin angular momentum (SAM) of $\pm\hbar$, where $\hbar$ is the reduced Planck constant and the $\pm$ sign represents left- and right-circular polarizations. For linear polarization, SAM is zero.

Helical beams are theoretically modeled using the Laguerre–Gaussian (LG) beams, which are uniquely identified by a phase singularity, a null intensity region, in the center of the beam cross section.[20] However, the singularity can be displaced to generate asymmetrical LG beams either by superimposing a Gaussian[27] or by translating the phase plate.[19] The asymmetrical LG beam with displaced singularity is shown in Fig. 1 and can be plotted using the following equation:

$$E^{\pm}(r,\theta,z) = E_0\left(\frac{\sqrt{2}}{\omega_0}\left(r\,\exp\left(\pm i\theta\right) \mp i\delta r_\delta\,\exp\left(\pm i\Theta\right)\right)\right)^{|l|} \times \exp\left(-\frac{r^2}{\omega_0^2}\right)L_{p-j}^{|l+j|}\left(\frac{2r^2}{w_0^2}\right)\exp\left[ikz\right], \tag{1}$$

where $r = \sqrt{x^2+y^2}$, $r_\delta = \sqrt{\zeta^2+\eta^2}$, $\theta = \tan^{-1}(y/x)$, and $\Theta = \tan^{-1}(\eta/\zeta)$. Here, η and ζ correspond to the displacement of singularity in x–y plane. In addition, E_0 is the normalization factor obtained by integrating the intensity over all space ($-\infty$ to $+\infty$); for ($l = 1$), it is given as:

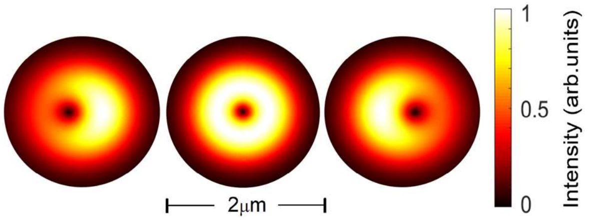

FIG. 1. Simulated intensity profiles of symmetric and asymmetric Laguerre–Gaussian beams. The beam size is defined at the focal region.

$$E_0 = \sqrt{\frac{p!}{(p+1)!}}\sqrt{\frac{\omega_0^2}{\pi\left(\left(\zeta^2+\eta^2\right)+\omega_0^2\right)}}. \tag{2}$$

The above-mentioned beam equation can also be extended to the longitudinal component of the field as a correction to the paraxial regime.[19]

The linearly polarized OAM beam was generated by a combination of a quarter-wave plate, a linear polarizer, and a birefringent liquid-crystal-based phase plate called a q-plate.[28–30] When an incident circularly polarized Gaussian beam propagates through the q-plate with a topological charge q, it acquires an OAM defined by $l = \pm 2$q with a phase singularity at the center of the beam. The conversion efficiency of the q-plate was 91% ± 2% for $l = 3$ beam. The singularity in the OAM beam was displaced by translating the q-plate, mounted on a x, y-stage, with a step size of 250 ± 40 μm. When focused by the objective, this translated to a displacement step size of 300 ± 20 nm with respect to the center of the beam. The calibration was achieved by measuring the total translation required to displace the singularity to the periphery of the defocused beam and comparing it to the measured spot size of 2 ± 0.2 μm.

Transmission experiments were performed by propagating a single femtosecond pulse focused by an aspheric objective (NA = 0.3) into an enantiomeric solution contained in a cuvette (10 mm thick and 3.5 ml volume). A second aspheric objective with the same numerical aperture collaminated the transmitted light onto a photodiode (PD2), positioned immediately after the objective. The incident pulse energy was monitored by deflecting a fraction of the incident beam onto another photodiode (PD1). The signals generated by PD1 and PD2 were stretched by an electronic pulse stretcher, discretized and recorded by a data acquisition card.

For every single laser shot, the transmitted light signal on PD2 was normalized with the incoming light signal on PD1 to produce a transmission curve. These curves, as shown in Fig. 2, are plotted as a function of incident pulse energies, which were varied using a combination of a half-wave plate and a polarizer. The incident pulse energies were measured after the first objective, i.e., energy reaching the sample, by defocusing the incident light. During the measurement, for every laser shot, the sample was translated by 4 μm to avoid micro-bubbles, and the pulse energy was increased in the steps of ~3 nJ. Multiple transmission curves similar to Fig. 2 were obtained for each sample to be averaged and smoothed, producing the normalized transmission curves of left- and right-helical light ($l = \pm 3$).

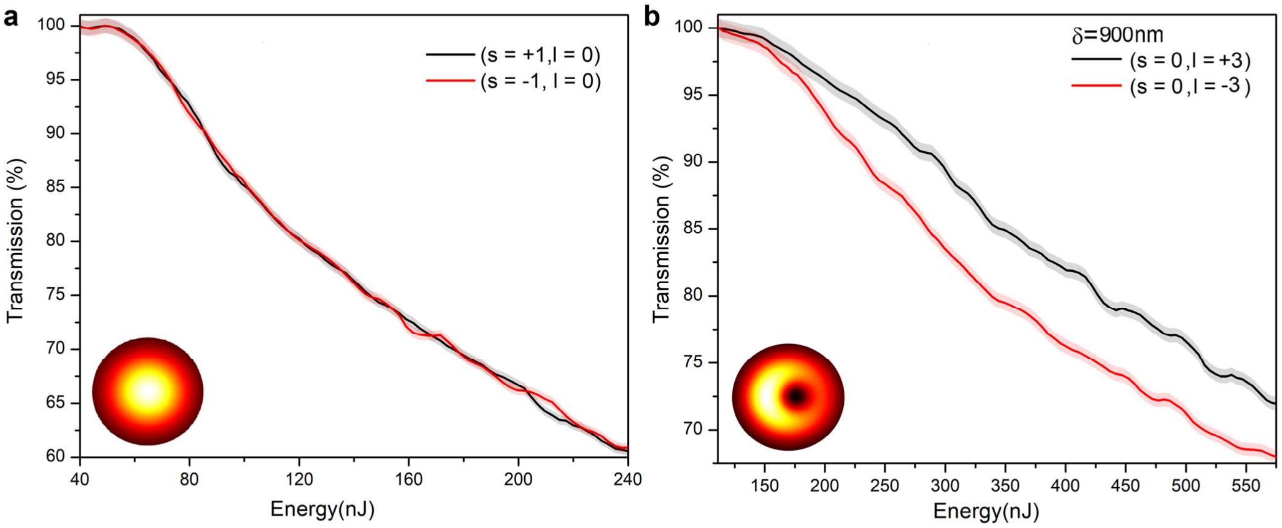

FIG. 2. Transmission curves for 0.5 g of S(−)-camphor diluted in 3.5 ml of chloroform (a) LCP and RCP Gaussian beam ($s = \pm 1$) and (b) linearly polarized helical light $s = 0, l = \pm 3, \delta = 900$ nm, where ± is for different helicities. The error bands represent the standard error of multiple independent transmission measurements. These experimental results were reproduced multiple times under identical conditions.

Helical dichroism is calculated by taking an average of the difference in transmission from the onset of nonlinear absorption to about two times the threshold value.

Femtosecond pulses were produced by a Ti: sapphire laser amplifier system (45 fs, 800 nm, 1 kHz, 2.5 W) operating in an external trigger mode. The pulse duration at the interaction region is about 100 fs and was continuously monitored using the single-shot autocorrelator. To ensure a shortest pulse in the interaction region, a negative chirp was introduced and optimized by measuring the second harmonic generation in a β-barium borate (BBO) crystal placed at the location of the cuvette. To minimize background noise resulting from any discrepancies between the photodiodes, transmission measurements were always performed in an empty cuvette prior to each experiment. In addition, the measured single-shot beam profile, pulse spectrum, and OAM value remained unchanged after transmission through the samples.[19] All the chemical samples used in the experiment were purchased from Sigma-Aldrich, Inc. The purity as specified by the supplier of R(−)- and S(+)-alanine was 98%. For R(+)-camphor, the purity was 98%, and for S(−)-camphor, the purity was 95%.

RESULTS AND DISCUSSION

To compare the role of SAM and OAM of light as a chiral reagent, we measured absorbance of a single femtosecond pulse in S(−)-camphor (0.5 g diluted in 3.5 ml of chloroform). Figure 2 shows normalized transmission as a function of incident pulse energy for (a) circularly polarized Gaussian ($s = \pm 1, l = 0$) and (b) linearly polarized helical beams ($s = 0, l = \pm 3$). The near overlap of both LCP and RCP transmission curves in Fig. 2(a) represents a conventional CD signal with $\Delta A \approx 0.005$. This signal is considered negligible for enantiomeric solutions due to overlapping error bands.

The transmission curves for both beams uniquely identify two absorption regimes i.e., linear and nonlinear absorption. When the energy of the incident laser pulse is below a certain threshold [≈60 nJ for Gaussian and 140 nJ for helical beams in S(−)-camphor], the incident light is not absorbed (transmission = 100%) by the enantiomeric solution because the ionization potential is greater than the photon energy 1.55 eV (800 nm). Above the threshold energy, nonlinear multiphoton absorption sets in leading to a decrease in transmission with increasing pulse energy. The threshold energies are different for the two types of beams. In OAM beams, due to the presence of the null intensity region, higher pulse energies (photon density) are required to reach the threshold for the onset of nonlinear absorption (to maintain similar photon flux) in comparison to Gaussian for the same spot size.[31] However, the response regime we investigated remained the same, where the pulse energies were always varied from below the threshold for onset of nonlinear absorption to approximately twice the threshold value.

In contrast to Fig. 2(a), significant difference in absorbance of left- and right-helical light was observed, as shown in Fig. 2(b). This differential absorbance ($\Delta A \approx 0.04$) in S(−)-camphor represents the HD (Type I) signal that is an order of magnitude higher than conventional CD. The HD (Type I) signal is only non-zero for the displaced position of the singularity, i.e., asymmetric beams (Fig. 1), and vanishes for symmetric beams. The above curves in Fig. 2(b) are obtained for $\delta = 900$ nm position of singularity.

To discern the effect of the achiral solvent on the HD signal, we performed transmission measurements in a control sample (achiral solvent in black) and in enantiomeric solution (in red) under identical conditions, as shown in Fig. 3 for asymmetric linearly polarized helical light ($s = 0, l = -3$) for (a) chloroform and 0.5 g of R(+)-camphor diluted in 3.5 ml of chloroform and (b) water and 0.5 g of R(−)-alanine diluted in 3.5 ml of water.

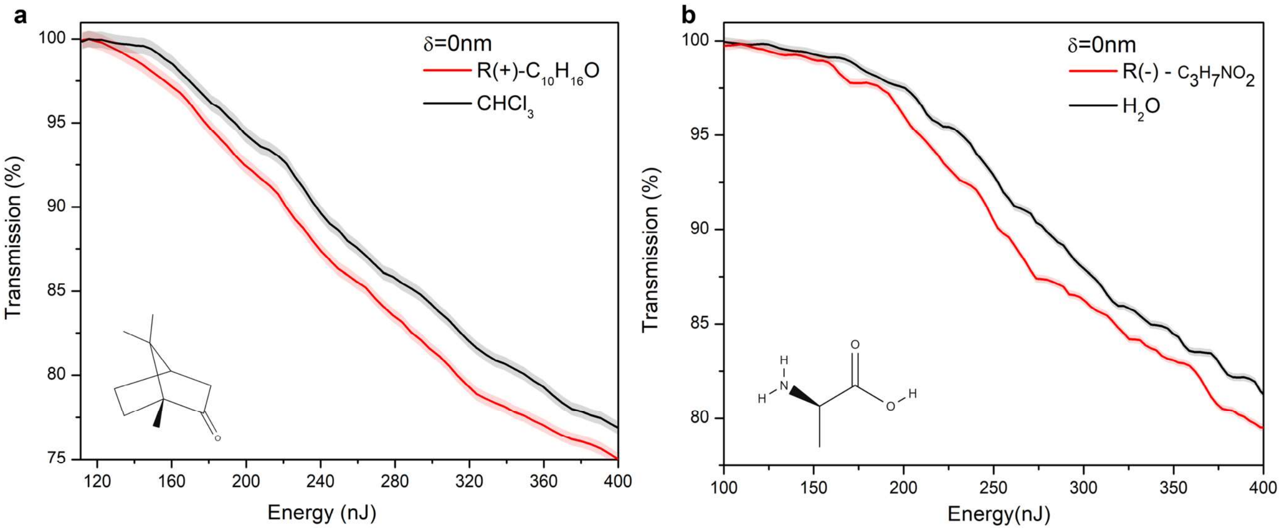

FIG. 3. Transmission curves of linearly polarized helical light ($l = -3$, $\delta = 0$) nm for (a) chloroform and 0.5 g of R(+)-camphor diluted in 3.5 ml of chloroform and (b) H_2O and 0.5 g of R(−)-alanine diluted in 3.5 ml of H_2O. The threshold dependence is independent of the singularity position. The error bands represent the standard error of multiple independent transmission measurements. These experimental results were reproduced multiple times under identical conditions.

Both plots show a lower onset of nonlinear absorption for chiral compounds relative to their respective achiral solvents. This behavior arises because multiphoton absorption depends on the ionization potential of a molecule, which is higher for achiral solvent. This signature property of the nonlinear multiphoton absorption makes it possible to differentiate the HD signal of chiral molecules with minimal interference from achiral molecules. This is crucial as achiral molecules also exhibit helical dichroism.[19] When the handedness of the helical light is changed the threshold energies remain the same. However, the amount of nonlinear absorption in chiral molecules as a function of pulse energy is slightly different, giving rise to differential absorption, HD (Type I).

Any chiroptical technique should be able to differentiate relatively low concentrations of enantiomeric solution as long as the solute's chiral center is maintained. Figure 4 shows HD (Type I) as a function of displacement of the phase singularity in the focal region in camphor and alanine at different concentrations. Figure 4(a) shows two concentration of R(+)-camphor (0.25 and 0.5 g) diluted in 3.5 ml of chloroform. For the lowest concentration, we also show results for S(−)-camphor to demonstrate the differences in the chiral signal between the enantiomers. In our case, the solubility of camphor is 1 g/ml; therefore, the concentrations (0.14 and 0.07 g/ml) in Fig. 4(a) are much below the solubility. The magnitude of the HD (Type I) signal increases with concentration up to ~0.3 g/ml (not shown) beyond which it decreased possibly due to increased solute–solvent interactions.[22]

HD (Type I) does not exist in a symmetric Laguerre–Gaussian beam as shown for zero displacement of the singularity ($\delta = 0$). Displacing the phase singularity leads to an asymmetric Laguerre–Gaussian beam [as depicted in Fig. 1 and described by Eq. (1)], resulting in differential absorption of left- and right-linearly polarized helical light. HD (Type I) increases with the displacement of the singularity, reaches a maximum at ≈1000 nm, and decreases with further displacement of the singularity. At extreme displacement of the singularity relative to the center of the focal region, the intensity profile of the OAM beam mimics a Gaussian beam. As a result, the HD (Type I) approaches the behavior of a Gaussian beam as shown in the transmission curves of Fig. 2(a).

Figure 4(b) shows HD (Type I) for S(+)- and R(−)-alanine, an amino acid dissolved in 3.5 ml of water (concentration of 0.14 g/ml). In contrast to Fig. 4(a) where the concentrations are an order of magnitude lower than the saturation value, Fig. 4(b) shows HD (Type I) for a concentration that is near the solubility of alanine 0.167 g/ml. While HD (Type I) exists, there are higher fluctuations in the signal for negative vs positive displacement of singularity between the two enantiomers in comparison to camphor [Fig. 4(a)]. This fluctuation can be attributed to the higher solute concentration (84% reference to solubility) in Fig. 4(b). In comparison, fluctuations are minimal at lower concentrations of 14% and 7% with respect to solubility as seen in Fig. 4(a). Fluctuations at higher concentrations could be due to intense laser-induced nucleation in saturated solutions and nonlinear propagation effects.

In addition, amino acid in an aqueous solution can exist as zwitterion forms. The concentration of zwitterion forms is dependent on the pH value of the enantiomeric solution. The change in pH between enantiomers can introduce spectroscopic differences in the chiroptical response. In our experiments, the measured pH value of R(−)-alanine [S(+)-alanine] solution is 5.80 ± 0.01[5.85 ± 0.01] with water solvent [pH 5.36 ± 0.01]. However, such small difference in pH value does not affect the HD signal. In addition, the presence of HD in non-zwitterion solution of camphor and enantiopure liquids[19] suggests that zwitterion forms of alanine do not play a major role.

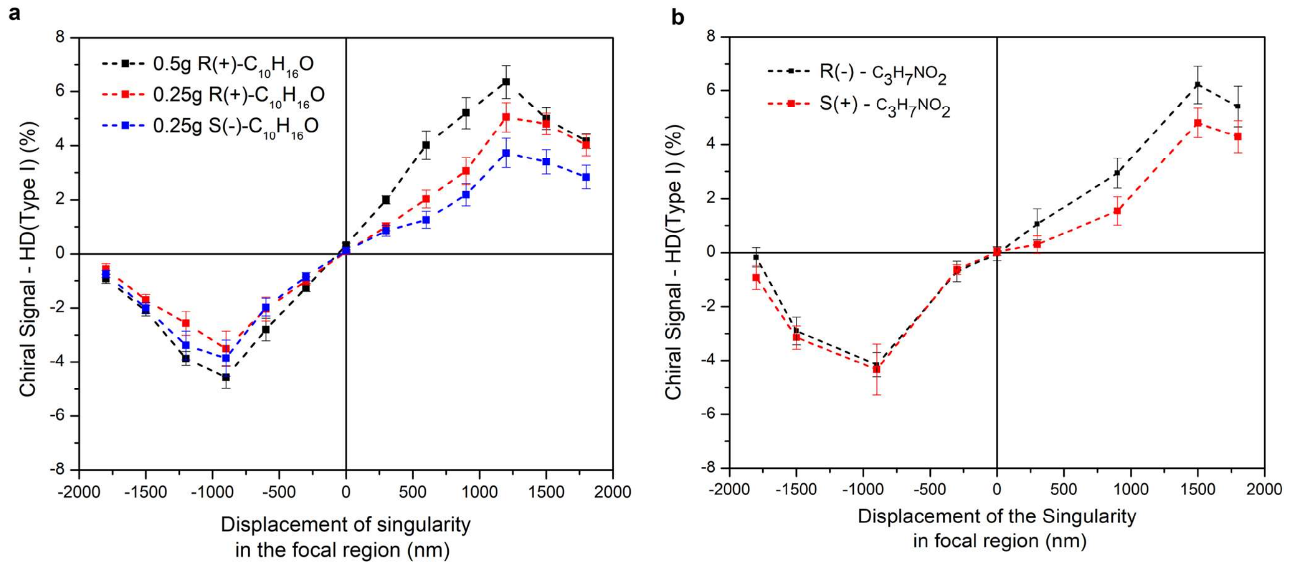

FIG. 4. Helical dichroism (Type I) of linearly polarized left- and right-helical light ($l = \pm 3$) as a function of displacement of the singularity in the focal region. (a) Camphor diluted in 3.5 ml of chloroform. Black curve represents 0.5 g of R(+)-camphor, and the red and blue curves represent 0.25 g of R(+)-camphor and S(−)-camphor. (b) 0.5 g of left- and right-handed alanine diluted in 3.5 ml of water. The dashed lines connecting the discrete experimental points are for visualization only. The error bars represent the standard error over the average energy range starting from the onset of nonlinear absorption to about two times the threshold value.

The helicity dependent differential absorption was described in terms of energy absorbed from the fields at an average rate as shown in the following [Eq. (3)].[19,32] This energy absorbed is proportional to absorption transition rates based on perturbation theory for single photon absorption[19,33] and extended to the multiphoton case,[19]

$$\Gamma_{\delta}^{\pm} = \frac{\omega}{2}\left\{\underbrace{\alpha''|\tilde{E}_{\delta}^{\pm}|^{2}}_{\text{E1E1}} + \underbrace{\chi''|\tilde{B}_{\delta}^{\pm}|^{2}}_{\text{M1M1}} + \underbrace{\rho G' \operatorname{Im}\left[\left(\tilde{E}_{\delta}^{\pm}\right)^{*}\cdot\tilde{B}_{\delta}^{\pm}\right]}_{\text{E1M1}} + \underbrace{\frac{2}{3}\rho A'' \operatorname{Re}\left[\left(\tilde{E}_{\delta}^{\pm}\right)^{*}\cdot\nabla\tilde{E}_{\delta}^{\pm}\right]}_{\text{E1E2}}\right\}, \quad (3)$$

where ω is the frequency of incident light, E and B are incident electric and magnetic fields, α'' represents the electric polarizability, χ'' is the magnetic susceptibility, G' represents the isotropic mixed electric–magnetic dipole polarizability, A'' is the mixed electric dipole–electric quadrupole polarizability, and ρ is the orientation-dependent weighting factor for anisotropic averaging. δ is the asymmetrical parameter, $\delta = 0$ for a symmetric LG beam and $\delta \neq 0$ for an asymmetric LG beam. The sign in $\Gamma^{\pm}$ represents the sign of OAM. E1 and M1 are electric and magnetic dipole, respectively, and E2 is the electric quadrupole. The coupling terms E1M1 and E1E2 are pseudoscalars and change sign under improper rotation.

HD (Type I) = $\Gamma(+l, s) - \Gamma(-l, s)$, defined as differential absorption between right- and left-helical light having identical polarization. The electric–magnetic dipole term (E1M1), responsible for conventional CD, vanishes because we take the difference between left- and right-helical beams for the same polarization. For symmetric LG beams, the E1E2 coupling term also vanishes due to isotropic averaging of random oriented molecules. The finite HD signal in chiral molecules arises from multipole coupling terms only in the case of asymmetric LG beams. The electric–magnetic dipole term (E1M1), responsible for conventional CD, also vanishes because we take the difference between left- and right-helical beams for the same polarization. The only non-zero contribution to the HD (Type I) signal arises from the electric dipole–quadrupole coupling (E1E2). This term survives isotropic averaging due to the preferential alignment of randomly orientated molecules along the light polarization as a consequence of dipole forces. Such alignment is dependent on the gradient of the light intensity. In our experiments, the laser intensity ranged from 8×10^{12} to 3×10^{13} W/cm^2. At these intensities, the nonlinear absorption regime is dominated by both multiphoton and multiphoton assisted tunneling since the Keldysh parameter[34] ~1.5. In both regimes, the contribution to HD comes from the induced electric dipole and quadrupole moments. In the case of elliptically polarized light, E1M1 term is non-zero and therefore can contribute to the HD signal along with the E1E2 term.

The HD (Type I) chiral signal for R/S enantiomers (Fig. 4) does not mirror each other. In contrast, all polarization based chiroptical techniques, such as CD and PECD, display mirroring behavior i.e., equal magnitude but opposite in sign. In CD, mirroring behavior arises due to the E1M1 coupling term, whereas in PECD, it arises from change in the sign of the photoelectron angular distribution (b_1 coefficient). The HD signal was obtained for the same polarization but opposite helicities; therefore, polarization dependent E1M1 does not contribute. HD arises due to the coupling E1E2 term, which is dependent on the phase (l value) of the beam. Therefore, HD does not exhibit the same symmetry properties as those arising from the polarization effects.

Figure 4(b) also exhibits a small difference in magnitude of HD (Type I) between the two enantiomers with respect to the displacement of singularity. This can be understood in terms of a slight energy difference between the ground states of the enantiomers due to an asymmetry in the molecular potential, resulting in symmetric (s) and antisymmetric (as) wavefunctions for the two enantiomers.[35] As a result, the enantiomeric transitions rates can be shown as (see the Appendix)

$$R^{S/R}_{m(as/s)} = \frac{\pi}{3\hbar^2}[\mathscr{D} \mp \mathscr{C}]\,\mathrm{Re}\big[E^*_\alpha \nabla_\alpha E_\beta\big]\rho\big(\omega_{m(as/s)} - \omega\big), \qquad (4)$$

where $R^{S/R}_{m(as/s)}$ is the single photon transition rate (initial to final state m) for S- and R-enantiomer, which is proportional to the energy absorbed ($\Gamma^{\pm}_{\delta}$) shown in Eq. (3). The $\mathscr{C}$ and $\mathscr{D}$ terms represent the mixed electric dipole–quadrupole response tensors (transitions moments) coupled with the electric field gradient dependence of the beam. The above equation represents the E1E2 coupling term of Eq. (3) expanded in case of enantiomer pairs. This expression shows that the transition rate for the R-enantiomer is of the form $\mathscr{D} + \mathscr{C}$ and for the S-enantiomer is of the form $\mathscr{D} - \mathscr{C}$, where $\mathscr{D}$ is bigger than $\mathscr{C}$ (see the Appendix for further details). Therefore, the above transition rates for enantiomers give rise to the difference in the magnitude of the HD signal. The analysis presented in the Appendix is only qualitative. A quantitative analysis of the HD magnitude further requires information about molecular response tensors and wavefunctions.

The key result of Fig. 4 is the tunability of the HD (Type I) signal with the displacement of the singularity. This is the inherent advantage of our technique in comparison to the conventional CD techniques that lack any sort of tunability. In addition, our technique is non-resonant, allowing measurements to be made at a single wavelength of light. In contrast conventional CD is a resonant process often requiring a tunable light source.

Another observable is HD (Type II: $\pm l; \pm s$) = $2\,\frac{R(\pm l;\pm s) - S(\pm l;\pm s)}{R(\pm l;\pm s) + S(\pm l;\pm s)}$ defined as differential absorption between the two enantiomers for a specific helicity and polarization. It is a material-dominated property arising due to collective contributions from both E1M1 and E1E2 coupling terms in the case of asymmetric LG beams. For symmetric LG beams, the E1E2 term isotropically averages out to zero, but the E1M1 term is non-zero and can contribute toward the HD signal.

Figure 5 shows HD (Type II) signal for (a) camphor and (b) alanine as a function of incident laser energy (nJ). The chiral signal in both compounds is for different handedness values of an asymmetric Laguerre–Gaussian beam ($l = \pm 3$). For both chiral compounds, the position of the phase singularity was 900 nm, and the concentration was 0.14 g/ml in their respective achiral solvents, chloroform and water. In both cases, after the onset of nonlinear absorption, the relative magnitude of HD (Type II) for different helicities increases with pulse energy and reaches a maximum of ≈4%. For comparison, we show the chiral signal for circularly polarized Gaussian beam (dashed-dotted line) with a relative magnitude of ~1%, mostly overlapped within the statistical error bands. The HD (Type II) signal is of opposite sign for S(−)- and R(+)-camphor

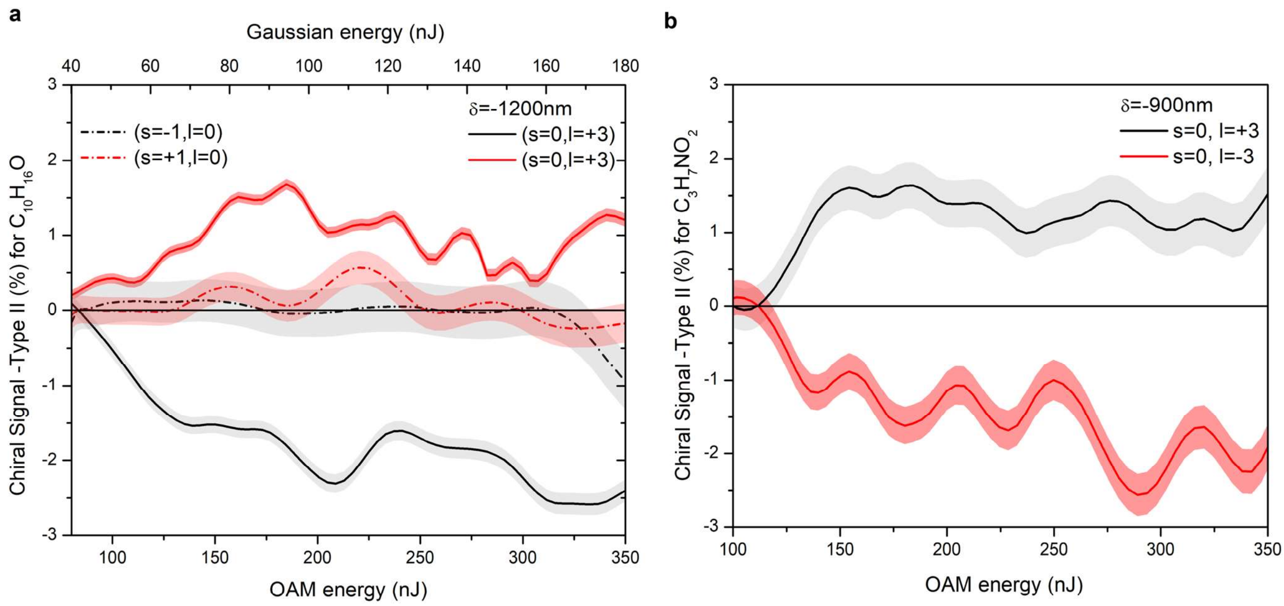

FIG. 5. (a) Chiral signal (Type II) for 0.5 g of camphor diluted in 3.5 ml of chloroform. Dashed-dotted lines are the chiral signal for the circularly polarized Gaussian ($l = 0$), and solid lines are for the linearly polarized helical light ($l = \pm 3$, $\delta = -1200$ nm) as a function of energy. (b) HD (Type II) for 0.5 g of alanine dissolved in 3.5 ml of water as a function of average energy of linearly polarized helical light ($l = \pm 3$, $\delta = -900$ nm). The error bands represent the propagation error of the chiral signal for three independent measurements (sample size). These experimental results were reproduced multiple times under identical conditions.

and S(+)- and R(−)-alanine because they rotate plane polarized light in opposite direction. The HD (Type II) signal is not influenced by the displacement of singularity although it is more stable at higher displacements.

CONCLUSION

Helical dichroism is a non-resonant, nonlinear chiroptical technique that is not limited to enantiopure samples but can also be extended to enantiomeric solutions. The differential absorbance between left- and right-handed helical light reached a high of 5% for 0.14 g/ml of camphor and alanine in achiral solvents. Despite the influence of concentration on the chiral signal, the observed signal efficiency is higher than ECD by an order of magnitude and VCD by a few orders of magnitude. Moreover, ECD and VCD are resonant linear optical techniques and therefore require a tunable light source for measurement. In contrast, HD measurements can be performed at fixed wavelengths by exploiting the nonlinear properties of the material. Other nonlinear chiroptical techniques, such as PECD, has efficiencies comparable to HD. However, PECD is primarily a gas-phase technique but has been recently extended to liquid micro-jets.[18] The ability of HD to differentiate enantiomeric solution adds an additional benefit for bio-relevant molecules, which are often in the powder form. This opens new opportunities to study bio-relevant molecules with helical light. HD (Type I) can also be tuned by displacing the phase singularity, an advantage over other chiroptical techniques that employ circularly polarized light as their chiral reagent. Finally, we have shown that chiral efficiencies for enantiomeric solutions can be enhanced by using an alternative chiroptical reagent that exploits the non-dipole regime.

ACKNOWLEDGMENTS

We thank Felix Hufnagel and Dr. Ebrahim Karimi for fabricating the q-plate used in the experiments. We also thank Dr. Thomas Brabec for valuable theoretical insight into the chiral light–matter interaction.

AUTHOR DECLARATIONS

Conflict of Interest

The authors have no conflicts to disclose.

Author Contributions

A.J. and J.-L.B. contributed equally to this work.

A.J., J.-L.B., and R.B. conceived, designed, and planned the experiments. A.J. and J.-L.B. conducted the experiments and analyzed the results. A.J., J.-L.B., and R.B. worked on the theory. All authors prepared the manuscript.

Ashish Jain: Conceptualization (equal); Data curation (equal); Formal analysis (equal); Investigation (equal); Methodology (equal); Project administration (equal); Validation (equal); Visualization (equal); Writing – original draft (equal); Writing – review & editing (equal). **Jean-Luc Bégin**: Conceptualization (equal); Data curation (equal); Formal analysis (equal); Investigation (equal); Methodology (equal); Project administration (equal); Validation (equal); Visualization (equal); Writing – original draft (equal); Writing – review & editing (equal). **Ravi Bhardwaj**: Conceptualization (equal); Formal analysis (equal); Funding acquisition (equal); Project administration (equal); Resources (equal); Supervision (equal); Validation (equal); Visualization (equal); Writing – original draft (equal); Writing – review & editing (equal).

DATA AVAILABILITY

The data that support the findings of this study are available from the corresponding author upon reasonable request.

APPENDIX: RATE OF ABSORPTION IN CASE OF ENANTIOMERS

The difference in the magnitude of HD (Type I) between the two enantiomers can be qualitatively understood in terms of parity violation arguments. The lack of the "perfect" symmetry state in enantiomers leads to a slight energy difference $\Delta_{pv}E$ between the ground states of the enantiomers, $(\Delta_{\mathrm{pv}}E = E_R^g - E_S^g)$.[35] This type of broken symmetry condition is often referred to as *de lege* ("*lawlike*").[35]

For single photon absorption transition rate, the Fermi's golden rule can be written as[36]

$$R_{m(s/as)} = \frac{2\pi}{\hbar^2}\left|\langle\Psi_m|V|\Psi^g_{s/as}\rangle\right|^2\delta\left(\omega_{m(s/as)} - \omega\right), \tag{A1}$$

where $\Psi^g_{s/as}$ represents the symmetric/antisymmetric ground state of the enantiomer pair. We assign the symmetrical ground state Ψ_s to the R-enantiomer and the antisymmetrical Ψ_{as} to the S enantiomer. This can be justified as the consequence of the slight asymmetry in the molecular potential, leading to eigenfunctions either symmetrical $\Psi^g_s = \frac{1}{\sqrt{2}}\left(\psi^g_+ + \psi^g_-\right)$ or antisymmetrical $\Psi^g_{as} = \frac{1}{\sqrt{2}}\left(\psi^g_+ - \psi^g_-\right)$, where Ψ_+ (Ψ_-) is even (odd) under parity. Therefore, the enantiomer pair is localized in opposite ground states; if R is even, then S is odd or vice versa. The excited states for both enantiomers are assumed to be a mixed party state given as $\Psi_m = \frac{1}{\sqrt{2}}(\psi_+ + i\beta\psi_\_)$, where $i\beta$ is a small phase lag factor between even and odd states.[37,38]

The single photon transition rate is proportional to the absorption cross section,[36] which is, in turn, proportional to the time averaged energy absorption [$\Gamma^{\pm}_{\delta}$ in Eq. (3)]. Since the HD (Type I) is defined as the difference between handedness of helical light for identical polarization, the E1M1 coupling term cancels out; therefore, the magnetic dipole term is neglected, leaving only the electric dipole and quadrupole terms in the interaction Hamiltonian, $V = -\mu_\alpha E_\alpha - \frac{1}{3}\theta_{\alpha\beta}\nabla_\alpha E_\beta$. Substituting above expression in (A1), we get

$$\begin{aligned} R^{R,S}_{m(s/as)} = \frac{2\pi}{\hbar^2}\big|\langle\Psi_m| \pm \mu_\alpha E_\alpha \\ + \frac{1}{3}\theta_{\alpha\beta}\nabla_\alpha E_\beta|\Psi^g_{s/as}\rangle\big|^2\delta\left(\omega_{m(s/as)} - \omega\right), \end{aligned} \tag{A2}$$

$$R^{R,S}_{m(s/as)} = \frac{2\pi}{\hbar^2}\left|\langle \Psi_m| \pm \mu_\alpha E_\alpha + \frac{1}{3}\theta_{\alpha\beta}\nabla_\alpha E_\beta |\Psi^g_{s/as}\rangle\right| \times \left|\langle \Psi^g_{s/as}| \pm \mu_\alpha E^*_\alpha + \frac{1}{3}\theta_{\alpha\beta}\nabla_\alpha E^*_\beta |\Psi_m\rangle\right| \delta\big(\omega_{m(s/as)} - \omega\big), \tag{A3}$$

where corresponding fields are complex quantities in the lab frame and multipole moments (dipole μ and quadrupole θ) are real quantities in the molecular frame,[6,39] which is considered in writing the above expression. The sign ± in the equation defines the direction of the intrinsic dipole, which is opposite for each enantiomer.[40]

The above expression was evaluated using the following properties: (i) $\left(E^*_\alpha \nabla_\alpha E_\beta + E_\alpha \nabla_\alpha E^*_\beta\right) = 2\,\mathrm{Re}\left[E^*_\alpha \nabla_\alpha E_\beta\right]$; (ii) symmetry property of an inner product, i.e., $\int \psi^*_\pm \boldsymbol{\mu} \psi_\pm d^3r = 0$, $\int \psi^*_\pm \boldsymbol{\theta} \psi_\mp d^3r = 0$ since μ is odd and θ is even under parity conversion; (iii) neglecting the β^2 term since it is small, and (iv) replacing the delta function by a lineshape function (ρ) to represent a physical system.

For the R-enantiomer,

$$\begin{aligned} R^R_{ms} = \frac{\pi}{3\hbar^2}\Big(& i\beta\left[\langle\psi_+|\mu_\alpha \ldots \theta_{\alpha\beta}|\psi_-\rangle - \langle\psi_-|\mu_\alpha \ldots \theta_{\alpha\beta}|\psi_+\rangle\right] \\ & \times \mathrm{Re}\left[E^*_\alpha \nabla_\alpha E_\beta\right] + \frac{1}{2}\Big[\langle\psi_+|\theta_{\alpha\beta}|\psi^g_+\rangle\langle\psi^g_-|\mu_\alpha|\psi_+\rangle \\ & \times \left[E^*_\alpha \nabla_\alpha E_\beta\right] + \langle\psi_+|\mu_\alpha|\psi^g_-\rangle\langle\psi^g_+|\theta_{\alpha\beta}|\psi_+\rangle\left[E_\alpha \nabla_\alpha E^*_\beta\right]\Big]\Big) \\ & \times \rho(\omega_{ms} - \omega). \end{aligned} \tag{A4}$$

The last two terms in the above expression contain inner products that are complex conjugate of each other. Since the multipole moments are real quantities, we can therefore write $\langle\psi_+|\theta_{\alpha\beta}|\psi^g_+\rangle\langle\psi^g_-|\mu_\alpha|\psi_+\rangle\left[E^*_\alpha \nabla_\alpha E_\beta\right] + \langle\psi_+|\mu_\alpha|\psi^g_-\rangle\langle\psi^g_+|\theta_{\alpha\beta}|\psi_+\rangle\left[E_\alpha \nabla_\alpha E^*_\beta\right] = 2\langle\psi_+|\theta_{\alpha\beta}|\psi^g_+\rangle\langle\psi^g_-|\mu_\alpha|\psi_+\rangle\,\mathrm{Re}\left[E_\alpha \nabla_\alpha E^*_\beta\right]$.

Therefore, we get

$$R^R_{ms} = \frac{\pi}{3\hbar^2}\Bigg[\underbrace{i\beta\left[\langle\psi_+|\mu_\alpha \ldots \theta_{\alpha\beta}|\psi_-\rangle - \langle\psi_-|\mu_\alpha \ldots \theta_{\alpha\beta}|\psi_+\rangle\right]}_{\mathscr{C}} + \underbrace{\langle\psi_+|\theta_{\alpha\beta}|\psi^g_+\rangle\langle\psi^g_-|\mu_\alpha|\psi_+\rangle}_{\mathscr{D}}\Bigg]\mathrm{Re}\left[E^*_\alpha \nabla_\alpha E_\beta\right]\rho(\omega_{ms} - \omega) \tag{A5}$$

for the S-enantiomer,

$$\begin{aligned} R^S_{m(as)} = \frac{\pi}{3\hbar^2}\Big(& -i\beta\left[\langle\psi_+|\mu_\alpha \ldots \theta_{\alpha\beta}|\psi_-\rangle - \langle\psi_-|\mu_\alpha \ldots \theta_{\alpha\beta}|\psi_+\rangle\right] \\ & \times \mathrm{Re}\left[E^*_\alpha \nabla_\alpha E_\beta\right] + \frac{1}{2}\Big[\langle\psi_+|\theta_{\alpha\beta}|\psi^g_+\rangle\langle\psi^g_-|\mu_\alpha|\psi_+\rangle \\ & \times \left[E^*_\alpha \nabla_\alpha E_\beta\right] + \langle\psi_+|\mu_\alpha|\psi^g_-\rangle\langle\psi^g_+|\theta_{\alpha\beta}|\psi_+\rangle\left[E_\alpha \nabla_\alpha E^*_\beta\right]\Big]\Big) \\ & \times \rho\big(\omega_{m(as)} - \omega\big). \end{aligned} \tag{A6}$$

Solving further for the last term as above, we get

$$R^S_{m(as)} = \frac{\pi}{3\hbar^2}\Bigg[\underbrace{-i\beta\left[\langle\psi_+|\mu_\alpha \ldots \theta_{\alpha\beta}|\psi_-\rangle - \langle\psi_-|\mu_\alpha \ldots \theta_{\alpha\beta}|\psi_+\rangle\right]}_{\mathscr{C}} + \underbrace{\langle\psi_+|\theta_{\alpha\beta}|\psi^g_+\rangle\langle\psi^g_-|\mu_\alpha|\psi_+\rangle}_{\mathscr{D}}\Bigg]\mathrm{Re}\left[E^*_\alpha \nabla_\alpha E_\beta\right]\rho\big(\omega_{m(as)} - \omega\big), \tag{A7}$$

where the terms $\langle\psi_-|\mu_\alpha \ldots \theta_{\alpha\beta}|\psi_+\rangle\,\mathrm{Re}\left[E^*_\alpha \nabla_\alpha E_\beta\right] = \frac{1}{2}\langle\psi_-|\mu_\alpha|\psi^g_+\rangle\langle\psi^g_+|\theta_{\alpha\beta}|\psi_+\rangle\left[E^*_\alpha \nabla_\alpha E_\beta\right] + \frac{1}{2}\langle\psi_-|\theta_{\alpha\beta}|\psi^g_-\rangle\langle\psi^g_-|\mu_\alpha|\psi_+\rangle\left[E_\alpha \nabla_\alpha E^*_\beta\right]$ are written using rotational average over symmetric and antisymmetric parity states. In addition, due to the presence of i in the expression, only the imaginary part of $(\mu_\alpha \theta_{\alpha\beta})$ mixed tensor contributes to the transition rate.

Hence, the transition rate for the R-enantiomer is of the form $\mathscr{D} + \mathscr{C}$ and for the S-enantiomer is of the form $\mathscr{D} - \mathscr{C}$, where $\mathscr{D}$ is bigger than $\mathscr{C}$ since the phase lag factor β is small.[37] This difference in the transition rates for the R- and S-enantiomers leads to the observed difference in the magnitude of HD (Type I) as shown in Fig. 4.

REFERENCES

[1] I. Warnke and F. Furche, "Circular dichroism: Electronic," Wiley Interdiscip. Rev.: Comput. Mol. Sci. **2**, 150 (2011).

[2] A. Cotton, C. R. Acad. Sci. **120**, 989 (1895).

[3] P. J. Stephens, "Theory of vibrational circular dichroism," J. Phys. Chem. **89**, 748 (1985).

[4] J. Neugebauer, "Induced chirality in achiral media—How theory unravels mysterious solvent effects," Angew. Chem., Int. Ed. **46**, 7738 (2007).

[5] W. Moffitt, "Optical rotatory dispersion of helical polymers," J. Chem. Phys. **25**, 467 (1956).

[6] L. Barron, *Molecular Light Scattering and Optical Activity* (Cambridge University Press, 2004), Vol. 1.

[7] E. A. Power, "Two-photon circular dichroism," J. Chem. Phys. **63**, 1348 (1975).

[8] T. Verbiest, M. Kauranen, A. Persoons, M. Ikonen, J. Kurkela, and H. Lemmetyinen, "Nonlinear optical activity and biomolecular chirality," J. Am. Chem. Soc. **116**, 9203 (1994).

[9] A. F. Ordonez and O. Smirnova, "Generalized perspective on chiral measurements without magnetic interactions," Phys. Rev. A **98**, 063428 (2018).

[10] D. Ayuso, A. F. Ordonez, and O. Smirnova, "Ultrafast chirality: The road to efficient chiral measurements," Phys. Chem. Chem. Phys. **24**, 26962 (2022).

[11] K. J. Chau, "Investigation of the chiral origins of electromagnetic activity," Opt. Lett. **35**, 1187–1189 (2010).

[12] H. Sato, "A new horizon for vibrational circular dichroism spectroscopy: A challenge for supramolecular chirality," Phys. Chem. Chem. Phys. **22**, 7671 (2020).

[13] R. D. Peacock and B. Stewart, "Natural circular dichroism in X-ray spectroscopy," J. Phys. Chem. **105**, 351 (2001).

[14] J.-L. Bégin, M. Alsaawy, and R. Bhardwaj, "Chiral discrimination by recollision enhanced femtosecond laser mass spectrometry," Sci. Rep. **10**, 14074 (2020).

[15] I. Powis, "Photoelectron circular dichroism of the randomly oriented chiral molecules glyceraldehyde and lactic acid," J. Chem. Phys. **112**, 301 (2000).

[16] M. H. M. Janssen and I. Powis, "Detecting chirality in molecules by imaging photoelectron circular dichroism," Phys. Chem. Chem. Phys. **16**, 856 (2014).

[17] C. Lux *et al.*, "Circular dichroism in the photoelectron angular distributions of camphor and fenchone from multiphoton ionization with femtosecond laser pulses," Angew. Chem., Int. Ed. **51**, 5001 (2012).

[18] M. N. Pohl *et al.*, "Photoelectron circular dichroism in angle-resolved photoemission from liquid fenchone," Phys. Chem. Chem. Phys. **24**, 8081 (2022).

[19] J.-L. Bégin, A. Jain, A. Parks *et al.*, "Nonlinear helical dichroism in chiral and achiral molecules," Nat. Photonics **17**, 82 (2023).

[20] L. Allen, M. W. Beijersbergen, R. J. C. Spreeuw, and J. P. Woerdman, "Orbital angular momentum of light and the transformation of Laguerre-Gaussian laser modes," Phys. Rev. A **45**, 8185 (1992).

[21] V. Vaquero *et al.*, "Alanine water complexes," J. Phys. Chem. A **118**, 2584 (2014).

[22] G. Gottarelli, M. A. Osipov, G. P. Spada, O. Bodley, and M. Simpson, "A study of solvent effect on the optical rotation of chiral biaryls," J. Phys. Chem. **95**, 3879 (1991).

[23] U. J. Meierhenrich, J.-J. Filippi, C. Meinert, J. H. Bredehöft, J.-i. Takahashi, L. Nahon, N. C. Jones, and S. V. Hoffmann, "Circular dichroism of amino acids in the vacuum-ultraviolet region," Angew. Chem., Int. Ed. **49**, 7799 (2010).

[24] G. Longhi, S. Abbate, R. Gangemi, E. Giorgio, and C. Rosini, "Fenchone, camphor, 2-methylenefenchone and 2-methylenecamphor: A vibrational circular dichroism study," J. Phys. Chem. A **110**, 4958 (2006).

[25] B. Jansík, A. Rizzo, and H. Ågren, "Ab initio study of the two-photon circular dichroism in chiral natural amino acids," J. Phys. Chem. B **111**, 446 (2007).

[26] C. S. Lehmann, N. B. Ram, I. Powis, and M. H. M. Janssen, "Imaging photoelectron circular dichroism of chiral molecules by femtosecond multiphoton coincidence detection," J. Chem. Phys. **139**, 234307 (2013).

[27] M. G. Rahimian *et al.*, "Spatially controlled nano-structuring of silicon with femtosecond vortex pulses," Sci. Rep. **10**, 12643 (2020).

[28] L. Marrucci, C. Manzo, and D. Paparo, "Optical spin-to-orbital angular momentum conversion in inhomogeneous anisotropic media," Phys. Rev. Lett. **96**, 163905 (2006).

[29] E. Karimi, B. Piccirillo, E. Nagali, L. Marrucci, and E. Santamato, "Efficient generation and sorting of orbital angular momentum eigenmodes of light by thermally tuned q-plates," Appl. Phys. Lett. **94**, 231124 (2009).

[30] F. Cardano, E. Karimi, S. Slussarenko, L. Marrucci, C. de Lisio, and E. Santamato, "Polarization pattern of vector vortex beams generated by q-plates with different topological charges," Appl. Opt. **51**, C1–C6 (2012).

[31] R. N. Oosterbeek, S. Ashforth, O. Bodley, and M. C. Simpson, "Measuring the ablation threshold fluence in femtosecond laser micromachining with vortex and Bessel pulses," Opt. Express **26**, 34558 (2018).

[32] N. Yang and A. E. Cohen, "Local geometry of electromagnetic fields and its role in molecular multipole transitions," J. Phys. Chem. B **115**, 5304–5311 (2011).

[33] K. A. Forbes and D. L. Andrews, "Optical orbital angular momentum: Twisted light and chirality," Opt. Lett. **43**, 435–438 (2018).

[34] L. V. Keldysh, "Ionization in the field of a strong electromagnetic wave," Sov. Phys. JETP **20**, 1307 (1965).

[35] M. Quack, G. Seyfang, and G. Wichmann, "Perspectives on parity violation in chiral molecules: Theory, spectroscopic experiment and biomolecular homochirality," Chem. Sci. **13**, 10598 (2022).

[36] R. Boyd, *Nonlinear Optics*, 4th ed. (Academic Press, 2020).

[37] G. Wagnière, *On Chirality and the Universal Asymmetry: Reflections on Image and Mirror Image* (John Wiley and Sons, 2007), p. 1.

[38] H. B. Tran Tan, D. Xiao, and A. Derevianko, "Parity-mixed coupled-cluster formalism for computing parity-violating amplitudes," Phys. Rev. A **105**, 022803 (2022).

[39] D. P. Craig and T. Thirunamachandran, *Molecular Quantum Electrodynamics: An Introduction to Radiation Molecule Interactions* (Academic Press, Inc., 1984), Vol. 1.

[40] D. Patterson, M. Schnell, and J. M. Doyle, "Enantiomer-specific detection of chiral molecules via microwave spectroscopy," Nature **497**, 475 (2013).

References

[1] G. Gottarelli, M. A. Osipov, G. P. Spada, O. Bodley, and M. Simpson. A study of solvent effect on the optical rotation of chiral biaryls. *The Journal of Physical Chemistry*, 95:3879, 1991.

[2] Georges H. Wagnière. *On Chirality and the Universal Asymmetry: Reflections on Image and Mirror Image*. Wiley-VCH, 2007.

[3] H. B. Tran Tan, D. Xiao, and A. Derevianko. Parity-mixed coupled-cluster formalism for computing parity-violating amplitudes. *Phys. Rev. A*, 105:022803, 2022.

Chapter 5

Intrinsic dichroism in amorphous and crystalline solids with helical light

5.1 Introduction

Thus far, we have observed that both liquids and solutions exhibit differential absorption of left- and right-handed helical light, irrespective of their molecular symmetry. This observation naturally prompts the question: *Do solids with different symmetries also exhibit phase-based helical dichroism (HD)?*.

Probing solids with light presents unique challenges, as the analysis of their structure and symmetry is constrained by the fact that the wavelength of light is significantly longer than interatomic distances. Despite this limitation, light scattering techniques such as Raman spectroscopy can still provide valuable information on the symmetry and structure [1, 2]. In general, solids can be divided into crystalline solids (c-solids) and amorphous solids (a-solids). Crystalline solids can be further divided into chiral and achiral, depending upon their molecular symmetry. In c-solids, the periodic arrangement of atoms results in anisotropy, causing physical properties to depend on the crystal orientation. These orientation-dependent effects have been utilized to map crystal symmetry through nonlinear high-harmonic generation processes [3, 4]. To study the chirality of c-solids, conventional chiroptical techniques like optical rotation and circular dichroism (CD) can also be extended to solids. However, the dichroism signal in the solid-state CD is often masked by the inherent birefringence signal and macroscopic anisotropies in c-solids [5]. Consequently, advanced techniques such as scanning electron microscopy and single-crystal X-ray diffraction [6, 7] are frequently used to differentiate chiral crystals. While these advanced techniques can accurately determine chirality in c-solids, they are limited by the requirement for large, high-purity single crystals.

A-solids lack long-range order due to their disordered atomic arrangement. Consequently, their physical properties exhibit isotropy, meaning they remain uniform in all directions. The absence of translational and rotational symmetry in a-solids also results in the absence of circular dichroism. However, a-solids are uniquely characterized by the presence of short- and medium-range order, which can extend up to 20 Å[8, 9, 10] in the case of amorphous glass. This short-range order is crucial for the formation of delocalized extended energy states, such as valence and conduction bands, while long-range disorder leads to the creation of band tail states between these energy bands. The band tail states are usually the highest occupied and lowest energy states in a-solids. The schematic of these states is shown in Fig.2.5. In addition, defects, impurities, and dangling bonds give rise to localized states in the middle of the bandgap [11]. Investigating the short- and medium-range order in a-solids remains an active field of research [12], as it can give rise to phenomena typically associated with c-solids [11].

Similar to liquids, most light-based techniques for examining solids have relied on polarization as a probe, analyzing interactions predominantly through electric dipole transitions. These transitions are typically independent of the phase of the incident light. Theoretically, several recent studies based on parity-time (PT) symmetry have proposed the existence of phase-based dichroism effects, but only in an ordered medium, and do not predict their presence in a-solids [13, 14]. Thus, for a quantitative understanding of the phase-based effects in c-solids, a comprehensive model is required that takes into account interband transition dynamics and the spatial structure of the beams.

Moreover, if HD exists in a-solids, then identifying the correct transition mechanism is essential for such isotropic materials. The theoretical explanation in the case of isotropic liquids has been attributed to electric dipole-electric quadrupole (E1E2) transitions. These transitions average out to zero in randomly oriented chiral and achiral molecules. The presence of a finite dipole force and the resulting torque in asymmetric helical beams partially orients the molecules, leading to nonzero isotropic averaging. However, in solids, although the dipole force exists, the molecules are fixed in their spatial positions and cannot be rotated. Therefore, the multiphoton interaction model developed for molecules cannot be directly applied to solids.

5.2 Results

This work demonstrated the existence of *intrinsic dichroism in amorphous solids using helical light beams*. This was achieved by probing the nonlinear absorption of linearly polarized, asymmetric helical light beams propagating through the solids. Similar to the case of liquids, two types of helical dichroism were observed: 1) HD (Type I), defined as the differential absorption of left- and right-helical light, was observed in both amorphous and crystalline solids. HD (Type I) was modeled by considering inter-band electron transitions via multiphoton-assisted tunneling (MPAT). 2) HD (Type II), defined as the difference in absorptance between left- and right-handed chiral solids for a specific-handed helical light, was observed in chiral solids. This effect demonstrated efficient chiral recognition in probing chiral solids.

This research was published in *Nature Communications*(2024) journal, where the first authorship was shared with my colleague due to our equal contributions to the work. The published version of the article and the supplementary file are reproduced in this chapter, where the theoretical framework, experimental methods, figures, and references are self-contained. The following section presents the key results and advances.

5.3 Key advances

- Extended the phase-based spectroscopy from liquids to solids. These results demonstrated that solid-state matter is responsive to the helical phase structure of the incident light.
- This research challenged the conventional wisdom that dichroism does not exist in amorphous solids. The observation of dichroism in a-solids was attributed to the presence of short- to medium-range order.
- Crystal chirality was probed with enhanced efficiency using helical light. These results extended our research on chiral liquids into another phase of chiral matter.
- The bandgap dependence of HD can be explored as a potential tool for material profiling, offering a unique fingerprint for solid-state materials.

The following section reproduces the author contribution and equal contribution statement from the published article. The published version of the article and supplementary file are attached later.

5.4 Statement of contribution

These authors contributed equally: Ashish Jain and Jean-Luc Bégin.

This project was conceived and designed in collaboration with my colleague Jean-Luc Bégin and my supervisor, Professor Ravi Bhardwaj. It commenced together with the project of nonlinear helical dichroism in liquids (Chapter 3), where the nonlinear model developed for liquids was instrumental in extending the theoretical framework to solids. My colleague and I built the experimental setup and conducted calibration experiments to minimize background noise. Together, we conducted all the experiments and analyzed the experimental data. Additionally, we extended the nonlinear multiphoton-assisted tunneling (MPAT) model from gases to solids. Professor Thomas Brabec and my supervisor provided invaluable guidance and worked collaboratively on the theoretical framework. Numerical simulations were performed jointly with my colleague. The q-plates used to generate helical light beams were fabricated by our collaborator, Professor Ebrahim Karimi, and his PhD student Felix Hufnagel. Professors Paul Corkum, Ebrahim Karimi, and Ravi Bhardwaj supervised the project. I prepared the initial draft of the research manuscript with my colleague, Professor Thomas Brabec, and Professor Ravi Bhardwaj. All authors reviewed the manuscript.

nature communications

Article

https://doi.org/10.1038/s41467-024-45735-9

Intrinsic dichroism in amorphous and crystalline solids with helical light

Received: 8 September 2023

Accepted: 2 February 2024

Ashish Jain[1,2], **Jean-Luc Bégin**[1,2], **Paul Corkum**[1], **Ebrahim Karimi**[1], **Thomas Brabec**[1] & **Ravi Bhardwaj**[1]

Amorphous solids do not exhibit long-range order due to the disordered arrangement of atoms. They lack translational and rotational symmetry on a macroscopic scale and are therefore isotropic. As a result, differential absorption of polarized light, called dichroism, is not known to exist in amorphous solids. Using helical light beams that carry orbital angular momentum as a probe, we demonstrate that dichroism is intrinsic to both amorphous and crystalline solids. We show that in the nonlinear regime, helical dichroism is responsive to the short-range order and its origin is explained in terms of interband multiphoton assisted tunneling. We also demonstrate that the helical dichroism signal is sensitive to chirality and its strength can be controlled and tuned using a superposition of OAM and Gaussian beams. Our research challenges the conventional knowledge that dichroism does not exist in amorphous solids and enables to manipulate the optical properties of solids.

Light as a tool to probe the structure and symmetry of solids is limited due to the fact that the wavelengths of photons (UV–visible–IR) are significantly longer than the interatomic distances. In spite of this limitation, some degree of information on symmetry and phonon modes can be obtained from light scattering techniques such as Raman spectroscopy[1,2]. In crystalline solids (c-solids), periodic arrangement of atoms leads to long-range order that gives rise to anisotropy in which the physical properties depend on the crystal orientation. Such an anisotropy in absorption and emission of light via high harmonic generation has been exploited to map the crystal symmetry[3,4]. In chiral c-solids, material handedness (non-superimposable mirror images), in principle, leads to differential absorption of right- and left-circularly polarized light, known as circular dichroism (CD). However, the chiroptical signal is often influenced by linear birefringence and inherent macroscopic anisotropies present in c-solids[5]. As a result, sophisticated techniques such as single-crystal X-ray diffraction[6], scanning and transmission electron microscope-based methods[7] are often utilized to differentiate chiral crystals but are limited by the need for large single crystal of high purity.

In contrast, amorphous solids (a-solids) do not have long-range order due to random arrangement of atoms and are isotropic. A consequence of the lack of symmetry in a-solids is that they do not exhibit CD. However, a-solids are characterized by short- and medium-range order in which the spatial variation of parameters (such as interatomic distances and angles between neighboring atoms) provides average structural information and the degree to which the short and medium-range order is conserved[8,9]. Studying short- and medium-range order of a-solids is an active field of research[9,10] because it can lead to some phenomena that are typically observed in c-solids. With recent technological advances, it is now possible to directly observe the local atomic structure of disordered solids[11,12]. The presence of short- and medium-range order in a-solids is in fact responsible for delocalized energy valence and conduction band states, whereas the long-range disorder causes the formation of bond tail energy states between energy bands[13]. In amorphous glass, the short to medium-range order extends up to 20 Å[9,14–16].

Most optical techniques to study solids, to date, relied on using polarized Gaussian beams (carrying spin angular momentum $0, \pm 1\hbar$) with the interaction described using the dipole dominant molecular transitions. Such transitions are generally independent of the phase associated with the wavefront of the incident beam. However, light can also carry orbital angular momentum (OAM), $\pm l\hbar$, associated with

---

[1]Nexus for Quantum Technologies, Department of Physics, University of Ottawa, Ottawa, ON K1N 6N5, Canada. [2]These authors contributed equally: Ashish Jain, Jean-Luc Bégin. e-mail: ajain067@uottawa.ca; ravi.bhardwaj@uottawa.ca

dynamical rotation of wavefront structure. The handedness of these beams is characterized by the twisting of the wavefront undergoing l intertwined rotations in one wavelength[17–19]. The intensity profile of such light is characterized by a phase singularity (optical vortex) and hence a null intensity region at the center of the beam. These vortex beams are also referred as helical light beams[19–21] where the helicity is associated with the helical wavefront structure which is chiral in nature. This is analogous to the chiral structure of the electric field associated with circular polarized light.

The theoretical unboundedness of OAM value generated significant interest in using helical light beams as a chiral probe to study light-matter interaction. Early studies on differential absorption of helical light beams focused mostly on the linear absorption involving coupling of electric–magnetic dipole (E1M1) term, which was known to be responsible for CD. These studies were not successful in demonstrating the efficacy of using OAM as a chiral reagent. Recently, Helical Dichroism (HD), defined as differential absorption of left- and right-handed helical light, was demonstrated in nanoparticle aggregates[22], chiral metasurfaces[23], powdered molecular media[24], and achiral/chiral liquids in nonlinear regime[25]. Theoretically, several recent studies proposed the phased-based dichroism effect originates from the higher-order transition moments, which were shown to be non-vanishing only in the medium with some degree of orientational order[26,27]. Traditionally, the origin of such effects can be understood in terms of parity-time (PT) symmetry arguments. Electric dipole transition moment E1 has odd spatial parity, magnetic dipole moment M1 and electric quadrupole moment E2 have even parity. Hence, the E1M1 and E1E2 coupling terms represent a time-even space-odd pseudoscalars which changes sign on spatial inversion indicating a broken symmetry. However, symmetry arguments can only provide qualitative insight into the existence of dichroism in crystals and does not predict its presence in amorphous solids. Therefore, comprehensive models are required for quantitative understanding of the behavior of HD that takes into account the interband transition dynamics in matter and spatial structure of the helical light beams.

In this article, we first demonstrate existence of intrinsic HD in amorphous solids using asymmetrical helical light beams. Such an effect is typically not expected in amorphous materials due to the disorderly state of the medium. We define differential absorption of left- and right-helical light for the same material as HD (Type I). Therefore, it is a beam-dominated property and can also be observed in achiral and chiral crystalline solids. In case of amorphous and achiral solids, HD (Type I) is not considered as true chirality as it does not involve chiral light and chiral matter interaction. Second, our technique demonstrates higher efficiency in probing chiral solids compared to conventional solid-state-based optical techniques.This was achieved in terms of HD (Type II), defined as difference of absorption between the left- and right-handed chiral solid for a specific-handed helical light. It is a material-dominated property and its definition requires both the material and light to be chiral entities. Third, we show that helical dichroism is tunable and can be precisely controlled by (i) superposition of OAM and Gaussian beams (ii) varying the l-value, and (iii) displacement of phase singularity in the beam. These features combined with the bandgap dependence of HD set our technique apart from any other existing chiroptical methods. Finally, we model HD by considering electron transitions via multiphoton-assisted tunneling (MPAT). This process ensures that electron displacement remains within the short- to medium-range order in solids, allowing us to effectively probe intrinsic dichroism.

Results

We studied HD in both amorphous and crystalline solids by measuring the absorption of loosely focused femtosecond helical light pulses (Supplementary Section 1 for experimental setup). We produced helical light beams carrying OAM using a birefringent plate, called q-plate, in which the incident Gaussian beam acquires an OAM that is two times the topological charge, q[21,28]. To disentangle the effects of spin and orbital angular momentum on helical dichroism we used linearly polarized helical light beams. In addition, asymmetric helical light beams were produced by displacing the phase singularity in the OAM beam by translating the q-plate in a plane perpendicular to the incident beam. Additional experimental details are provided in “Methods” (“Differential absorption measurements”, “Generation of OAM beams”, and “Displacement of singularity”) and Supplementary (Sections 5–7).

Achiral crystalline solids

Helical dichroism, HD (Type I)=$A(+l,s)-A(-l,s)$, defined as differential absorption of linearly polarized ($s=0$) left- and right-helical light ($l=\pm3$) in the same material, is shown in Fig. 1a for a MgO achiral crystal as a function of the position of the singularity in the OAM beam. The inset shows normalized transmission of a single left- and right-handed helical light pulse as a function of peak laser fluence (Supplementary Section 4) when the singularity was displaced by 900 nm. Each curve in the inset is an average of three independent measurements, and the color band represents the statistical standard error. Differences in the transmission of the two helicities start to appear at a fluence of ~0.8 J/cm^2 from the onset of nonlinear absorption and persist over a broad range of peak laser fluences. For each position of the singularity, HD (Type I) was obtained by averaging transmission (shown in the inset) over a fluence range from the onset of nonlinear absorption to 5 J/cm^2.

Dichroism does not exist in achiral solids for a circularly polarized Gaussian beam and also for a linearly polarized symmetric OAM beam ($\delta=0\pm\Delta$ in Fig. 1a). However, when the singularity in the OAM beam is displaced from the center, the material exhibits helical dichroism. HD (Type I) signal increases with the displacement, reaches a maximum around ±1500 nm and displays a sinusoidal behavior with a change in sign as the singularity traverses the zero-position (Supplementary Section 7). This can be understood in terms of parity-time symmetry argument. HD (Type I) is odd under PT resulting in a change in sign with respect to the δ position. In the experiment, alignment of the singularity at the center of the OAM beam can only be defined before the objective, which translates to an uncertainty $\Delta\sim\pm100$ nm at the focus (see “Displacement of singularity” for calibration). HD (Type I) signal decreases at large displacement of singularity, as expected, since the intensity profile of asymmetric OAM beam starts to resemble a Gaussian beam.

Orientation-dependent nonlinear absorption of helical light pulses in MgO crystal is shown in Fig. 1b–d for three different displacements of the singularity as labeled in Fig. 1a. MgO (100) has a cubic unit cell with a fourfold rotational symmetry and therefore shows a modulation with a periodicity of $\pi/2$. For $\delta=0$, there is no difference in absorption of left- and right-handed helical light and the curves overlap (Fig. 1b). When the singularity is shifted to either side from the center of the beam, the dominance of absorption switches between the two helicities of light (Fig. 1c, d). The orientation-dependent transmission is invariant of the position of the singularity. However, the magnitude of HD (Type I) signal remains unaffected with crystal orientation but depends on the position of the singularity. Similar results were obtained for ZnO (11–20) and α-quartz (z-cut) (Supplementary Section 2). Orientation dependence in crystals can also be obtained with non-OAM beams[29] (Supplementary Section 2) and via high harmonic generation[3,4] in nonlinear regime. Extraction of crystal symmetry is due to the multiphoton nature of the interaction and direction dependence of the effective mass of the electron that acts as a local probe.[29].

Amorphous solids

In a-solids, dichroism and modulation in nonlinear absorption are not expected due to the absence of long-range order. However, Fig. 2a

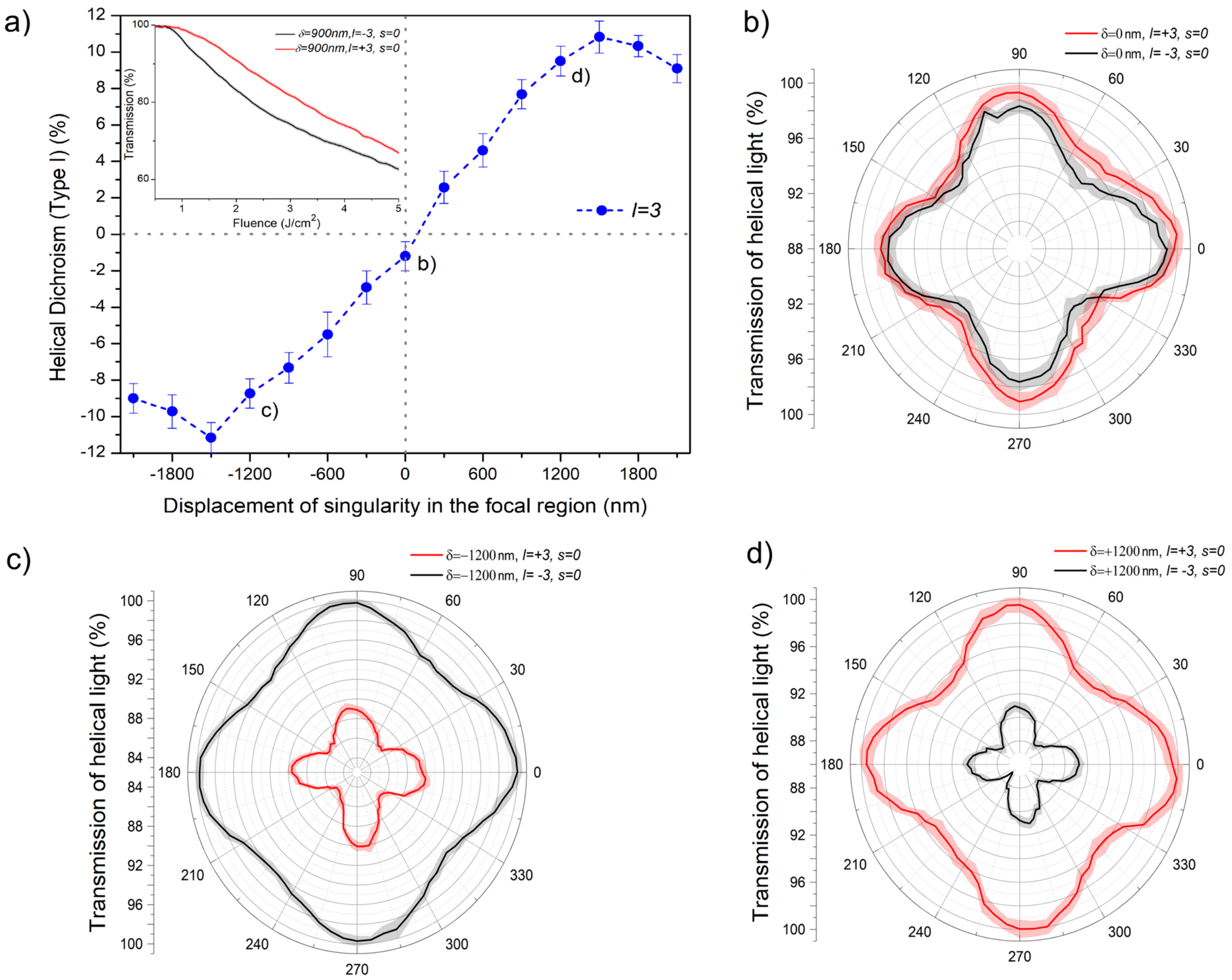

Fig. 1 | Helical dichroism and orientational dependent transmission of helical light in a crystal. a HD(Type I) = $A(+l, s) - A(-l, s)$ for crystalline MgO (100) as a function of the displacement of the singularity (δ) in linearly polarized ($\epsilon = 0.05$) asymmetrical OAM beam ($l = \pm 3$). Inset shows transmission of $l = \pm 3$ beam as a function of peak laser fluence for $\delta = 900$ nm. **b–d Orientation-dependant** transmission of $l = \pm 3$ in MgO at the position of displaced singularities marked in (**a**). The error bars in (**a**) represent the standard error, of multiple measurements ($n = 3$), calculated for an average fluence range used to obtain HD (see text for details). The error bands in (**b–d**) represent the standard error at every position of the crystal for $n = 20$ points.

shows that dichroism exits even in a-solids. For asymmetric helical beams, HD (Type I) in fused silica and borosilicate glass, plotted as a function of the displacement of the singularity, shows similar behavior as in c-solids (Fig. 1a). Figure 2b shows orientation-dependent transmission of helical light in fused silica (for $\delta = -1200$ nm), confirming the lack of symmetry since periodic modulation is absent at all positions of the singularity. However, nonlinear absorption of light with opposite helicities is different representing the HD (Type I) shown in Fig. 2a. The results of Figs. 1 and 2 suggest that helical dichroism is independent of the crystal orientation and is intrinsic to both materials. This is in contrast to conventional understanding that dichroism with circularly polarized light is absent in disordered solids (Supplementary Section 5).

Helical dichroism in liquids was recently shown to arise from coupling between the electric dipole and the electric quadrupole transition terms[25,30]. In disordered solids, this coupling term is expected to vanish upon isotropic averaging while it can survive in gas and liquid phases due to laser-induced dipole force. The presence of HD (Type I) in a-solids and its resemblance to c-solids, while displaying no symmetry in the orientation-dependent transmission due to the absence of long-range order, suggests that HD (Type I) can be attributed to short- to medium-range order. The origin of HD in solids can be understood in terms of electron transitions via Multiphoton-assisted tunneling (MPAT). The electron displacement during the MPAT serves as a local probe of the short- and medium-range order whereas the helicity dependence arises from higher-order multipoles.

In MPAT process, nonlinear absorption of the incident light is first initiated by multiphoton absorption which promotes an electron from the valence band to an intermediate excited state within the bandgap from which tunneling to conduction band takes place. In a-solids, such intermediate states are the so-called band tail states that extend into the bandgap. Long-range disorder leads to localized states near the bottom (top) of the conduction (valence) band and their density decreases exponentially away from the band edges. In addition, defects, impurities and dangling bonds give rise to localized states in the middle of the bandgap[13].

MPAT occurs at moderate intensities where the nonlinear absorption is not dominated by either ground-state tunneling or multiphoton transition alone. These two regimes are typically identified by Keldysh parameter[31] given by Eq. (3) (see “Electron displacement during interband transition” for details). Multiphoton (or tunneling) transition is dominant when the Keldysh parameter is larger than ~2 (or smaller than 1)[32–34]. In fused silica, the Keyldysh parameter corresponding to our experimental intensities used to obtain HD are in the range of ~1.1–2.5 where MPAT process is predominant resulting in strong-field induced interband excitation.

In ground-state tunneling, the electron that is promoted from valence to conduction band gains a spatial displacement ($\mathbf{x}_0$) that is proportional to the bandgap E_g and can be approximated by Eq. (2) ("Electron displacement during interband transition"). In MPAT process, E_g has to be replaced by the energy difference between the band tail state and conduction band edge. This leads to a smaller $\mathbf{x}_0$ compared to the upper limit set by tunneling from valence to conduction band, which is in the range of 6–18 Å for fused silica ($E_g \approx 9ev$[34,35]). In comparison, the short- to medium-range order in fused silica is <20 Å[9,14–16]. The total electron displacement which is a sum of the displacements during tunneling from the intermediate state to the conduction band and multiphoton absorption from valence to intermediate state, is within this range.

Therefore, in a-solids photons are absorbed in a quasi-ordered environment over distances defined by the short- to medium-range order. This results in nonzero isotropic averaging of molecular response tensor. The three-dimensional network of SiO_2 could still consist of periodic clusters each oriented in a different direction. However, these clusters of ordered molecules will absorb the incident light at varying degrees depending on the overlap between the laser polarization and their absorption transition moments[36]. Therefore, the total absorbed energy by these clusters give rise to a finite contribution towards interband transitions and a nonzero l-dependence (see "Origin of Helical dichroism in solids" for details). As a result, the behavior of HD (Type I) signal is the same in disordered and ordered solids. In c-solids, the ordered environment always ensures nonzero isotropic averaging where HD(Type I) arises from electric dipole electric quadrupole coupling term. Electron transitions via MPAT process can still play a role where the intermediate states could be due to degenerate exciton states, defects, impurities, and boundary effects[37–39].

Chiral crystalline solids

C-solids also exhibit chirality, typically studied using sophisticated diffraction and imaging techniques[6,7]. Conventional CD using Gaussian light (Supplementary Section 5) is inefficient as it is convoluted by competing signals from optical and material properties[5]. Using helical light we show in Fig. 3 that the handedness of a chiral solid can be probed. Figure 3a shows HD (Type I) signal in crystalline (z-cut) left-quartz (L) and right-quartz (R) for different positions of the singularity in OAM beam. The spatial variation of HD(Type I) is similar to other crystals and amorphous solids (Figs. 1a and 2a). A key difference is that with asymmetric OAM beam, the magnitude of helicity-dependent absorption in the two chiral structures is different. This difference suggests that chiral solids exhibit another type of dichroism, defined as HD (Type II: $\pm l; \pm s$) = $2\,\frac{R(\pm l;\pm s)-L(\pm l;\pm s)}{R(\pm l;\pm s)+L(\pm l;\pm s)}$. HD (Type II) is the difference in absorption of a specific-handed helical light in the left- and right-handed chiral solid. It represents a chiral light–chiral matter interaction and is odd under PT symmetry.

HD (Type II) signal, shown in Fig. 3b, as a function of peak laser fluence changes sign with the helicity of the incident light enabling to efficient differentiation the handedness of crystal structure. This chiral signal, obtained at a specific position of the singularity marked by the rectangle in Fig. 3a, is more prominent with asymmetric OAM beam and is weakly influenced by the position of the singularity within the OAM beam. Chiral signal using circularly polarized Gaussian beam (with $l = 0$, $s = \pm 1$) is also shown in Fig. 3b and demonstrates the signal fluctuations with lower average efficiency. The obtained chiral signal is an order of magnitude higher than the reported values from solid-state-based CD in complex chiral crystals[40,41] and is comparable to recently demonstrated hard X-ray-based HD in powdered molecular media[24].

Another representation of HD (Type II) is the orientation-dependent transmission in different-handed quartz for specific helicity shown in Fig. 3c, obtained when the singularity is at the positions marked by a solid rectangle in Fig. 3a. A modulation of $\pi/3$ shows the sixfold rotational symmetry for quartz (Supplementary Section 2). This shows that transmission for specific helicity and position of singularity is different for both chiral solids. Therefore, crystal structure and chirality can be probed simultaneously.

Bandgap dependence of helical dichroism

Figure 4 demonstrates HD (Type I) in materials with different bandgaps. Figure 4a, shows spatial variation of HD (Type I) as a function of displacement of the singularity, for TeO_2 (red, bandgap of 3 eV)[42], ZnO (cyan, 3.4 eV)[43], MgO (black, 7.7 eV)[44], fused silica (magenta, 9eV)[34,35], and quartz (blue, 9.5 eV)[45]. The different magnitudes of HD(Type I) suggest it is a material-dependent property and HD signal increases with the bandgap. This material dependence can also be observed in

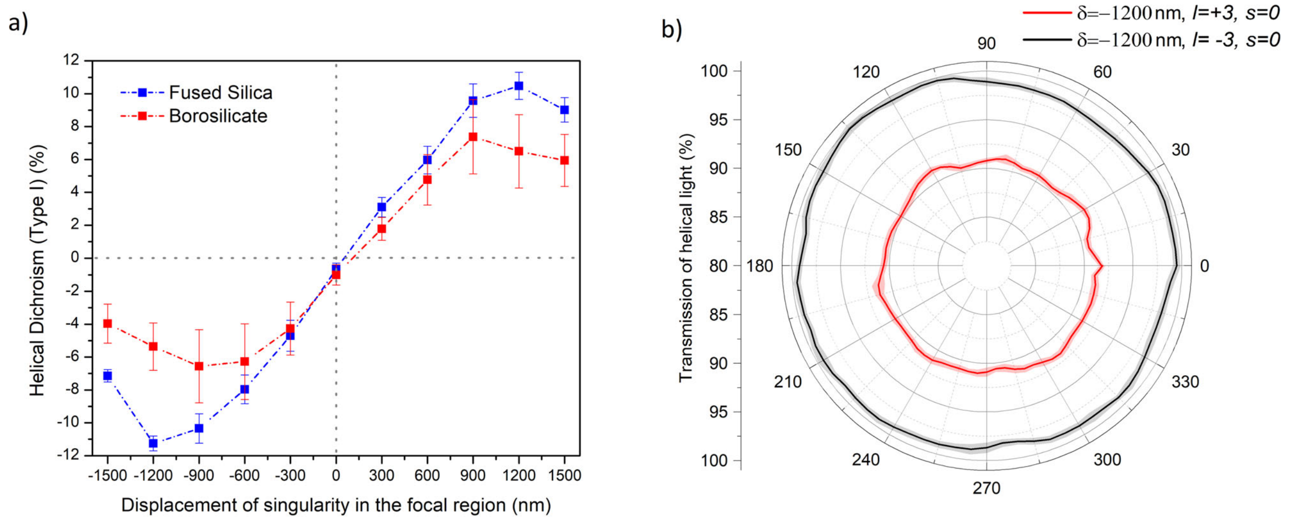

Fig. 2 | Helical dichroism in amorphous solids. a HD (Type I) for fused silica (blue) and borosilicate (red) as a function of displacement of the singularity with linearly polarized ($\epsilon = 0.05$) asymmetrical OAM beam ($l = \pm 3$). **b** Orientation-dependent transmission of $l = \pm 3$ in fused silica at $\delta = -1200$ nm. The error bars in (**a**) represent the standard error, of multiple measurements ($n = 3$), calculated for an average fluence range used to obtain HD. The error bands in (**b**) represent the standard error at every position of the crystal for $n = 20$ points.

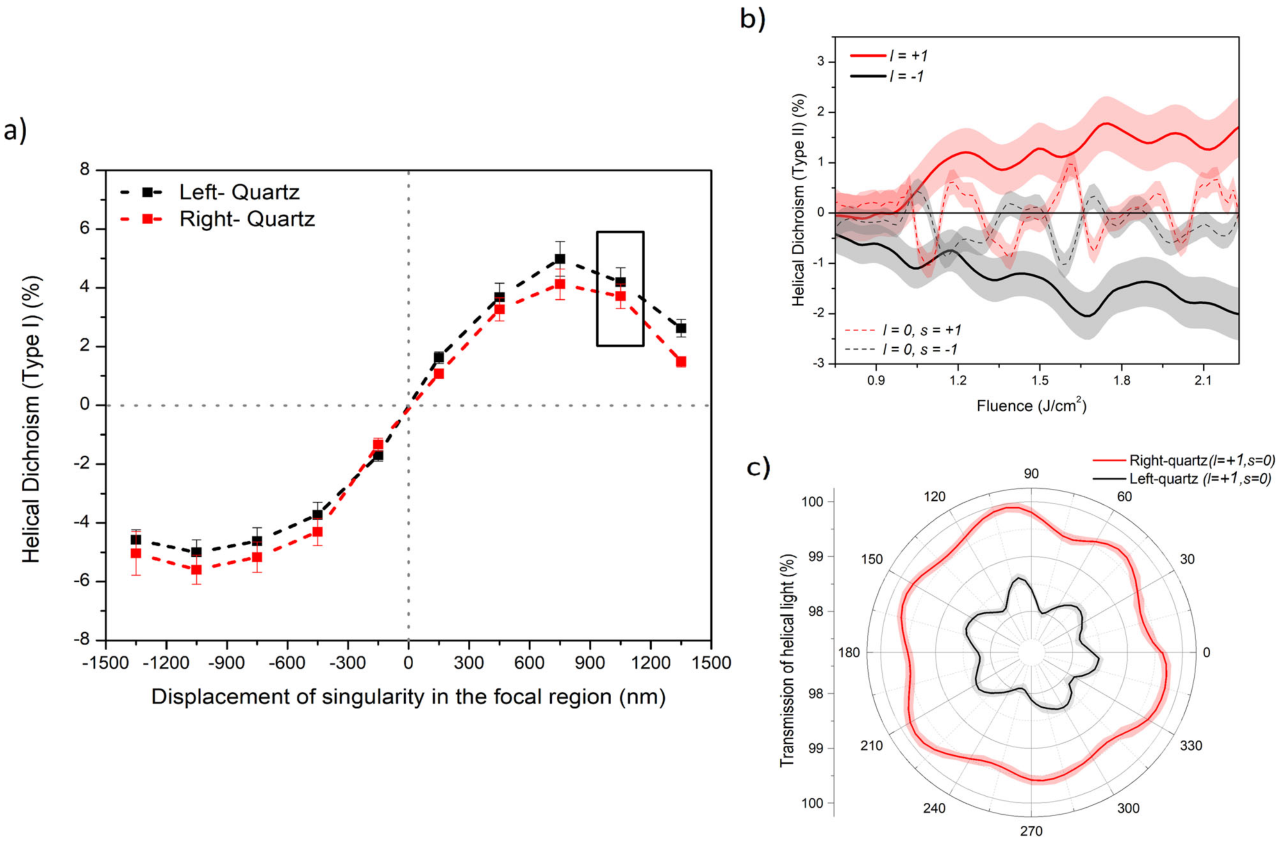

Fig. 3 | Probing chirality in quartz with linearly polarized ($\epsilon = 0.05$) asymmetrical OAM beams. **a** HD (Type I) for left- and right-handed quartz as a function of displacement of the singularity ($l = \pm 1$). **b** Chiral signal, HD (Type II: $\pm l; \pm s$) = $2\frac{R(\pm l;\pm s)-L(\pm l;\pm s)}{R(\pm l;\pm s)+L(\pm l;\pm s)}$ as function of peak laser fluence for linearly polarized $l = \pm 1$ and circularly polarized $l = 0$ beams. **c** Orientation-dependent transmission of $l = +1$ in right- and left-handed quartz. **b**, **c** were obtained when the singularity was at the position marked by a solid rectangle in (**a**). The error bars in (**a**) represent the standard error, of multiple measurements ($n = 3$), calculated for an average fluence range used to obtain HD. The error bands in (**b**) represent the error propagation of the standard error of multiple transmission curves. The error bands in (**c**) represent the standard error at every position of the crystal ($n = 20$ points).

our qualitative model discussed in "Origin of Helical dichroism in solids". Figure 4b, depicts an average HD (Type I) signal, for three $+\delta$ positions (600, 900, and 1200 nm) of Fig. 4a, plotted as a function of bandgap.

Control and tunability of HD (Type I)

Figure 5 shows simulated and experimental curves obtained by (i) superimposing Gaussian and OAM beams, and (ii) varying the l-value. To model HD (Type I), we considered the total rate of interband transition ($W_{cv}^{\pm}$) evaluated using Eq. (20). It is a product of multiphoton transition probability amplitude from the ground to the intermediate state and tunnel ionization probability amplitude from the intermediate state to the conduction band. HD (Type I) is defined in terms of differential averaged energy absorbed $\Delta\Gamma$, normalized with respect to the incident laser energy (see "Origin of Helical dichroism in solids" for details).

$$\Delta\boldsymbol{\Gamma} = \Gamma^+ - \Gamma^- = \mathcal{D}\left(\Upsilon^+ - \Upsilon^-\right) = \mathcal{D}\left(\mathrm{Re}\left[\nabla_i E_j^+ E_i^{+*}\right] - \mathrm{Re}\left[\nabla_i E_j^- E_i^{-*}\right]\right) \quad (1)$$

where $\Upsilon^{\pm}$ is optical helicity which describes the handedness of helical light and $E_{i,j}$ is the electric field described by Eq. (23) ("Superposition of OAM and Gaussian" and Supplementary Section 7 for details). $\mathcal{D}$ represents a collection of physical quantities (given by Eqs. (18)–(20)) that are independent of helicity within our approach, and can be estimated to be 7.3×10^{-5} ("Origin of Helical dichroism in solids" and Supplementary Section 9). Therefore, HD (Type I) is a beam-dominated property and does not exist for symmetric LG beams ($\delta = 0$). For asymmetric LG beams ($\delta \neq 0$), the electric–magnetic dipole coupling term in Eq. (17) vanishes (because we take the difference between the left- and right-helical beams for the same polarization), and the electric dipole–quadrupole coupling term is nonzero resulting in HD (Type I). The electric dipole–quadrupole coupling term also contains the gradient of the electric field giving rise to l-dependence, as can be seen in Fig. 5c. The simulation curves shown in Fig. 5 are plotted by integrating HD (Type I) over the whole beam cross-section, HD (Type I) = $\int_{-w_0}^{w_0} \Delta\boldsymbol{\Gamma}\,dxdy$.

For simplicity, we treated intermediate state tunneling within the dipole approximation and reduced the multiphoton absorption to a single-photon transition expanded to higher-order multipoles. We simulate HD(Type I) for different ratios of superposition of Gaussian and OAM beams (Fig. 5a) and l-values (Fig. 5c) using the above equation. For a specific l-value of an asymmetric OAM beam, the magnitude of HD (Type I) signal is maximum for a pure OAM beam and decreases as the amount of Gaussian beam in the superposition increases (Fig. 5a). In case of linearly polarized light, HD signal vanishes for a pure Gaussian beam. Experimental results shown in Fig. 5b for fused silica agrees with the simulations (Fig. 5a). Also, simulated and experimental HD signals scale with l-value as shown in Fig. 5c, d for two different l-values. Similar control and tunability of HD was also observed in c-solids such as MgO (Supplementary Section 3). The simulated HD values differ by few orders of magnitude compared to experimental values. This variation could be due the approximate values used for electric dipole and quadrupole moment, and material response.

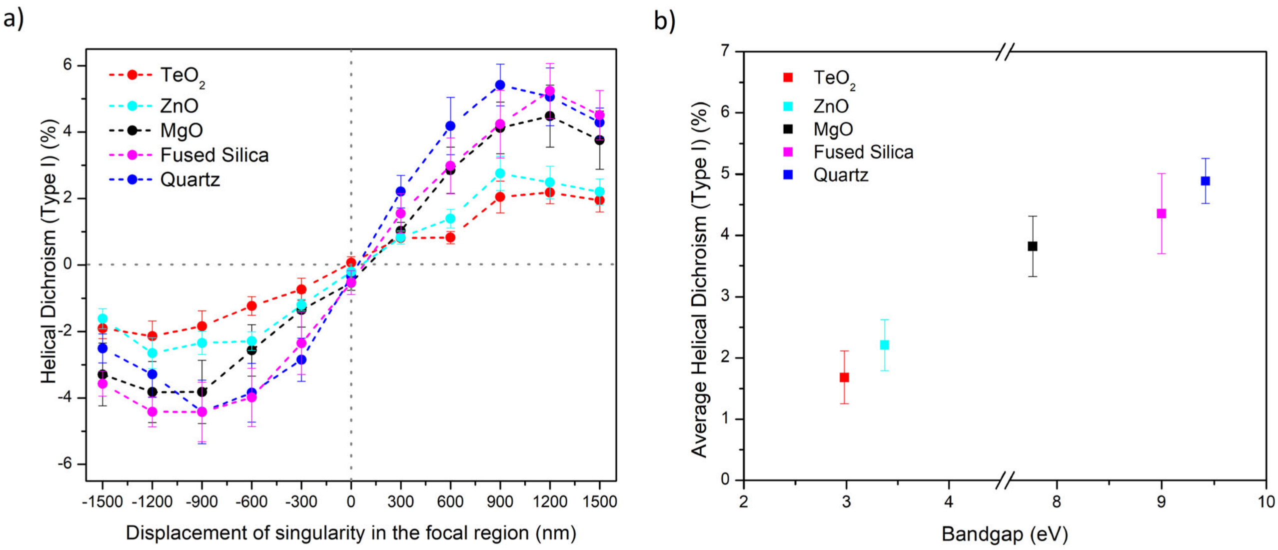

Fig. 4 | Bandgap dependence of helical dichroism. a HD(Type I) in different materials as a function of displacement of singularity in the OAM beam for $l = \pm 1$ in crystalline and amorphous solids. **b** Average magnitude of HD (Type I) as a function of bandgap for $l = \pm 1$. The error bars in (**a**) represent the standard error, of multiple measurements ($n = 3$), calculated for an average energy range used to obtain HD. The error bars in (**b**) represent the average of three δ positions in (**a**) where the HD (Type I) signal is maximum. All curves are obtained under identical experimental conditions.

HD signal changes in discrete steps when *l*-value is varied but can be tuned almost continuously by changing the superposition of OAM and Gaussian beams. In addition, HD signal can also be varied by changing the ellipticity of laser polarization[25]. These are the features of our technique that has no comparable equivalent in other existing solid-state-based chiroptical techniques. Continuous tunability of HD by superposition of OAM and Gaussian beams by electrical detuning of optical retardation offers instrumental advantage. A single higher-order q-plate is sufficient to reproduce the results of all lower-order q-plates by controlling the voltage on the q-plate.

Discussion

In conclusion, we demonstrate HD in both amorphous and crystalline solids including chiral systems. HD in the condensed phase provides valuable information on chirality. Conventional solid-state chiroptical techniques such as CD have poor efficiency because the chiral signal is weaker than the artifact signals from macroscopic anisotropies such as linear birefringence. The efficiency of HD enables to achieve chiral recognition on a solid surface and is of fundamental importance in various fields of surface and material sciences. In addition, the control and tunability of HD provides new opportunities in the development of enantioselective catalysis[46] and asymmetric synthesis of bioactive molecules[47], chiral sensors[48,49], and molecular electronic devices[50,51]. In laser processing of transparent materials, localized changes induced in the bulk can result in structural changes on sub-micron dimensions confined to the laser focal volume[52,53]. These changes modify the bandgap and are hard to study due to lack of in situ probes. Pump-probe spectroscopy involving Gaussian and OAM beams can shed light on such changes by monitoring the magnitude of HD signal due to its dependence on the bandgap.

The presence of intrinsic dichroism in amorphous materials is due to the existence of short- to medium-range order. Material response to the phase of light associated with OAM beams will aid the efforts to understand the mysterious nature of amorphous materials. Furthermore, HD can be extended to conjugated polymers that are used as active materials in devices for printed and flexible organic electronics[54]. Transport properties in such polymers is widely believed to be due to long-range order, so research focused primarily on increasing the crystallinity of polymers. However, recent studies showed that local aggregation over few chains is sufficient to ensure high mobility[55]. In other words, the key to designing high-mobility polymers is not to increase their crystallinity but rather to improve their tolerance for disorder. Typically, information on short-range ordering in polymers is often achieved by means of radial distribution function derived from X-ray diffraction[56]. HD can shed light on short-range order that influences electronic properties in polymers and semiconducting alloys.

Methods

Differential absorption measurements

Transmission measurements were performed using a Ti: Sapphire laser amplifier system, operating in an external trigger mode producing 45 fs, 800 nm pulses with a maximum pulse energy of 2.5 mJ. An aspheric objective lens (NA = 0.3) was used to focus the femtosecond pulses into solid samples with typical dimensions of 10 × 10 × 1 mm. A second aspheric objective with the same or higher numerical aperture (NA = 0.5) collected and collimated the transmitted light onto a photodiode (PD2), positioned immediately after the objective (Supplementary Section 1 for a schematic of the experimental setup). For every laser shot, the transmitted light signal on PD2 was normalized with the incoming light signal on PD1, reflected off a glass plate positioned in the beam path at an angle of ~20° to avoid Brewster's angle. The signals generated by PD1 and PD2 were stretched by an electronic pulse stretcher, discretized, and recorded by a data acquisition card. A combination of a half-wave plate and a polarizer was used to vary the pulse energy (Supplementary Section 1). The incident pulse energies were measured before the objective. During the measurement, for every laser shot, the pulse energy was increased by ~3 nJ and the sample was translated by 5 µm to irradiate a fresh sample. Multiple transmission curves similar to the inset of Fig. 1a were obtained for each sample to be averaged and smoothed. The difference in the normalized transmission of left- and right-helical light is proportional to the differential absorption. To ensure shortest pulses in the interaction region, a negative chirp was introduced and optimized by measuring the second harmonic generation in a BBO crystal placed at the location of the sample. A single-shot auto-correlator then continuously monitored the pulse duration. The pulse duration at the interaction region is about 100 fs. Prior to each experiment,

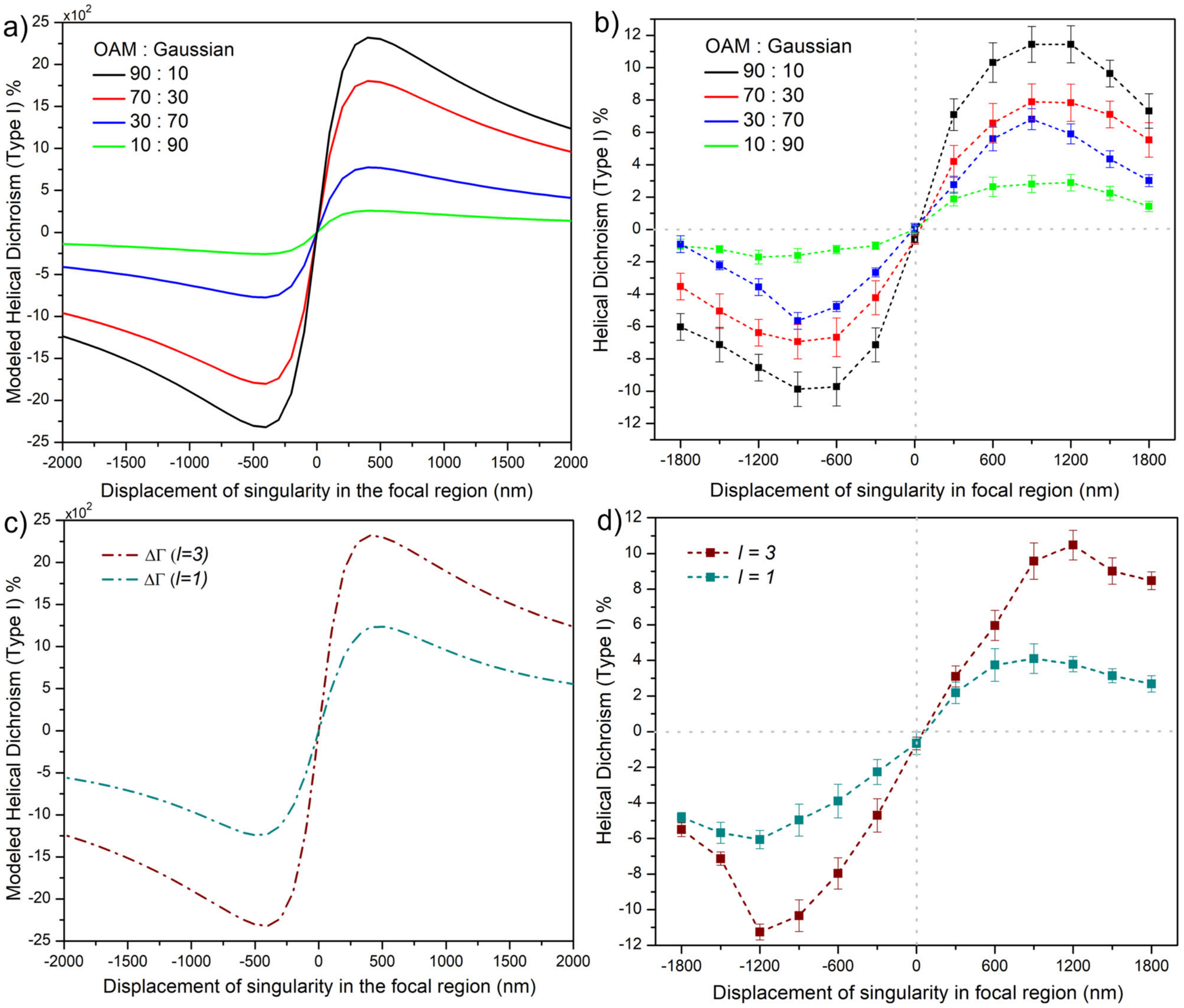

Fig. 5 | Tunability of Helical dichroism. Simulated and measured HD (Type I), in fused silica as a function of the displacement of singularity for (**a**, **b**) variable ratios of superposition of linearly polarized ($\epsilon = 0.05$) OAM ($l = \pm 3$) and Gaussian beams, and **c**, **d** linearly polarized ($\epsilon = 0.05$) helical light with $l = \pm 1, \pm 3$. In simulation, displacement of the singularity was considered perpendicular to the polarization following experimental conditions. The error bars in (**b**, **d**) represent the standard error, of multiple measurements ($n = 3$), calculated for an average fluence range used to obtain HD. The HD (Type I) was modeled using the relation $\int_{-w_0}^{w_0} \Delta\boldsymbol{\Gamma} \mathrm{d}x, \mathrm{d}y = \int_{-w_0}^{w_0} \mathcal{D}(\Upsilon^+ - \Upsilon^-)\mathrm{d}x, \mathrm{d}y$ where $\mathcal{D}$ represents a collection of physical quantities and $\Upsilon^{\pm}$ is optical helicity which describes the handedness of helical light (see text and "Methods" for details).

transmission measurements were always performed without a sample (in air) to determine and minimize background errors resulting from any discrepancies between the photodiodes (Supplementary Section 6). In addition, the measured single-shot beam profile, pulse spectrum, and OAM value remained unchanged after transmission through the samples[25]. The crystal samples were procured from MTI Corp., MSE Supplies and chiral quartz from Knight Optical. Fused silica was bought from SPI Supplies.

Generation of OAM beams

Light beams carrying orbital and/or spin angular momentum were generated and controlled by OAM/SAM unit (Supplementary Fig. 1) consisting of a combination of half- and quarter-wave plates (HWP and QWP), linear polarizer (LP) and a birefringent liquid crystal based phase plate called q-plate[21,28,57]. When an incident Gaussian beam propagates through the q-plate with a topological charge q, it acquires an OAM defined by $l = \pm 2q$ with a phase singularity and hence a null intensity region at the center of the beam - an optical vortex. The wavefront structure of such beams undergo l intertwined rotations in one wavelength, the direction of rotation is determined by the sign of the input polarization. The conversion efficiency of the q-plates were 91 ± 2% for $l = 1, 3$. Linearly polarized OAM light $s = 0, l = \pm 1$ was generated using a combination of QWP, q-plate, QWP, and LP. The ellipticity of linearly polarized OAM light was 5 ± 2% reaching the sample.

Displacement of singularity

The singularity/null intensity region in the OAM beam was displaced by translating the q-plate, mounted on a x, y-stages with a step size of 250 ± 10 µm. When focused by the objective, this translated to a displacement step size of 300 ± 20 nm with respect to the center of the beam. The calibration was achieved by measuring the total translation required to displace the singularity to the periphery of the defocused beam and comparing it to the measured spot size of 2 ± 0.2 µm obtained by knife-edge measurements. The helical vortex beams can be further classified into vector and scalar vortex beams. The superposition of vector vortex beams with linear Gaussian leads to the shifting of singularity towards the periphery of the beam for $l=1$ and splitting of the singularity for higher-order l-value[58]. The superposition of linear Gaussian with scalar vortex beam causes the null intensity region to fade and does not lead to the shifting of singularity, which was used in the experiments.

Electron displacement during interband transition

Classically, in atoms, tunneling results in spatial displacement of the electron given by $\mathbf{x}_0 = I_p/(e\mathbf{E})$, where I_p is the ionization potential[31,59]. $\mathbf{x}_0$ is the distance traversed by the electron through the barrier to the tunnel exit. This concept can also be extended to solids. The energy absorbed from the incident laser fields is proportional to the associated injection current given by $\mathbf{J} = en_0\mathbf{x}_0\dot{\rho}$[60], where e is the electron charge, n_o is electron density in the conduction band, $\dot{\rho}$ is the injection rate which is proportional to the transition rate W, $\mathbf{x}_0$ is the spatial displacement of the electrons after being promoted from the valence band to the conduction band. ($\mathbf{J}$) is fundamental to maintain energy conservation ($\dot{u} = -\mathbf{J}\cdot\mathbf{E}$). In optical tunneling, energy conservation is fulfilled when this current reflects a spatial displacement of the electrons given by[60]

$$\mathbf{x}_0 = \mathbf{E}E_g\big/\left(eE^2\right) \tag{2}$$

where E_g is the bandgap and $\mathbf{E}$ is the electric field. We assume a parabolic conduction band to eliminate contributions from band anharmonicities and Bloch oscillations due to reflections at zone boundaries[60].

Injection current was recently used to explain the origin of strong-field-induced harmonic generation in fused silica[60]. In amorphous fused silica ($E_g \approx 9$ ev[34,35]), $\mathbf{x}_0$ varies from 6 to 18 Å for the laser intensities used in our experiments. Transition of electron from valence to conduction band can occur via two mechanisms, multiphoton or tunneling, depending on the laser intensity. They are typically identified by the Keldysh parameter (γ)[31,33]. For solids, it is defined as

$$\gamma = \frac{\omega}{e}\left[\frac{mcn\varepsilon_0 E_g}{I}\right]^{1/2} \tag{3}$$

where ω is the laser frequency, I is the incident laser intensity (Supplementary Section 4), m and e are the reduced mass and charge of the electron, c is the velocity of light, n is the refractive index of the material, E_g is the bandgap of the material and ϵ_0 is the permittivity of free space. When $\gamma > 2$, interband excitations are dominated by multiphoton process and when $\gamma < 1$ it is dominated by tunneling.

For the laser intensities in the range of 2×10^{13} to 8×10^{13} W/cm^2 that were used in the experiments, Keldysh parameter varied from ~2.5 to 1.1 for fused silica. In the intermediate regime when $1 \lesssim \gamma \lesssim 2$ the electron transitions are dominated by multiphoton-assisted tunneling (MPAT)[33,61]. The MPAT process, developed for atoms, can be extended to solids and visualized as electron transition from valence band to an intermediate state by mulitphoton absorption and subsequent tunneling from that state to the conduction band[31,61].

In MPAT process, there will be two contributions to electron displacement—one from multiphoton transition to the intermediate state and the other from subsequent tunneling to the conduction band ($\mathbf{x}_0$ is given by Eq. (2) where E_g needs to be replaced by the energy gap between intermediate and conduction band states). However, $\mathbf{x}_0$ in MPAT will be smaller compared to direct tunneling transitions from valence band to conduction band which sets the upper limit for electron displacement[32,61]. $\mathbf{x}_0$ in MPAT is comparable to short-medium-range order in fused silica which is < 20 Å[9,14–16]. As a result, isotropic averaging is restricted to an ordered environment giving rise to finite contribution in a-solids. In c-solids, the ordered environment always ensures a nonzero HD signal upon isotropic averaging. Moreover, our transmission curves reproduce the crystal symmetry due to its dependence upon the injection current, similar to the results that were obtained from the high harmonic yields[60].

Origin of Helical dichroism in solids

Helical Dichroism in solids can be understood in terms of molecular multipole moments during light-matter interaction. When the incident laser intensity is not sufficient for direct interband tunneling, electron transitions are facilitated by multiphoton excitation to intermediate states and subsequent tunneling to the conduction band. The transition amplitude for MPAT process involving a single-photon absorption (SPA) from the valence band (ψ_v) to an intermediate excited state (ψ_m) and subsequent tunneling to the conduction band (ψ_c) is given by (Supplementary Section 8 for further details)

$$M_{cv} = \sum_m \underbrace{\frac{\langle\psi_m|\hat{V}_i|\psi_v\rangle}{\hbar(\omega_{mv}-\omega)}}_{M_{SPA}} \underbrace{\frac{i}{\hbar}\int_{t_0}^{t} d\tau\langle\psi_c(\tau)|\hat{V}_f(\tau)|\psi_m(\tau\rangle e^{i(\omega_{mv}-\omega)\tau}}_{M_{TNL}} \tag{4}$$

where ω is the laser frequency, $\omega_{mv} = (E_m - E_v)/\hbar$, E_m, and E_v are the energies of the intermediate and valence band states, respectively. In addition, $\hat{V}_i$ and $\hat{V}_f$ are multiphoton and tunneling interaction Hamiltonians written in multipole expansion and dipole approximation, respectively. The MPAT transition amplitude is a product of two factors; a time-independent single-photon transition amplitude M_{SPA} and a time-dependent excited state tunneling amplitude M_{TNL}. The interaction Hamiltonian is given by $\hat{V}(t') = \frac{1}{2m}[2e\mathbf{p}\cdot\mathbf{A}(R,t) + e^2\mathbf{A}^2(R,t)]$, where the m is the electron mass, $\mathbf{p}$ is the momentum vector in the molecular frame ($\mathbf{r}$) and $\mathbf{A}(\mathbf{R},t)$ is the vector potential in the laboratory frame ($\mathbf{R}$).

In crystals, the eigenstates are written in terms of bloch wavefunctions (plane wave modulated by the crystal periodicity function $u_{\mathbf{k}}(\mathbf{r})$. For a-solids, we can approximate the eigenstates as bloch-like wavefunctions (as long as the electron displacement is within $\mathbf{x}_0$[13]) with effective wave vectors $\mathbf{k}'$, $\mathbf{k}''$ and $\mathbf{k}$ for valence band state, intermediate state and the conduction band state, respectively. The valence band and intermediate state wavefunctions are given by

$$|\psi_v(\mathbf{r},\tau)\rangle = u^{v}_{\mathbf{k}'}(\mathbf{r})e^{i\mathbf{k}'\cdot\mathbf{r}}e^{-i\frac{E_v}{\hbar}\tau} \tag{5}$$

$$|\psi_m(\mathbf{r},\tau)\rangle = u^{m}_{\mathbf{k}''}(\mathbf{r})e^{i\mathbf{k}''\cdot\mathbf{r}}e^{-i\frac{E_m}{\hbar}\tau} \tag{6}$$

The conduction band state is approximated by a Volkov-type solution[62]

$$|\psi_c(\mathbf{r},\tau)\rangle = u^{c}_{\mathbf{k}}(\mathbf{r})\exp\left[\mathrm{i}\left(\mathbf{k}\cdot\mathbf{r} - \frac{1}{\hbar}\int_0^{\tau} E_c[\mathbf{k}(t'')]\mathrm{d}t''\right)\right] \tag{7}$$

$$E_c[\mathbf{k}(t'')] = E_g + \frac{1}{2m_1}(\hbar\mathbf{k} - e\mathbf{A}(t''))^2 \tag{8}$$

where $E_v = \frac{\hbar^2k^2}{2m_0}$, m_0 and m_1 are the effective mass of the valence and the conduction bands, E_g is the bandgap, $\mathbf{r}$ is the spatial coordinate in molecular frame and $\mathbf{A}$ is the vector potential in laboratory frame given by ($\mathbf{A}(t) = A_0(\alpha\cos\omega t\hat{x} + \beta\sin\omega t\hat{y})$ for elliptical polarization. In our intensity range, the above Volkov-like wavefunction can be limited to a linear dependency of the vector potential. Solving the time integral leads to

$$|\psi_c(\mathbf{r},\tau)\rangle = \frac{u^{c}_{\mathbf{k}}(\mathbf{r})}{(2\pi)^{3/2}}e^{i\mathbf{k}\cdot\mathbf{r} - \frac{i}{\hbar}\left(E_g\tau + E_c\tau + \gamma_0\hbar\left[k_x\alpha sin(\omega\tau) - k_y\beta cos(\omega\tau)\right]\right)} \tag{9}$$

where $E_c = \frac{\hbar^2k^2}{2m_1}$ is the kinetic energy of the conduction band and $\gamma_0 = \frac{eA_0}{m_1\omega}$ is the quiver amplitude. Substituting all the above states (Eqs. (5)–(7)) in the transition amplitude (Eq. (4)) and taking the evolution of states over $t_0 = -T/2$, $t = T/2$, with the limit $T \to \infty$[62,63], we obtain

$$M_{cv} = \frac{iA_0 e}{m\hbar(2\pi)^{3/2}} \sum_m \frac{1}{\hbar(\omega_{mv} - \omega)} \int_{-\infty}^{\infty} u_{\mathbf{k}''}^{m*}(\mathbf{r}') \hat{V}_i u_{\mathbf{k}'}^{v}(\mathbf{r}') e^{i(\mathbf{k}'-\mathbf{k}'')\cdot\mathbf{r}'} d^3r' \int_{-\infty}^{\infty} u_{\mathbf{k}}^{c*}(\mathbf{r}) u_{\mathbf{k}''}^{m}(\mathbf{r}) e^{i(\mathbf{k}''-\mathbf{k})\cdot\mathbf{r}} d^3r$$
$$\times \lim_{T\to\infty} \int_{-T/2}^{T/2} e^{\frac{i}{\hbar}(E_g+\epsilon-\hbar\omega)\tau} (\alpha p_x \cos\omega\tau + \beta p_y \sin\omega\tau) e^{i\gamma_0[k_x\alpha sin(\omega\tau) - k_y\beta cos(\omega\tau)]} d\tau \tag{10}$$

Solving the time integral using Jacobi–Anger expansion $\cos\omega t e^{i\alpha\sin\omega t} = \frac{1}{\alpha}\sum_{n=-\infty}^{\infty} n J_n(\alpha) e^{in\omega t}$, we obtain

$$M_{cv} = \frac{iA_0 e}{m\hbar(2\pi)^{3/2}} \frac{1}{\gamma_0} \sum_m p_{mv}^{SPA} \sum_{\eta,\zeta=-\infty}^{\infty} i^{\zeta} \int_{-\infty}^{\infty} u_k^{c*}(\mathbf{r}) \left[\frac{p_x}{k_x}\eta + \frac{p_y}{k_y}\zeta\right] u_{\mathbf{k}''}^{m}(\mathbf{r}) e^{i(\mathbf{k}''-\mathbf{k})\cdot\mathbf{r}} d^3r$$
$$\times J_\eta(-\gamma_0 k_x \alpha) J_\zeta(\gamma_0 k_y \beta) \left[\lim_{T\to\infty} \frac{2\hbar sin\left((E_g+\epsilon-N\hbar\omega)\frac{T}{2\hbar}\right)}{(E_g+\epsilon-N\hbar\omega)}\right] \tag{11}$$

where $\epsilon = \frac{\hbar^2 k^2}{2m^*}$ is the total kinetic energy, $m^{*-1} = m_1^{-1} - m_0^{-1}$ is the total effective electron mass, and $N\hbar\omega = (\eta + \zeta)\hbar\omega + \hbar\omega$ is the total number of photons absorbed during the MPAT process. Use of Jacobi–Anger expansion allowed us to discretize the tunneling contribution and, for analytical analysis, treated the transition from intermediate state to conduction band state non-perturbatively. p_{mv}^{SPA} represents the single-photon absorption probability amplitude given by

$$p_{mv}^{SPA} = \frac{1}{\hbar(\omega_{mv} - \omega)} \int_{-\infty}^{\infty} u_{\mathbf{k}''}^{m*}(\mathbf{r}') \hat{V}_i u_{\mathbf{k}'}^{v}(\mathbf{r}') e^{i(\mathbf{k}'-\mathbf{k}'')\cdot\mathbf{r}'} d^3r' \tag{12}$$

We further define the tunneling probability amplitude as

$$p_{cm}^{TNL} = \frac{m_1}{m\hbar(2\pi)^{3/2}} \sum_{\eta,\zeta=-\infty}^{\infty} i^{\zeta} J_\eta(-\gamma_0 k_x \alpha) J_\zeta(\gamma_0 k_y \beta) \int_{-\infty}^{\infty} u_{\mathbf{k}}^{c*}(\mathbf{r}) \left[\frac{p_x}{k_x}\eta + \frac{p_y}{k_y}\zeta\right] u_{\mathbf{k}''}^{m}(\mathbf{r}) e^{i(\mathbf{k}''-\mathbf{k})\cdot\mathbf{r}} d^3r \tag{13}$$

Using the property $\lim_{T\to\infty} T^2 \frac{sin^2(x)}{x^2} = 2\pi\hbar T\delta(\epsilon + E_g - N\hbar\omega)$ where $x = (E_g + \epsilon - N\hbar\omega)\frac{T}{2\hbar}$[64], the transition rate from the valence to the conduction band, defined as $W_{cv} = \frac{d}{dt}|M_{cv}|^2$, can be expressed as

$$W_{cv}(\mathbf{k}) = 2\pi\hbar\omega^2 \sum_m |p_{cm}^{TNL}|^2 |p_{mv}^{SPA}|^2 \delta\left(\epsilon + E_g - N\hbar\omega\right) \tag{14}$$

where the delta function demonstrates the energy conservation for the full transition. The transition rate $W_{cv}(\mathbf{k})$ is proportional to a product of the single-photon absorption probability $|p_{mv}^{SPA}|^2$ (electron promoted from the valence band to intermediate state) and the tunneling probability $|p_{cm}^{TNL}|^2$ (electron tunneling from intermediate state to conduction band). Expanding $|p_{mv}^{SPA}|^2$ in Eq. (14) in terms of higher-order multipoles[25], the absorption rate for left- and right-helical light (with identical polarization) represented by ± sign, $W_{cv}^{(\pm)}$, can be written as

$$W_{cv}^{(\pm)}(\mathbf{k}) = 2\pi \sum_m \left[\langle|p_{cm}^{TNL}|^2 |\mu_i^{mv}|^2\rangle_P |E_i^{\pm}|^2 + \langle|p_{cm}^{TNL}|^2 |m_i^{mv}|^2\rangle_P |B_i^{\pm}|^2 + 2\langle|p_{cm}^{TNL}|^2 \mu_i^{mv} m_i^{vm}\rangle_P\right.$$
$$\left. \text{Im}\left[E_i^{\pm*} B_i^{\pm}\right] + \frac{2}{3}\langle|p_{cm}^{TNL}|^2 \mu_i^{mv} \theta_{ij}^{vm}\rangle_P \text{Re}\left[\nabla_i E_j^{\pm} E_i^{\pm*}\right]\right] \frac{\delta\left(\epsilon + E_g - N\hbar\omega\right)}{\hbar\left(\omega_{mv} - \omega\right)^2} \tag{15}$$

where, E and B are incident electric and magnetic fields (Supplementary Section 7 for asymmetric Laguerre–Gaussian beam equation), μ_i represents the intrinsic electric dipole, m_i is the intrinsic magnetic dipole, θ_{ij} represents the intrinsic electric quadrupole. Since photons are absorbed in an ordered environment within the short-range distances in both c-solids and a-solids, we assume that the anisotropic averaging, $\langle\rangle_P$, results in a finite orientation-dependent weighing factor $\Omega_{i=1,4}$. As a result of this simplification, the above expression reduces to

$$W_{cv}^{(\pm)}(\mathbf{k}) = 2\pi \sum_m |p_{cm}^{TNL}|^2 \left[\underbrace{\Omega_1 |\mu_i^{mv}|^2 |E_i^{\pm}|^2}_{\text{E1E1}} + \underbrace{\Omega_2 |m_i^{mv}|^2 |B_i^{\pm}|^2}_{\text{M1M1}} + \underbrace{\Omega_3 (2\mu_i^{mv} m_i^{vm}) \text{Im}\left[E_i^{\pm*} B_i^{\pm}\right]}_{\text{E1M1}}\right.$$
$$\left. + \underbrace{\Omega_4 \left(\frac{2}{3}\mu_i^{mv} \theta_{ij}^{vm}\right) \text{Re}\left[\nabla_i E_j^{\pm} E_i^{\pm*}\right]}_{\text{E1E2}}\right] \frac{\delta(\epsilon + E_g - N\hbar\omega)}{\hbar\left(\omega_{mv} - \omega\right)^2} \tag{16}$$

where E1 and M1 are electric and magnetic dipoles, respectively, and E2 is the electric quadrupole. The coupling terms E1M1 and E1E2 are pseudoscalars and change signs under improper rotation. $W_{cv}^{(\pm)}(\mathbf{k})$ is a product of tunneling probability amplitude $|p_{cm}^{TNL}|^2$ and single-photon absorption probability amplitude $|p_{mv}^{SPA}|^2$. The above equation can be generalized to the multiphoton case and was also shown to be responsible for the origin of HD in chiral and achiral molecules[25].

HD (Type I) is proportional to the difference in the interband transition rates between left- and right-handed helical light with beam asymmetry parameter δ can be expressed as:

$$\Delta W_{cv} = W_{\delta}^{+} - W_{\delta}^{-} = 2\pi \sum_m |p_{cm}^{TNL}|^2 \left[\Omega_3 (2\mu_i^{mv} m_i^{vm}) \left(\text{Im}\left[E_i^{+*} B_i^{+}\right] - \text{Im}\left[E_i^{-*} B_i^{-}\right]\right)\right.$$
$$\left. + \Omega_4 \left(\frac{2}{3}\mu_i^{mv} \theta_{ij}^{vm}\right) \left(\text{Re}\left[\nabla_i E_j^{+} E_i^{+*}\right] - \text{Re}\left[\nabla_i E_j^{-} E_i^{-*}\right]\right)\right] \frac{\delta(\epsilon + E_g - N\hbar\omega)}{\hbar\left(\omega_{mv} - \omega\right)^2} \tag{17}$$

E1E1 and M1M1 terms do not contribute to HD (Type I) because the field intensities and profiles remain the same for both helicities. Evaluation of above equation shows that HD (Type I) is a beam-dominated property as the material tensors are identical for both the helicities. Moreover, within dipole approximation, the tunneling contribution $|p_{cm}^{TNL}|^2$ results in identical rates for both helicities.

The HD (Type I) is dependent on the beam asymmetry parameter δ where $\delta = 0$ represents symmetric beam and $\delta \neq 0$ asymmetric beam (Supplementary Section 7 for beam profiles). The E1M1 contribution for both symmetric and asymmetric beam vanishes because we take the difference between the left- and right-helical beams for the same polarization. Therefore, HD (Type I) arises due to E1E2 coupling term. The E1E2 term contains the gradient of the electric field giving rise to l-dependence. Therefore, for symmetric beams E1E2 contributions average out to zero and only exist for asymmetric beams. For left- and right-circularly polarized light, the E1M1 term is nonzero and gives rise to conventional chiral signal

The total transition rate, W_{cv}, can be obtained by integrating, $W_{cv}(\mathbf{k})$, over all momentum states. For numerical estimation, shown in Fig. 5, we assume the summation over all intermediate states in the above equation is dominated by a single state that is pre-determined by the incident photon. The total transition rate is enhanced when the intermediate state is in resonance with the incident photon energy. In addition, we use linearly polarized light to simplify $W_{cv}(\mathbf{k})$ and perform the integration using the properties of Bessel's functions and the weak-field limit for the non-perturbative discrete transition rate[31,62,63] (Supplementary Section 9 for details) to obtain

$$\Delta \text{W} = \text{W}_{\delta}^{+} - \text{W}_{\delta}^{-} = \frac{2\Omega_4(\mu_i^{mv}\theta_{ij}^{vm})}{3\hbar^2\left(\omega_{mv} - \omega\right)^2} \widetilde{\text{W}} \left(\text{Re}\left[\nabla_i E_j^{+} E_i^{+*}\right] - \text{Re}\left[\nabla_i E_j^{-} E_i^{-*}\right]\right) = D(\Upsilon^{+} - \Upsilon^{-}) \tag{18}$$

where $\Upsilon^{\pm} = \text{Re}[\nabla_i E_j^{\pm} E_i^{\pm*}]$ represent the optical helicity describing the handedness of the helical light, its association with the field gradient gives rise to l-dependence. This quantity is odd under parity with a change in the sign of the displacement of the singularity, δ, and time reversal changes the handedness of helical light. Also,

$$\tilde{\mathrm{W}} = \frac{1}{(2\pi)^4\hbar}\left(\frac{m_1\omega p_{\mathrm{cm}}}{m(\eta-1)!}\right)^2\left(\frac{eA_0}{2m_1\omega}\right)^{2\eta}\left(\frac{2m^*}{\hbar^2}\right)^{(2\eta+1)/2}\left(\frac{(n\hbar\omega-E_{\mathrm{g}})}{(2\eta-1)}\right)^{(2\eta-1)/2} \tag{19}$$

where $n=\eta+1$ is the total photons absorbed for linearly polarized light. HD(Type I) can now be defined in terms of energy absorbed Γ normalized with respect to the incident laser energy, $\mathcal{E}_{inc}$ as:

$$\Delta\boldsymbol{\Gamma} = \Gamma^+ - \Gamma^- = \frac{\hbar\left(\mathrm{W}_\delta^+ - \mathrm{W}_\delta^-\right)}{\mathcal{E}_{inc}} = \mathcal{D}\left(\Upsilon^+ - \Upsilon^-\right) \tag{20}$$

where $\mathcal{D} = \frac{\hbar\mathrm{D}}{\mathcal{E}_{inc}}$. HD (Type I) is obtained by integrating over the beam cross-section $\int_{-w_0}^{w_0}\Delta\boldsymbol{\Gamma}\,\mathrm{d}x\mathrm{d}y$

For an order of magnitude estimation of $\mathcal{D}$, we used the following values; the intrinsic dipole as $\mu_i \approx 1.65\times10^{-30}$ Cm[65], the quadrupole for fused silica molecule as $\theta_{ij}\approx 9.3\times10^{-49}$ Cm^2(glass)[66], $A_0 = E_0/\omega$ where $E_0 = 7.1\times10^9$ to 1.5×10^{10} V/m and $\omega = 2.35\times10^{15}$ Hz. $p_{cm}/m \approx E'_g/m^*$[67]$E'_g$ is the bandgap between intermediate and conduction band (~7.4 eV), $m^* = m_0 = m_1 \approx 10^{-30}$ kg[34], and $E_g \approx 9$ eV is the full bandgap. We assumed (i) $\Omega_4 = 1$ (ordered environment for crystals and amorphous materials within the short-medium-range distances), (ii) single level dominates the total transition rate, (iii) The summation of the Bessel functions is evaluated by retaining in the sum over n only the term closest to resonance for the intermediate state tunneling contribution and (iv) one-photon transition is highly nonresonant so that $\omega_{mv} - \omega \approx \omega$[64] (v) dominant component of optical helicity (ϒ) with respect to displacement of singularity. Due to discretization of transition from intermediate state to the conduction band during the tunneling process we assume $\eta = 5$ and $n = \eta + 1$ corresponding to bandgap energy. Thus, the value of $\mathcal{D}$ is 7.3×10^{-5}. The above numerical estimate was plotted in Fig. 5a, c as a function of displacement of singularity. The estimated HD values differ by few orders of magnitude compared to experimental values. This variation could be due the approximate values used for electric dipole and quadrupole moment and the material response.

For n-photon transitions, $|\mathrm{p}_{mv}^{SPA}|^2$ should be substituted by the multiphoton contribution ($|\mathrm{p}_{mv}^{MPA}|^2$) in the transition rate $W_{cv}(\mathbf{k})$ and will contain multitude of cross-correlation terms arising from the summation in the modulus square of the transition amplitude. However, optical helicity $\Upsilon^\pm$ will still be present giving rise to the observed HD (Type I)[25].

Helical dichroism obtained using MPAT is not only limited to the tunneling interaction Hamiltonian $\hat{V}_f$ written in the dipole approximation. Our experimental results can also be described as long as one or both of the interaction Hamiltonian either $\hat{V}_f$ ($\hat{V}_i$) used in the tunneling (multiphoton) probability amplitude includes the contribution of higher-order multipoles to obtain the E1E2 coupling term. For higher incident intensities, the interband excitations are dominated by ground-state tunneling transitions. In this regime, the HD can be explained as long as the interaction Hamiltonian contains the contribution of higher-order multipoles which gives rise to the l-dependence.

Superposition of OAM and Gaussian

The experimental optical setup consists of a combination of waveplates and a q-plate (Supplementary Section 1). When an incident circularly polarized Gaussian beam propagates through the q-plate, it acquires an OAM defined by $l = \pm 2q$. Experimentally, we can measure the efficiency of the the conversion process. If the conversion efficiency is not 100%, as is often the case, the transmitted light will consists of a superposition of Gaussian and Laguerre–Gaussian beam. In other words, a portion of the incident Gaussian will transmit unaffected and the remaining portion will be converted to OAM. In our setup, the incident light is vertically polarized.

$$\begin{gathered}|V\rangle \longrightarrow \mathrm{QWP}(\pm 45)\overset{\mathrm{LHC}}{\rightarrow} \\ \mathrm{RHCQ\text{-}plate}\overset{l+}{\rightarrow} \\ {}_{l-}\mathrm{QWP}(\mp 45) \longrightarrow \mathrm{QWP}\,(\theta)\end{gathered} \tag{21}$$

Vertically polarized light incident onto the first quarter-wave plate (QWP) generates left-CPL (Right-CPL) if the angle of incidence is 45° (−45°) with respect to the horizontal axis. Experimentally, the transmitted light has an ellipticity between 90 and 95% therefore the major and minor axes are not identical. We must take this in account by introducing two variables α and β (such that $|\alpha|^2 + |\beta|^2 = 1$) which are used to vary the ellipticity of the transmitted light that is subsequently incident on the q-plate. Depending on the conversion efficiency of the q-plate, a portion of the light will remain unchanged and the other will acquire an l-value with opposite polarization due to the retardance of π radians. The ratio of Gaussian to Laguerre–Gaussian is determined by the retardation angle ξ. The second QWP was used to generate linearly polarized superimposed Gaussian and OAM beam. The third QWP could be used to produce the desired ellipticities. To determine the polarization state after each optics we will implement the Jones matrices convention for QWP(θ) and HWP(θ), where θ is the angle with respect to the horizontal axis[68,69]. We can define the operation of the q-plate by means of a unitary operator M_Q[57,70]. The handedness of the helical light is determined by the incident circular polarization on the q-plate.

$$\begin{cases} M_Q|\mathrm{LHC}\rangle = \cos\left(\frac{\xi}{2}\right)|\mathrm{LHC}\rangle + i\sin\left(\frac{\xi}{2}\right)|\mathrm{RHC}\rangle e^{il\phi} \\ M_Q|\mathrm{RHC}\rangle = \cos\left(\frac{\xi}{2}\right)|\mathrm{RHC}\rangle + i\sin\left(\frac{\xi}{2}\right)|\mathrm{LHC}\rangle e^{-il\phi} \end{cases} \tag{22}$$

The portion of the light that acquires an l-value also gains a π phase shift between polarization components i.e., the q-plate acts like a HWP with respect to the incident polarization. The output unit vectors of the electromagnetic field can be determined via Jones matrix multiplication of the second and third QWP. Introducing the spatial components of the incident light we can express the electric field for both helicities as

$$\begin{pmatrix}E_{\mathrm{x}}\\E_{\mathrm{y}}\end{pmatrix}_{l\pm} = \frac{1}{\sqrt{2}}\left[\cos(\xi/2)\begin{pmatrix}\alpha\\i\beta\end{pmatrix}e^{-\frac{i\pi}{2}}u_g(x,y,z) + \sin(\xi/2)\begin{pmatrix}\beta\\-i\alpha\end{pmatrix}u_0^\pm(x,y,z)\right] \tag{23}$$

The magnetic field can be obtained via the relation $\mathbf{B}(x,y,z) = \hat{z}\times\mathbf{E}(x,y,z)$.

$$\begin{pmatrix}B_{\mathrm{x}}\\B_{\mathrm{y}}\end{pmatrix}_{l\pm} = \frac{1}{\sqrt{2}}\left[\cos(\xi/2)\begin{pmatrix}\beta\\i\alpha\end{pmatrix}e^{-i\pi}u_g(x,y,z) + \sin(\xi/2)\begin{pmatrix}i\alpha\\\beta\end{pmatrix}u_0^\pm(x,y,z)\right] \tag{24}$$

These expressions were used for the simulations shown in Fig. 5a, c. The $u_0^\pm(x,y,z)$ and $u_g(x,y,z)$ are the Laguerre–Gaussian and Gaussian beam expressions given in Supplementary Section 7[25]. The ± sign represents the handedness of the helical light.

Data availability

The minimum dataset necessary to interpret the results can be obtained from the corresponding authors upon request. The raw and processed data are not deposited in a repository because transmission measurements generate multiple sets of columns and without proper context the data could be hard to interpret.

Code availability

The simulation data were obtained by evaluating the equations using standard technical software. The code is available upon request to the corresponding authors.

References

1. Weber, W. H. & Merlin, R. *Raman Scattering in Materials Science* (Springer, 2000).
2. Zhao, Y. F. et al. Raman spectra of bulk and few-layer GeSe from first-principles calculations. *Front. Mater.* **8**, 736057 (2021).
3. You, Y., Reis, D. & Ghimire, S. Anisotropic high-harmonic generation in bulk crystals. *Nat. Phys.* **13**, 345–349 (2017).
4. Heinrich, T. et al. Chiral high-harmonic generation and spectroscopy on solid surfaces using polarization-tailored strong fields. *Nat. Commun.* **12**, 3723 (2021).
5. Kuroda, R., Novoa, J. J. (Ed.), Braga, D. (Ed.), & Addadi L. (Ed.) Chirality in crystals. *Engineering of Crystalline Materials Properties.* 251 (Springer, 2008).
6. Valentín-Pérez, Á., Rosa, P., Hillard, E. A. & Giorgi, M. Chirality determination in crystals. *Chirality* **34**, 163–181 (2021).
7. Dong, Z. & Ma, Y. Atomic-level handedness determination of chiral crystals using aberration-corrected scanning transmission electron microscopy. *Nat. Commun.* **11**, 1588 (2020).
8. Mavracic, J. et al. Similarity between amorphous and crystalline phases: the case of TiO2. *J. Phys. Chem. Lett.* **9**, 2985–2990 (2018).
9. Lan, S. et al. A medium-range structure motif linking amorphous and crystalline states. *Nat. Mater.* **20**, 1347–1352 (2021).
10. Hufnagel, T. Finding order in disorder. *Nat. Mater.* **3**, 666–667 (2004).
11. Hirata, A. et al. Direct observation of local atomic order in a metallic glass. *Nat. Mater.* **10**, 28–33 (2011).
12. Hirata, A. & Chen, M. Angstrom-beam electron diffraction of amorphous materials. *J. Non-Cryst. Solids* **383**, 52–58 (2014).
13. Singh, J. & Shimakawa, K. *Advances in Amorphous Semiconductors*, 1 edn. (CRC Press, 2003).
14. Elliott, S. R. Medium-range structural order in covalent amorphous solids. *Nature* **354**, 445–452 (1991).
15. Price, D. L. Intermediate-range order in glasses. *Curr. Opin. Solid State Mat. Sci.* **1**, 572–577 (1996).
16. Salmon, P. et al. Topological versus chemical ordering in network glasses at intermediate and extended length scales. *Nature* **435**, 75–78 (2005).
17. Allen, L. et al. Orbital angular momentum of light and the transformation of Laguerre-Gaussian laser modes. *Phys. Rev. A* **45**, 8185 (1992).
18. Andrews, D. L., & Babiker, M. *The Angular Momentum of Light* (Cambridge University Press, 2013).
19. Padgett, M., Courtial, J. & Allen, L. Light's orbital angular momentum. *Physics Today* **57**, 35–40 (2004).
20. Andrews, D. L., Davila Romero, L. C. & Babiker, M. On optical vortex interactions with chiral matter. *Opt. Comm.* **237**, 133–139 (2004).
21. Marrucci, L. et al. Optical Spin-to-orbital angular momentum conversion in inhomogeneous anisotropic media. *Phys. Rev. Lett.* **96**, 163905 (2006).
22. Brullot, W. et al. Resolving enantiomers using the optical angular momentum of twisted light. *Sci. Adv.* **2**, 150134 (2016).
23. Ni, J. et al. Giant helical dichroism of single chiral nanostructures with photonic orbital angular momentum. *ACS Nano* **15**, 2893–2900 (2021).
24. Rouxel, J. R. et al. Hard X-ray helical dichroism of disordered molecular media. *Nat. Photon.* **16**, 570–574 (2022).
25. Bégin, J. L. et al. Nonlinear helical dichroism in chiral and achiral molecules. *Nat. Photon.* **17**, 82–88 (2023).
26. Forbes, K. A. & Andrews, D. L. Spin-robit interactions and chiroptical effects engaging orbital angular momentum of twisted light in chiral and achiral media. *Phys. Rev. A.* **99**, 023837 (2019).
27. Forbes, K. A. & Andrews, D. L. Optical orbital angular momentum: twisted light and chirality. *Opt. Lett.* **43**, 435–438 (2018).
28. Hugo, L. et al. Arbitrary optical wavefront shaping via spin-to-orbit coupling. *J. Opt.* **18**, 124002 (2016).
29. Gertsvolf, M. et al. Orientation-dependent multiphoton ionization in wide band gap crystals. *Phys. Rev. Lett.* **101**, 243001 (2008).
30. Jain, A., Bégin, J. L. & Bhardwaj, R. Helical dichroism in enantiomeric solutions. *J. Chem. Phys.* **7**, 014504 (2023).
31. Keldysh, L. V. Ionization in the field of a strong electromagnetic wave. *Sov. Phys. Jetp.* **20**, 5 (1965).
32. Klaiber, M. & Briggs, J. S. Crossover from tunneling to multiphoton ionization of atoms. *Phys. Rev. A.* **94**, 053405 (2016).
33. Schaffer, C. B. et al. Laser-induced breakdown and damage in bulk transparent materials induced by tightly focused femtosecond laser pulses. *Meas. Sci. Technol.* **12**, 1784 (2002).
34. Wu, A. Q. et al. Femtosecond laser absorption in fused silica: numerical and experimental investigation. *Phys. Rev. B* **72**, 085128 (2005).
35. Sudrie, L. et al. Femtosecond laser-induced damage and filamentary propagation in fused silica. *Phys. Rev. Lett.* **89**, 186601 (2002).
36. Vorobiev, A. K. ESR study of photoselection and photo-orientation. *J. Phys. Chem.* **98**, 11835 (1994).
37. Lee, C. C. & Fan, H. Y. Two-photon absorption with exciton effect for degenerate valence bands. *Phys. Rev. B* **9**, 3502 (1974).
38. Gnani, E. et al. Band-structure calculations of SiO_2 by means of Hartree-Fock and density-functional techniques. *IEEE Trans.* **47**, 10 (2000).
39. Gnani, E., Reggiani, S. & Rudan, M. Density of states and group velocity of electrons in SiO_2 calculated from a full band structure. *Phys. Rev. B* **66**, 195205 (2002).
40. Alagna, L. et al. X-ray natural circular dichroism. *Phys. Rev. Lett.* **80**, 21 (1998).
41. Peacock, D. R. & Stewart, B. Natural circular dichroism in X-ray spectroscopy. *J. Phys. Chem. B* **105**, 351–360 (2001).
42. Naseri, M. et al. Electronic and optical properties of paratellurite TeO_2 under pressure: a first-principles calculation. *Optik* **139**, 9–15 (2017).
43. Davis, K. et al. Band gap engineered zinc oxide nanostructures via a sol-gel synthesis of solvent driven shape-controlled crystal growth. *RSC Adv.* **9**, 14638 (2019).
44. Chang, K. J. & Cohen, M. L. High-pressure behavior of MgO: structural and electronic properties. *Phys. Rev. B* **30**, 8 (1984).
45. Güler, E. et al. A theoretical study for the band gap energies of the most common silica polymorphs. *Chi. J. Phys* **65**, 472 (2020).
46. Nuggent, W. et al. Beyond nature's chiral pool: enantioselective catalysis in industry. *Science* **259**, 479–483 (1993).
47. Rouf, A. & Taneja, S. C. Synthesis of single-enantiomer bioactive molecules: a brief overview. *Chirality* **26**, 63–78 (2014).
48. Torsi, L. et al. A sensitivity-enhanced field-effect chiral sensor. *Nat. Mater.* **7**, 412–417 (2008).
49. Lee, Y. Y. et al. Plasmonic metamaterials for chiral sensing applications. *Nanoscale* **12**, 58 (2020).
50. Aiello, C. D. et al. A chirality-based quantum leap. *ACS Nano.* **16**, 4989 (2022).
51. Shang, Z. et al. Chiral-molecules-based spintronic devices. *Small* **18**, 2203015 (2022).
52. Gross, S. et al. Femtosecond laser induced structural changes in fluorozirconate glass. *Opt. Mater. Express* **3**, 574 (2013).
53. Juodkazis, S. et al. Structural changes in femtosecond laser modified regions inside fused silica. *J. Opt.* **12**, 12400 (2010).
54. Facchetti, A. π Conjugated polymers for organic electronics and photovoltaic cell applications. *Chem. Mater.* **23**, 733 (2011).

55. Wang, S. et al. Experimental evidence that short-range intermolecular aggregation is sufficient for efficient charge transport in conjugated polymers. *Proc. Natl. Acad. Sci. USA* **112**, 10599–10604 (2015).
56. Longman, G. W. et al. Investigation of short range ordering in polymers by means of radial distribution functions derived from X-ray diffraction. *J. of Mat. Sci.* **11**, 1339–1346 (1976).
57. Rubano, A. et al. Q-plate technoloy: a progress review. *J. Opt. So. Am. B* **36**, 5 (2019).
58. Rahimian, M. G. et al. Spatially controlled nano-structuring of silicon with femtosecond vortex pulses. *Sci. Rep.* **10**, 12643 (2020).
59. Geissler, M. et al. Light propagation in field-ionizing media: extreme nonlinear optics. *Phys. Rev. Lett.* **83**, 15 (1999).
60. Jürgens, P. et al. Origin of strong-field-induced low-order harmonic generation in amorphous quartz. *Nat. Phys.* **16**, 1035–1039 (2020).
61. Serebryannikov, E. E. & Zheltikov, A. M. Strong-field photoionization as excited-state tunneling. *Phys. Rev. Lett.* **116**, 123901 (2016).
62. Brandi, H. S. & de Araujos, C. B. Multiphoton absorption coefficients in solids: a universal curve. *J. Phys. C Solid State Phys.* **16**, 5929 (1983).
63. Brandi, H. S. et al. High-intensity approximations applied to multiphoton ionization. *Phys. Rev. A* **24**, 2044 (1981).
64. Boyd, R. W. *Nonlinear Optics,* 3rd edn. (Academic Press, 2020).
65. Golding, B. et al. Intrinsic electric dipole moment of tunneling systems in silica glasses. *Phys. Rev. Lett.* **43**, 1817 (1979).
66. Burin, A. L. et al. Low-temperature breakdown of coherent tunneling in amorphous solids induced by the nuclear quadrupole interaction. *Phys. Rev. B* **73**, 014205 (2006).
67. Vaidyanathan, A. et al. Two-photon absorption in several direct-gap crystals. *Phys. Rev. B* **21**, 743 (1980).
68. Pedrotti, F. & Pedrotti, L. *Introduction to Optics,* 2nd edn. (Prentice-Hall International, Inc., 1993).
69. Saleh, B. E. A. & Teich, M. C. *Fundamentals of Photonics,* 3rd edn. (John Wiley & Sons, Inc, 2019).
70. Delaney, S. et al. Arithmetic with q-plates. *App. Opt.* **56**, 596–600 (2007).

Acknowledgements

The authors thank PhD student Felix Hufnagel from Prof. Karimi's group for fabricating the q-plate used in the experiments. We also acknowledge financial support from the Natural Science and Engineering Council of Canada, Canada Research Chairs, and Canadian Foundation for Innovation.

Author contributions

A.J., J.-L.B., and R.B. conceived, designed, and planned the experiments. A.J. and J.-L.B. conducted the experiments and analyzed the results. A.J., J.-L.B., T.B., and R.B. worked on the theory and conducted numerical simulations. P.C., E.K., and R.B. supervised the project. A.J., J.-L.B., T.B., and R.B. prepared the first draft, and all authors reviewed the manuscript.

Competing interests

The authors declare no competing interests.

Additional information

Supplementary information The online version contains supplementary material available at https://doi.org/10.1038/s41467-024-45735-9.

Correspondence and requests for materials should be addressed to Ashish Jain, Jean-Luc Bégin or Ravi Bhardwaj.

Peer review information *Nature Communications* thanks the anonymous reviewer(s) for their contribution to the peer review of this work. A peer review file is available.

Reprints and permissions information is available at http://www.nature.com/reprints

Intrinsic dichroism in amorphous and crystalline solids with helical light

Ashish Jain[1,*,+], **Jean-Luc Bégin**[1,*,+], **Paul Corkum**[1], **Ebrahim Karimi**[1], **Thomas Brabec**[1], **and Ravi Bhardwaj**[1,*]

[1]Department of Physics, University of Ottawa, Ottawa, ON, K1N 6N5, Canada

[*]Corresponding Author. Ashish Jain, Jean-Luc Bégin, Ravi Bhardwaj. ajain067@uottawa.ca, ravi.bhardwaj@uottawa.ca

[+]These authors contributed equally to this work

Contents

1 Experimental setup

Transmission measurement were performed using a Ti: Sapphire laser amplifier system (45 fs, 800 nm pulses, pulse energy of 2.5 mJ). Figure S1 shows the schematic of our experimental setup. For each successive laser pulse, the energy was varied using a combination of half-wave plate (HWP) and polarizer. Light beams carrying orbital and/or spin angular momentum were generated and controlled by OAM/SAM unit consisting of a combination of quarter-wave plates (QWP), linear polarizer (LP) and a birefringent liquid crystal based phase plate called q-plate[1,2]. When an incident Gaussian beam propagates through the q-plate with a topological charge q, it acquires an OAM defined by $l = \pm 2q$ with a phase singularity (optical vortex). The singularity/null intensity region in the OAM beam was displaced by translating the q-plate, mounted on a x-,y-stages. Moving the q-plate with a step size of $250 \pm 10\mu$m translates to a displacement of the singularity by 300 ± 20nm at the focus.

For every laser shot, the transmitted light signal on the photodiode (PD2) was normalized with the incoming light signal on PD1, reflected off a glass plate positioned in the beam path. An aspheric objective lens (NA=0.3) was used to focus the femtosecond pulses to a spot size 2 ± 0.2 μm into solid samples mounted on a three-axis translation stage. A second aspheric objective with the same NA collected and colliminated the transmitted light onto a photodiode (PD2), positioned immediately after the objective. For each experiment, laser was focussed in the middle of solid sample with typical dimensions $10 \times 10 \times 1$ mm. This was achieved by accurately finding the surface of the sample using back-reflected light that was imaged by a CCD camera. The signals generated by PD1 and PD2 were stretched by an electronic pulse stretcher, discretized and recorded by a data acquisition card. The incident pulse energies were measured before the objective. During the measurement, for every laser shot, the sample was translated by 5μm to irradiate fresh sample. A single-shot auto-correlator (not shown) continuously monitored the pulse duration. The pulse duration at the interaction region was about 100fs.

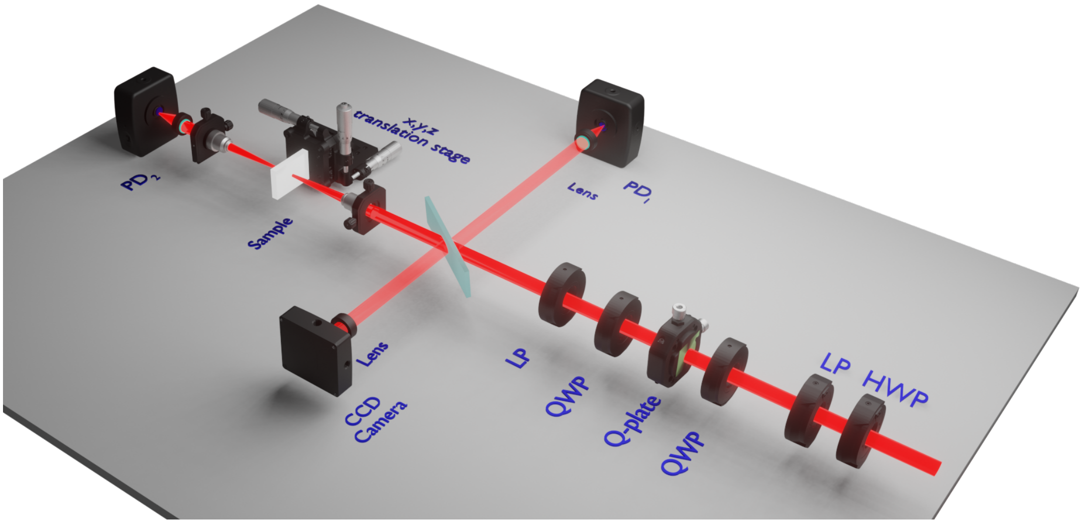

FIG. S 1. Schematic of the experimental setup. The power control consists of a combination of linear polarizer (LP) and half-wave plate (HWP). The OAM and SAM control consists of a combination of quarter-wave plates (QWPs), a birefringent liquid-crystal phase plate (q-plate) and LP (a third QWP can be used to generate elliptically polarized OAM light). Photodiode PD1 (PD2) monitors the incident (transmitted) light. The CCD camera was used to find the surface of the sample. A (x,y,z) translation stage was used to displace the sample. A combination of two aspheric lens (NA=0.3) was used to focus and collimate the incident and transmitted light.

2 Crystal symmetry from transmission measurement

Orientation dependent nonlinear absorption of helical light pulses in ZnO (11-20) and left-handed quartz (z-cut) crystal are shown in Fig. S2 for a specific displacements of the singularity. ZnO (11-20) has a cubic unit cell with 4-fold rotational symmetry and therefore shows a modulation with a periodicity of $\pi/2$. Quartz has a cubic unit cell with 6-fold rotational symmetry and therefore shows a modulation with a periodicity of $\pi/3$. Both crystals exhibit differential absorption between left- and right-handed asymmetrical helical light, defined as HD(Type I). The orientation dependence of transmission is independent of the position of the singularity. However, the magnitude of HD(Type I) signal remains invariant with crystal orientation. Similar results obtained for MgO (100) were presented in the main text.

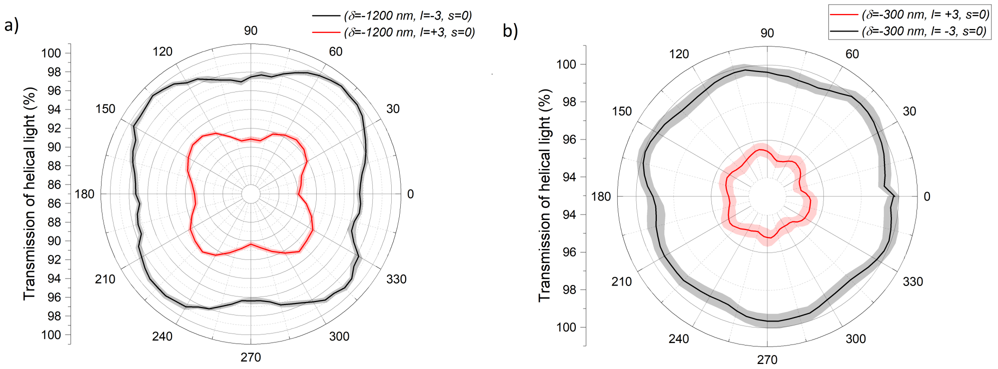

FIG. S 2. Orientational dependent transmission of helical light in crystal. For linearly polarized ($\varepsilon = 0.05$) asymmetrical OAM beam ($l = \pm 3$) in **(a)** ZnO (11-20) for a displaced singularity ($\delta = -1200$ nm) and **(b)** Left-handed α-quartz (z-cut) for a displaced singularity ($\delta = -300$ nm). The error bands represent the standard error at every position of the crystal for n=20.

The crystal structure can also be reproduced using linearly polarized Gaussian light pulses as shown in Fig. S3a for MgO (100) crystal, similar to the case of helical light (fig 1b-d). Therefore, the orientation dependent transmission is not limited to helical light. Fig. S3b shows the energy dependent transmission for a linearly polarized symmetric OAM beam ($l = +1, \delta = 0$) plotted as a function of crystal orientation. As the pulse energy is increased, the transmission of helical light decreased due to the increase in nonlinear absorption. For all three pulse energies above the onset for nonlinear absorption, the 4-fold symmetry is present.

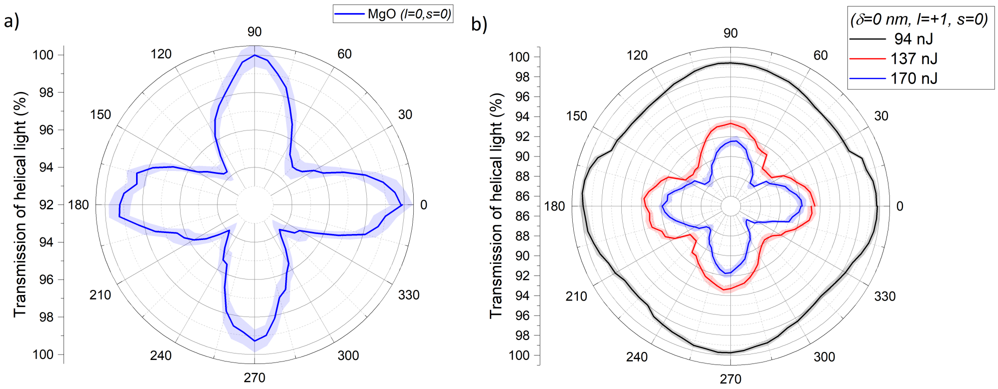

FIG. S 3. Angle dependent transmission of helical light in MgO (100). **(a)** For linearly polarized ($\varepsilon = 0.05$) Gaussian beam. **(b)** Energy dependent transmission as a function of crystal orientation for linearly polarized ($\varepsilon = 0.05$) symmetrical OAM beam ($l = \pm 3$). The error bands represent the standard error at every position of the crystal for n=20.

Fourier analysis of the orientation dependent transmission identifies the different modulation periodicities associated with the crystal symmetry. Figure S4 shows the Fourier power spectrum for the orientation dependent transmission curves of MgO (black) and quartz (blue). For MgO, single peak at 90° corresponds to a 4-fold symmetry. The quartz exhibits a dominant peak at 60 degrees and a smaller one at 120 degrees demonstrating the 6-fold symmetry. Stronger modulation depth in MgO than in quartz could be due to different crystal nonlinearities.

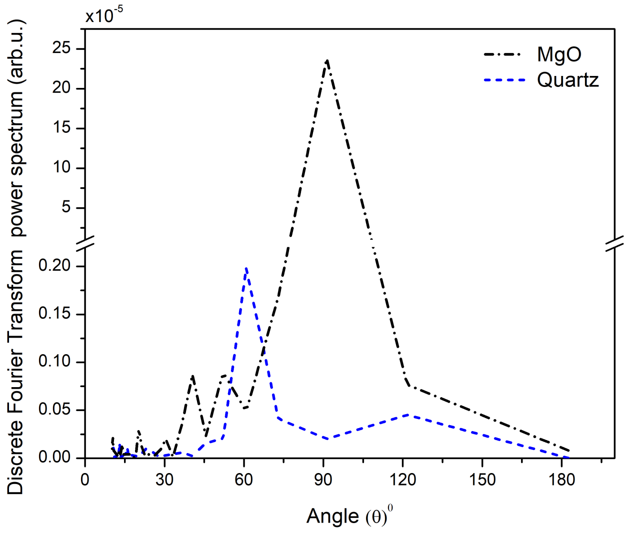

FIG. S 4. Discrete Fourier transform of the orientational dependent transmission in crystals. The black (blue) curve demonstrate the $\pi/2$ ($\pi/3$) periodicity in MgO (left-handed, z-cut, α-quartz).

3 Tunability and scalability of HD(Type I) in crystals

Figure S5 shows experimental results on control and tunability of HD(Type I) in MgO, obtained by (i) superimposing Gaussian and OAM beams, and (ii) varying the l-value. Similar to a-solids (Figure 5), the electric dipole-quadrupole coupling term is non-zero for asymmetric LG beams resulting in HD(Type I). Since this coupling term contains the gradient of the electric field it gives rise to l-dependence, both on its sign and value.

In c-solids, the MPAT process can still play a role, although ordered environment, both short and long range always ensures non-zero HD(Type I) signal upon isortropic averaging. In this case the intermediate states could be due to degenerate exciton states, defects, impurities, and boundary effects[3,4].

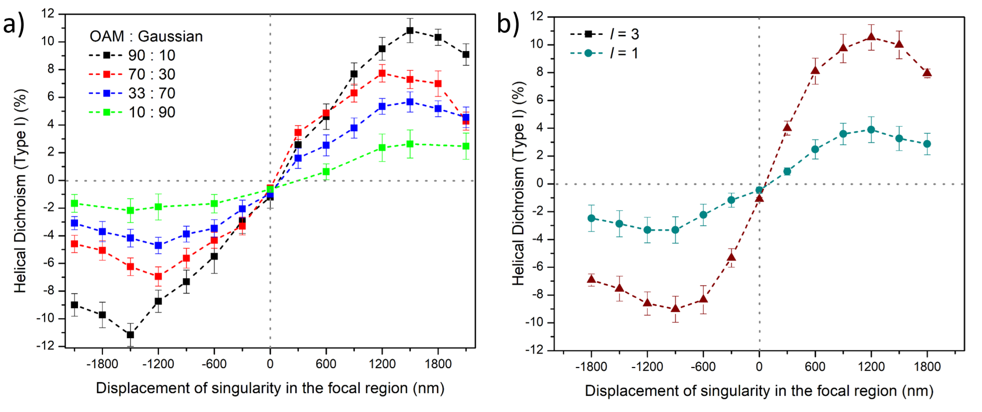

FIG. S 5. Tunability of Helical dichroism. Measured HD(Type I) in MgO as a function of the displacement of singularity for **a)** variable ratios of superposition of linearly polarized ($\varepsilon = 0.05$) OAM ($l = \pm 3$) and Gaussian beams, and **b)** linearly polarized ($\varepsilon = 0.05$) helical light with $l = \pm 1, \pm 3$. The error bars in **a)** and **b)** represent the standard error, of multiple measurements (n=3), calculated for an average peak fluence range used to obtain HD.

4 Fluence Calculation

In Laguerre-Gaussian beams with increasing l-value, the size of the null intensity region at the center increases. Consequently, for the same spot size higher pulse energies are required to reach the threshold for the onset of nonlinear absorption[5]. However, the peak fluence and intensity remains the same for all l-values as can be seen from the inset of Fig. 1a for l=3 and Fig.S6 for l=0.

From the threshold energies and peak power, the l-dependent peak fluence and the intensity was calculated based on the following equations[6]:

$$F_l\left[\frac{J}{cm^2}\right]=\frac{2^{(|l|+1)}r^{2|l|}e^{\frac{-2r^2}{w(z)^2}}}{|l|!\pi w(z)^{2(|l|+1)}}E_l\left[J\right] \qquad I\left[\frac{W}{cm^2}\right]=\frac{2^{(|l|+1)}r^{2|l|}e^{\frac{-2r^2}{w(z)^2}}}{|l|!\pi w(z)^{2(|l|+1)}}P_l\left[W\right] \tag{1}$$

where $l = 0; \pm 1; \pm 2; \pm 3\ldots$ is the orbital angular momentum value, r is the radial direction, $w(z)$ is the radius of a beam evaluated at z and E_l is the threshold pulse energy, and P_l is the peak power for different l-values.

The peak fluence was obtained by evaluating the radial parameter r at the maxima of the intensity profile, which occurs when $r_l^2 = w_0^2|l|/2$. So, for a Gaussian beam ($l = 0$) $r = 0$, and at for OAM beam with $l = 1$ $r_1 = \pm\frac{w_0}{\sqrt{2}}$and so on. Substituting the above values for radial parameter, we obtain

$$\text{For } l = 0 \text{ beam} : F_0\left(r_0\right) = 2\frac{E_0}{\pi w_0^2} \tag{2}$$

$$\text{For l = 1 beam} : F_1\left(r_1\right) = 2e^{-1}\frac{E_1}{\pi w_0^2} \tag{3}$$

The l-dependent peak intensity was used to obtain the Keldysh parameter (eq - main text) and the spatial displacement x_0. Similarly, peak laser fluences or intensities were obtained for higher order OAM beams. In our experiments with different

l-values (Fig-1,4), HD was obtained by taking an average of differential absorption between left- and right- handed helical light over a peak fluence range after the the onset of nonlinear absorption. This insured that response regime we investigated remained the same.

5 Differential absorption with circulary polarized Gaussian beam

Circular dichroism (CD), defined as differential absorption of circularly polarized (CP) Gaussian beam, is not expected to be observed in amorphours solids. On the other hand, chiral solids such as quartz exhibit CD. However, solid-state CD signal is often overshadowed by signals arising from macroscopic anisotropies and linear birefringence[7], as can be seen in the figure below.

To discern the role of polarization and phase of light, we performed transmission measurements with CP Gaussian beams (l=0) in crystalline and amorphous solids. Figure S6 shows normalized transmission of a left- and right-CP Gaussian beam propagating through left-handed quartz and fused silica. In the absence of phase, the two curves overlap in the linear regime exhibiting no differential absorption. In the nonlinear regime, any signal fluctuations are within noise for both types of solids. Similar results were obtained in the case of MgO and right- handed quartz (not shown).

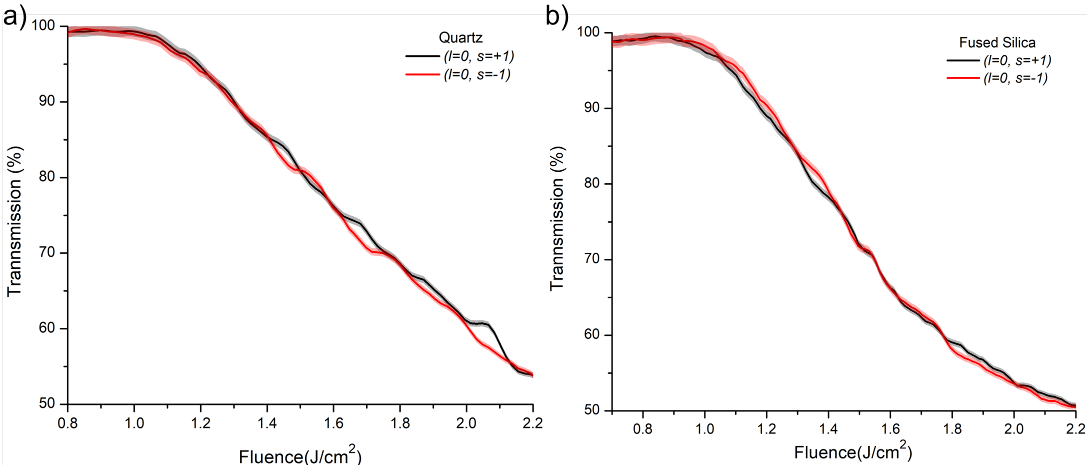

Fig S 6. Normalized transmission of Gaussian beams as a function of peak fluence in crystalline and amorphous solids. Transmission curves for left-circularly polarized ($s = +1$) and right-circularly polarized ($s = -1$) light in **a)** left-handed α-quartz and **b)** fused silica. The error bands represent the standard error for for n=3 independant measurements.

6 Noise check: Transmission measurements in air in the absence of sample

In order to check the background noise in our experimental setup, we performed transmission measurements conducted in air (absence of a sample). Such measurements enable us to ensure that the photodiodes detect identical signals when changing the helicity of the incoming linearly polarized light from $+l$ to $-l$. Fig. S7 a) shows transmission curves (ratio of PD_2/PD_1) of left (black) and right (red) handed asymmetrical LG beams through air. The red and black curves overlaps (within 0.5%) over the entire fluence range. In addition, Fig. S7 b) shows the difference between the PD1 (PD2) signal for linearly polarized $+l$ and $-l$. Signals are centered about zero with a fluctuation of $\pm 0.05V$ and curves almost overlap over the entire energy range. Both these results demonstrates that there is no arbitrary signal/noise introduced by the experimental setup to the observed differential absorption in crystalline and amorphous solids. Transmission measurements in air were performed before every experimental run and for every position of the displaced singularity.

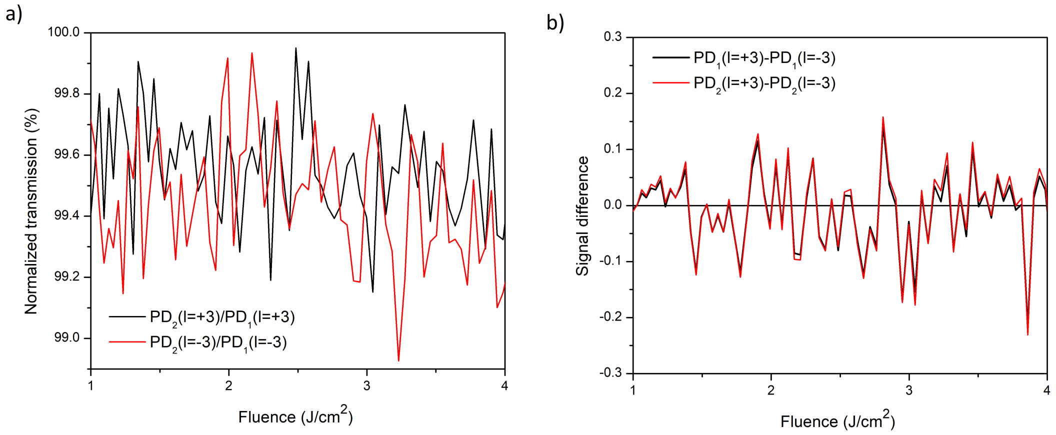

FIG. S 7. Transmission of linearly polarized ($\varepsilon = 0.05$) helical light in air for symmetrical OAM beam. a) Ratio of PD2 and PD1 signals for $l = +3$ (black) and $l = -3$ (red). **b**) The difference in photodiode signals for the two helicities, PD1 in black and PD2 in red. PD1 (PD2) monitors the incident (transmitted) light.

7 Asymmetric Laguerre-Gaussian beams

Asymmetric Laguerre-Gaussian beams denoted by an asymmetry parameter, δ, was used in our theoretical analysis. For arbitrary polarization in the paraxial regime, the field components can be written as[5]

$$u_o^{\pm}(x,y,z) = E_0 \exp[ikz]\left(\frac{\sqrt{2}\left((x\mp i\eta\delta)\pm i(y\mp i\zeta\delta)\right)}{w_0}\right)^{|l|}\exp\left(-\frac{(x^2+y^2)}{w_0^2}\right)L_{p-j}^{|(l+j)|}\left(\frac{2\rho^2}{w_0^2}\right) \tag{4}$$

$$\mathbf{E}^{\pm}(x,y,z) = \begin{cases} \alpha u_0^{\pm}(x,y,z) \\ \beta u_0^{\pm}(x,y,z) \\ if\left[(\alpha \pm i\beta)\frac{|l|w_0((x\mp i\eta\delta)\mp i(y\mp i\zeta\delta))}{(x\mp i\eta\delta)^2+(y\mp i\zeta\delta)^2}u_0^{\pm}(x,y,z) - \frac{2}{w_0}\left(\alpha(x)+\beta(y)\right)u_0^{\pm}(x,y,z)\right] \end{cases} \tag{5}$$

$$\mathbf{B}^{\pm}(x,y,z) = \begin{cases} -\beta\frac{k}{\omega}u_0^{\pm}(x,y,z) \\ \alpha\frac{k}{\omega}u_0^{\pm}(x,y,z) \\ if\frac{k}{\omega}\left[(\alpha \pm i\beta)\frac{|l|w_0((y\mp i\zeta\delta)\pm i(x\mp i\eta\delta))}{(x\mp i\eta\delta)^2+(y\mp i\zeta\delta)^2}u_0^{\pm}(x,y,z) - \frac{2}{w_0}\left(\alpha(y)-\beta(x)\right)u_0^{\pm}(x,y,z)\right] \end{cases} \tag{6}$$

where $f = \lambda/2\pi w_0$, ω is the laser frequency and $\rho = \sqrt{x^2+y^2}$. The $\pm$ represents the rotational direction of l with no radial node, $p = 0$. The polarization factors α and β are normalized such that $|\alpha|^2 + |\beta|^2 = 1$. Displacement of singularity in the x-y plane was achieved by varying η and ζ. For generalization, we substituted $\eta = 3/2$ and $\zeta = 1/8$, considering the movement of singularity to be perpendicular to the polarization following experimental conditions.

E_0 is the normalization factor obtained by integrating the intensity over all space ($-\infty$ to $+\infty$), for ($l = 1$) it is given as :

$$E_0 = \sqrt{\frac{2k^2w_0^2}{\pi\left(\alpha^2+\beta^2\right)\left(2w_0^2+k^2w_0^4+2\left(\zeta^2+\eta^2\right)\delta^2\left(1+k^2w_0^2\right)\right)}} \tag{7}$$

Intensity profile of asymmetrical Laguerre-Gaussian beam with varying singularity position (δ) is shown in Fig. S8. As a correction to the paraxial regime (due to its finite l dependence) the longitudinal component of the field (E_z) can be considered[8,9]. The contribution of the longitudinal component becomes significant when light is focused tightly using a higher NA objective and is recently demonstrated in differentiating nanoparticle aggregates using helical light[10].

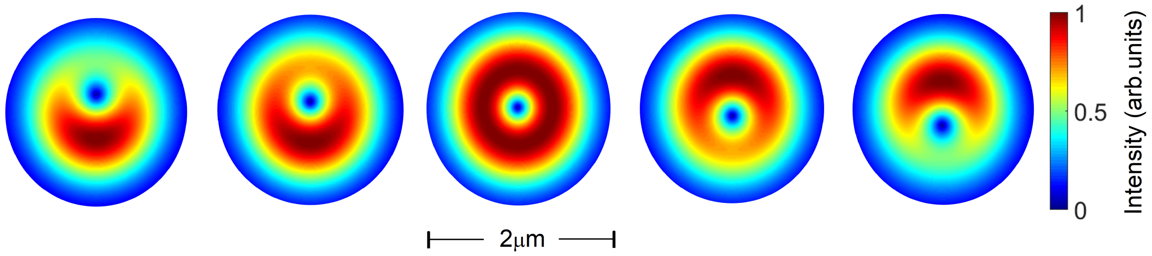

FIG. S 8. Asymmetrical Laguerre-Gaussian beam. Simulated intensity profiles of asymmetric OAM beams obtained by varying the δ parameter.

8 Multiphoton assisted tunneling

Absorption of electromagnetic field by any material results in electron transition from an unperturbed ground state to an excited state or continuum (conduction band in case of solids). The transition mechanism is primarily governed by the energy of the incident photon and energy difference between the ground and excited/continuum states. When photon energy is lower than the energy difference, absorption is dominated by nonlinear process either via multiphoton absorption when the incident field intensity is low or via tunneling when the field intensity is sufficiently large. The type of mechanism can be identified by Keldysh parameter, γ, for both solids and gases. When $\gamma \gtrsim 2$, transitions are dominated by multiphoton and when $\gamma < 1$ they are dominated by tunnelling[11–13]. $1 < \gamma < 2$ is the intermediate regime in which combination of both multiphoton and tunneling contribute to electron transitions, known as Multiphoton Assisted Tunneling (MPAT).

In MPAT, electron transitions from the ground state (valence band in solids) to an intermediate state (band tail/defect states in solids) by absorption of a single or multiple photons followed by transition to the continuum (conduction band in solids) via tunneling. MPAT is therefore responsible for the smooth and continuous transition from the dominant multiphoton ionization to the pure tunneling regime characterized by the varying Keldysh parameter. The idea of MPAT is based on the fact that whenever an incident photon is absorbed it causes the wavefunction to extend to larger distances depending on the wavelength and intensity of the incident light. Ionization via tunneling can readily occur from such extended and weakly bound states[11].

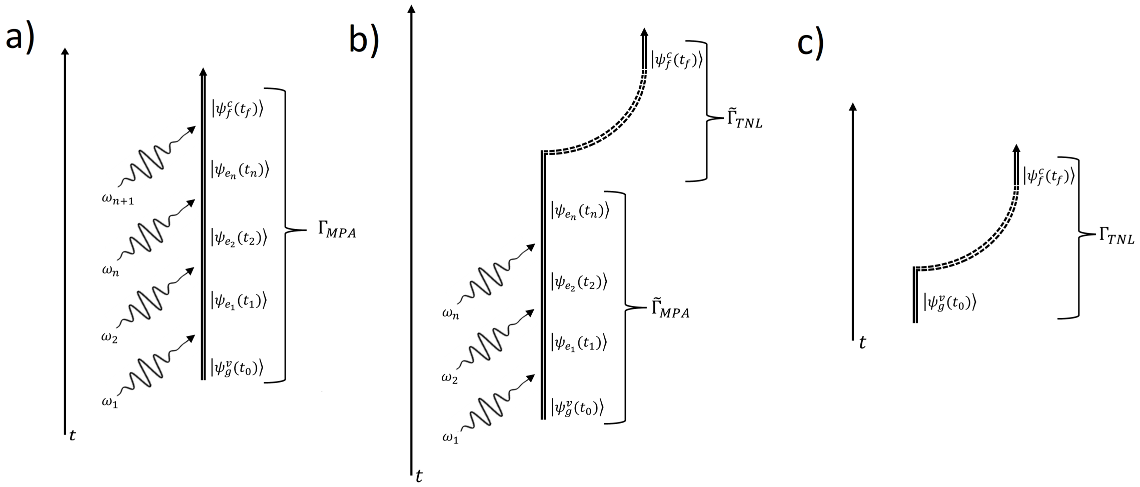

FIG. S 9. Feynman diagrams for a) multiphoton regime, it takes an absorption of $(n+1)\hbar\omega$ to reach the conduction band. b) MPAT process, absorption of n-photon leading to an excited/tail state and subsequent tunneling to the conduction band. c) tunneling regime, the incident field is strong enough to force the electron to tunnel from the valence band(ψ_g^v) to the conduction band(ψ_f^c).

Ionization probability for MPAT process can be qualitatively understood by a unified approach where the total probability amplitude consists of a product of two separate amplitudes corresponding to single/multiphoton absorption and tunneling. It can also be visually understood using Feynman diagram shown in Fig. S9 for all three different regimes. In general, transition amplitude is defined as a projection of non-interacting state to a fully evolved state at large times[14–16] given by

$$M_{fi} = \lim_{t\to\infty}\langle\psi_f(t)|\Psi_i(t)\rangle \tag{8}$$

where $\Psi_i(t)$ is the total wave function of time-evolved ground state, ψ_g, when the laser field is turned on. $\Psi_i(t)$ is a solution of the time-dependent Schrodinger equation, $[i\hbar\frac{\partial}{\partial t} - \hat{H}(t)]\Psi_i(t) = 0$. In the presence of the laser field, the full Hamiltonian is given by $\hat{H}(t) = \hat{H}_0 + \hat{V}(t)$ where $\hat{H}_0$ is the field-free Hamiltonian and $\hat{V}(t)$ represents the interaction Hamiltonian of the system at time t. The final state $\psi_f(t)$, and initial state are orthogonal, $\langle\psi_f|\psi_g\rangle = 0$. The total wavefunction is obtained by solving the the time-dependent Schrodinger equation using the Green function $\hat{G}(t,t')$. The Green function is closely related to the time evolution operators, $\hat{G}(t,t') = -i\Theta(t-t')\hat{U}(t,t')$[14, 16] where $\Theta(t-t')$ is the Heaviside step function and $\hat{U}(t,t')$ is a unitary time operator. Therefore, the total wavefunction can be expressed as

$$|\Psi_i(t)\rangle = \hat{U}_0(t,t_0)|\psi_g\rangle - \frac{i}{\hbar}\int_{t_0}^{t}\Theta(t-t')\hat{U}(t,t')V(t')|\psi_g(t')\rangle dt' \tag{9}$$

The first term corresponds to unperturbed evolution, $\hat{U}_0(t,t_0)$, of the ground state and the second term corresponds to evolution of the ground state when the laser is turned on at time t_0.

The transition amplitude is not limited to just initial and final states. We can partition the total Hamiltonian to introduce intermediate excited states, which can be obtained by expanding the time propagator $\hat{U}(t,t')$ in terms of the Dyson series[14–17]. In the Dyson expansion, we consider up to the second order term which corresponds to first order MPAT process (a single photon absorption to the intermediate state and subsequent tunnelling from this intermediate state to the continuum/conduction band). By substituting the expanded time propagator into the total wavefunction (eq. 9) and afterwards inserting this expanded wavefunction into the transition amplitude (eq. 8) we obtain

$$M_{fg} = \frac{1}{i\hbar}\int_{t_0}^{t}\langle\psi_f(\tau_1)|\hat{V}_i(\tau_1)|\psi_g(\tau_1)\rangle d\tau_1 + \frac{1}{\hbar^2}\int_{t_0}^{t}\int_{t_0}^{\tau}\langle\psi_f(\tau)|\hat{V}_f(\tau)\hat{U}(\tau,\tau_1)\hat{V}_i(\tau_1)|\psi_g(\tau_1)\rangle d\tau_1 d\tau \tag{10}$$

where $\hat{V}_i$ and $\hat{V}_f$ are the interaction Hamiltonian at time τ_1 and τ, respectively. Also, we used the property of the Heaviside step function $\lim_{t\to\infty}\Theta(t-\tau) = 1$. The first term in the above equation represents standard ground state tunneling and the second term represents the first order MPAT process. When experimental intensities are not sufficient for ground state tunneling (intermediate regime, $1 \lesssim \gamma \lesssim 2$) the second term becomes dominant. Therefore, for a multitude of intermediate states, the MPAT transition amplitude is given by

$$M_{fg} = \frac{1}{\hbar^2}\sum_m\int_{t_0}^{t}\int_{t_0}^{\tau}\langle\psi_f(\tau)|\hat{V}_f(\tau)|\psi_m(\tau)\rangle\langle\psi_m(\tau)|\hat{U}(\tau,\tau_1)\hat{V}_i(\tau_1)|\psi_g(\tau_1)\rangle d\tau_1 d\tau \tag{11}$$

where we introduced the projection of the intermediate state $\mathbb{1} = \sum_m|\psi_m(\tau)\rangle\langle\psi_m(\tau)|$[18]. Using the property $\langle\psi_m(\tau)|\hat{U}(\tau,\tau_1) = \langle\psi_m(\tau_1)|$, and explicitly writing the time component we obtain

$$M_{fg} = \frac{1}{\hbar^2}\sum_m\int_{t_0}^{t}\langle\psi_f(\tau)|\hat{V}_f(\tau)|\psi_m(\tau)\int_{t_0}^{\tau}\langle\psi_m|\hat{V}_i(\tau_1)|\psi_g\rangle e^{i\omega_{mg}\tau_1}d\tau_1 d\tau \tag{12}$$

The multiphoton component of the interaction Hamiltonian, $\hat{V}_i$, can be written in a non-dipole form containing E1, M1 and E2 terms. For single photon absorption, we substitute $\hat{V}_i(t') = \hat{V}_i e^{-i\omega t'}$ in the above equation (where ω is the laser frequency) to get

$$M_{fg} = \sum_m \underbrace{\frac{\langle\psi_m|\hat{V}_i|\psi_g\rangle}{\hbar(\omega_{mg}-\omega)}}_{M_{SPA}}\underbrace{\frac{i}{\hbar}\int_{t_0}^{t}d\tau\langle\psi_V(\tau)|\hat{V}_f(\tau)|\psi_m(\tau)e^{i(\omega_{mv}-\omega)\tau}}_{M_{TNL}} \tag{13}$$

The transition amplitude M_{fg} is a product of time-independent transition amplitude, M_{SPA}, corresponding to a single photon absorption to an intermediate state and time-dependent amplitude, M_{TNL}, corresponding to tunneling from intermediate state to continuum/conduction band. $\hat{V}_i$ ($\hat{V}_f$) is the multiphoton (tunneling) interaction Hamiltonian.

For the nth order MPAT process, the transition amplitude consists of a product of the n-photon absorption and subsequent tunneling.

$$M_{fg}=\left(\frac{1}{i\hbar}\right)^2\sum_m\sum_l\int_{t_0}^{t}d\tau\langle\psi_f(\tau)|\hat{V}_f(\tau)|\psi_m(\tau)\rangle\int_{t_0}^{\tau}dt'\langle\psi_m|\hat{V}\left(t'\right)|\psi_l\rangle c_l^{(n-1)}\left(t'\right)e^{i\omega_{ml}t'} \tag{14}$$

where $c_l^{(n-1)}(\tau)$ is the probability amplitude of the $(n-1)^{\text{th}}$ order perturbation (multiphoton probability amplitude)[19]. The n$^{\text{th}}$ order probability amplitude can be expressed as

$$c_m^{(n)}\left(\tau\right)=\left(\frac{1}{i\hbar}\right)\sum_l\int_{t_0}^{\tau}dt'\langle\psi_m|\hat{V}\left(t'\right)|\psi_l\rangle c_l^{(n-1)}\left(t'\right)e^{i\omega_{ml}t'} \tag{15}$$

Multiphoton transitions in MPAT will result in multitiude of excited state cross-correlation terms and coupling terms arising from multipole expansion due to the tensor nature of the material response. However, the material cross terms (such as electric–magnetic dipole and electric dipole–quadrupole coupling) will have similar qualitative behaviour as that of a single photon case. Therefore, to keep the equations tractable, we consider the MPAT process using single photon absorption in the manuscript.

Equations 12 can also be obtained by writting the time evolved initial state $\psi_g(\tau)$ as a linear combination of eigenstates (bound-state) of the unperturbed Hamiltonian[19,20], as

$$|\psi_g^{(n)}(\mathbf{r},\tau)\rangle=\sum_m c_m^{(n)}(\tau)e^{-i\frac{E_m}{\hbar}\tau}|\psi_m(\mathbf{r})\rangle=\sum_m c_m^{(n)}(\tau)|\psi_m(\mathbf{r},\tau)\rangle \tag{16}$$

where E_m is the energy of the m$^{\text{th}}$ eigenstate, $\psi_m(\mathbf{r})$, where $\omega_{ml}=(E_m-E_l)/\hbar$

9 Total MPAT transition rate for linear polarization

To obtain a numerical estimate of the total transition rate, for simplicity, we consider the incident field as linearly polarized. Therefore the probability amplitude from the main text (equation 11) becomes:

$$M_{cv}=\frac{iA_0e}{m\hbar(2\pi)^{3/2}}\frac{1}{\gamma_0}\sum_m \mathrm{p}_{mv}^{SPA}\frac{p_{cm}}{k_x}\sum_{\eta=-\infty}^{\infty}\eta\mathrm{J}_\eta(-\gamma_0k_x)\left[\lim_{T\to\infty}\frac{2\hbar sin\left((E_g+\varepsilon-n\hbar\omega)\frac{T}{2\hbar}\right)}{(E_g+\varepsilon-n\hbar\omega)}\right] \tag{17}$$

where $\varepsilon=\frac{\hbar^2k^2}{2m^*}$ is the total kinetic energy, $m^{*-1}=m_1^{-1}-m_0^{-1}$ is the total effective electron mass and $n\hbar\omega=\eta\hbar\omega+\hbar\omega$, and assuming the intermediate and conduction band states have similar $\mathbf{k}$ ($\mathbf{k}''\approx\mathbf{k}'\approx\mathbf{k}$) the material response $p_{cm}=\int_{-\infty}^{\infty}u_{\mathbf{k}}^{c*}(\mathbf{r})p_xu_{\mathbf{k}''}^{m}(\mathbf{r})d^3r$

Following the main text, we further define the tunneling transition contribution as

$$\mathrm{p}_{cm}^{TNL}=\frac{m_1}{m\hbar(2\pi)^{3/2}}\frac{p_{cm}}{k_x}\sum_{\eta=-\infty}^{\infty}\eta\mathrm{J}_\eta(-\gamma_0k_x) \tag{18}$$

Using the property $\lim\limits_{T\to\infty}T^2\frac{sin^2(x)}{x^2}=2\pi\hbar T\delta\left(\varepsilon+E_g-n\hbar\omega\right)$ where $x=\left(E_g+\varepsilon-n\hbar\omega\right)\frac{T}{2\hbar}$[19], the transition rate from valence to the conduction band, defined as $W_{cv}=\frac{d}{dt}|M_{cv}|^2$, can be expressed as

$$W_{cv}\left(\mathbf{k}\right)=2\pi\hbar\omega^2\sum_m\left|\mathrm{p}_{cm}^{TNL}\right|^2\left|\mathrm{p}_{mv}^{SPA}\right|^2\delta\left(\varepsilon+E_g-n\hbar\omega\right) \tag{19}$$

The total transition rate (per unit of volume) can be obtained by integrating over crystal momentum associated with the discrete transition:

$$W=\int\frac{\mathrm{d}^3k}{(2\pi)^3}W_{cv}(\mathbf{k})$$

Using the properties of Bessel's functions, the weak-field limit for the non-perturbative discrete transition rate is given by[21,22]

$$\mathrm{W} = \frac{1}{(2\pi)^4\hbar}\sum_m \left(\frac{m_1\omega p_{\mathrm{cm}}}{m(\eta-1)!}\right)^2 |\mathrm{p}_{mv}^{SPA}|^2 \left(\frac{eA_0}{2m_1\omega}\right)^{2\eta} \left(\frac{2m^*}{\hbar^2}\right)^{(2\eta+1)/2} \left(\frac{(n\hbar\omega - E_{\mathrm{g}})}{(2\eta-1)}\right)^{(2\eta-1)/2} \tag{20}$$

where

$$\left|\mathrm{p}_{mv}^{SPA}\right|^2 = \frac{1}{\hbar^2\left(\omega_{mv}-\omega\right)^2}\left[|\mu_i^{mv}|^2|E_i^{\pm}|^2 + |m_i^{mv}|^2|B_i^{\pm}|^2 + 2\langle\mu_i^{mv}m_i^{vm}\rangle_P \mathrm{Im}\left[E_i^{\pm*}B_i^{\pm}\right] + \frac{2}{3}\langle\mu_i^{mv}\theta_{ij}^{vm}\rangle_P \mathrm{Re}\left[\nabla_i E_j^{\pm}E_i^{\pm*}\right]\right] \tag{21}$$

Difference in the interband transition rates between left- and right-handed helical light with beam asymmetry parameter δ can be expressed as:

$$\Delta\mathbf{W} = \mathrm{W}_{\delta}^{+} - \mathrm{W}_{\delta}^{-} = \frac{1}{\hbar^2\left(\omega_{mv}-\omega\right)^2}\tilde{\mathrm{W}}\left[\Omega\left(\frac{2}{3}\mu_i^{mv}\theta_{ij}^{vm}\right)\left(\mathrm{Re}\left[\nabla_i E_j^{+}E_i^{+*}\right] - \mathrm{Re}\left[\nabla_i E_j^{-}E_i^{-*}\right]\right)\right] = D\left(\Upsilon^{+} - \Upsilon^{-}\right) \tag{22}$$

HD(Type I) can now be defined in terms of energy absorbed Γ normalized with respect to incident energy, $\mathscr{E}_{inc}$ as:

$$\Delta\Gamma = \underbrace{\Gamma^{+} - \Gamma^{-}}_{\text{HD (Type I)}} = \frac{\hbar}{\mathscr{E}_{inc}}\left(\mathrm{W}_{\delta}^{+} - \mathrm{W}_{\delta}^{-}\right) = \mathscr{D}\left(\Upsilon^{+} - \Upsilon^{-}\right) \tag{23}$$

where $\mathrm{W} = \left|\mathrm{p}_{mv}^{SPA}\right|^2 \tilde{\mathrm{W}}$ from eq-29, $\mathscr{D} = \frac{\hbar \mathrm{D}}{\mathscr{E}_{inc}}$ and $\Upsilon^{\pm} = \mathrm{Re}\left[\nabla_i E_j^{\pm}E_i^{\pm*}\right]$ represent the optical helicity term describing the handedness of helical light. Optical helicity can be expanded as[23], $\Upsilon^{\pm} = \left[\left(\nabla_\alpha E_\beta E_\alpha^* + E_\alpha(\nabla_\alpha E_\beta)^{\dagger}\right)\right] = \mathrm{Re}\left[E_i^{\pm*}\nabla_i E_j^{\pm\dagger}\right]$. The above equation was plotted in Fig.5 as a function of displacement of singularity in the main text.

10 Supplementary References

1. Marrucci, L., Manzo, C., & Paparo, D., Optical Spin-to-Orbital Angular Momentum Conversion in Inhomogeneous Anisotropic Media. *Phys. Rev. Lett.*, **96**, 163905 (2006).
2. Hugo, L., et al. Arbitrary optical wavefront shaping via spin-to-orbit coupling. *J. Opt.* **18**, 124002 (2016).
3. Lee, C.C., & Fan, H.Y. Two-photon absorption with exciton effect for degenerate valence bands *Phys. Rev. B* **9**, 3502 (1974).
4. Gnani, E., et al. Band-structure calculations of SiO_2 by means of Hartree-Fock and Density-Functional Techniques *IEEE transactions on electron devices* **47**, no. 10 (2000)
5. Bégin, JL., Jain, A., & Parks, A. et al. Nonlinear helical dichroism in chiral and achiral molecules. *Nat. Photon.* **17**, 82–88 (2023).
6. Hnatovsky, C., et al. Materials processing with a tightly focused femtosecond laser vortex pulse. *Opt. Lett.* 35 **20**, 3417 (2010).
7. Kuroda, R., Novoa, J.J., Chirality in crystals. Engineering of crystalline materials properties, *Springer*; New York. p. 251 (2008)
8. Cerjan, A., et al. Orbital angular momentum of Laguerre-Gaussian beams beyond the paraxial approximation. *J. Opt. Soc. Am.A* **28**, 2253-2260 (2011).
9. Forbes, K.A., et al. Relevance of longitudinal of paraxial optical vortices *J. Opt.* **23**, 075401 (2021).
10. Brullot, W., et al. Resolving enantiomers using the optical angular momentum of twisted light. *Sci. Adv.* **2**, 150134 (2021).
11. Klaiber, M. & J.S. Briggs Crossover from tunneling to multiphoton ionization of atoms. *Phys. Rev. A.* **94**, 053405 (2016)
12. Schaffer, C.B., et al. Laser-induced breakdown and damage in bulk transparent materials induced by tightly focused femtosecond laser pulses *Meas. Sci. Technol.* **12**, 1784 (2002)
13. Wu, A.Q., et al. Femtosecond laser absorption in fused silica: Numerical and experimental investigation *Phys. Rev. B* **72**, 085128 (2005)
14. Long, Z.J. & Liu, W-K. Keldysh theory of strong-field ionization *Canadian journal of Physics* **88**, 4, (2010)

15. Becker, A. & Faisal F.H.M. Intense-field many-body S-matrix theory *J. Phys. B: At. Mol. Opt. Phys.* **38** (2005)

16. Reiss, H.R. Theoretical methods in quantum optics: S-matrix and Keldysh techniques for strong-field processes *Prog. Quant. Electr.* **16**, 1-71 (1992)

17. Becker, W. et al. Above-Threshold Ionization: From Classical Features to Quantum Effects. *Advances In Atomic, Molecular, and Optical Physics, Academic Press,* **48** (2002).

18. Sakurai, J., & Napolitano, J. *Modern Quantum Mechanics (2nd ed.)* Cambridge University Press (2017).

19. Boyd, R.W., *Nonlinear Optics (3rd ed.)* (Academic Press, 2020).

20. Serebryannikov, E.E., & Zheltikov, A.M., Strong-Field Photoionization as Excited-State Tunneling *Phys. Rev. Lett.* **116**, 123901, (2016)

21. Brandi, H.S. & de Araujos, C.B., Multiphoton absorption coefficients in solids: a universal curve. *J. Phys. C: Solid State Phys.* **16** 5929 (1983)

22. Brandi, H.S., Davidovich, L., & Zagury N., High-intensity approximations applied to multiphoton ionization. *Phys. Rev. A* **24**, 2044 (1981)

23. Bégin, J.L., Jain, A., & Parks, A. et al. Nonlinear helical dichroism in chiral and achiral molecules. *Nat. Photon.* **17**, 82–88 (2023).

References

[1] W. H. Weber and R. Merlin. *Raman Scattering in Materials Science.* Springer, 2000.

[2] Y. F. Zhao et al. Raman spectra of bulk and few-layer gese from first-principles calculations. *Frontiers in Materials*, 8:736057, 2021.

[3] Y. You, D. Reis, and S. Ghimire. Anisotropic high-harmonic generation in bulk crystals. *Nature Physics*, 13:345–349, 2017.

[4] T. Heinrich et al. Chiral high-harmonic generation and spectroscopy on solid surfaces using polarization-tailored strong fields. *Nature Communications*, 12:3723, 2021.

[5] R. Kuroda, J. J. Novoa, D. Braga, and L. Addadi. *Chirality in Crystals*, page 251. Springer, 2008.

[6] Z. Dong and Y. Ma. Atomic-level handedness determination of chiral crystals using aberration-corrected scanning transmission electron microscopy. *Nature Communications*, 11:1588, 2020.

[7] Á. Valentín-Pérez, P. Rosa, E. A. Hillard, and M. Giorgi. Chirality determination in crystals. *Chirality*, 34:163–181, 2021.

[8] S. R. Elliott. Medium-range structural order in covalent amorphous solids. *Nature*, 354:445–452, 1991.

[9] D. L. Price. Intermediate-range order in glasses. *Current Opinion in Solid State and Materials Science*, 1:572–577, 1996.

[10] P. Salmon et al. Topological versus chemical ordering in network glasses at intermediate and extended length scales. *Nature*, 435:75–78, 2005.

[11] J. Singh and K. Shimakawa. *Advances in Amorphous Semiconductors.* CRC Press, 1 edition, 2003.

[12] S. Lan et al. A medium-range structure motif linking amorphous and crystalline states. *Nature Materials*, 20:1347–1352, 2021.

[13] K. A. Forbes and D. L. Andrews. Optical orbital angular momentum: twisted light and chirality. *Optical Letters*, 43:435–438, 2018.

[14] K. A. Forbes and D. L. Andrews. Spin-orbit interactions and chiroptical effects engaging orbital angular momentum of twisted light in chiral and achiral media. *Physical Review A*, 99:023837, 2019.

Chapter 6

Selective absorption of helical light in achiral and chiral plasmonic metasurfaces

6.1 Intoduction

Until now, we have seen how matter behaves when helical light interacts in the nonlinear interaction regime. From the multiphoton interaction regime in liquids and to the multiphoton-assisted tunneling (MPAT) regime in solids, the phenomenon of phase-based differential response was observed. However, a spectroscopy technique can only be considered universal (in terms of application across various disciplines) if it also operates within the linear regime. A straightforward way to investigate the linear interaction of helical light is by using metals.

This work demonstrated the presence of helical dichroism in plasmonic nano- and microstructured achiral and chiral metasurfaces. Similar to liquids and solids, the achiral structures exhibited a phase-based differential response, which had previously been shown to be nonexistent in earlier studies [1, 2]. The results were consistent with numerical simulations based on linear absorption theory using helical light and were further validated through light propagation simulations using the Lumerical FDTD software. This work has been accepted for publication in the *ACS Nano* journal.

6.2 Statement of contribution

Ashish Jain and Ravi Bhardwaj conceived, designed, and planned the experiments. Howard Northfield fabricated the plasmonic metasurfaces. Ashish Jain performed the experiments and conducted the Lumerical FDTD and numerical simulations. Ashish Jain and Ravi Bhardwaj analyzed the results. Pierre Berini, Ebrahim Karimi, and Ravi Bhardwaj supervised the project. Ashish Jain and Ravi Bhardwaj prepared the first draft, and all authors reviewed the manuscript.

ACS NANO
www.acsnano.org

Selective and Tunable Absorption of Twisted Light in Achiral and Chiral Plasmonic Metasurfaces

Ashish Jain,* Howard Northfield, Ebrahim Karimi, Pierre Berini, and Ravi Bhardwaj*

Cite This: https://doi.org/10.1021/acsnano.4c06983 Read Online

ACCESS | Metrics & More | Article Recommendations | Supporting Information

ABSTRACT: **The symmetry of achiral metasurfaces suggests selective absorption is nonexistent when irradiated either by circularly polarized Gaussian or twisted light beams carrying orbital angular momentum (OAM). In chiral metasurfaces, the lack of symmetry leads to differential absorption when probed with chiral light either in the form of circular polarization (circular dichroism) or helical phase fronts (helical dichroism). Here, we demonstrate differential absorption of asymmetric twisted light beams, known as helical dichroism, which exist in an array and a single achiral structure and can be controlled. When extended to chiral structures, these asymmetrical chiral light modes enable to enhance and tune chiroptical sensitivity. Our technique offers more control parameters than just changing the OAM value, as presented in previous studies. Selective response to asymmetric helical light beams is qualitatively explained in terms of induced multipole moments. The presence of dichroism in achiral nanostructures offers a significant fabrication advantage over complex chiral structures and enables the development of next-generation plasmonic-based chiroptical spectroscopy and molecular sensing.**

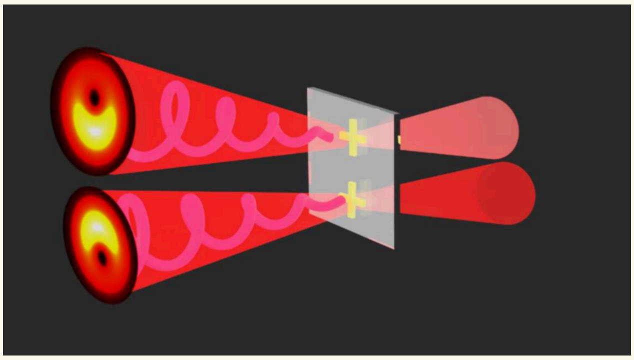

KEYWORDS: *OAM beams, controlled light absorption, helical dichroism, chiral spectroscopy, achiral nanostructures, optical activity, plasmonics*

INTRODUCTION

Chiroptical spectroscopy exploits chiral light-matter interaction where an object's handedness or asymmetry creates optical activity. Probing chirality at the molecular level is challenging because optical activity is inherently weak due to the mismatch between the size of the molecule and the wavelength of light. To enhance the chiroptical signal, metallic/dielectric nanoparticles[1−4] and metasurfaces[5−9] have been employed to leverage local field effects associated with plasmon resonances. Chiral metasurfaces offer advanced light-manipulating abilities because their optical response is dependent on the design parameters.[9] In addition, they offer design flexibility by reducing the complexity involved in their fabrication in comparison to 3D chiral structures.[10,11] A metasurface is structured as an array (matrix) of nanostructures in order to produce a large enough chiroptical response when illuminated by a loosely focused beam (an individual chiral nanostructure produces a weak chiroptical response).

Conventional chiroptical techniques based on optical rotation (OR) and circular dichroism (CD) utilize the spin angular momentum (SAM) of light associated with circular polarization as an excitation to probe a chiroptical response. Recently, the orbital angular momentum (OAM) of light, denoted $\pm l\hbar$ per photon, associated with the dynamical rotation of the phase front was proposed as an alternative probe. The handedness of these beams is characterized by the twisting of the wavefront undergoing l intertwined rotations in one wavelength.[12,13] Such beams are referred to as optical vortex or helical light beams. The phase singularity at the center of a vortex beam leads to a null intensity at that location. Helical dichroism (HD) arises from the differential absorptance of left- and right-handed helical light by a chiral structure illuminated by a vortex beam. HD has been observed in chiral molecules,[14,15] solids,[16] nanostructures[17,18] and single micron-

Received: May 26, 2024
Revised: September 18, 2024
Accepted: September 20, 2024

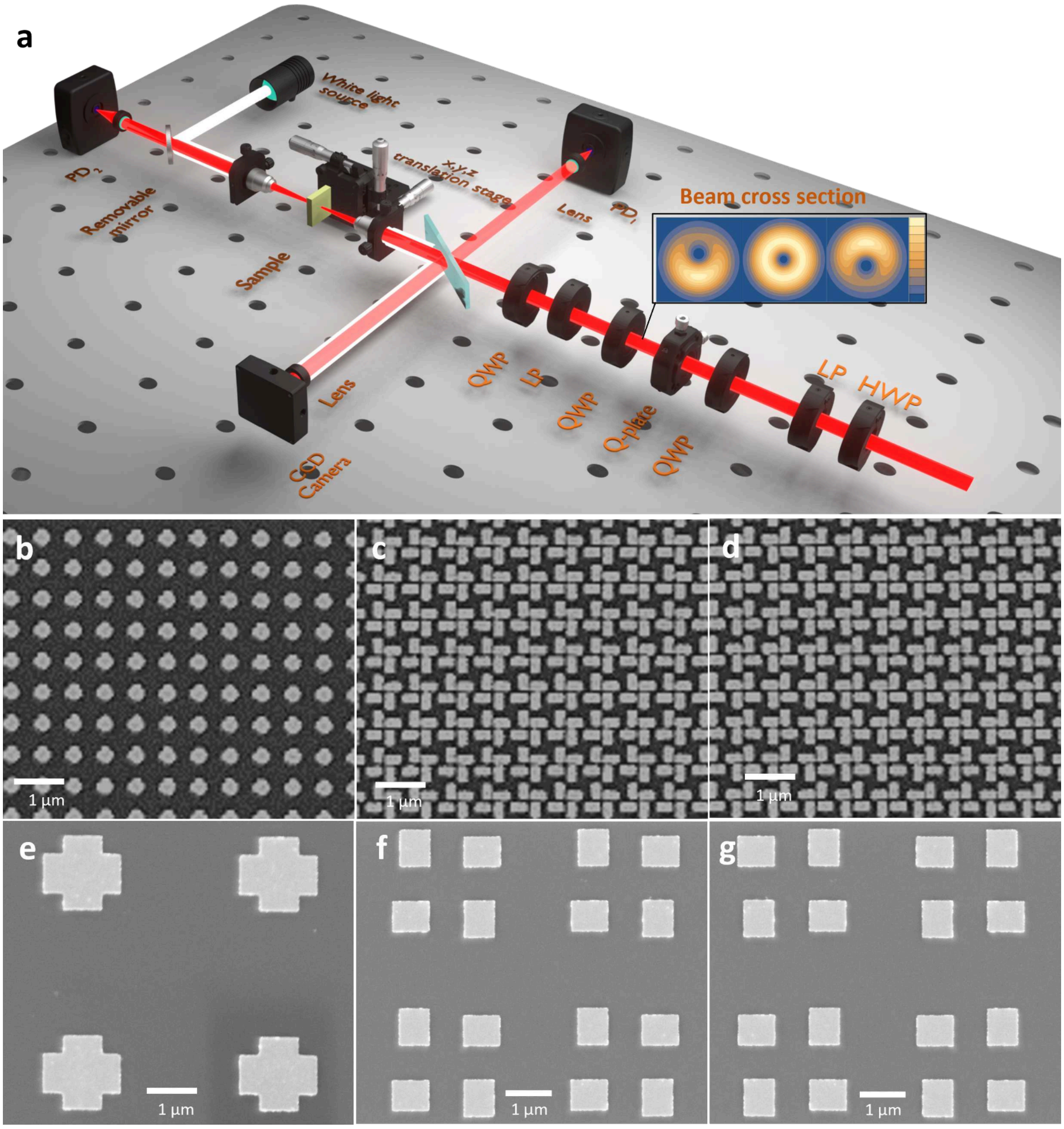

Figure 1. Experimental setup and SEM images of plasmonic structures. (a) The linear polarizer (LP) and half-wave plate (HWP) control the laser power. The desired OAM and SAM states are generated using the combination of quarter-wave plates (QWPs), a birefringent liquid-crystal phase plate (q-plate), a linear polarizer (LP), and a QWP. Two aspheric lenses (NA = 0.3) focus and collimate the incident and transmitted beams. Photodiode PD1 (PD2) monitors the incident (transmitted) light. The charge-coupled camera (CCD) and the white light source are used to find the surface of the sample and position the incident beam onto the structures of interest in the sample. SEM images of plasmonic (b-d) nano- and (e-g) microstructure arrays. (b,e) are achiral and (c,f,d,g) are left- and right-handed chiral structures. Each SEM image is scaled such that the 1 μm scale bar is identical on each. See the supplementary section 1 for all structure dimensions.

sized dielectric and metallic structure.[19,20] The key advantage of HD is that l has no upper bound, so the HD response can, in principle, be enhanced. In contrast, CD depends on the polarization state of light, which has only two bound values (SAM = 0 for linear and SAM = ± 1 for circular).

Optical activity typically arises from the intrinsic chirality present in any chiral structure. This is primarily a material-dominated property where both the system and the probe are chiral and can be explained through parity-time symmetry. Intrinsic chirality has been shown to originate from the coupling of (a) electric and magnetic dipole moments in a linear intensity regime and, (b) electric dipole and electric quadrupole moments in a nonlinear regime.[14]

Optical activity can also originate from extrinsic chirality, produced by oblique incidence of light on achiral metastructures.[21−23] When the incident wave vector does not lie on the plane of symmetry, an effective chiral geometry is created. By varying the angular orientation of the achiral metastructure with respect to the incident circularly polarized beam, a chiroptical response is generated due to the asymmetric distribution of the electric field. However, extrinsic chirality does not exist at normal incidence. Chiroptical responses are not confined to only intrinsic or extrinsic chiral geometries. The OAM-induced CD was demonstrated in a nonchiral circular nanoaperture[24] by exploiting the combined effect of helical phase and circular polarization of light. However, the

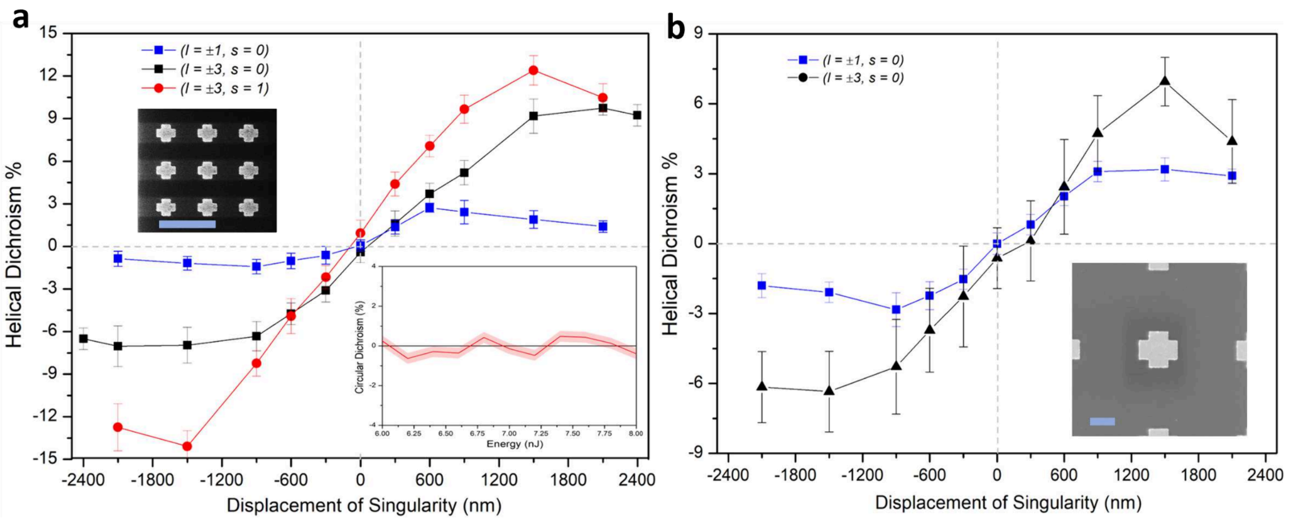

Figure 2. Helical dichroism in achiral plasmonic structures. (a) Plasmonic nanostructure array and (b) a single plasmonic microstructure, vs. displacement of the singularity, δ. Helical dichroism is defined as HD(l, s) = $A(l, s) - A(-l, s)$. SEM images of structures similar to those excited are shown as insets with a scale bar of 1 μm shown on each. The blue and black curves are for linearly polarized (ϵ = 0.05) OAM beams with l = ±1 and l = ±3, respectively. The red curve is for circularly polarized (ϵ = 0.95) OAM beams with (l = ±3). The error bars represent the standard error over multiple measurements (n = 3), calculated for an average energy range used to measure the HD (see text for details). The bottom right inset of part (a) shows the measured circular dichroism (CD) response as a function of incident pulse energy, where the band represents the standard error.

chiroptical response from achiral nanostructures using only OAM as a probe has been elusive.[19]

In this article, first, we show that an achiral plasmonic metasurface, consisting of an array of nanostructures and single micron-sized structures, exhibits selective absorption of linearly polarized asymmetric left- and right-helical light at normal incidence, leading to HD. The observation of HD without involving SAM confirms the existence of a phase-based differential response in achiral nanostructures, a phenomenon that has remained elusive in prior studies. Second, we demonstrate a giant HD response (25%) in chiral plasmonic metasurfaces with asymmetric helical beams without the need for high OAM values. Moreover, our technique offers tunability and control of the HD response in both chiral and achiral metasurfaces by (i) displacing the phase singularity of the incident beam, and (ii) varying its OAM value. Third, we show that a single micron-sized plasmonic chiral structure also exhibits HD, providing insight into the chiral light-matter interaction of individual objects by eliminating averaging and coupling effects present in an array. Lastly, the origin of HD in achiral and chiral metasurfaces is explained qualitatively in terms of induced multipole moments. Theoretically, we show that HD arises from coupling the induced electric dipole with the magnetic dipole (E1M1) and the electric dipole with the electric quadrupole (E1E2).

RESULTS AND DISCUSSION

To study achiral nanostructures, we expanded the HD technique by incorporating asymmetric helical light beams, in contrast to previous studies that employed symmetric beams. Here, the displacement parameter associated with the phase singularity provides an additional degree of freedom with adjustable l- value control. HD experiments were conducted by measuring the differential absorptance of weakly focused left- and right-handed asymmetric helical light passing through the metasurface sample for a specific polarization of light, as shown in Figure 1a. The asymmetric helical light beams were generated by displacing the phase singularity in the OAM beams by translating the q-plate by δ in a plane perpendicular to the incident circularly polarized Gaussian beam. The inset of Figure 1a shows the beam cross sections after the q-plate for different δ positions. The transmitted signal was normalized to the partially reflected incident signal. The white light source and CCD camera were used to position the incident beam focus over the desired metasurface. Additional experimental details are presented in the Methods section.

Figures 1(b-g) shows SEM images of the achiral and chiral (right- and left-handed) gold plasmonic nanostructure (b-d) and microstructure (e-g) arrays fabricated on a fused silica substrate. All SEM images were scaled identically to highlight the size differences between them. The gold thickness was set to 65 ± 5 nm (see Methods for sample fabrication), and the dimensions of each structure are provided in the supplementary section 1. The helical light beam was focused to a spot size (w_0) of ~2 μm by a 0.3 NA aspheric objective (see Methods). The transverse dimensions of the large microstructures (Figures 1e-g) are ~2 μm × 2 μm each, facilitating the study of light-matter interaction on individual structures. In contrast, an array of at least 6 × 6 of the nanostructures (Figures 1b-d) is irradiated, enabling the investigation of coupling effects associated with surface plasmons and lattice resonances.[25] The observation of HD (if any) in individual large microstructures would ease fabrication requirements and eliminate the need for large nanostructure arrays and metasurfaces for chiroptical measurements.

Achiral nanostructures are not expected to show any optical activity.[19,26] The bottom right inset of Figure 2a reaffirms this fact since the average CD response of ~0.13% is below the noise level. The CD response was obtained by taking the difference in the transmittance of left- and right-circularly polarized light, as a function of pulse energy. The pulse energy was varied for each successive pulse without changing the sample position. The error bands represent the standard error obtained by averaging over three transmittance curves. See the

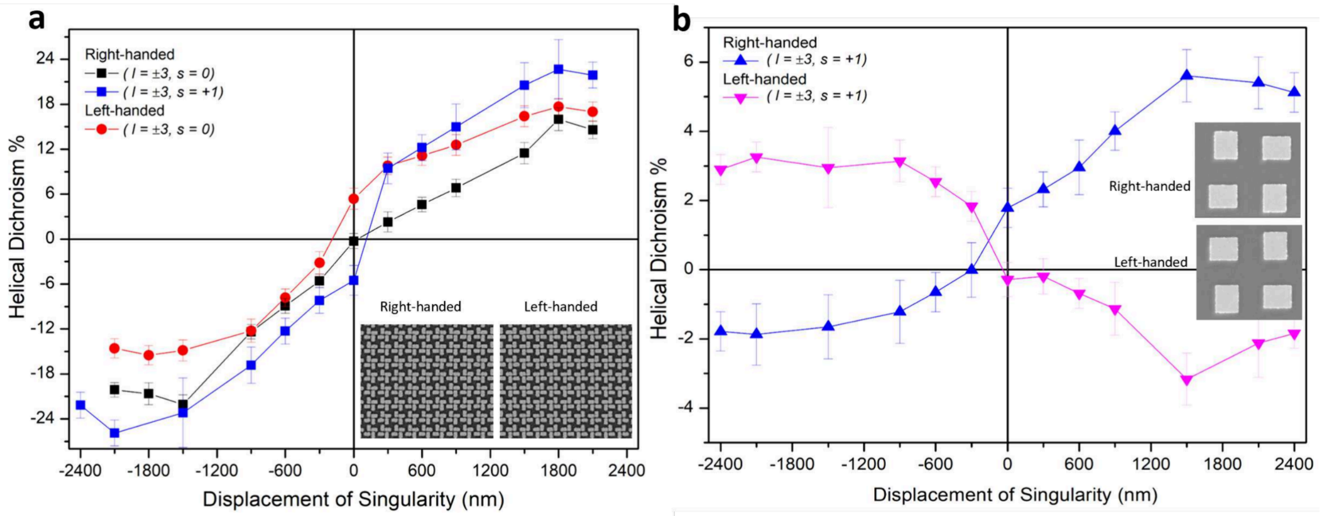

Figure 3. Helical dichroism in chiral plasmonic metasurfaces. Left- and right-handed OAM HD responses of (a) nanostructure arrays and (b) microstructures, vs displacement of the singularity, δ. SEM images of structures similar to those excited are shown as insets. The black and red curves are for linearly polarized ($\epsilon = 0.05$) OAM beams with $l = \pm 3$. The blue and pink curves are for circularly polarized ($\epsilon = 0.95$) OAM beams with ($l = \pm 3$). The error bars represent the standard error over multiple measurements ($n = 3$), calculated for an average energy range used to measure the HD (see text for details).

supplementary section 2 for the CD response of the microstructure.

To study HD as a function of displacement of the singularity in an OAM beam, we employed the same methodology as for the CD measurements. For a specific position of the singularity, δ, the transmittance was measured for left- and right-helical light and averaged over an energy range of 6−8 nJ for the nanostructure arrays and 14−16 nJ for the microstructures. The HD response of the sample can originate from two contributions - one from the plasmonic metasurface and the other from the substrate (fused silica). Recently, HD was observed in amorphous fused silica when pulse energies were above the nonlinear absorption threshold.[16] To eliminate the contribution of the substrate, transmittance measurements were carried out in the linear absorption regime. To minimize the background errors and quantize the instrumental noise, transmittance measurements were always performed on a blank surface and in the air before each experiment (see supplementary section 4). The average noise in our HD measurements was <0.5%.

Figures 2a,b show the differential absorptance of polarized left- and right-helical light incident on achiral structures, determined as $\mathrm{HD}(l, s) = A(l, s) - A(-l, s)$, where $A(\pm l, s)$ is absorptance. The insets show SEM images of nano- and microstructures similar to those irradiated within the cross-section of the laser beam. For a symmetric OAM beam, $\delta = 0$, the HD response is zero within experimental error, as observed in previous studies.[19] The finite HD observed in some instances is due to the error in defining $\delta = 0$ experimentally (See Methods). The HD response for $l = \pm 3$ increases by a factor of ~4 relative to $l = \pm 1$ and by a factor of ~2 when the polarization changes from linear to circular.

The HD responses in Figure 2a exhibit a sinusoidal behavior as a function of δ, reaching a maximum and then decreasing when the beam profile starts to mimic the Gaussian profile. This behavior can be qualitatively understood by considering the dependency of the HD signal on the field gradients (see E1E2 coupling term in eq 1), where the dichroism signal primarily arises from the difference in coupling term for opposite helicities. The field gradients have different magnitudes for asymmetric left- and right-handed helical beams. For a symmetric OAM beam, the difference in coupling term cancels out (averaged over the beam cross-section), resulting in a null HD signal. When the singularity is displaced within the beam cross-section, the nonzero field gradient in the coupling term gives rise to HD signal. As the singularity is displaced from the center, the field gradients increase, and the HD signal reaches a maximum. Any further increase in displacement leads to a decreasing HD signal because the beam starts approaching a symmetric Gaussian profile.

Figure 2b shows the HD of an individual microstructure as a function of δ for linearly polarized OAM light of $l = \pm 1$ and $l = \pm 3$. The behavior of the HD response is similar to that of the nanostructure array. However, the signal strength for a single microstructure is weak compared to that of a nanostructure array. This is due to the lower fill factor as the dimension of the microstructure of 1.6 μm is comparable to the laser beam waist of 2 μm. As a result, coupling effects between different structures, such as surface lattice resonance, are minimal. Indeed, to obtain a measurable HD response, the beam was slightly defocused to about 6 μm in diameter. A portion of the neighboring structures (shown in the inset) might also have been irradiated. These results demonstrate the robustness of our HD technique over conventional techniques, which are restricted to exciting large arrays of nanostructures and where optical activity is absent for achiral structures. Also, unlike the nanostructure array, HD signal for an individual microstructure does not get enhanced by changing the polarization of light from linear to circular (not shown).

In chiral dielectric microstructures, the HD response obtained with symmetric OAM beams is known to enhance with increasing l-value, approaching ~25% for $l > 5$ for a specific handed structure.[19] Figure 3a shows the HD response of chiral plasmonic nanostructure arrays as a function of displacement of the singularity of OAM beams, for $l = \pm 3$ and linear and circular polarizations. For linearly polarized symmetric OAM beams ($\delta = 0$), the HD response is ~4% and increases as the singularity is displaced, reaching a

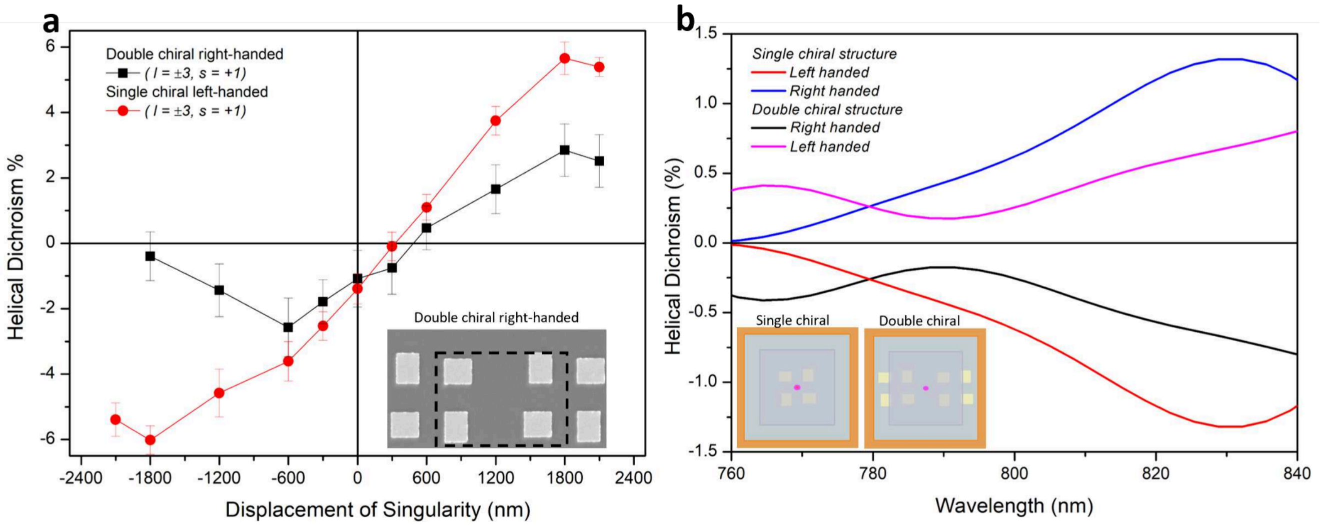

Figure 4. Experimental and simulated helical dichroism in single and double chiral microstructures. (a) Measured HD response of a single left-handed (red) and double right-handed chiral microstructure vs displacement of the singularity (δ) for circularly polarized (ϵ = 0.95) OAM beams with $l = \pm 3$. The inset shows a SEM image of two adjacent right-handed microstructures. Shifting the laser focus (dashed black box) irradiates two chiral microstructures that effectively represent a left-handed structure, labeled as a double chiral structure. (b) FDTD simulations of HD responses as a function of wavelength for single (left-handed, red curve; right-handed, blue curve) and double (left-handed, black curve; right-handed, pink curve) microstructures. The OAM beam is symmetric (δ = 0) with $l = \pm 1$ and s = 1 (circular polarization). The FDTD simulation domain for single and double chiral microstructures is shown in the inset where the shadowed region identifies the laser beam grid.

maximum of ~15% for left-handed nanostructures. However, the difference between the HD responses of opposite-handed structures (red and black curves) is small on average for most displacements δ. The HD responses for a specific handed nanostructure are further enhanced to ~25% by changing the polarization from linear to circular (See the supplementary section 5 for other handedness). Figure 3a shows that the HD responses can be tuned and enhanced even for lower l-values by employing asymmetric OAM beams. This is in contrast to earlier studies where very high l-values were used with no tuning capabilities (see supplementary section 6 in which the table summarizes various studies on HD).

Figure 3b shows the HD responses for different δ positions of an individual chiral plasmonic microstructure. Unlike nanostructure arrays where the HD response remained the same irrespective of the handedness of the structures, the HD responses of an individual microstructure differ by a sign change between the opposite-handed structures. This could be due to the absence of averaging effects, which highlights the subtle difference in how light interacts with individual and arrayed structures. Also, the HD response is comparatively weak, which could be attributed to the lack of interaction between structures and a lower fill factor. In addition, the HD signal remains the same irrespective of the laser polarization (not shown), in contrast with nanostructure arrays (Figure 3a).

When microstructures are arranged in an array, the laser beam can be adjusted to irradiate an individual structure or slightly shifted to straddle two adjacent structures, as shown by the dotted box in the inset of Figure 4a. The latter case leads to a change in the handedness of the structure from left to right and vice versa. As a result, the HD response will not exhibit the behavior of Figure 3b when the laser focus partially irradiates two adjacent structures of one-handedness while the opposite-handed structure is individually irradiated. This is shown in Figure 4a, where the HD response is plotted as a function of δ for a left-handed chiral structure (red curve) and a right-handed double chiral structure (black curve), which effectively becomes left-handed. However, the response is weak due to the low fill factor of a single structure.

This behavior was simulated by employing the Finite Difference Time Domain (FDTD) method (Lumerical Inc.) in which the transmittance of linearly polarized symmetric OAM beams through the chiral structures was computed for different wavelengths over the bandwidth of the femtosecond pulse centered at 800 nm. The insets of Figure 4b show the two left-handed chiral structures used in the simulation. In one case, the laser beam partially irradiates two adjacent structures, while in the other, it fully irradiates a single structure. The computed HD response is shown in Figure 4b for both handed structures in each of the two scenarios. In shifting the laser focus from an individual left-handed structure (blue curve) to a double left-handed structure (pink curve), the response becomes similar to an individual right-handed structure (blue curve) and *vice versa*.

The origin of HD in molecules and solids was recently shown to arise from higher-order multipole moments, specifically, the electric dipole to electric quadrupole coupling term.[14−16] The same theory can be extended to metasurfaces by analogy. For linearly polarized symmetric OAM beams, the induced higher-order multipole moments do not contribute to HD. Therefore, FDTD simulations can provide insight into symmetric OAM light-matter interactions because the input material parameters (e.g., refractive index) are scalar quantities, leading to the dominance of induced dipole effects. However, the FDTD method is limited when extended to asymmetric OAM beams. This is largely because multipole effects require tensor properties of materials that need to be evaluated for specific geometries, and this requires further investigation.

To gain insight into HD with asymmetric OAM beams, we evaluated the contribution of higher order multipoles to the total energy absorbed, Γ, based on a recently proposed theory involving single-photon interaction with matter.[14−16] HD was

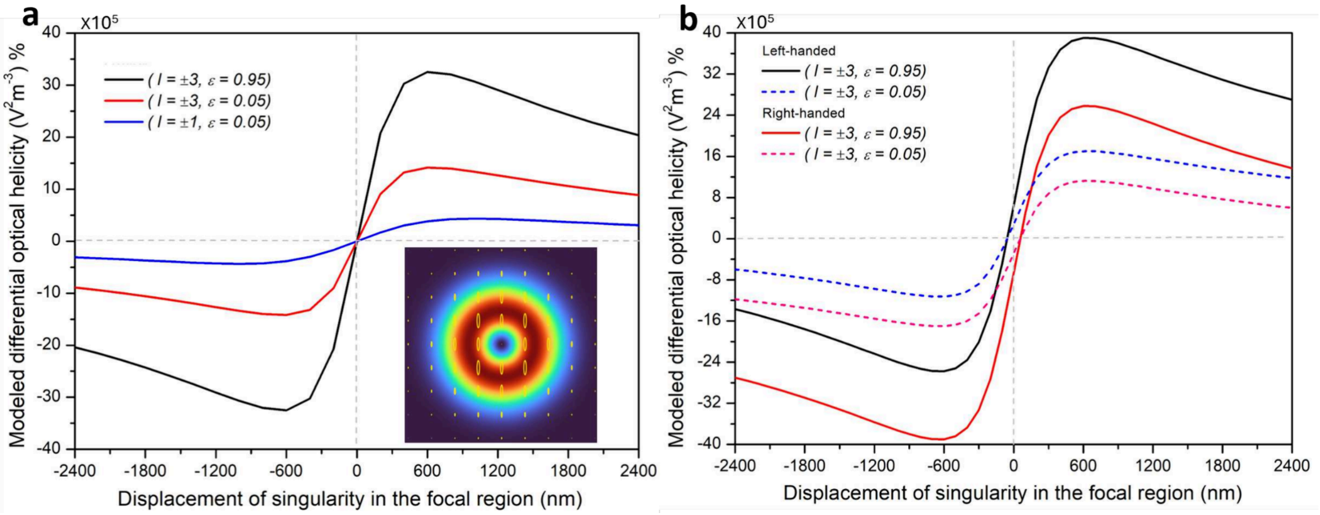

Figure 5. Modeled differential response. (a) HD of an achiral metasurface for different positions of the singularity (δ) for linearly (blue, red) and circularly (black) polarized OAM beams with $l = \pm 1, \pm 3$. HD was modeled using the relation $\Delta W \approx A''\Delta \Upsilon$ where $\Delta \Upsilon = \int_{-\omega_0}^{\omega_0}[\Upsilon^+ - \Upsilon^-]\mathrm{d}x\mathrm{d}y$ is the differential optical helicity with contributions from only the E1E2 coupling term (see text for details). The inset shows the polarization ellipses (for $\epsilon = 0.05$) distributed across the symmetric OAM beam profile. (b) HD of left- and right-handed chiral metasurfaces for linearly (pink, blue) and circularly (black, red) polarized OAM beams with $l = \pm 3$. The differential response is plotted by considering the contributions from the E1M1 and E1E2 coupling terms (see text for details).

defined as the difference in the absorption of left- and right-handed helical light in an achiral or a specific-handedness chiral metasurface. We computed the HD by integrating the differential energy absorbed over the beam cross-section given by (see Methods):

$$\mathrm{HD}_\delta = \int_{-w_0}^{w_0} (\Gamma_\delta^+ - \Gamma_\delta^-)\mathrm{d}x\mathrm{d}y$$
$$= \int_{-w_0}^{w_0} ([G''^+C^+ + G''^-C^-] + [A''^+\Upsilon^+ - A''^-\Upsilon^-])\,\mathrm{d}x\mathrm{d}y \quad (1)$$

where δ is the asymmetry parameter, $\delta = 0$ for symmetric and $\delta \neq 0$ for asymmetric helical beams. The sign ± represents the handedness of OAM of light. $C^\pm = \frac{\omega}{2}\mathrm{Im}[(\tilde{E}_\delta^\pm)^*\cdot\tilde{B}_\delta^\pm]$ is the electromagnetic field chirality, and the optical helicity is defined by $\Upsilon^\pm = \frac{2\omega}{3}\mathrm{Re}[\nabla\tilde{E}_\delta^\pm\cdot(\tilde{E}_\delta^\pm)^*]$. E and B are the complex electric and magnetic field vectors, G'' is the mixed electric dipole magnetic dipole polarizability vector, and A'' is the mixed electric dipole electric quadrupole polarizability tensor. Optical helicity contains the gradient of the electric field, which gives rise to l dependence, leading to scaling of the HD magnitude with increasing l value. Optical properties are contained in C and Υ while material properties are contained in G'' and A''. For specific geometries of metasurfaces, HD can, in principle, be evaluated quantitatively if the mixed polarizability tensors A'' and vector G'' are available. In their absence, qualitative analysis can still be performed by substituting the material responses by their dominant components with respect to the beam components (i.e., by approximating them as a scalar).

Figure 5 shows the qualitative modeling of HD in achiral and chiral structures involving contributions from the E1M1 ($G''C$) and E1E2 ($A''\Upsilon$) coupling terms. The structural dimensions were not considered within the scalar approximation. Consequently, the modeled response is similar for nano- and microstructures. For an achiral structure, due to symmetry, the contribution of the E1M1 term vanishes as the induced electric dipole is orthogonal to the magnetic dipole leading to $G'' \propto \mathrm{Im}\ (\tilde{\boldsymbol{\mu}}^* \cdot \tilde{\mathbf{m}}) = 0$. Moreover, the mixed polarizability tensor A'' ($\propto \mathrm{Im}\ \tilde{\boldsymbol{\mu}}^* \cdot \tilde{\boldsymbol{\theta}}$)) is identical for both helicities of the beam ($A''^+ = A''^-$). Therefore, HD was evaluated by the equation $\mathrm{HD}_\delta \approx A'' \int_{-w_0}^{w_0} (\Upsilon^+ - \Upsilon^-)\mathrm{d}x\mathrm{d}y$, shown in Figure 5a as a function of displacement of the singularity in the OAM beam. For symmetric LG beams ($\delta = 0$), HD does not exist since the field gradient contained in Υ vanishes when integrated over the beam cross-section. For asymmetric beams ($\delta \neq 0$), the nonzero field gradient in the E1E2 coupling term gives rise to a sinusoidal behavior, where HD increases with increasing δ, reaches a maximum, then decreases as the beam starts mimicking a Gaussian profile. HD also scales with l value for linearly polarized helical light (blue $l = 1$, red $l = 3$) and is further enhanced by changing the polarization from linear to circular (black $l = 3$). Recently, G'' was theoretically shown to exist in plasmonic achiral nanostructures for circularly polarized helical beams.[27] This can, in principle, lead to a weak HD response for $\delta = 0$. However, the finite response in our experiments (Figures 2a,b) is comparable to the background noise, thus making it inconclusive. HD can also be understood in terms of parity-time symmetry arguments for both chiral and achiral plasmonic structures (see the supplementary section 7).

Figure 5b shows the modeled differential absorption in chiral metasurface for linearly and circularly polarized asymmetric helical light. Within scalar approximation, HD was evaluated by considering both E1M1 and E1E2 coupling terms in eq 1. HD was evaluated for $\epsilon = 0.05$ and 0.95 to match the conditions of the experiments (Figure 3a). When $\delta = 0$, the E1E2 term vanishes (discussed above) and a nonzero HD response arises due to the E1M1 coupling term, which is also responsible for conventional CD when circularly polarized light is used. For a nonzero delta, we assumed the E1M1 and E1E2 terms to be of the same order.[28,29] The separation of the

HD curves for the left-handed (black) and right-handed (red) structures remains the same around $\delta = 0$ but increases with δ for circularly polarized light. This separation changes with the relative strength of E1M1 and E1E2 terms. For linearly polarized light, the magnitude of HD and the separation between the left- and right-handed structures are small, even for large δ. For an individual micron-sized chiral structure, the opposite behavior in the HD response for different handedness shown in Figure 4b could be explained by considering a change in the sign of the induced dipole, as in the case of chiral molecules.[30]

CONCLUSION

To summarize, we have shown that helical dichroism can exist in achiral plasmonic structures excited by linearly polarized asymmetric OAM beams. Our method allows for precise control and tunability of HD by (i) displacing the singularity in the OAM beam, (ii) changing the OAM value, and (iii) varying the laser polarization. This approach enhanced the HD response in chiral plasmonic structures with low OAM values, enabling the development of helical phase-based chiroptical spectroscopy. The presence of dichroism in achiral microstructures is technologically advantageous as it simplifies fabrication compared to complex chiral nanostructures. The controlled absorption of helical light in achiral nano- and microstructures could potentially enhance the functionality and efficacy of existing plasmonic optical devices such as switches,[31] modulators,[32] and sensors.[33]

METHODS

Helical Dichroism Measurements. Transmission measurements were performed using a Ti: Sapphire laser amplifier system, operating in an external trigger mode, producing 45 fs, 800 nm pulses with a maximum pulse energy of 2.5 mJ. An aspheric objective lens (NA = 0.3) was used to focus the femtosecond pulses onto the samples. A second aspheric objective with the same numerical aperture collected and collimated the transmitted light onto a photodiode (PD2), positioned immediately after the objective. Regions of interest in the metasurface were identified by monitoring the reflection of the focused light on the CCD camera. The position of the structures within the sample was determined by an in situ transmission microscope consisting of a white light source introduced after the second objective (Figure 1). The magnification of the image was adjusted by changing the converging lens before the camera.

For every laser shot, the transmitted light signal on PD2 was normalized to the incoming light signal on PD1, reflected off a glass plate positioned in the beam path. After identifying the metasurface position, the glass plate was rotated at an angle of ~20° to avoid Brewster's angle so that the polarization of light remains unaffected. The signals generated by PD1 and PD2 were stretched by an electronic pulse stretcher, discretized, and recorded by a data acquisition card. A combination of a half-wave plate and a polarizer was used to vary the pulse energy. The incident pulse energies were measured before the objective. During the measurement, for every laser shot, the pulse energy was increased without translating the sample. Multiple transmission curves similar to Figure S4 (see supplementary section 3) were obtained for each sample and averaged. Helical dichroism was obtained by taking the difference between the transmission of left- and right-helical light. A single-shot autocorrelator continuously monitored the pulse duration, which was about 100 fs in the interaction region. Prior to each experiment, transmission measurements were always performed on a blank surface and without a sample (in the air) to determine the background response (see supplementary section 4), quantize instrumental noise, and minimize it. The average noise in our HD measurements was <0.5%.

Generation of Asymmetric OAM Beams. Light beams carrying orbital and/or spin angular momentum were generated by a birefringent liquid crystal-based phase plate, termed a q-plate,[34−36] as shown in Figure 1. When a circularly polarized Gaussian beam propagates through the q-plate with a topological charge q, it acquires OAM given by $l = \pm 2q$, with a phase singularity and a null intensity region at the center of the beam. Such beams are termed optical vortex beams. The generated OAM beam has a circular polarization. Its wavefront undergoes l intertwined rotations in one wavelength, and the direction of rotation is determined by the sign of the input circular polarization. A combination of a quarter-wave plate (QWP) and a linear polarizer (LP) was used to manipulate the polarization of the OAM beam. The ellipticity of linearly ($s = 0$) and circularly ($s = \pm 1$) polarized OAM light was 5 ± 2% and 95 ± 2%, respectively, for $l = \pm 1, \pm 3$. The conversion efficiency of the q-plate was 91 ± 2% for $l = \pm 1, \pm 3$. The singularity/null intensity region in the OAM beam was displaced by translating the q-plate, mounted on a precision x-y stage with a step size of 250 ± 10 μm. When focused by the objective, this translated to a displacement step size of 300 ± 20 nm with respect to the center of the beam. The calibration was achieved by measuring the total translation required to displace the singularity to the periphery of the defocused beam and comparing it to the measured spot size of 2 ± 0.2 μm obtained by knife-edge measurements.

Metasurface Fabrication. The chiral and achiral metasurfaces were fabricated using electron beam lithography (EBL). First, a PMMA (950A2) resist monolayer of thickness ~110 nm was prepared on a fused silica substrate by spin-coating and curing. Second, the substrate bearing the resist monolayer was exposed to the electron beam to write the prescribed pattern into the resist. Third, the PMMA (positive resist) was developed with MIBK/IPA 1:3 developer, leaving re-entrant-profiled resist wherever it was not exposed. Fourth, the metal layers were deposited in the order of chromium of thickness ~3 nm (adhesion) followed without breaking vacuum by the gold of thickness ~60 nm. The final metasurface structures were obtained after the lift-off removal of the residual resist layer. Details of the structure dimensions are provided in the supplementary section 1.

Asymmetric Laguerre-Gaussian Beams. Asymmetric Laguerre-Gaussian beams, identified by an asymmetry parameter δ, were used in our numerical simulations. Under the paraxial regime, the field components for arbitrary polarization can be written as[14,37]

$$u_o^{\pm}(x, y, z) = E_0 \exp[ikz]\left(\frac{\sqrt{2}\,((x \mp i\eta\delta) \pm i(y \mp i\zeta\delta))}{w_0}\right)^{|l|} \exp\left(-\frac{(x^2 + y^2)}{w_0^2}\right) L_p^{|(l)|}\left(\frac{2\rho^2}{w_0^2}\right) \tag{2}$$

$$\mathbf{E}^{\pm}(x, y, z) = \begin{cases} E_x^{\pm} = \alpha u_0^{\pm}(x, y, z) \\ E_y^{\pm} = \beta u_0^{\pm}(x, y, z) \\ E_z^{\pm} = if\left[(\alpha \pm i\beta)\dfrac{|l| w_0((x \mp i\eta\delta) \mp i(y \mp i\zeta\delta)}{(x \mp i\eta\delta)^2 + (y \mp i\zeta\delta)^2} u_0^{\pm}(x, y, z) - \dfrac{2}{w_0}(\alpha(x) + \beta(y)) u_0^{\pm}(x, y, z)\right] \end{cases} \tag{3}$$

where $f = \lambda/2\pi w_0$, k is the wavevector, w_0 is the spot size, ω is the laser radian frequency and $\rho = \sqrt{x^2 + y^2}$. $L_p^{|(l)|}$ is the generalized Laguerre polynomial and ± represents the rotational direction of l with no radial node, $p = 0$. The polarization factors α and β are normalized such that $|\alpha|^2 + |\beta|^2 = 1$. Displacement of the singularity in the x−y plane was achieved by varying η and ζ. For generalization, we substituted $\eta = 1$ and $\zeta = 0$, considering the movement of the singularity to be parallel to the polarization following experimental conditions. E_0 is the normalization factor obtained by integrating the intensity overall space (-∞ to + ∞) for $l = 1$:

$$E_0 = \sqrt{\frac{2k^2w_0^2}{\pi(\alpha^2 + \beta^2)(2w_0^2 + k^2w_0^4 + 2(\zeta^2 + \eta^2)\delta^2(1 + k^2w_0^2))}} \tag{4}$$

In the paraxial regime, as was the case in our experiments, the z-component was not considered as the light was focused using a 0.3 NA objective. The corresponding diameter of the focused beam was ≈4 μm, considerably larger than the wavelength (λ) of the light. The contribution of the longitudinal component (E_z) becomes significant only for tight focusing (≥0.6 NA) due to its finite l dependence. The longitudinal contribution is typically treated as a correction to the paraxial regime, as was recently demonstrated in differentiating nanoparticle aggregates using helical light.[17]

FDTD Simulations. Finite Difference Time-Domain simulations (Figure 4b) were performed using Lumerical FDTD Solutions, Inc. To match experimental parameters imposed by the fabrication method, the simulations used a 0.5 mm thick fused silica substrate with a 3 nm chromium layer on which 65 nm thick gold nanostructures were deposited. The built-in optical parameters from Johnson and Christy were used for the refractive index of gold. A plane wave source and periodic boundary conditions on the x and y boundaries, along with perfectly matched layers placed along the z boundaries, were employed to model circular dichroism (Supporting Information file). The symmetric OAM beam ($\delta = 0$) was inserted as a custom import source where the incident electrical field distribution of defined polarization (eqs 2 3) was inserted in the k-space (Fourier space) beam profile description based on the method by M. Mansuripur.[38] Helical dichroism was obtained with perfectly matched layer boundary conditions along the x, y, and z directions. The mesh accuracy setting of 4 was used to obtain a fine grid in the FDTD solver region. The dimensions of the metasurface were finalized after optimizing for the CD and HD responses.

Numerical Simulations. Energy absorbed by the metasurface was computed in terms of the induced multipole response of the material. The induced electric dipole, $\tilde{\mu}$, magnetic dipole, $\tilde{m}$, and electric quadrupole, $\tilde{\theta}$, were expressed in terms of multipole expansions given by[27,39,40]

$$\begin{aligned}\tilde{\mu}_\alpha &= \sum_\beta \tilde{\alpha}_{\alpha\beta}\tilde{E}_\beta - i\sum_\beta \tilde{G}_{\alpha\beta}\tilde{B}_\beta + \frac{1}{3}\sum_{\beta\gamma} \tilde{A}_{\alpha\beta\gamma}\tilde{E}_{\beta\gamma};\ \tilde{\theta}_{\alpha\beta}\\ &= \sum_\gamma \tilde{a}_{\gamma\alpha\beta}\tilde{E}_\gamma;\ \tilde{m}_\alpha = \sum_\beta \tilde{\chi}_{\alpha\beta}\tilde{B}_\beta + i\sum_\beta \tilde{G}_{\alpha\beta}\tilde{E}_\beta\end{aligned} \tag{5}$$

where the Greek alphabet represents the Cartesian indices. The presence of i in the second term of the induced $\tilde{\mu}$ and $\tilde{m}$differentiates metasurfaces from the molecular case.[6,27,41] $\tilde{\alpha}_{\alpha\beta}$ represents the electric dipole polarizability, and $\tilde{\chi}_{\alpha\beta}$ is the magnetic susceptibility. The coupling between the magnetic dipole, electric dipole and electric quadrupole modes gives rise to the electric dipole magnetic dipole polarizability $\tilde{G}_{\alpha\beta}$, and electric dipole electric quadrupole polarizability $\tilde{A}_{\alpha\beta\gamma}$ and $\tilde{A}_{\alpha\beta\gamma} = \tilde{a}_{\gamma\alpha\beta}$. The field gradient $\nabla_\beta\tilde{E}_\gamma$ is denoted $\tilde{E}_{\beta\gamma}$.[39,40] The complex electric and magnetic fields are written $\tilde{E}(t) = \tilde{E}_0e^{-i\omega t}$ and $\tilde{B}(t) = \tilde{B}_0e^{-i\omega t}$, where $\tilde{E}_0$ and $\tilde{B}_0$ are arbitrary complex vectors and ω is the radian frequency of the incident light. The terms with a tilde are complex quantities $\tilde{\alpha}_{\alpha\beta} = \alpha'_{\alpha\beta} + i\alpha''_{\alpha\beta} = \tilde{\alpha}^*_{\beta\alpha}$, $\tilde{A}_{\alpha\beta\gamma} = A'_{\alpha\beta\gamma} + iA''_{\alpha\beta\gamma} = \tilde{A}_{\gamma\alpha\beta}$, and $\tilde{G}_{\alpha\beta} = G'_{\alpha\beta} + iG''_{\alpha\beta}$.

The interaction Hamiltonian expanded in terms of multipoles is given by

$$H_{int} = -\mu_\alpha E_\alpha - \frac{1}{3}\theta_{\alpha\beta}E_{\alpha\beta} - m_\alpha B_\alpha - \ldots \tag{6}$$

Energy absorbed from the electromagnetic fields is given by the time-averaged rate of change of the Hamiltonian:[27,39,40]

$$\Gamma = \left\langle \dot{\mu}_\alpha E_\alpha + \dot{m}_\alpha B_\alpha + \frac{1}{3}\dot{\theta}_{\alpha\beta}E_{\alpha\beta} \right\rangle_t \tag{7}$$

where $\dot{\mu}$, $\dot{m}$, $\dot{\theta}$, $E_\alpha = \frac{1}{2}(\tilde{E}_\alpha e^{-i\omega t} + \tilde{E}^*_\alpha e^{i\omega t})$ and $B_\alpha = \frac{1}{2}(\tilde{B}_\alpha e^{-i\omega t} + \tilde{B}^*_\alpha e^{i\omega t})$ are real quantities. Considering the component of dipole moment along the electric field direction ($\alpha = \beta$), the total rate of excitation in case of asymmetric OAM beam is given as[14,16]

$$\begin{aligned}\Gamma^\pm_\delta = \frac{\omega}{2}\Bigg\{ &\underbrace{\alpha''|\widetilde{E}^\pm_\delta|^2}_{\text{E1E1}} + \underbrace{\chi''|\widetilde{B}^\pm_\delta|^2}_{\text{M1M1}} \pm \underbrace{G''\mathrm{Im}[(\widetilde{E}^\pm_\delta)^*\cdot\widetilde{B}^\pm_\delta]}_{\text{E1M1}}\\ &+ \underbrace{\frac{2}{3}A''\mathrm{Re}[\nabla\widetilde{E}^\pm_\delta\cdot(\widetilde{E}^\pm_\delta)^*]}_{\text{E1E2}}\Bigg\}\end{aligned} \tag{8}$$

δ is the asymmetrical parameter, $\delta = 0$ for a symmetric OAM beam and $\delta \neq 0$ for asymmetric OAM beam. The sign in $\Gamma^\pm$ represents the sign of OAM. The mixed polarizability tensor G'' changes sign with the handedness of OAM beam[27] and also with the handedness of the chiral nanostructure.[42] E1E1, M1M1, E1M1, and E1E2 are electric dipole electric dipole, magnetic dipole, electric dipole magnetic dipole, and electric dipole electric quadrupole coupling terms, respectively. Other higher-order multipole transitions were ignored because the material response tensor for these transitions is very small.

ASSOCIATED CONTENT

Supporting Information

The Supporting Information is available free of charge at https://pubs.acs.org/doi/10.1021/acsnano.4c06983.

> Sections: (S1) Dimensions of chiral and achiral metasurfaces, (S2) Experimental and simulated analysis of the CD in nano- and microstructures, (S3) Helical light transmission experimental curves in achiral metasurface, (S4) Background noise check in terms of transmission measurements in the air (absence of a sample) and on the substrate surface without metasurface (blank area), (S5) HD signal in chiral metasurface with circularly polarized helical light, (S6) HD signal strength comparison with published literature, (S7) Helical dichroism explained in terms of parity-time symmetry arguments (PDF)

AUTHOR INFORMATION

Corresponding Authors

Ashish Jain – *Nexus for Quantum Technologies Institute-NEXQT, Department of Physics, University of Ottawa, K1N 6N5 Ottawa, Ontario, Canada*; orcid.org/0000-0002-1398-2213; Email: Ajain067@uottawa.ca

Ravi Bhardwaj – *Nexus for Quantum Technologies Institute-NEXQT, Department of Physics, University of Ottawa, K1N 6N5 Ottawa, Ontario, Canada*; Email: Ravi.Bhardwaj@uottawa.ca

Authors

Howard Northfield – *Nexus for Quantum Technologies Institute-NEXQT, Department of Physics, University of Ottawa, K1N 6N5 Ottawa, Ontario, Canada*

Ebrahim Karimi – *Nexus for Quantum Technologies Institute-NEXQT, Department of Physics, University of Ottawa, K1N 6N5 Ottawa, Ontario, Canada*

Pierre Berini – *Nexus for Quantum Technologies Institute-NEXQT, Department of Physics, University of Ottawa, K1N 6N5 Ottawa, Ontario, Canada; School of Electrical Engineering and Computer Science, University of Ottawa, Ottawa, Ontario K1N 6N5, Canada*; orcid.org/0000-0002-6795-7275

Complete contact information is available at:
https://pubs.acs.org/10.1021/acsnano.4c06983

Author Contributions

A.J. and R.B. conceived, designed, and planned the experiments. H.N. fabricated the plasmonic metasurfaces. A.J. performed the experiments and conducted the Lumerical FDTD and numerical simulations. A.J. and R.B. analyzed the results. P.B., E.K., and R.B. supervised the project. A.J. and R.B. prepared the first draft, and all authors reviewed the manuscript.

Notes

The authors declare no competing financial interest.

ACKNOWLEDGMENTS

The authors thank PhD student Felix Hufnagel from Prof. Karimi's group for fabricating the q-plate used in the experiments and Jean-Luc Bégin for the insightful discussions. We also acknowledge financial support from the Natural Science and Engineering Council of Canada, Canada Research Chairs, and the Canadian Foundation for Innovation.

REFERENCES

(1) Helgert, C.; Pshenay-Severin, E.; Falkner, M.; Menzel, C.; Rockstuhl, C.; Kley, E.-B.; Tünnermann, A.; Lederer, F.; Pertsch, T. Chiral Metamaterial Composed of Three-Dimensional Plasmonic Nanostructures. *Nano Lett.* **2011**, *11*, 4400−4404.

(2) Fan, Z.; Govorov, A. O. Chiral Nanocrystals: Plasmonic Spectra and Circular Dichroism. *Nano Lett.* **2012**, *12*, 3283−3289.

(3) Hu, Z.; Meng, D.; Lin, F.; Zhu, X.; Fang, Z.; Wu, X. Plasmonic Circular Dichroism of Gold Nanoparticle Based Nanostructures. *Advanced Optical Materials* **2019**, *7*, 1801590.

(4) Vestler, D.; Ben-Moshe, A.; Markovich, G. Enhancement of Circular Dichroism of a Chiral Material by Dielectric Nanospheres. *J. Phys. Chem. C* **2019**, *123*, 5017.

(5) Kuwata-Gonokami, M.; Saito, N.; Ino, Y.; Kauranen, M.; Jefimovs, K.; Vallius, T.; Turunen, J.; Svirko, Y. Giant Optical Activity in Quasi-Two-Dimensional Planar Nanostructures. *Phys. Rev. Lett.* **2005**, *95*, 227401.

(6) Hu, L.; Tian, X.; Huang, Y.; Fang, L.; Fang, Y. Quantitatively analyzing the mechanism of giant circular dichroism in extrinsic plasmonic chiral nanostructures by tracking the interplay of electric and magnetic dipoles. *Nanoscale* **2016**, *8*, 3720−3728.

(7) Khaliq, H. S.; Nauman, A.; Lee, J.-W.; Kim, H.-R. Recent Progress on Plasmonic and Dielectric Chiral Metasurfaces: Fundamentals, Design Strategies, and Implementation. *Advanced Optical Materials* **2023**, *11*, 2300644.

(8) Ali, A.; Khaliq, H. S.; Asad, A.; Akbar, J.; Zubair, M.; Mehmood, M. Q.; Massoud, Y. Dielectric chiral metasurfaces for enhanced circular dichroism spectroscopy at near infrared regime. *RSC Adv.* **2023**, *13*, 20958−20965.

(9) Wang, Z.; Wang, Y.; Adamo, G.; Teh, B. H.; Wu, Q. Y. S.; Teng, J.; Sun, H. A Novel Chiral Metasurface with Controllable Circular Dichroism Induced by Coupling Localized and Propagating Modes. *Advanced Optical Materials* **2016**, *4*, 883−888.

(10) Esposito, M.; Tasco, V.; Todisco, F.; Cuscunà, M.; Benedetti, A.; Sanvitto, D.; Passaseo, A. Triple-helical nanowires by tomographic rotatory growth for chiral photonics. *Nat. Commun.* **2015**, *6*, 6484.

(11) Hentschel, M.; Schäferling, M.; Weiss, T.; Liu, N.; Giessen, H. Three-Dimensional Chiral Plasmonic Oligomers. *Nano Lett.* **2012**, *12*, 2542−2547.

(12) Allen, L.; Beijersbergen, M. W.; Spreeuw, R. J. C.; Woerdman, J. P. Orbital angular momentum of light and the transformation of Laguerre-Gaussian laser modes. *Phys. Rev. A* **1992**, *45*, 8185−8189.

(13) Torres, J. P., Torner, L., Eds.; *Twisted Photons: Applications of Light with Orbital Angular Momentum*; John Wiley and Sons, Inc., 2011.

(14) Begin, J.-L.; Jain, A.; Parks, A.; Hufnagel, F.; Corkum, P.; Karimi, E.; Brabec, T.; Bhardwaj, R. Nonlinear helical dichroism in chiral and achiral molecules. *Nat. Photon. Nature Photonics* **2023**, *17*, 82−88.

(15) Jain, A.; Bégin, J.-L.; Bhardwaj, R. Helical dichroism in enantiomeric solutions. *J. Chem. Phys.* **2023**, *159*, 014504.

(16) Jain, A.; Begin, J.-L.; Corkum, P.; Karimi, E.; Brabec, T.; Bhardwaj, R. Intrinsic dichroism in amorphous and crystalline solids with helical light. *Nat. Commun.* **2024**, *15*, 1350.

(17) Brullot, W.; Vanbel, M. K.; Swusten, T.; Verbiest, T. Resolving enantiomers using the optical angular momentum of twisted light. *Science Advances* **2016**, *2*, e1501349.

(18) Kerber, R. M.; Fitzgerald, J. M.; Oh, S. S.; Reiter, D. E.; Hess, O. Orbital angular momentum dichroism in nanoantennas. *Communication Physics* **2018**, *1*, 87.

(19) Ni, J.; Liu, S.; Hu, G.; Hu, Y.; Lao, Z.; Li, J.; Zhang, Q.; Wu, D.; Dong, S.; Chu, J.; Qiu, C.-W. Giant Helical Dichroism of Single Chiral Nanostructures with Photonic Orbital Angular Momentum. *ACS Nano* **2021**, *15*, 2893−2900.

(20) Dai, N.; Liu, S.; Ren, Z.; Cao, Y.; Ni, J.; Wang, D.; Yang, L.; Hu, Y.; Li, J.; Chu, J.; Wu, D. Robust Helical Dichroism on Microadditively Manufactured Copper Helices via Photonic Orbital Angular Momentum. *ACS Nano* **2023**, *17*, 1541−1549.

(21) Plum, E.; Fedotov, V. A.; Zheludev, N. I. Optical activity in extrinsically chiral metamaterial. *Appl. Phys. Lett.* **2008**, *93*, 191911.

(22) Plum, E.; Liu, X.-X.; Fedotov, V. A.; Chen, Y.; Tsai, D. P.; Zheludev, N. I. Metamaterials: Optical Activity without Chirality. *Phys. Rev. Lett.* **2009**, *102*, 113902.

(23) Mun, J.; Kim, M.; Yang, Y.; Badloe, T.; Ni, J.; Chen, Y.; Qiu, C.-W.; Rho, J. Eletromagnetic chirality: from fundamentals to nontraditional chiroptical phenomena. *Light: Science and Applications* **2020**, *9*, 139.

(24) Zambrana-Puyalto, X.; Vidal, X.; Molina-Terriza, G. Angular momentum-induced circular dichroism in non-chiral nanostructures. *Nat. Commun.* **2014**, *5*, 4922.

(25) Kravets, V. G.; Kabashin, A. V.; Barnes, W. L.; Grigorenko, A. N. Plasmonic Surface Lattice Resonances: A Review of Properties and Applications. *Chem. Rev.* **2018**, *118*, 5912−5951.

(26) Spaeth, P.; Adhikari, S.; Le, L.; Jollans, T.; Pud, S.; Albrecht, W.; Bauer, T.; Caldarola, M.; Kuipers, L.; Orrit, M. Circular Dichroism Measurement of Single Metal Nanoparticles Using Photothermal Imaging. *Nano Lett.* **2019**, *19*, 8934−8940.

(27) Guo, Y.; Zhu, G.; Bian, W.; Dong, B.; Fang, Y. Orbital angular momentum dichroism caused by the interaction of electric and magnetic dipole moments and the geometrical asymmetry of chiral metal nanoparticles. *Phys. Rev. A* **2020**, *102*, 033525.

(28) Babicheva, V. E.; Evlyukhin, A. B. Metasurfaces with Electric Quadrupole and Magnetic Dipole Resonant Coupling. *ACS Photonics* **2018**, *5*, 2022−2033.

(29) Arikawa, T.; Hiraoka, T.; Morimoto, S.; Blanchard, F.; Tani, S.; Tanaka, T.; Sakai, K.; Kitajima, H.; Sasaki, K.; Tanaka, K. Transfer of orbital angular momentum of light to plasmonic excitations in metamaterials. *Science Advances* **2020**, *6*, eaay1977.

(30) Patterson, D.; Schnell, M.; Doyle, J. M. Enantiomer-specific detection of chiral molecules via microwave spectroscopy. *Nature* **2013**, *497*, 475−477.

(31) Dhama, R.; Panahpour, A.; Pihlava, T.; Ghindani, D.; Caglayan, H. All-optical switching based on plasmon-induced Enhancement of Index of Refraction. *Nat. Commun.* **2022**, *13*, 3114.

(32) Haffner, C.; Chelladurai, D.; Fedoryshyn, Y.; Josten, A.; Baeuerle, B.; Heni, W.; Watanabe, T.; Cui, T.; Cheng, B.; Saha, S.; Elder, D. L.; Dalton, L. R.; Boltasseva, A.; Shalaev, V. M.; Kinsey, N.; Leuthold, J. Low-loss plasmon-assisted electro-optic modulator. *Nature* **2018**, *556*, 483−486.

(33) Athira, E. T.; Satija, J. Plasmonic nanoparticle etching-based optical sensors: current status and future prospects. *Analyst* **2023**, *148*, 6188−6200.

(34) Marrucci, L.; Manzo, C.; Paparo, D. Optical Spin-to-Orbital Angular Momentum Conversion in Inhomogeneous Anisotropic Media. *Phys. Rev. Lett.* **2006**, *96*, 163905.

(35) Larocque, H.; Gagnon-Bischoff, J. Arbitrary optical wavefront shaping via spin-to-orbit coupling. *J. Opt.* **2016**, *18*, 124002.

(36) Rubano, A.; Cardano, F.; Piccirillo, B.; Marrucci, L. Q-plate technology: a progress review. *J. Opt. Soc. Am. B* **2019**, *36*, D70−D87.

(37) Cerjan, A.; Cerjan, C. Orbital angular momentum of Laguerre-Gaussian beams beyond the paraxial approximation. *J. Opt. Soc. Am. A* **2011**, *28*, 2253−2260.

(38) Mansuripur, M. Distribution of light at and near the focus of high-numerical-aperture objectives. *J. Opt. Soc. Am. A* **1986**, *3*, 2086−2093.

(39) Yang, N.; Cohen, A. E. Local Geometry of Electromagnetic Fields and Its Role in Molecular Multipole Transitions. *J. Phys. Chem. B* **2011**, *115*, 5304−5311.

(40) Barron, L. D. *Molecular Light Scattering and Optical Activity*, 2nd ed.; Cambridge University Press: Cambridge, UK, 2004.

(41) Collins, J. T.; Kuppe, C.; Hooper, D. C.; Sibilia, C.; Centini, M.; Valev, V. K. Chirality and Chiroptical Effects in Metal Nanostructures: Fundamentals and Current Trends. *Advanced Optical Materials* **2017**, *5*, 1700182.

(42) Canaguier-Durand, A.; Hutchison, J. A.; Genet, C.; Ebbesen, T. W. Mechanical separation of chiral dipoles by chiral light. *New J. Phys.* **2013**, *15*, 123037.

Selective and tunable absorption of twisted light in achiral and chiral plasmonic metasurfaces

Ashish Jain[1,*,+], **Howard Northfield**[1,], **Ebrahim Karimi**[1], **Pierre Berini**[1], **and Ravi Bhardwaj**[1,*]

[1]Nexus for Quantum Technologies Institute-NEXQT, Department of Physics, University of Ottawa, K1N 6N5, Ottawa, Ontario, Canada
[*]Corresponding Author. Ashish Jain, Ravi Bhardwaj. ajain067@uottawa.ca, ravi.bhardwaj@uottawa.ca

Contents

1 Metasurface dimensions

All the chiral and achiral metasurfaces were designed with a gold layer thickness of 65nm on top of a $\sim 3nm$ chromium thin film deposited on 500μm fused silica substrate using the Lumerical FDTD (Ansys Inc).

Fig S1a shows the achiral nanostructure array designed with dimensions of a = 150 nm, b = 310 nm, center-to-center distance of 650nm, edge-to-edge distance of 330nm. Fig S1b shows a chiral nanostructure array with 810nm periodicity from the center with c = 320nm, d = 170nm, and e = 70nm. The dimensions were identical for both left- and right-handed chiral nanostructure arrays.

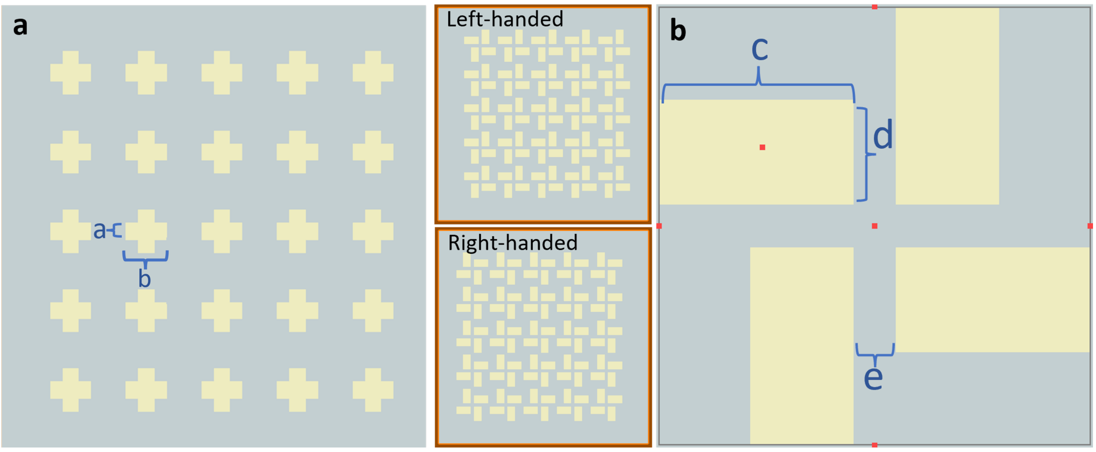

Fig S 1. Achiral and chiral nanostructure arrays dimensions (a) achiral nanostructure array with a= 150 nm and b= 310nm **(b)** chiral left handed nanostructure with c = 320nm, d = 170nm, e = 70nm. The dimensions were identical for both left- and right-handed chiral nanostructure arrays.

Fig S2a shows an achiral microstructure array with design with dimensions: a = 800 nm, b = 1600 nm, c= 1500nm center to center distance of 4μm. Fig S2b shows chiral microstructures with 4μm periodicity from the center with d = 700nm, e = 850nm, f = 750nm. The dimensions were identical for both left- and right-handed microstructure arrays.

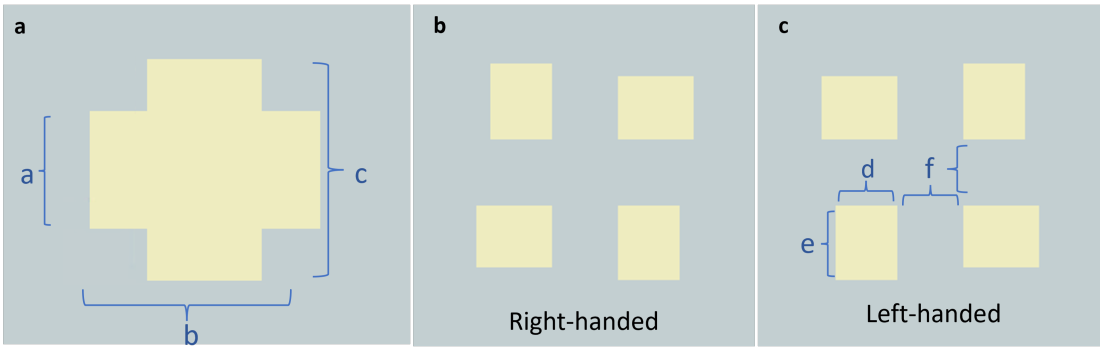

Fig S 2. Achiral and chiral microstructure dimensions (a) achiral microstructure with a = 800 nm, b = 1600 nm, c= 1500nm **(b-c)** chiral left- and right- handed microstructure with d = 700nm, e = 850nm, f = 750nm. The dimensions were identical for both left- and right-handed microstructure arrays.

2 Circular Dichroism

Circular dichroism (CD), defined as differential absorption of left- and right-circularly polarized (CP) Gaussian beam, is not expected to be observed in achiral geometry. This is because achiral structures do not have a ‘handedness’, and thus, they treat light waves with left- and right-rotating electric fields equally. On the other hand, chiral structures, which are asymmetric and have a ‘handedness’ like our left and right hands, exhibit CD. These structures can interact differently with the left- and right-rotating light waves. This difference in interaction leads to a difference in absorption, which leads to circular dichroism.

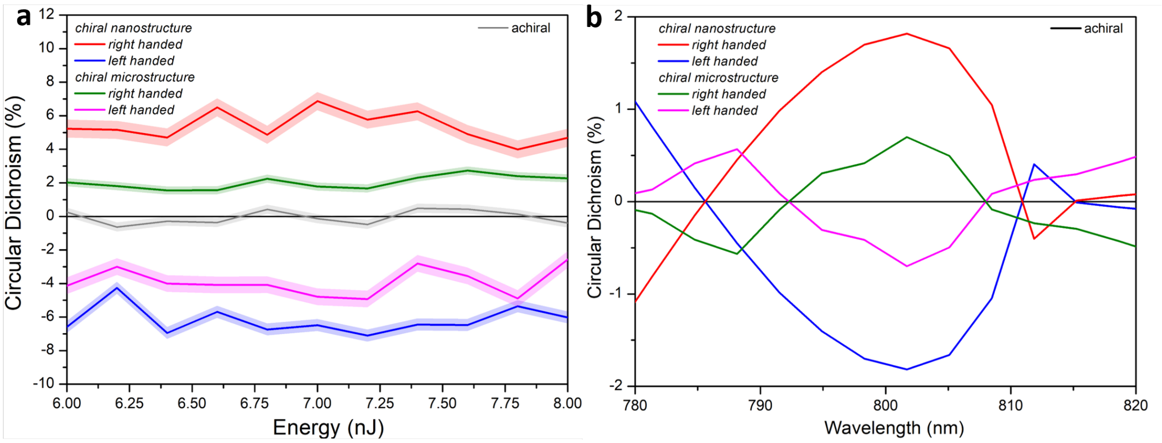

Fig S 3. Circular Dichroism in achiral, chiral nanostructures and microstructure arrays (a) Experimental measurements as a function of pulse energy at 800 nm. **(b)** FDTD simulation as a function of wavelength covering the bandwidth of the laser pulse. In both, the figures, the black curve represents the achiral nanostructure, and the red (blue) curve represents the right (left) handed chiral nanostructure. The green (pink) curve represents the CD signal for chiral right(left) handed chiral microstructures. The error bands in a) and b) represent the standard error of multiple measurements (n=3).

Fig S3a shows experimental CD signal as a function of pulse energy obtained experimentally for an achiral nanostructure (black curve), left- and right-handed chiral nanostructures (red and blue curve), and microstructures arrays (green and pink curve). The average CD signal for an achiral nanostructure array is close to zero. A similar curve with a vanishing CD signal was obtained for achiral microstructure arrays(not shown). For chiral structures, the average CD signal for specific handed nanostructure arrays is $\sim$ 6% and $\sim$ 2-3% in microstructures.

S3b shows a simulated CD signal using FDTD software with left- and right-handed circularly polarized plane wave source. The achiral structure does not exhibit a CD signal as expected. The CD signal obtained for chiral nanostructure is $\sim$ 2% and $\sim$ 1% in the case of microstructure arrays. Qualitatively, CD signals obtained experimentally and through simulation are in agreement. However, quantitatively, the magnitude of CD obtained experimentally is higher than the simulated value. This discrepancy could potentially be attributed to the use of a plane wave source in the simulations, as opposed to the Gaussian source used in the experiment.

3 Transmission curves

Transmission experiments were performed to measure the phase-based differential response in the achiral and chiral metasurfaces. $\mathrm{HD}(l,s) = A(l,s) - A(-l,s)$ was evaluated by taking the difference between the transmission curves for left- and right-handed helical light. Fig S4 shows the transmission curves in achiral nanostructures with left- and right-handed linearly polarized symmetric and asymmetric helical light beams, plotted as a function of incident pulse energies. The inset in the figure shows the beam profile. The error bands represent the standard error of multiple measurements (n=3).

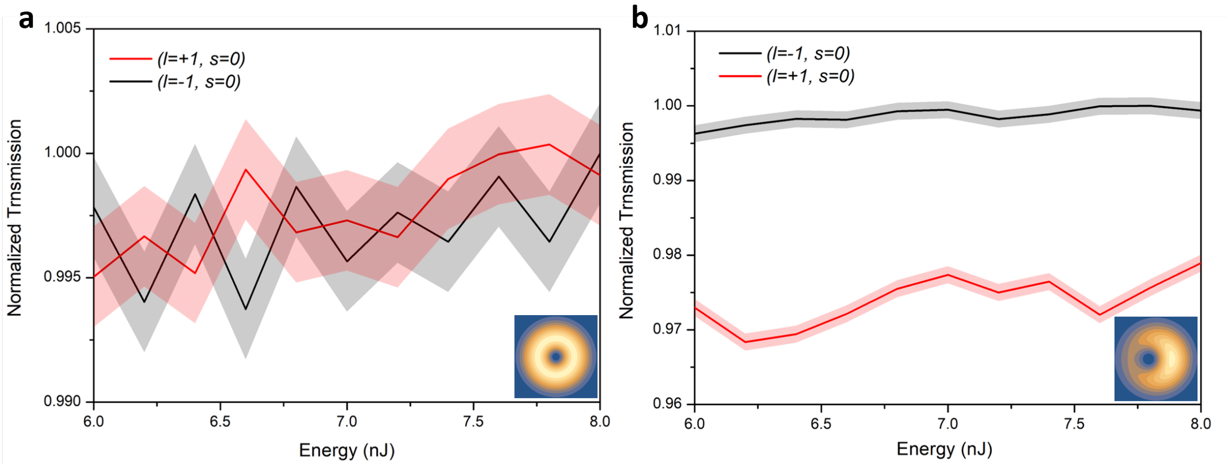

Fig S 4. Normalized transmission curves in achiral nanostructures for left- and right-handed linearly polarized helical light plotted as a function of incident pulse energy for **(a)** for a symmetrical and **(b)** asymmetrical LG beams ($l = 1$). Insets show the beam profiles. The difference between the curves is the HD signal. The error bands in a) and b) represent the standard error of multiple measurements (n=3)

The HD signal is only non-zero for the displaced position of the singularity, i.e., asymmetric beams (Fig. 1), and vanishes for symmetric beams ($l = 1$). The transmission curves in Fig. S4(b) are obtained for $\delta = -600$ nm position of singularity. The difference between these curves for different positions of singularity produces the sinusoidal behavior of the HD curve, as shown in the main text.

4 Background noise check

In order to check the background noise in our experimental setup, transmission measurements were conducted in the air (absence of a sample) and on the substrate surface without metasurface (blank area). Such measurements enabled us to ensure that the photodiodes detect identical signals when changing the helicity of the incoming linearly polarized light from $+l$ to $-l$. Additionally, any signal produced in these check experiments was regarded as background noise arising from the instrument and calibration errors. Fig. S5 (a-b) shows helical dichroism obtained without the sample (in the air) and on the blank substrate surface, plotted as a function of displacement of singularity.

Results for both in air and on blank substrate surface demonstrate that an average $\leq 0.5\%$ signal/noise was introduced by the experimental setup to the observed differential absorption in chiral and achiral metasurface. The maximum background noise can be subtracted from the obtained HD for each position of singularity. Transmission measurements on the substrate and in the air were performed before every experimental run and for every position of the displaced singularity.

5 HD in chiral metasurface with circularly polarised helical light

To discern the role of phase and polarization, the helical dichroism was evaluated for linearly and circularly polarized helical light beams for both achiral and chiral geometries. $\mathrm{HD}(l,s) = A(l,s) - A(-l,s)$, was obtained by changing the phase and keeping the polarization constant. When the polarization is switched from linear (s=0) to circular (s=±1), the magnitude of HD increases, as shown in the results presented in the main text. However, results for only one-handedness of circular polarization (s=+1) were presented. Here we present the HD curve for both left- and right- handed polarization.

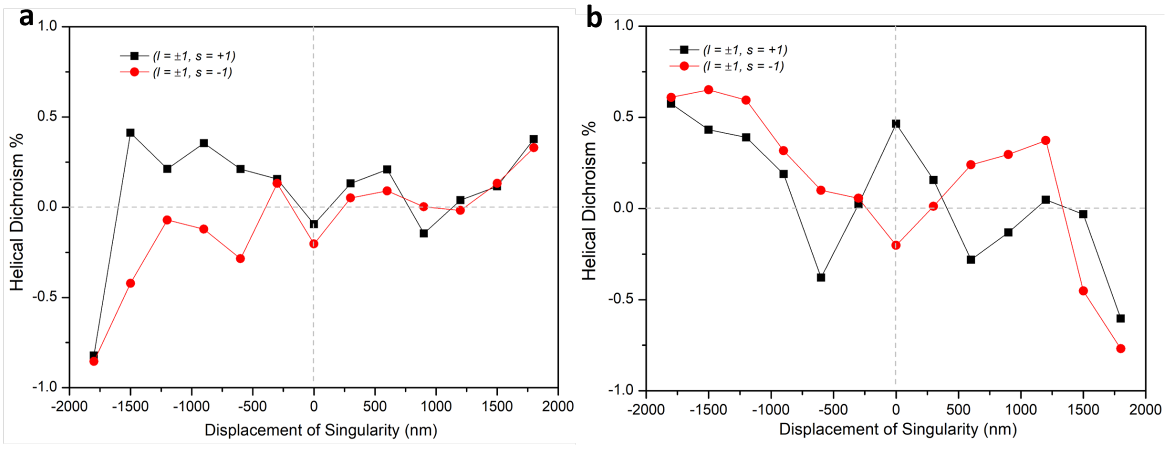

FIG. S 5. Background noise check in transmission experiments obtained by evaluating helical dichroism in **(a)** air (without the sample) **(b)** the surface of the substrate (blank area without metasurface). The average of $\leq 0.5\%$ signal/noise was introduced by the experimental setup to the observed helical dichroism.

Figure 6a shows HD in left- handed nano structure, plotted as a function of displacement of singularity . The results shows HD signal is slightly displaced and almost overlapping (considering errors) when the polarization is switched from left to right. These results confirms that HD is predominantly a phase effect and polarization plays minimal role. Figure 6b is continuation of fig. 3a of main text where the HD signal for only right handed structure was presented. The difference between the curves suggest that another form of HD exists that can be defined as HD$(l,s) = R(l,s) - S(l,s)$, which is the difference between signal for right- and left- handed chiral structures keeping the phase and polarization constant. This shows that our method can also be used to differentiate between the handedness of structures.

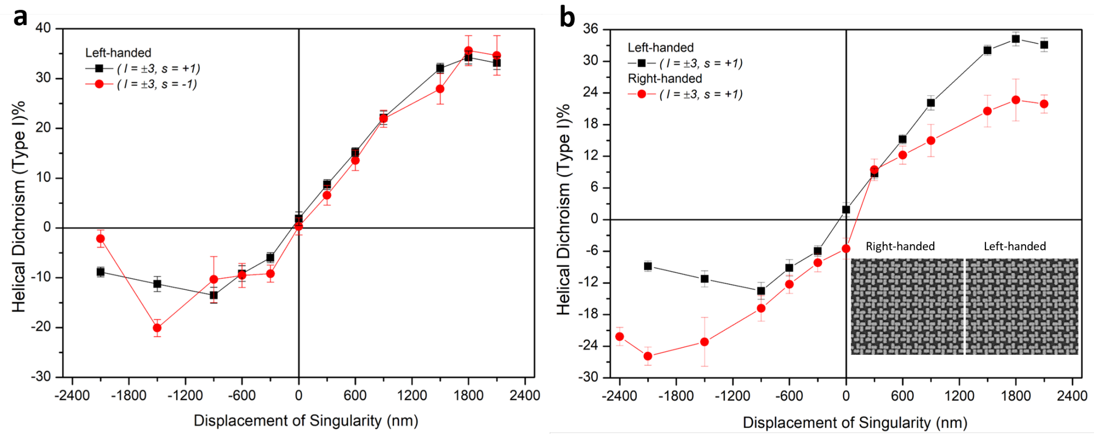

Fig S6 6. Helical dichroism in chiral plasmonic metasurfaces for $l = \pm 3$ **(a)** Differential absorption of left-and right-handed helical light in left-handed nanostructures as a function of displacement of the singularity for left-circular (black) and right-circular (red) polarization. **(b)** HD in left-handed (black) and right-handed (red) chiral nanostructures as a function of displacement of the singularity, δ, for a specific circular polarization ($\varepsilon = 0.95$). Insets show the SEM images of the structures. The error bars represent the standard error of multiple measurements (n=3), calculated for an average energy range used to obtain HD (see text for details)

6 HD signal strength comparison with published literature

Study	Dimensions	Material	SAM and OAM states	Structure symmetry	HD strength
This work	Micro- and nano-structures	Gold	$s = 0, \pm 1$ $l = \pm 1, \pm 3$	Achiral and chiral	Achiral = 15% Chiral = 25%
Ni et al.[1]	Micro-structures	Dielectric	$s = 0$ $l = \pm 1$ to 20	Achiral and chiral	Achiral = 0% Chiral = 20%
Cao et al.[2]	Microspeheres	Gold-plated 3D oligomers	$s = 0$ $l = \pm 1$ to 30	Achiral and chiral	Achiral = 0% Chiral = 23%
Ni et al.[3]	Microhelix	Gold	$s = 0$ $l = \pm 1$ to 30	Achiral and chiral	Achiral = 0% Chiral = 120%
Dai et al.[4]	Microhelix	Copper	$s = 0$ $l = \pm 1$ to 30	Chiral	Chiral = 50%

7 Chiral effects in terms of parity-time symmetry

HD is defined as the difference in absorption of left- and right-handed helical light irrespective of material symmetry. When a chiral structure is involved in the interaction with chiral light, HD represents true chirality (traditionally represented by PT odd symmetry) and is analogous to the definition of CD. In the case of achiral structures, it represents a difference in absorption of left- and right-handed helical light and is also explained by PT odd symmetry.

In chiral structures, HD arises due to the contribution of both E1M1 and E1E2 (as explained in eq. 1 of main text). In achiral structures, only the E1E2 coupling term (paragraphs following eq. 1) contributes to HD. The multipolar coupling terms E1M1 and E1E2 can be further expanded in terms of PT symmetries.

- Conventional CD is described by the electric-magnetic dipole coupling term $E1M1 \propto \langle \mathrm{G}'' \rangle C^{\pm}$where C represents optical chirality defined as $C^{\pm} = 2\omega \operatorname{Im}\left[\left(\tilde{E}^{\pm}_{\delta}\right)^{*} \cdot \tilde{B}^{\pm}_{\delta}\right]$. This coupling term is a space odd-time even pseudoscalar and can be shown as

$$PT\left\{\frac{\omega}{2}\operatorname{Im}\left[E^{*}\cdot B\right]\right\} \to P\left\{-\frac{\omega}{2}\operatorname{Im}\left[E\cdot B^{*}\right]\right\} \to P\left\{\frac{\omega}{2}\operatorname{Im}\left[E^{*}\cdot B\right]\right\} = -\frac{\omega}{2}\operatorname{Im}\left[E^{*}\cdot B\right]$$

Therefore, optical chirality is odd under PT symmetry.

- HD is described by the electric dipole-quadrupole coupling term $E1E2 \propto \langle A'' \rangle \Upsilon\pm$ where optical helicity Υ is defined as $Y^{\pm}_{\pm} = \operatorname{Re}\left[\nabla_i E^{\pm}_j E^{\pm *}_i\right]$. The optical helicity is a vector quantity that is odd under parity with a change in the sign of the displacement of the singularity, δ, and time reversal only changes the handedness of helical light. Also, optical helicity is polarization invariant. Therefore, the optical helicity under PT symmetry is given as

$$\begin{aligned}
&\mathrm{PT}\left[\Upsilon^{\pm}_{\pm\delta}\right] \to \mathrm{PT}\left[\operatorname{Re}\left[\nabla_i E_j(\pm l, \pm\delta) E_i(\pm l, \pm\delta)^{*}\right]\right] \to \mathrm{P}\left[\operatorname{Re}\left[\nabla_i E_j(\pm l, \pm\delta) * E_i(\pm l, \pm\delta)\right]\right] \to \\
&P\left[\operatorname{Re}\left[\nabla_i E_j(\mp l, \pm\delta) E_i(\mp l, \pm\delta)^{*}\right]\right] \to -\operatorname{Re}\left[\nabla_i E_j(\mp l, \mp\delta) E_i(\mp l, \mp\delta)^{*}\right] = -\Upsilon^{\mp}_{\mp\delta}
\end{aligned}$$

Using this property, the symmetry of the E1E2 term in the case of achiral and chiral systems is as follows:

In achiral system (interaction with asymmetrical left- and right-handed helical beams): According to equation 1 in the article, PT[HD] $= \mathrm{PT}\left[A''\left[\Upsilon^{+}_{+\delta} - \Upsilon^{-}_{+\delta}\right]\right] = \{\mathrm{PT}\left[A''\right]\}\left[-\Upsilon^{-}_{-\delta} + \Upsilon^{+}_{-\delta}\right] = -A''\left[\Upsilon^{+}_{-\delta} - \ Y^{-}_{-\delta}\right]$where $\mathrm{PT}\left[A''\right] = -A''$, since electric dipole moment is space odd-time even and quadrupole is space even-time even moments. Therefore, HD is odd under PT symmetry with respect to $\pm\delta$ position. This is observed in our experimental results (Figs. 2).

In Chiral system (interaction with asymmetrical left- and right-handed helical beams for a fixed-handedness of chiral structures): For simplicity, we use the concept of considering the chiral nanostructures as an effective metamolecule. Therefore, PT symmetry on right-handed metamolecule(R) will lead to left-handed metamolecule(S) $PT\left[\mathscr{D}_{\mathrm{R}}\right] = -\left[\mathscr{D}_{s}\right]$. This simply means the operation of PT symmetry on a one-handed chiral system generates the other-handed system with odd symmetry. If the parallel to molecular enantiomer is drawn, this odd parity can be explained in terms of symmetric and antisymmetric wavefunctions[5,6]. Therefore, PT[HD] $= \mathrm{PT}\left[\mathscr{D}_{R}\left[\mathrm{Y}^{+}_{+\delta} - \Upsilon^{-}_{+\delta}\right]\right] = \{\mathrm{PT}\left[\mathscr{D}_{R}\right]\}\left[-\Upsilon^{-}_{-\delta} + \Upsilon^{+}_{-\delta}\right] = -\mathscr{D}_{s}\left[\Upsilon^{+}_{-\delta} - \Upsilon^{-}_{-\delta}\right]$. This is observed in our experimental results (Fig. 3). In this case, HD can be considered as intrinsic chirality and is analogous to CD.

References

1. Ni, J. *et al.* Giant helical dichroism of single chiral nanostructures with photonic orbital angular momentum. *ACS Nano* **15** (2021).

2. Cao, Y. *et al.* Photonic orbital angular momentum dichroism on three-dimensional chiral oligomers. *ACS Photonics* **10**, 1873–1881 (2023).

3. Ni, J., Liu, S., Wu, D., Qiu, C.-W. *et al.* Gigantic vortical differential scattering as a monochromatic probe for multiscale chiral structures. *Proc. Natl. Acad. Sci.* **118** (2020).

4. Dai, N. *et al.* Robust helical dichroism on microadditively manufactured copper helices via photonic orbital angular momentum. *ACS Nano* **17** (2023).

5. Wagnière, G. H. *On Chirality and the Universal Asymmetry: Reflections on Image and Mirror Image* (John Wiley & Sons, 2008).

6. Jain, A., Bégin, J.-L. & Bhardwaj, R. Helical dichroism in enantiomeric solutions. *J. Chem. Phys.* **159**, 014504 (2023).

References

[1] Patrick Spaeth, Subhasis Adhikari, Laurent Le, Thomas Jollans, Sergii Pud, Wiebke Albrecht, Thomas Bauer, Martín Caldarola, L. Kuipers, and Michel Orrit. Circular dichroism measurement of single metal nanoparticles using photothermal imaging. *Nano Letters*, 19(12):8934–8940, 2019. PMID: 31790264.

[2] Jincheng Ni, Shunli Liu, Guangwei Hu, Yanlei Hu, Zhaoxin Lao, Jiawen Li, Qing Zhang, Dong Wu, Shaohua Dong, Jiaru Chu, and Cheng-Wei Qiu. Giant helical dichroism of single chiral nanostructures with photonic orbital angular momentum. *ACS Nano*, 15(2):2893–2900, 2021. DOI: 10.1021/acsnano.0c08941.

Chapter 7

Controlled material manipulation using helical light

7.1 Introduction

So far, we have learned how matter exhibits a differential response when investigated with asymmetric helical light beams. The asymmetry in both the phase and intensity profile was employed to probe the differential response of matter and to demonstrate the helical phase-based spectroscopy. This prompts the question: *Can these asymmetric beams be utilized in other applications where light-matter interactions play a dominant role?*

Direct laser processing (DLP) of materials is one such application. DLP exploits the nonlinear nature of light-matter interactions to achieve sub-diffraction spatial resolution in nanofabrication [1, 2]. Ultrafast laser pulses have been employed to fabricate 3D structures with sub-wavelength feature sizes. DLP has enabled the creation of nanoholes [3, 4], dots [5], and laser-induced periodic surface structures (LIPSS) [6, 7] through ablation or above-threshold material modification. Another widely used direct-write technique in nanofabrication is the Laser-Induced Forward Transfer (LIFT) [8, 9]. This method involves depositing small volumes of complex materials into user-defined, high-resolution patterns. The spatial resolution achievable is constrained by the size of the laser spot and the dynamics of material transfer. Additionally, DLP has enabled the fabrication of nanocones. When silicon is irradiated with ultrafast OAM beams, its intensity distribution is mapped onto the silicon surface, causing localized melting. The molten material moves from high- to low-temperature regions due to thermocapillary and hydrodynamic forces, leading to the formation of nanocones at the positions of the null intensity (phase singularity) in the OAM beams [10, 11, 12]

Although light-induced nanostructures with sub-diffraction feature sizes can be fabricated through various techniques, the degree of spatial control with light remains limited. For instance, in the case of nanocone formation using OAM beams, the spatial position of the nanocone is fixed to the beam center, and active positioning cannot be achieved. But why is the ability to achieve spatially controlled nanofabrication significant?”

Nanoscale spatial precision and control are critical for engineering material properties in the development of nano-devices. For instance, in the LIFT technique, enhanced spatial control and precision in material deposition would enable the nano-printing of complex patterns. In the case of nanocones, controlled fabrication has applications across various fields; for example, semiconductor and metal nanocones can be used as field emission tips [13, 14] and for scanning probe technologies.

7.2 Results

Our research demonstrated controlled material manipulation in 2D with nanoscale positional precision. This was achieved by the spatially controlled formation of nanocones on a silicon surface with a sub-wavelength positional precision of 50 nm. This technique exploited the coherent superposition of an optical vector vortex beam (VVB) and a Gaussian beam to actively position the fabricated nanocones. VVBs are helically phased light beams characterized by the spatially variant polarization structure in the transverse plane of the beam.

Electrical detuning of the q-plate led to the superposition of the incident Gaussian beam with VVBs, which resulted in the displacement of the phase singularity. Angular positional precision in displacing the singularity was achieved by varying the phase retardation of the input Gaussian beam. Fine electrical control over the phase retardation and q-plate detuning enabled a nanoscale positional resolution.

Apart from the numerous advances of our technique (outlined in the following section), it suffered from certain limitations. The primary limitation was that nanocones could be efficiently fabricated only on non-transparent materials, where the melt layer remained two-dimensional. In transparent materials, light penetration into the medium resulted in a three-dimensional melt layer, leading to surface swelling and material ejection rather than the formation of a well-defined nanocone. Additionally, nanocones were consistently accompanied by an outer rim, the relative height of which could be minimized by adjusting the laser parameters, albeit with a corresponding reduction in the nanocone height.

This research was published in the *Scientific Reports* journal (2020). The published version of the article and supplementary file are reproduced in this chapter, where experimental methods, figures, and references are self-contained within each. The following section presents the key advances of this research.

7.3 Key advances

- *Phase-based material manipulation*: A new phase-based laser ablation method was introduced. By utilizing the superposition of different-order helical beams and the phase retardation of the input beam, a controlled material manipulation was achieved.
- *Sub-wavelength spatial positioning*: Nanocones formed during the ablation process were positioned with a 50 nm precision in an area of 40 μm^2. The light wavelength used in our experiments was 800 nm. Therefore, the spatial positioning resolution obtained was approximately eight times below the diffraction limit ($\sim \lambda/2$).
- *Complex unconventional structures* involving multiple nanocones were fabricated using our method. The control and precision shown for a single nanocone could be translated to multiple cones with the same precision.

7.4 Femtosecond laser interaction and nanocone formation

The first step in the laser ablation process is the absorption of the incident photons by the target solid material. This absorption can occur via a linear process when the energy of an incident photon exceeds the bandgap, or through nonlinear processes if multiple lower-energy photons collectively exceed the bandgap. Irrespective of the light absorption regime, the material in the focal region is heated to its melting point. Depending on the laser intensity and pulse width, the material may be further heated to its vaporization temperature. The absorption mechanisms vary among different materials, such as metals, semiconductors, and transparent dielectrics [16]. In transparent materials, linear absorption is absent, and laser energy is primarily absorbed through nonlinear processes. Conversely, in opaque materials, linear absorption typically dominates when dealing with long pulse widths (i.e., low peak intensity). However, at ultrashort pulse widths with extremely high peak intensities, nonlinear absorption can become the dominant mechanism [17].

When a solid-state material is exposed to femtosecond (fs) pulses, it undergoes several stages of excitation and relaxation before returning to equilibrium. These stages include 1) carrier excitation, 2) thermalization, 3) carrier removal, and 4) thermal and structural effects. Each stage occurs over specific timescales, as depicted in Fig.7.1. The interaction of fs pulses is unique in the sense that the pulse imparts energy to the material in a time frame smaller than the electron-phonon coupling relaxation time. Therefore, only the electrons receive energy from the incident pulse, leaving the ions in a relatively ‘cold’ state. The transfer of thermal energy to the lattice occurs at sub-nanosecond (ns) timescales when the pulse is no longer active. Thus, for fs pulse interactions, optical absorption and lattice thermalization are independent processes

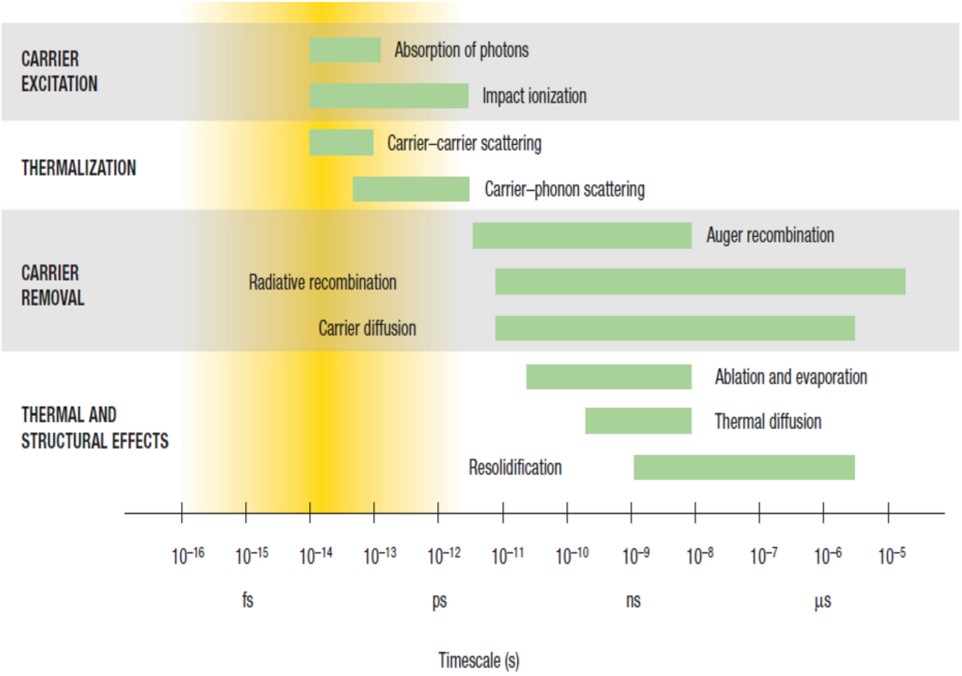

Figure 7.1: Timescales of various electron and lattice processes in laser-excited solids are illustrated, with each green bar representing the approximate range of characteristic times. The figure depicts the excitation and relaxation dynamics of both electrons and the lattice in a laser-excited direct bandgap semiconductor. This figure is reproduced from Sundaram et al. [15].

that uniquely characterize the interaction. The following paragraphs briefly discuss each step in the excitation process and are based on the detailed review by Sundaram et al. [15].

Carrier excitation: In opaque solid materials, photon absorption is facilitated through either linear or nonlinear processes, depending on the material's bandgap. For absorbing materials, such as metals and semiconductors, with a lower bandgap than the incident photon energy and a large density of free electrons, linear absorption is the dominating mechanism. The free electrons simply wiggle (oscillate) under the incident field and do not gain net energy (when averaged over an optical pulse cycle). However, they can gain energy through scattering processes such as carrier-carrier scattering and carrier-phonon scattering. This energy transfer is known as laser-induced heating. Carrier-carrier scattering occurs on the timescale of the pulse duration, while interactions with the lattice can extend up to picoseconds (ps), as shown in Fig. 7.1. This step is characterized as thermalization. If carriers are accelerated to kinetic energies exceeding the bandgap energy, impact ionization may occur. In this process, energized electrons excite bound electrons, imparting enough energy to overcome their bandgap energy, thereby generating additional free electrons. This process continues post-pulse for tens of ps, as shown in Fig.7.1.

In the case of transparent materials, light absorption is facilitated by a nonlinear process[16]. The nonlinear absorption process can occur through mechanisms like avalanche ionization and multiphoton absorption. Avalanche ionization, a repetitive impact ionization, leads to an exponential increase in free-electron density from an initially low seed electron density. When this density reaches the critical density, where the plasma oscillation frequency equals the laser frequency, the material becomes highly absorptive (completely opaque in the case of transparent materials). In multiphoton absorption, when the laser peak intensity is sufficiently high, bound electrons can be directly excited to the conduction band by simultaneously absorbing n photons in the laser pulse such that $nh\nu \geq E_g$, where $h\nu$ is the energy of the photon, and E_g is the bandgap.

Thermalization: This phase involves energized electrons transferring their energy to other bound carriers and the atomic lattice through scattering processes, as previously discussed. Following the carrier excitation process, electrons and holes undergo redistribution across conduction and valence energy bands through interactions involving carrier-carrier and carrier-phonon scattering. In carrier-carrier scattering, a free electron impact ionizes another electron, leading to energy transfer and material heating, often referred to as laser-induced heating. Although this type of scattering can dephase the coherence between the excited carrier and the electromagnetic field in less than ten fs, transitioning the carrier distribution towards a Fermi-Dirac distribution under equilibrium conditions requires several hundred fs.

In the carrier-phonon scattering process, energy is transferred to the lattice by the emission of a phonon. This scattering process does not alter the carrier density, but their energy decreases. In opaque materials, such as metals and semiconductors, following the excitation process, carrier-carrier and carrier-phonon scattering take place simultaneously. However, since energy transfer is facilitated by phonons, which carry minimal energy, numerous subsequent scattering events are needed before the carriers and the lattice achieve thermal equilibrium, extending this phase to tens of picoseconds, as shown in Fig.7.1.

Carrier removal: This phase describes the mechanisms by which charge carriers (electrons and holes) are removed from the conduction and valence band. After the thermalization step, upon reaching equilibrium between the carriers and the lattice, the material stabilizes at a consistent temperature. Despite the carrier distribution sharing the same temperature as the lattice, there is a surplus of free carriers compared to what is present in thermal equilibrium. These excess carriers are eliminated through radiative, diffusion, and non-radiative processes, as shown in Fig.7.1.

Radiative recombination, as the name suggests, results in the release of energy in the form of photons, which are generated when electrons and holes recombine. This process reduces the overall number of free carriers and typically takes place over timescales ranging from several picoseconds to microseconds. Carrier diffusion drives carriers from areas of high concentration to regions of lower concentration. Unlike recombination, this process does not reduce the free carrier density and typically takes place over timescales ranging from several picoseconds to microseconds. In the non-radiative process, also known as Auger recombination, an electron and a hole recombine, and the energy from this recombination is transferred to a third carrier, exciting it to a higher state in the conduction band. This occurs quickly, within picoseconds to nanoseconds, and is significant in materials with high carrier densities, such as metals and semiconductors.

Thermal and structural effects: This phase is critical for understanding the physical changes that materials experience under conditions of extreme thermal stress. It describes the series of transformations a material undergoes following the carrier and lattice attaining an equilibrium temperature and the removal of surplus free carriers. It comprises processes like ablation and evaporation, thermal diffusion, and resolidification, each occurring over distinct timescales that range from picoseconds to microseconds, as shown in Fig.7.1. Additionally, the quick heating and cooling associated with this method can create substantial thermal gradients within the material, potentially causing thermal stress and cracking.

If the carrier-lattice equilibrium temperature exceeds the melting point of the material, vaporization or melting can occur on the ps timescale. This process can be described as an ablation process, which is characterized by the explosive removal or vaporization of the material's surface within nanoseconds to microseconds. The ablation process involves the conversion of the laser pulse's energy into the kinetic energy of the lattice ions, which results in the detachment of atoms, ions, molecules, or clusters from the surface, leading to evaporation and sublimation. Subsequently, thermal diffusion redistributes the heat from the heated regions to cooler areas of the material. This process decreases the rate of temperature increase by cooling the photoexcited region but does not prevent further thermal effects. This occurs over hundreds of picoseconds to tens of nanoseconds. After the peak temperature is reached and if energy absorption ceases, the material begins to cool. Consequently, resolidification occurs, returning it to a solid state below critical temperature thresholds. If no significant phase transition happens, the material cools to ambient temperature within microseconds due to thermal diffusion.

Nanocone formation: From the above discussion, we can understand the formation of nanocones on silicon when it is exposed to a helically-phased OAM beam. Initially, the interaction starts with carrier excitation in silicon, driven by both single and two-photon absorption processes. This excitation is influenced by the annular intensity distribution of the OAM beams, which leads to a similar spatial distribution of the free carriers produced. After this phase, during the thermalization step, a stable equilibrium temperature is achieved within a few picoseconds, preserving the temperature distribution in the shape of the beam's intensity. Energy from these free carriers is then transferred to the lattice, primarily through non-radiative recombination and thermal diffusion.

Subsequently, due to thermal and structural effects, melting occurs on the nanosecond scale, transforming only a thin layer of silicon into liquid. Thermocapillary and hydrodynamic forces propel the molten silicon both radially outward to the edges and inward towards the center of the crater. The outward motion forms a rim akin to that observed with a Gaussian beam, while the inward motion exerts a compressive force that ejects the molten material from the surface. This rapid movement results in the material's resolidification into a nanocone. Mitra et al.[11] have modeled the nanocone formation by considering the dynamics of the molten material, using the continuity equation and the Navier-Stokes equation.

The author contributions are presented in the following section. The published version of the article and supplementary file are attached later.

7.5 Statement of contribution

Ashish Jain and Mitra G. Rahimian contributed equally to the experimental work.

Mitra G. Rahimian analyzed the data and prepared figures and graphs. Ashish Jain performed the simulations and theoretical calculations.

Hugo Larocque built the q-plate and assisted in producing vortex beams. Paul Corkum, Ebrahim Karimi, and Ravi Bhardwaj supervised and designed the experiment.

All authors contributed to writing the manuscript.

www.nature.com/scientificreports

SCIENTIFIC REPORTS

natureresearch

OPEN

Spatially controlled nano-structuring of silicon with femtosecond vortex pulses

M. G. Rahimian, A. Jain, H. Larocque, P. B. Corkum, E. Karimi & V. R. Bhardwaj

Engineering material properties is key for development of smart materials and next generation nanodevices. This requires nanoscale spatial precision and control to fabricate structures/defects. Lithographic techniques are widely used for nanostructuring in which a geometric pattern on a mask is transferred to a resist by photons or charged particles and subsequently engraved on the substrate. However, direct mask-less fabrication has only been possible with electron and ion beams. That is because light has an inherent disadvantage; the diffraction limit makes it difficult to interact with matter on dimensions smaller than the wavelength of light. Here we demonstrate spatially controlled formation of nanocones on a silicon surface with a positional precision of 50 nm using femtosecond laser ablation comprising a superposition of optical vector vortex and Gaussian beams. Such control and precision opens new opportunities for nano-printing of materials using techniques such as laser-induced forward transfer and in general broadens the scope of laser processing of materials.

The fundamental limit to spatial resolution of any optical system is governed by diffraction and is approximately half the wavelength of light[1]. Diffraction also dictates how tightly a laser beam can be focused, which in turn determines the feature size one can achieve in laser ablation of materials. Therefore, shorter wavelengths (ultraviolet) are often used in combination with lithographic techniques to produce sub-wavelength features as small as 50 nm[2]. Driven primarily by the semiconductor industry, research efforts are ongoing to use coherent and non-coherent extreme ultraviolet light to produce features smaller than 10 nm to meet the ever increasing demand for miniaturization[3,4]. Concurrently, alternate methods are also being explored to overcome the diffraction limit of light that does not involve the use of a photomask. These fall into two categories—near field and far field approaches.

Nanofabrication using near field approach exploits local field enhancement around a nanoparticle to confine light to sub-wavelength dimensions and thereby induce local deformations (melting or ablation) of the substrate. Large scale periodic array of nanoholes were fabricated by laser irradiation of a monolayer of microspheres[5]—a multistep process with no direct control on the position of nanostructures, analogous to lithographic techniques[6]. Alternately, controlled fabrication of individual nanostructures can be achieved using scanning probe microscope either directly[7] or by irradiating the tip with light[8].

Direct laser processing of materials is a far field approach that exploits the nonlinear nature of the light-matter interaction and localized energy deposition. Using ultrashort laser pulses, three-dimensional (3D) control was achieved in transparent materials[9,10] and sub-wavelength structures were created with enhanced spatial precision in a cold ablation process due to negligible lateral heat transport to the surrounding material. Exploiting near threshold ablation, feature dimensions far below the diffraction limit were demonstrated[11,12]. However, in such a threshold based material response, the ablation features were found not to be dependent on the nonlinear process responsible for light absorption but rather correspond to a one-to-one mapping of the beam profile at threshold intensity[13]. Nanoholes[14,15], nanocones[16–19], nanodots[5] and self-organized periodic nano-ripple patterns[20–22] were also fabricated in different materials either by ablation or material modification using above threshold laser pulse energies.

Another non-contact direct laser-write technique that is widely used in nano-printing is Laser Induced Forward Transfer (LIFT) to "drop and place" small volumes of complex materials into user-defined, high-resolution patterns[23,24]. A thin film of material on a donor substrate is melted locally by the laser beam and lifted off in the form of a droplet that gets deposited onto a receiver substrate separated by a small gap. The spatial resolution one could achieve in placing individual droplets is few hundreds of nanometers.

Department of Physics, University of Ottawa, K1N 6N5 Ottawa, ON, Canada. email: ravi.bhardwaj@uottawa.ca

Although light induced nanostructures with feature sizes smaller than diffraction limit could be fabricated either by ablation or material modification[25], the degree of spatial control with light is restrictive. For example, it is not feasible to position individual structures with nanoscale precision. Only partial spatial control has been achieved with nano-ripples whose orientation and spacing was varied by changing the laser polarization and wavelength (λ)[21]. In this context, the present article addresses how light can be used to actively manipulate materials in two dimensions with a precision of $\sim \lambda/20$. It demonstrates positioning of $\sim 0.1\,\mu m^3$ of the molten material in the form of a nanocone with 50 nm precision in an area of $40\,\mu m^2$ by manipulating the beam shape. The technique is extended to fabricate complex, unconventional structures involving multiple nanocones and control their relative positions with the same precision.

Apart from laser fabrication and spatial control of nanostructures, surpassing the diffraction barrier imposed by the wave nature of light is also critical in imaging/microscopy. It is accomplished by using the same (a) near field techniques that exploit the information contained in the evanescent wave[26,27] or confine light using plasmonic nanostructures[28,29], and (b) far field techniques that exploits the optical nonlinearity of the medium as in stimulated emission depletion microscopy[30].

Our approach to sub-wavelength precision in nano-fabrication is based on the coherent superposition of optical vector vortex beam (VVB) and a Gaussian beam[31]. VVBs are characterized by spatially variant linear polarization in the beam transverse plane. They may possess phase singularities in the transverse plane at which the field amplitude vanishes. VVBs can be expanded in terms of orbital angular momentum (OAM) carrying, i.e. twisted, beams. Twisted beam carry an OAM value of $\ell\hbar$ per photon, where $\hbar$ is the redueced Plank constant, and ℓ indicates the number of twists in the helical wavefront in one wavelength which its sign determines the chirality of the helix. We produce VVBs using a birefringent plate enclosing a patterned liquid crystal layer, known as a q-plate. The liquid crystals in the q-plate have an optic axis whose orientation depends on the azimuthal coordinate, thereby forming a pattern defined by a topological charge q consisting of either a full or a half-integer value. As light propagates in the q-plate, spin angular momentum associated with light polarization is coupled to photon OAM of $\ell = \pm 2q$. The conversion efficiency is determined by the q-plate's optical retardation, which can be controlled by an externally applied electric field.

Results

Our technique exploits two unique properties of VVBs. First, the annular intensity distribution of the VVB when focused is mapped onto the silicon surface causing melting of a thin layer, determined by the optical penetration depth of light. Thermo-capillary and/or hydrodynamic forces displace the molten silicon radially outward to the periphery and also radially inward to the centre of the crater. Compressive forces arising from radial inward motion of the molten material pushes it away from the surface. Rapid expansion causes re-solidification into a nanocone formed (Fig. 1a) at the centre where VVB has a zero intensity point[18]. Simultaneously, the radial outward motion of the molten material re-solidifies after reaching the cold boundary of the ablation region to form a rim. The height of the nanocone is ~ 500 nm and increases with the increasing pulse energy while the rim height is only ~ 100 nm[18]. Longer nanocones or nanoneedles have been produced with vortex beams using nanosecond and picosecond pulses on silicon[32] and metals[33]. They were shown to exhibit chirality and has been attributed to (a) mapping of the orbital angular momemtum of the beam on to the handedness of the nanoneedles[33], and/or (b) tailored chiral intensity distribution that also controls the handedness of nanoneedles[34]. In contrast, there was no clear signature of the chirality-control fabrication (by changing OAM value) of nanocones produced by femtosecond pulses.

Second, when a pure VVB is perturbed by adding coherently a tunable amount of a linearly polarized Gaussian beam, the central singularity either shifts or unfolds into multiple singularities depending on the topological charge. The shift can be precisely controlled by adjusting the applied external field to the q-plate. This action varies the optical retardation and thereby detunes the strength of the spin-to-orbital angular momentum coupling of light. A fraction of the input Gaussian beam co-propagates with a partly converted VVB. As a result, for q=1/2 or $\ell = \pm 1$, the position of the nanocone within the ablation region can be varied with nanometers precision (Fig. 1b,c). As the weight of the Gaussian beam increases, the position of the singularity shifts towards the outer region of the ablated region (also see Supplementary Fig. S2). For a pure VVB produced by q=1/2 plate, the output polarization was radial, azimuthal, or spiral[22] when the angle of the incident linear polarization with respect to the q-plate axis was 0°, 90°, or 45°, respectively.

The nanocone position can be controlled by moving the singularity anywhere in the transverse plane of the beam as shown in Fig. 2, for azimuthally polarized VVB. For a fixed optical retardation (relative weight of Gaussian beam to VVB), a half-wave plate (HWP) in front of the detuned q-plate rotates the input polarization with respect to the q-plate axis and changes the angular position of the singularity at the transverse plane rotating it in a circular arc. Radius of the circular arc depends on the optical retardation. Varying the applied electric field to the q-plate and rotating the incident linear polarization, the nanocone can be positioned anywhere in 2D space within the interaction region of $\sim 40\,\mu\,m^2$ with a precision of 50 nm. Similar results were obtained for radial and spiral VVBs.

Figure 3 shows unfolding of the singularity when a pure VVB with a star-shaped polarization pattern[22] with $\ell = \pm 2$ (topological charge of $q = -1$) is perturbed by a Gaussian beam. The perturbation is achieved by electrically detuning the q-plate. In VVBs, the total field orientation is undefined along the beam axis and this polarization singularity is typically referred to as a V-point. A small perturbation to pure VVB causes the local polarization states to acquire a tiny ellipticity. The V-point no longer exists, instead two pairs of C-points appear where the orientation of the polarization ellipse is undefined. Unfolding of the polarization singularity also deforms the intensity pattern of the pure VVB giving rise to two null intensity points. The separation between these points can be controlled by varying the relative weight of Gaussian beam superimposed on the VVB and

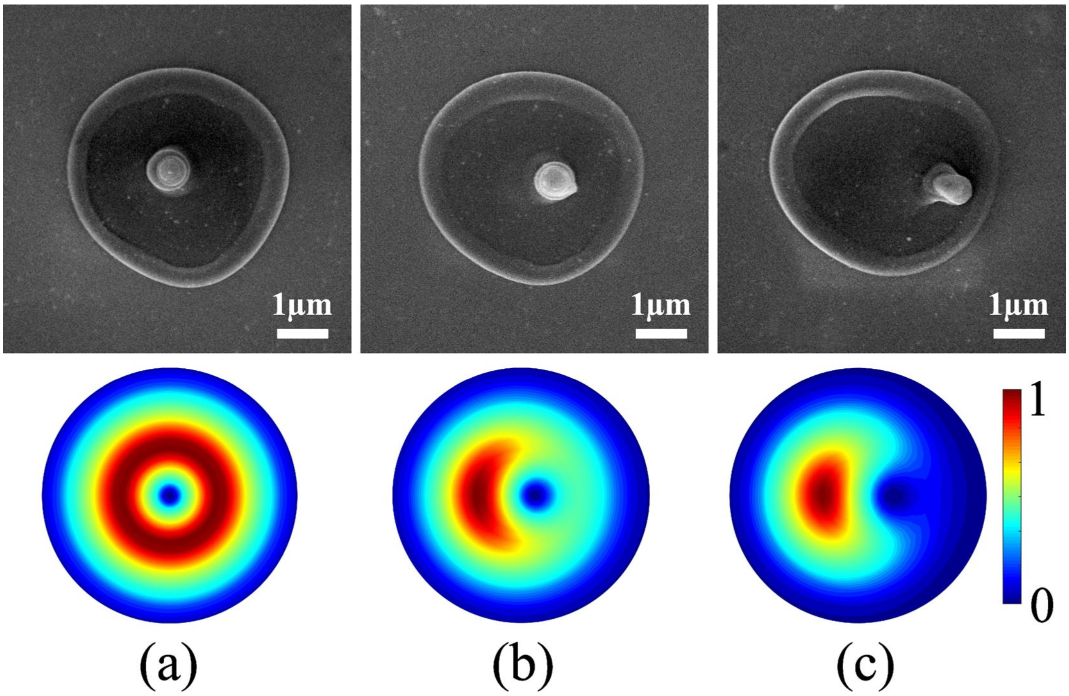

Figure 1. Displacement of the nanocone and phase singularity with retardation. Superposition of linearly polarized Gaussian beam with VV beam produced by a q-plate with topological charge of $q = +1/2$, having different weights (**a**) 0:100 (pure VV beam), (**b**) 10:90, and (**c**) 15:85. The top row shows SEM images of the nanocone position and the bottom row shows the corresponding intensity profile of the superposition beams. A single laser pulse with an energy of 280 nJ created the nanocone. The corresponding peak fluence is 2.3 ± 0.3 J/cm^2.

increases with the amount of Gaussian contribution. This results in the formation of two nanocones whose separation and relative orientation can be precisely controlled by detuning the q-plate and adding an extra phase to the superimposed beams (as in Fig. 2), respectively (see Supplementary Fig. S4).

Figure 4 shows how complex intensity patterns can be generated by superimposing different VVBs produced by a combination of two q-plates with topological charges of $q = -1$ and $q = 1/2$. A HWP between the $q = -1$ and a detuned $q = 1/2$ plates produces a superposition state $\alpha(e^{i2\phi}\,\mathbf{e}_R + e^{-i2\phi}\,\mathbf{e}_L) + \beta(e^{i\phi}\,\mathbf{e}_L + e^{-i\phi}\,\mathbf{e}_R)$, where α and β are given by the detuning parameter. The resultant intensity distribution displays three singularities around the central region where the intensity is also minimum (Fig. 4c). As a result 4 nanocones are formed (Fig. 4a). In the absence of the HWP the output corresponds to a superposition state defined by $\alpha(e^{i2\phi}\,\mathbf{e}_R + e^{-i2\phi}\,\mathbf{e}_L) + \beta(e^{i3\phi}\,\mathbf{e}_L + e^{-i3\phi}\,\mathbf{e}_R)$. The intensity pattern consists of 5 null points around the central null region (Fig. 4d). This should lead to 6 nanocones. However, any slight detuning of the $q = -1$ plate leads to splitting of the central singularity resulting in the formation of 7 nanocones (Fig. 4d) (see Supplementary Fig. S6).

Discussion

There are some similarities between our laser processing technique and stimulated emission depletion (STED) microscopy/ lithography in surpassing the diffraction barrier. Both use superpositions of Gaussian and non-Gaussian beams. In STED microscopy, a focused Gaussian beam that excites the fluorophores is superimposed with a beam having a doughnut intensity distribution that switches off the fluorophores except at its centre. In STED lithography the doughnut beam is used to inhibit photo-polymerization induced by the writing beam. However, the main drawback of STED lithography is the design and development of suitable photoresists[35]. In our method, varying the phase retardation between the VVB and Gaussian beam shifts the null intensity positions within the focal region enabling us to control the position of the nanocone.

However, the underlying physics is different between the two methods. In STED microscopy, the doughnut beam depletes the fluorescent state by stimulated emission in all molecules in the intense regions of the beam. The intensity of the doughnut beam determines (a) the probability of fluorescence switching that scales exponentially, and (b) the area to which fluorescence is confined that scales inversely thereby enhancing the spatial resolution. In our technique, VVB induces localized melting via multiphoton absorption and the subsequent fluid dynamics around the unmodified region of the material (due to null intensity region) displaces matter on nanoscale. The probability of such nonlinear interaction scales with n^{th} power of laser intensity, where n is the number of photons involved in the multiphoton process. In silicon (band gap of 1.14 eV), the interaction of 800 nm light (photon energy of 1.55 eV) is dominated by single and two photon absorption. The intensity of the VVB

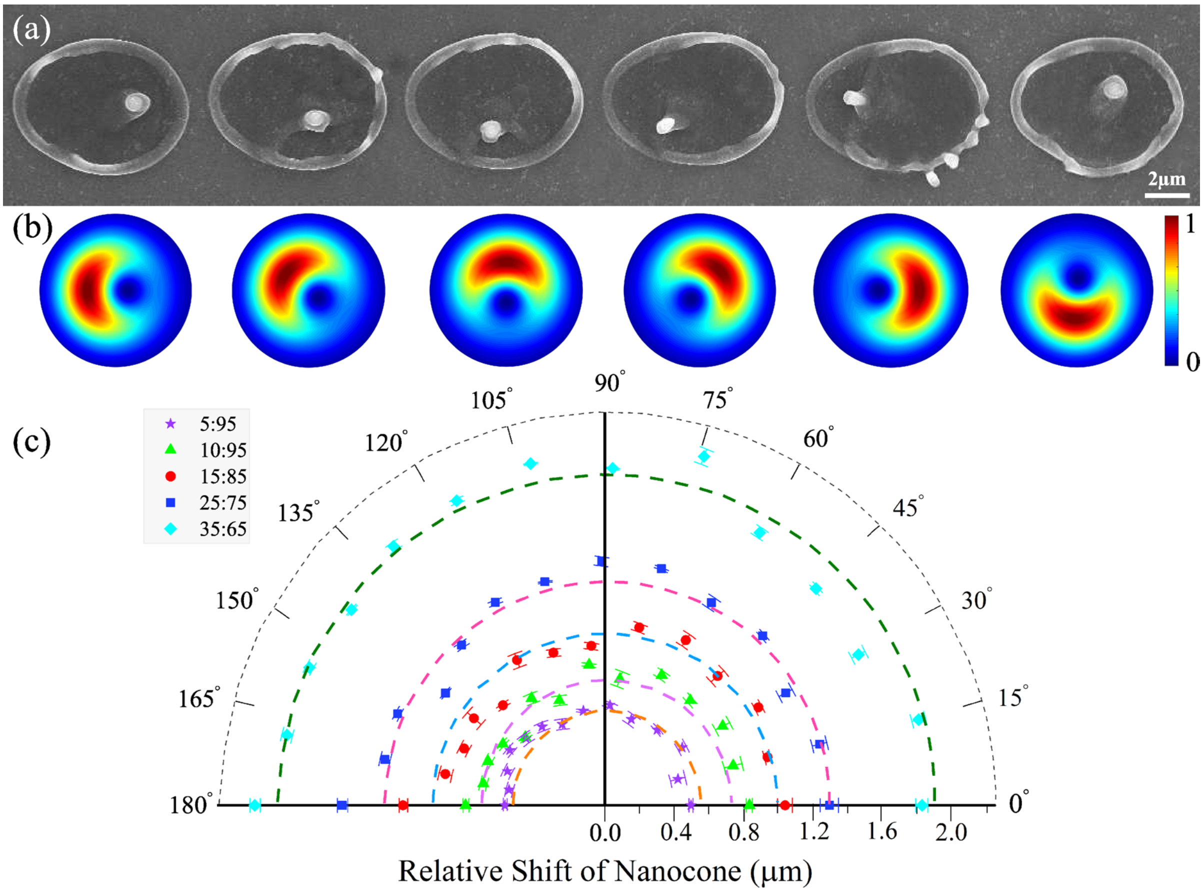

Figure 2. Controlled positioning of the nanocone in 2D space. (**a**) For a fixed relative weight (25:75) of Gaussian and VV beams produced by an electrically detuned *q*-plate with topological charge of $q=+1/2$, SEM images show the motion of the nanocone in a circular arc when an additional phase is added to the superimposed beams by rotating the polarization axis of the incident Gaussian beam with respect to the *q*-plate axis. A single laser pulse irradiated the sample with a pulse energy of 600 nJ. (**b**) The corresponding simulated intensity profiles. (**c**) Polar plot showing the measured relative shift of the nanocone with respect to its position for a pure VV beam as a function of the rotation angle of the HWP (relative phase of the linearly polarized Gaussian beam) for different optical retardations (different weights of Gaussian and VV beams). The dashed lines are the simulated nanocone position.

determines the amount of the material displaced leading to nanocone formation whose height increases but the apex angle remains the same[18]. Therefore, the spatial resolution remains the same.

In our experiments, the spatial precision of ~ 50 nm is due to loose focusing of the laser beam. The use of a high numerical aperture lens will reduce the size of the null intensity region and will lead to a smaller lateral extent and apex angle of the nanocone (see Supplementary Fig. S3). However, at very high numerical apertures the longitudinal component of the field can hinder the interference process and limit the spatial resolution. The spatial precision can be further improved to 10 nm by (a) using a highly stable power supply that can change the small voltage applied to the *q*-plate in 1 mV steps, and/or (b) changing the angle of the half-wave plate in front of the detuned *q*-plate in smaller steps of 0.1°. The laser pulse duration is not critical in our technique. In fact, longer durations were found to give rise to μm sized nano-needles likely due to larger melt volume[19].

The main limitation is that the nanocones can be efficiently created only on non-transparent materials where the melt layer is two dimensional. In transparent materials, light penetration into the medium leads to a 3D melt layer whose dynamics lead to surface swelling and ejection of the material instead of a well-defined nanocone. Also, the nanocones are always accompanied by an outer rim whose relative height can be minimized by laser parameters albeit with concomitant reduction in nanocone height[18]. Controlled fabrication of nanocones in semiconductors and metals can be used as field emission tips[36,37], scanning probes, whispering gallery optical resonator[38], and for enhanced solar absorption in photovoltaics[39]. When implemented with LIFT, our technique provides the ability to control the deposited material with sub-wavelength precision in nano-printing of complex materials with applications ranging from microelectronics to bio-photonics.

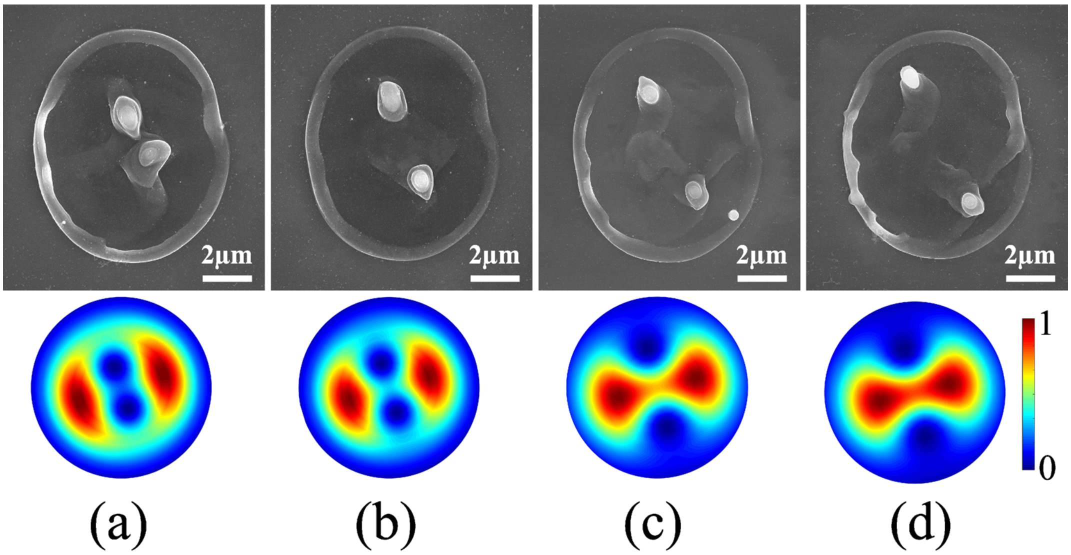

Figure 3. Separation of nanocones with unfolding singularity. Superposition of linearly polarized Gaussian and VV beams produced by a detuned q-plate, topological charge of $q = -1$, with different relative weights of (**a**) 10:90, (**b**) 15:85, (**c**) 20:80 (**d**) 25:75. Top panels shows the SEM images of two nano-cones generated by a single laser pulse with an energy of 310 nJ. The bottom panels show the corresponding intensity profiles. Separation between the singularities increases with increase in the Gaussian component.

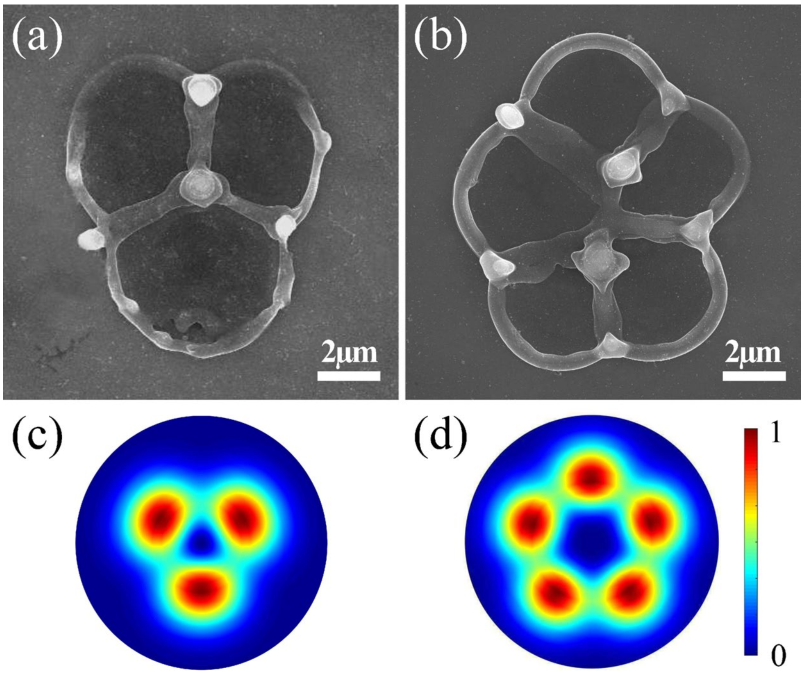

Figure 4. Fabrication of complex nanostructures. Mapping of complex intensity profiles generated by VVB produced by two q-plates with topological charge of $q = -1$, and $q = 1/2$. (**a**) A HWP between the $q = -1$ ($\ell = \pm 2$) plate and a detuned $q = 1/2$ ($\ell = \pm 1$) plate, and (**b**) without the HWP between the two q-plates. The corresponding calculated intensity profiles are shown in (**c**, **d**). Experimental patterns were produced by a single pulse with an energy of 700 nJ.

Methods

Experiment. Femtosecond light pulses from a Ti:sapphire laser system (800 nm, 1 kHz, 45 fs, 2.5 mJ/pulse) were focused on a silicon surface with a 0.25 NA (16X) aspheric lens. The sample was mounted on three-axis translation stages with a resolution of 100 nm. The sample was irradiated with a single pulse selected by operating the laser in an external trigger mode. The incident pulse energies, varied using a half-wave plate (HWP) and a polarizer, were measured after the microscope objective taking into account the transmission and reflection losses of all the optics. The pulse duration before the microscope objective was 70 fs. The laser-ablated regions were characterized by a scanning electron microscope (SEM), with the electron beam incident normal to the sample surface and atomic force microscopy (AFM) in non-contact mode.

In our experiment, complex intensity profiles were generated using birefringent-based liquid crystal beam converters, called q-plates[40,41], with topological charges of $q = +1/2$ and -1. The optical retardation of the q-plates was changed by varying the voltage applied to them. At the optimal voltage, the q-plates converted linearly polarized Gaussian beams to optical VVBs composed of OAM states with $\ell = \pm 1$ and $\ell = \pm 2$, respectively[42]. Complex spatial intensity profiles were produced by varying the voltage applied on the q-plate. This process called voltage tuning of the q-plate results in varying the extent of coherent superposition of laser beam components. In other words, detuning the individual q-plate produced a superposition of partially converted VVBs with the incident Gaussian beam. A combination of different q-plates resulted in complex intensity profiles due to the superposition of VVBs. See Supplementary Fig. S1 for additional details.

Numerical. Intensity profiles of different order VVBs and their superposition states were simulated using the Laguerre Gaussian beam

$$U(r,\phi,z) = \frac{C_{\ell p}^{LG}}{w(z)}\left(\frac{r\sqrt{2}}{w(z)}\right)^{|\ell|} exp\left(\frac{-r^2}{w^2(z)}\right) L_p^{|\ell|}\left(\frac{2r^2}{w^2(z)}\right) exp\left(\frac{-ikr^2}{2R(z)} - i\ell\phi - ikz + i\Psi(z)\right), \quad (1)$$

where $p \geq 0$ is the radial index and ℓ is the azimuthal index. L_p^{ℓ} are the generalized Laguerre polynomials and $C_{\ell p}^{LG}$ is a normalization constant. $R(z)$ is the radius of curvature of the wavefront, $w(z)$ is the beam width and $\Psi(z)$ is the Gouy phase. r and z are the radial and axial distances. k is the wave number and $e^{i\ell\phi}$ is the phase factor containing the ℓ term.

Received: 17 December 2019; Accepted: 8 July 2020

References

1. Abbe, E. A contribution to the theory of the microscope and the nature of microscopic vision. *Proc. Bristol Nat. Soc.* **1**, 20017261 (1874).
2. Lin, B.-J. Immersion lithography and its impact on semiconductor manufacturing. *J. Micro/Nanolithogr. MEMS MOEMS* **3**, 377–395 (2004).
3. Wagner, C. & Harned, N. Lithography gets extreme. *Nat. Photonics* **4**, 24 (2010).
4. Bakhsi, V. *EUV Lithography* 2nd edn. (SPIE Press, Bellingham, 2009).
5. Pereira, A. *et al.* Laser fabricated porous alumina membranes for the preparation of metal nanodot arrays. *Small* **4**, 572 (2008).
6. Ito, T. & Okazaki, S. Pushing the limits of lithography. *Nature* **406**, 1027 (2000).
7. Xie, X. N., Chung, H. J., Sow, C. H. & Wee, A. T. S. Nanoscale materials patterning and engineering by atomic force microscopy nanolithography. *Mater. Sci. Eng. R Rep.* **54**, 1–48 (2006).
8. Jersch, J. & Dickmann, K. Nanostructure fabrication using laser field enhancement in the near field of a scanning tunneling microscope tip. *Appl. Phys. Lett.* **68**, 868 (1996).
9. Kawata, S., Sun, H.-B., Tanaka, T. & Takada, K. Finer features for functional microdevices. *Nature* **412**, 697 (2001).
10. Yanik, M. F. *et al.* Functional regeneration after laser axotomy. *Nature* **432**, 822 (2004).
11. Joglekar, A. P., Liu, H.-H., Meyhöfer, E., Mourou, G. & Hunt, A. J. Optics at critical intensity: applications to nanomorphing. *Proc. Natl. Acad. Sci.* **101**, 5856 (2004).
12. Juodkazis, S., Mizeikis, V., Seet, K. K., Miwa, M. & Misawa, H. Two-photon lithography of nanorods in SU-8 photoresist. *Nanotechnology* **16**, 846 (2005).
13. Garcia-Lechuga, M., Utéza, O., Sanner, N. & Grojo, D. Evidencing the nonlinearity independence of resolution in femtosecond laser ablation. *Opt. Lett.* **45**, 952 (2020).
14. Taylor, R. S. *et al.* Femtosecond laser fabrication of nanostructures in silica glass. *Opt. Lett.* **28**, 1043–1045 (2003).
15. Zhang, Q., Lin, H., Jia, B., Xu, L. & Gu, M. Nanogratings and nanoholes fabricated by direct femtosecond laser writing in chalcogenide glasses. *Opt. Express* **18**, 6885–6890 (2010).
16. Her, T.-H., Finlay, R. J. , Wu, C., Deliwala, S. & Mazur, E. Microstructuring of silicon with femtosecond laser pulses. *Appl. Phys. Lett.* **73**, 1673 (1998).
17. Nayak, B. K., Gupta, M. C. & Kolasinski, K. W. Formation of nano-textured conical microstructures in titanium metal surface by femtosecond laser irradiation. *Appl. Phys. A* **90**, 39917402 (2008).
18. Rahimian, M. G. *et al.* Polarization dependent nanostructuring of silicon with femtosecond vortex pulse. *App. Phys. Lett. Photonics* **2**, 086104 (2017).
19. Toyoda, T., Miyamoto, K., Aoki, N., Morita, R. & Omatsu, T. Using optical vortex to control the chirality of twisted metal nanostructures. *Nano Lett.* **12**, 3645 (2012).
20. Nivas, J. J. J. *et al.* Direct femtosecond laser surface structuring with optical vortex beams generated by a q-plate. *Sci. Rep.* **5**, 17929 (2015).
21. Bhardwaj, V. R. *et al.* Optically produced arrays of planar nanostructures inside fused silica. *Phys. Rev. Lett.* **96**, 057404 (2006).
22. Alameer, M. *et al.* Mapping complex polarization states of light on a solid. *Opt. Lett.* **43**, 5757 (2018).
23. Serra, P. & Pique, A. Laser-induced forward transfer: fundamentals and applications. *Adv. Mater. Technol.* **4**, 1800099 (2019).
24. Morales, M., Munoz-Martin, D., Marquez, A., Lauzurica, S. & Molpeceres, C. *Laser-Induced Forward Transfer Techniques and Applications, Advances in Laser Material Processing* 2nd edn, 339–379 (Woodhead publishing, Sawston, 2018).
25. Makarov, S. V. *et al.* Light-induced tuning and reconfiguration of nanophotonic structures. *Laser Photonics Rev.* **11**, 1700108 (2017).
26. Betzig, E., Trautman, J. K., Harris, T. D., Weiner, J. S. & Kostelak, R. L. Breaking the diffraction barrier: optical microscopy on a nanometric scale. *Science* **251**, 1468–1470 (1991).
27. Betzig, E. & Trautman, J. K. Near-field optics: microscopy, spectroscopy, and surface modification beyond the diffraction limit. *Science* **257**, 189–195 (1992).
28. Gramotnev, D. K. & Bozhevolnyi, S. I. Plasmonics beyond the diffraction limit. *Nat. Photonics* **4**, 831791 (2010).
29. Schuller, J. A. *et al.* Plasmonics for extreme light concentration and manipulation. *Nat. Mater.* **9**, 19317204 (2010).

30. Hell, S. W. & Wichmann, J. Breaking the diffraction resolution limit by stimulated emission: stimulated emission depletion microscopy. *Opt. Lett.* **19**, 78017782 (1994).
31. DErrico, A. *et al.* Topological features of vector vortex beams perturbed with uniformly polarized light. *Sci. Rep.* **7**, 40195 (2017).
32. Takahashi, F. *et al.* Picosecond optical vortex pulse illumination forms a monocrystalline silicon needle. *Sci. Rep.* **6**, 21738 (2016).
33. Toyoda, K., Miyamoto, K., Aoki, N., Morita, R. & Omatsu, T. Using optical vortex to control the chirality of twisted metal nanostructures. *Nano Lett.* **12**, 3645 (2012).
34. Syubaeva, S. *et al.* Chirality of laser-printed plasmonic nanoneedles tunable by tailoring spiral-shape pulses. *Appl. Surf. Sci.* **470**, 526 (2019).
35. Gan, Z., Cao, Y., Evans, R. A. & Gu, M. Three-dimensional deep sub-diffraction optical beam lithography with 9 nm feature size. *Nat. Commun.* **4**, 2061 (2013).
36. Kim, T., Kim, J.-H., Son, S. J. & Seo, S.-M. Gold nanocones fabricated by nanotransfer printing and their application for field emission. *Nanotechnology* **19**, 295302 (2008).
37. Li, W. *et al.* Field emission from a periodic amorphous silicon pillar array fabricated by modified nanosphere lithography. *Nanotechnology* **19**, 1355308 (2008).
38. Yang, Y. H. *et al.* ZnO nanocone: application in fabrication of the smallest whispering gallery optical resonator. *Nanoscale* **3**, 59217597 (2011).
39. Wang, B. & Leu, P. W. Enhanced absorption in silicon nanocone arrays for photovoltaics. *Nanotechnology* **23**, 194003 (2012).
40. Marrucci, L., Manzo, C. & Paparo, D. Optical spin-to-orbital angular momentum conversion in inhomogeneous anisotropic media. *Phys. Rev. Lett.* **96**, 163905 (2006).
41. Larocque, H. *et al.* Arbitrary optical wavefront shaping via spin-to-orbit coupling. *J. Opt.* **18**, 124002 (2016).
42. Marrucci, L. *et al.* Spin-to-orbital conversion of the angular momentum of light and its classical and quantum applications. *J. Opt.* **13**, 064001 (2011).

Acknowledgements

A.J. thanks Sastri Indo-Canada foundation for fellowship. We acknowledge financial support from Natural Science and Engineering Research Council of Canada, Canadian Foundation for Innovation and Canada Research Chairs.

Author contributions

M.G.R. and A.J. contributed equally to the experimental work. M.G.R. analysed the data and prepared figures and graphs. A.J. performed the calculations. H. L. built the q-plate and assisted in producing vortex beams. P.B.C., E.K., and V.R.B. designed the experiment and analysed the data. All authors contributed to writing the manuscript.

Competing interest

The authors declare no competing interests.

Additional information

Supplementary information is available for this paper at https://doi.org/10.1038/s41598-020-69390-4.

Correspondence and requests for materials should be addressed to V.R.B.

Reprints and permissions information is available at www.nature.com/reprints.

Spatially controlled nano-structuring of silicon with femtosecond vortex pulses

M. G. Rahimian, A. Jain, H. Larocque, P. B. Corkum, E. Karimi, V. R. Bhardwaj
Department of Physics, University of Ottawa, 25 Templeton Street, Ottawa, K1N 6N5, Canada

I. EXPERIMENTAL SETUP

A schematic of the experimental setup used to demonstrate spatially controlled formation of nanocones on silicon with femtosecond vortex pulses is shown in Fig. S1. Linearly polarized input pulses with a Gaussian spatial profile were converted to optical vortex pulses by employing *q*-plates with topological charges of $q = +½$ and -1. The resultant radial profile of the vector vortex (VV) pulse is similar to that of Hyper-Geometric Gaussian modes [1].

The *q*-plate is a slab of a birefringent material based on liquid crystal technology with uniform birefringent phase retardation (δ) and a transverse optical axis pattern with a topological charge of *q* [2]. The optical phase of the generated modes varies by $2\pi q$ when circling once the beam axis. The topological charge *q* is an integer or semi-integer, positive or negative value. A circular aperture after the *q*-plate filtered the central part of the beam resulting in a vortex beam with an annular spatial profile similar to that of Laguerre-Gauss modes.

Different polarization states with a variety of spatial intensity distributions were produced by (i) using a combination of different *q*-plates and wave plates, and (ii) varying the optical retardation of the *q*-plate, resulting in the superposition of pure vortex and Gaussian beams. The pulse energies of the emerging vortex beam with complex polarization and spatial structure were controlled by a combination of half wave plate (HWP) and polarizer. A glass plate (G) reflected a portion of the incident pulse on to a fast photodiode (PD) that was used for power calibration by operating it in the linear regime with the help of neutral density filters (ND).

An aspheric lens (16x with 0.25 NA, f = 11mm, Newport) focused the vortex pulses on to a crystalline (100) p-type silicon mounted on a precision 3-axis (x, y, z) motion control system. The position of the laser focus relative to the sample's surface was determined accurately (±5 μm) by imaging the back-reflected light from the silicon surface. Glass plate directed the back-reflected light towards a charge-coupled-device (CCD) camera (MCE-B013-US, Mightex) after propagating through a focusing lens (Thorlabs, f = 100 mm, plano-convex lens). The Si surface morphology was analyzed using a field emission scanning electron microscope (Zeiss Gemini SEM 500) with both In-Lens detection mode (top-view images) and secondary electrons detection mode (side–view images) and a Park NX10 atomic force microscope in a non-contact mode.

The setup shown in Fig. S1(a) produces a nanocone whose position can be shifted by changing the voltage applied on the *q*-plate with a topological charge of ½ (QP1). This corresponds to Fig. 1 in the main text. A half-wave plate in front of the QP1, as shown in Fig. S1(b), enables to change the angular position of the nanocone. This corresponds to Fig. 2 in the main text. A *q*-plate with topological charge of -1, QP2, as shown in Fig. S1(c) is used to produce two nanocones whose separation can be varied by changing the voltage applied on the

QP2. This corresponds to Fig. 3 in the main text. The setup shown in Fig. S1(d) produces three-petal shaped flower like structure with four nanocones, corresponding to Fig. 4a in the main text. Removing the half-waveplate between QP2 and QP1, as shown in Fig. S1 (e), produces five-petal shaped flower like structure with 6 nanocones. This can be increased to 7 nanocones by detuning QP2, corresponding to Fig. 4b in the main text.

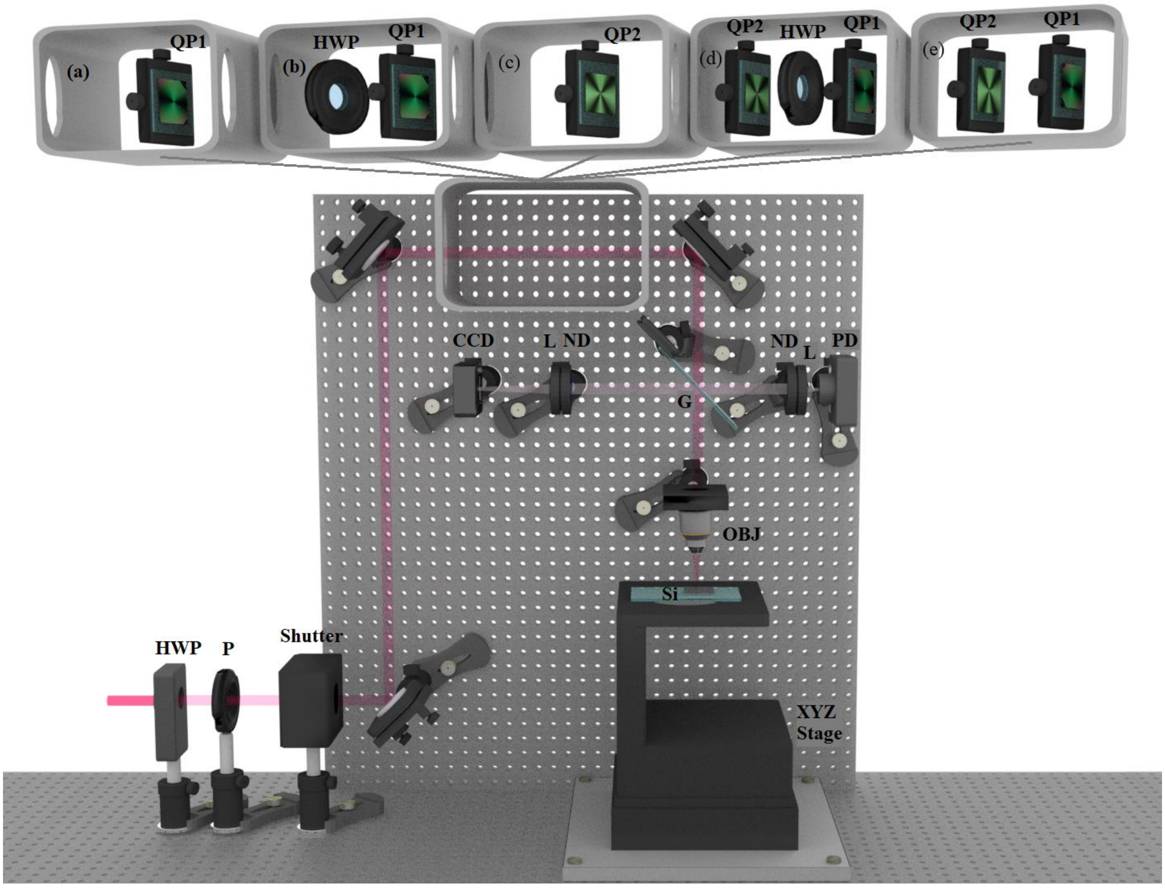

Figure S1. The schematic shows the experimental setup. ND: neutral density filter, CCD: charge-coupled-device camera, G: glass plate, PD: photodiode, P: polarizer, L: Lens, OBJ: objective, QP1: *q*-plate with topological charge of ½, QP2: *q*-plate with topological charge of -1, HWP: Half-wave plate.

II. OPTICAL RETARDATION CALIBRATION WITH THE APPLIED VOLTAGE

A square-wave signal generator operating at 7 KHz and 4 KHz was used to adjust the driving voltages to the $q = +½$ and $q = -1$ plates, respectively. At optimal voltage of 2.97V, both *q*-plates produced pure VV beams. Varying the voltage on the *q*-plates causes a change in the optical retardations (δ) enabling the tuning of the *q*-plates. When the *q*-plate is detuned, if the input Gaussain beam is circularly polarized, the resultant output beam will be a coherent superposition of two fundamental optical states; (i) the unconverted part of the input Gaussian beam with the same polarization as the input and (ii) the converted annular VV beam with opposite handedness to the input polarization with $\ell = \pm 1$(or ± 2). Invoking different input polarization states, optical retardation values, and/or different location of polarization optics within the setup produced a combination of converted and unconverted parts of the beam.

In a simple configuration, with only q = ½ plate in the setup we were able to control the relative position of the nanocone with respect to its original location (produced by a pure vortex beam with $\ell = \pm 1$). For a fixed relative phase between the LG beam components, varying the optical retardation shifted the nanocone as shown in Fig. S2. This was achieved by detuning the voltage on the q-plate. As the relative weight of the Gaussian beam increased with respect to a pure VV beam (voltage decreased) the vortex and hence the nanocone position shifted linearly away from the center of the ablated region and moved towards the boundary (rim). The first data point corresponds to the nanocone's position when the composite beam is dominated by the Gaussian component while the last data point corresponds to a pure VV beam.

The following procedure illustrates how the optical retardation was calibrated with the voltage applied on the q-plate. Left-circular (L) polarized light was passed through the q = ½ plate to achieve spin to orbital angular momentum conversion. After the q-plate, a quarter wave plate (QWP) whose optics axis is at 45° with respect to the q-plate and a polarizing beam-splitter (PBS) produced two output beams; a pure converted beam with a doughnut-shaped profile as a transmitted component, and an unconverted beam with a Gaussian profile as a reflected component. The transmitted component corresponds to the pure VV beam with right circular polarization (R, ℓ=1) while the reflected component corresponds to pure Gaussian beam with left circular polarization (L, ℓ=0).

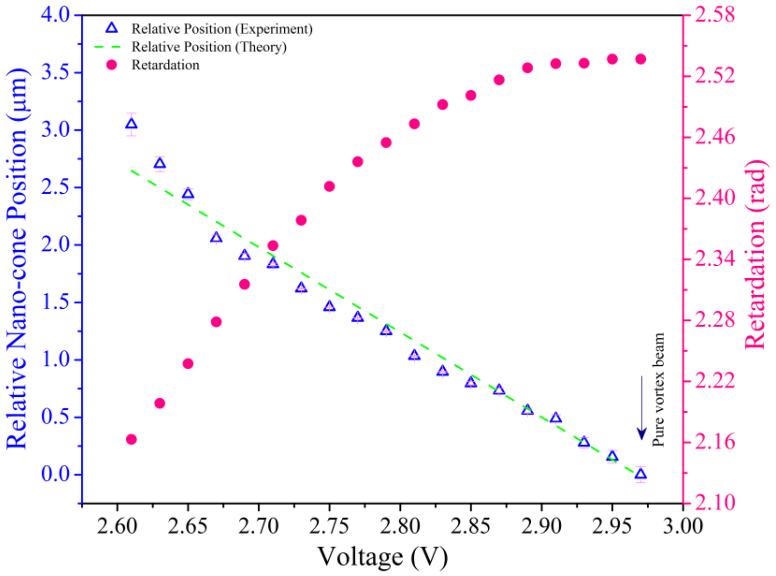

Figure S2. The left ordinate in blue shows relative position of the nanocone as a function of voltage on the q-plate, measured with respect to its original location when a pure OAM beam irradiated the silicon surface. The green dashed line corresponds to the theoretical value demonstrating linear dependence. Right ordinate in pink demonstrates variation of optical retardation with applied voltage.

For a total power of P_0, the powers of the coherently converted ($P_{R,1}$) and unconverted ($P_{L,0}$) components depend on the optical retardation as,

$$\begin{aligned} P_{R,1} &= P_0 \sin^2\left(\frac{\delta}{2}\right) \\ P_{\mathrm{L},0} &= P_0 \cos^2\left(\frac{\delta}{2}\right) \end{aligned} \tag{S1}$$

Varying the applied voltage to the *q*-plate and measuring the power of the two output beams of the PBS determined the optical retardation. The torque exerted on the liquid crystal molecules by the applied electric field is responsible for such dependency [3].

III. NA=0.25 VERSUS NA=0.55

Spatial precision of ~ 50nm was achieved in placing the nanocone within the ablated region by focusing vortex pulses with a numerical aperture (NA) of 0.25, determined primarily by the dimensions of the nanocone tip. The spatial precision can be improved further by tighter focusing with a high NA lens. This creates a smaller null intensity region leading to a smaller/sharper nanocone as shown in Fig. S3. The graph shows two nanocones with radii of curvature of 30 nm and 80 nm produced by aspheric lenses with NA=0.25 and NA=0.55, respectively. The results confirm that the radius of curvature of the nanocone tip decreases as the numerical aperture of the objective increases. Figure S3(b) presents a side-view SEM image of a nanocone produced by a single vortex pulse with an energy of 400 nJ.

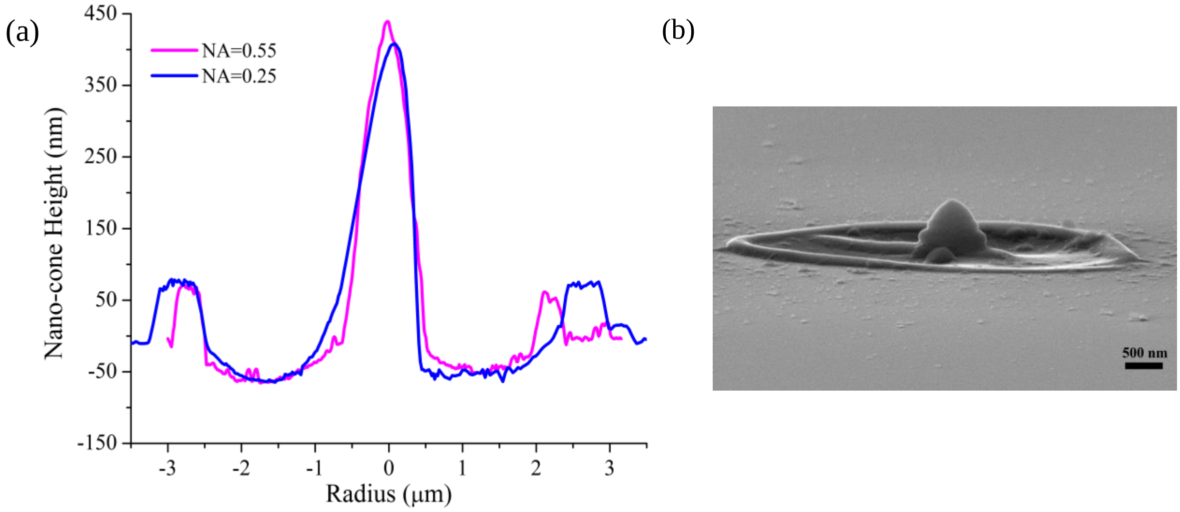

Figure S3. (a) The AFM measurements for two nanocones produced by aspheric lenses with NA=0.25 and NA=0.55. The radii of curvature of 30 nm and 80 nm were achieved, respectively. (b) A side-view SEM image of a nanocone created by a 400 nJ vortex pulse.

IV. NANOCONES SEPARATION VS OPTICAL RETARDATION

When a pure VV beam of ℓ=2 is perturbed, two nanocones are formed within the ablated region. Their separation can be precisely controlled by detuning the *q*-plate as shown in Fig. S4. In a detuned *q*-plate, Gaussian beam is superimposed on the VV beam. Such superposition results in decomposition of the vortex into two single-charged vortices (each dark spot with charge of ℓ=1). Varying the voltage on the *q*-plate changes the relative weights of the Gaussian and vortex components. In other words, the optical retardation hence the separation between the nanocones changes.

Figure S4 shows the nanocones separation decreases as the portion of the Gaussian beam decreases or the optical retardation increases. The orientation of the two nanocones can also be precisely controlled by varying the relative phase between the two components of the superimposed beams, as shown in Fig.2 of the main text. This can be achieved by rotating a HWP introduced before the *q*-plate.

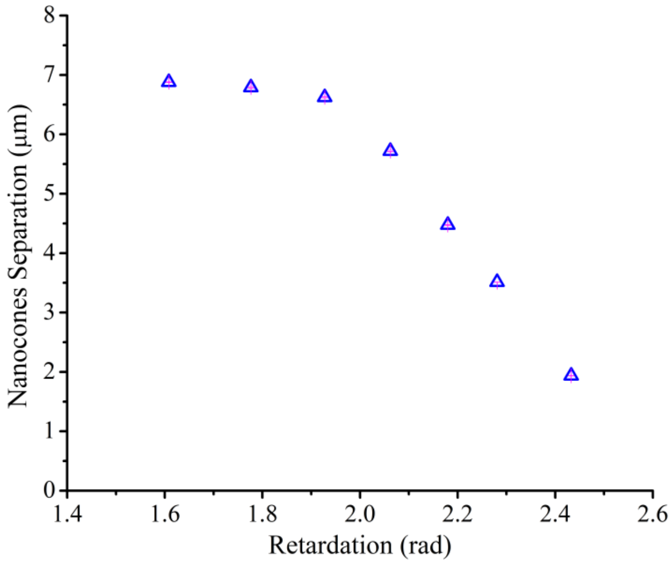

Figure S4. Decrease in nanocones separation as the optical retardation of *q* = -1 plate is increased. For a tuned *q*-plate, only one nanocone exists at the center of the ablated region. When *q*-plate is detuned, optical retardation decreases leading to an increase in the weight of the Gaussian beam and the nanocones separation.

V. MANIPULATING THE NUMBER AND POSITION OF THE NANOCONES

Optical retardation and topological charge of the *q*-plate play a crucial role in determining the number and the location of the nanocones. For a fixed topological charge, changing the optical retardation changes the relative weight of the optical states present in the coherent superposition leading to different asymmetric intensity distributions. For instance, a three-petal flower intensity profile was produced by an experimental configuration consisting of a *q*-plate with topological charge of $q = -1$ followed by a HWP and a q-plate with topological charge of $q = ½$. Varying the voltage applied on the second $q = ½$ plate while the applied voltage on the first $q = -1$ plate was fixed for a maximum conversion ($\delta = \pi$), allowed us to set the intensity ratio and achieve several position-controlled nanocones. In this case, a superposition of two beams with $\ell = +1$ and $\ell=-2$ was generated which allowed to have an optical vortex of charge $\ell= +1$ at the centre surrounded by three vortices of charge -1 arranged symmetrically and located at the same radial distance from the centre at the angles of $\pi/3$, π, and $5\pi/3$ [4]. As the relative amplitude of the $\ell=-2$ component in the superimposed beam was decreased (increased), the peripheral vortices and hence the nanocones positions moved radially in (out), as shown in Fig. S5.

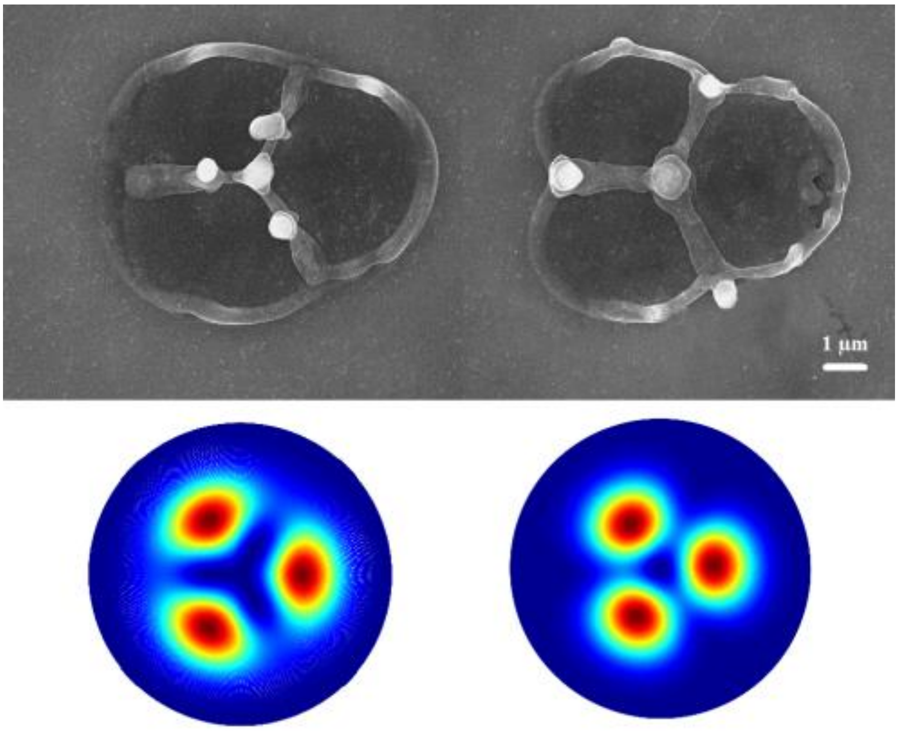

Figure S5. (Top panel) the SEM images show the peripheral nanocones moving radially outward as the relative amplitude of the $\ell=-2$ component in the superimposed beam increased. Three nanocones are located at the same radial distance from the centre at the angles of $\pi/3$, π, and $5\pi/3$. (Bottom panel) Simulation of intensity profiles corresponding to the SEM images.

We were also able to generate a five-petal flower intensity distribution by using a sequence of a HWP, a tuned q-plate with topological charge of $q = -1$, and a $q = ½$ plate with an adjustable voltage. When the alignment is accurate, the vortex laser beam regenerated in this configuration produced a structure consisting of a single nanocone at the centre and five peripheral nanocones located at the same radial distance from the central cone, as shown in Fig. S6(a). A small detuning of the first q-plate with topological charge of $q = -1$ resulted in the central nanocone to split into two, as shown in Fig. 4b of the main text. The corresponding AFM image is shown in Fig. S6(b). The nanocones height varies between 400 nm and 670 nm.

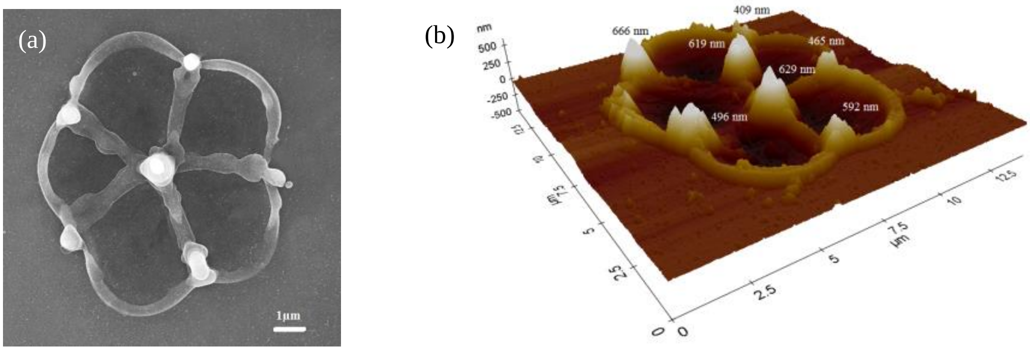

Figure S6. (a) The SEM image shows a 5-petal flower-shaped structure produced by a tuned *q* = -1 and detuned *q* = ½ plates. The structure consists of a single nanocone at the centre of the ablated region surrounded by 5 nanocones located at the same radial distance from the centre. (b) The AFM image of the 5-petal flower-shaped structure, shown in the Fig. 4b of the main text, with the central cone splitting into two due to detuning of the *q* = -1 plate. The heights of the nanocones vary from 400 nm to 670 nm.

References

[1] E. Karimi, B. Piccirillo, L. Marrucci, and E. Santamato, "Hypergeometric-Gaussian modes", Opt. Lett. 34, 1225 (2009).

[2] L.Marrucci, E. Karimi, S. Slussarenko, B. Piccirillo, E. Santamato, E. Nagali, and F. Sciarrino, "Spin-to-orbital conversion of the angular momentum of light and itsclassical and quantum applications", J. Opt. 13, 064001(2011).

[3] B. Piccirillo, V. D'Ambrosio, S. Slussarenko, L. Marrucci, and E. Santamato , "Photon spin-to-orbital angular momentum conversion via an electrically tunable *q*-plate", APPLIED PHYSICS LETTERS 97, 241104 (2010).

[4] S. Baumann, D. Kalb, L. MacMillan, E. Galvez, "Propagation dynamics of optical vortices due to Gouy phase" Opt. Express, 17, 9818–9827 (2009).

References

[1] A. P. Joglekar, H-H. Liu, E. Meyhfer, G. Mourou, and A. J. Hunt. Optics at critical intensity: Applications to nanomorphing. *Proceedings of the National Academy of Sciences*, 101:5856, 2004.

[2] S. Juodkazis, V. Mizeikis, K. K. Seet, M. Miwa, and H. Misawa. Two-photon lithography of nanorods in su-8 photoresist. *Nanotechnology*, 16:846, 2005.

[3] R. S. Taylor, C. Hnatovsky, E. Simova, D. M. Rayner, V. R. Bhardwaj, and P. B. Corkum. Femtosecond laser fabrication of nanostructures in silica glass. *Optics Letters*, 28:1043–1045, 2003.

[4] Q. Zhang, H. Lin, B. Jia, L. Xu, and M. Gu. Nanogratings and nanoholes fabricated by direct femtosecond laser writing in chalcogenide glasses. *Optics Express*, 18:6885–6890, 2010.

[5] A. Pereira, D. Grojo, M. Chaker, P. Delaporte, D. Guay, and M. Sentis. Laser fabricated porous alumina membranes for the preparation of metal nanodot arrays. *Small*, 4:572, 2008.

[6] V. R. Bhardwaj, E. Simova, P. P. Rajeev, C. Hnatovsky, R. S. Taylor, D. M. Rayner, and P. B. Corkum. Optically produced arrays of planar nanostructures inside fused silica. *Physical Review Letters*, 96:057404, 2006.

[7] J. J. J. Nivas, S. He, A. Rubano, A. Vecchione, D. Paparo, L. Marrucci, R. Bruzzese, and S. Amoruso. Direct femtosecond laser surface structuring with optical vortex beams generated by a q-plate. *Scientific Reports*, 5:17929, 2015.

[8] P. Serra and A. Pique. Laser-induced forward transfer: Fundamentals and applications. *Advanced Materials Technologies*, 4:1800099, 2019.

[9] M. Morales, D. Munoz-Martin, A. Marquez, S. Lauzurica, and C. Molpeceres. *Laser-Induced Forward Transfer Techniques and Applications*, pages 339–379. Woodhead Publishing, 2018.

[10] F. Takahashi, S. Takizawa, H. Hidai, K. Miyamoto, R. Morita, and T. Omatsu. Title of the article. *Physica Status Solidi A*, 213:1063, 2016.

[11] M.G. Rahimian, F. Bouchard, H. Al-Khazraji, E. Karimi, P.B. Corkum, and V.R. Bhardwaj. Polarization dependent nanostructuring of silicon with femtosecond vortex pulse. *APL Photonics*, 2:086104, 2017.

[12] T. Toyoda, K. Miyamoto, N. Aoki, R. Morita, and T. Omatsu. Using optical vortex to control the chirality of twisted metal nanostructures. *Nano Letters*, 12:3645, 2012.

[13] T. Kim, J-H. Kim, S. J. Son, and S-M. Seo. Gold nanocones fabricated by nanotransfer printing and their application for field emission. *Nanotechnology*, 19, 2008.

[14] W. Li, J. Zhou, X-G. Zhang, J. Xu, L. Xu, W. Zhao, P. Sun, F. Song, J. Wan, and K. Chen. Field emission from a periodic amorphous silicon pillar array fabricated by modified nanosphere lithography. *Nanotechnology*, 19:1355308, 2008.

[15] S. K. Sundaram and E. Mazur. Inducing and probing non-thermal transitions in semiconductors using femtosecond laser pulses. *Nature Materials*, 1:217–224, 2002.

[16] X. Liu, D. Du, and G. Mourou. Laser ablation and micromachining with ultrashort laser pulses. *IEEE Journal of Quantum Electronics*, 33(10), 1997.

[17] K. C. Phillips, H. H. Gandhi, E. Mazur, and S. K. Sundaram. Ultrafast laser processing of materials: a review. *Advances in Optics and Photonics*, 2015.

Chapter 8

Conclusion

The research work presented in this dissertation establishes a novel helical phase-based spectroscopy technique. This technique probes the helical phase-dependent linear and nonlinear absorption of helical light beams across different material phases. In contrast to conventional methods that rely on polarization as a primary optical probe, this technique utilizes the helical phase carried by orbital angular momentum (OAM) beams, offering a new way to investigate light-material interactions.

Controlled phase-dependent light absorption across various material phases is demonstrated. At the core of this technique is the introduction of asymmetry in the phase and intensity profile of the helical light beams. This additional degree of control enabled us to observe the phase-based dichroism effect in amorphous solids, achiral metasurfaces, and achiral molecules. This intrinsic phase-based dichroism effect can be qualitatively understood in terms of parity violation in helical light-matter interactions caused by the added asymmetry in the beam. In solids, these findings will aid in understanding the mysterious nature of amorphous materials and serve as an indirect method to calculate the upper limit of their short- and medium-range order. The bandgap dependence of the phase-based dichroism is a potential tool for material profiling, a unique fingerprint of solid-state materials. In plasmonic achiral nano- and micro-structures, the controlled absorption of helical light could potentially enhance the efficiency of existing plasmonic-based optical sensors. Additionally, the phase-based preferential response observed in achiral molecules would expand the scope of absorption-based spectroscopic techniques in investigating isotropic materials.

A *new phase-based chiroptical detection* method is also proposed, which can be used to study chiral liquids, solutions, solids, and engineered nanostructures. In the case of enantiopure liquids and enantiomeric solutions, the chiral signal strength of our non-resonant, nonlinear chiroptical technique is an order of magnitude higher than the conventional industry-standard electronic circular dichroism (CD) and on the same order as the other standard nonlinear techniques such as two-photon CD and PECD. In the linear interaction regime, enhanced chiroptical detection was observed with plasmonic metasurfaces. Additionally, the scaling of the dichroism signal by changing the OAM value, along with controlled tuning of its strength by varying the polarization and singularity displacement, sets our technique apart from other conventional chiroptical techniques. Moreover, the ability to differentiate enantiomeric bio-relevant molecules positions this technique as a strong candidate for industrial applications, especially in the pharmaceutical industry.

This dissertation also explores the application of asymmetric helical light beams in laser ablation. Controlled material manipulation was achieved by utilizing the superposition of different-order helical beams. The spatial resolution achieved in positioning the nanocones was approximately eight times below the diffraction limit. This work can potentially complement advanced nanofabrication techniques such as STED-based lithography and laser-induced forward transfer (LIFT).

The research presented in this dissertation was organized into three parts to effectively establish the results and outcomes discussed above. These can be summarized as follows:

- In the first part of this dissertation (Chapters 1 and 2), the theoretical basis of helical light-carrying OAM and SAM was established. Various experimental methods for generating these beams were also discussed. Later, theoretical models for studying and simulating helical light-matter interactions were derived in linear and nonlinear regimes. The effect of material symmetry in governing helical light-matter interactions was also examined. Lastly, experimental methods to observe and characterize such helical phase-based differential effects were presented.
- In part two of this dissertation (Chapters 3 to 6), published research articles establishing the presence of helical dichroism in chiral and achiral liquids, enantiomeric solutions, amorphous and crystalline solids, and plasmonic metasurfaces are presented. The key results and advances for each case were summarized to present the findings of the attached articles effectively.
- In part three of this dissertation (Chapter 7), a novel direct laser lithography technique for the fabrication of nanocones with sub-wavelength positional resolution is presented. The key advances and limitations of the proposed technique are also discussed.

In summary, a new helical phase-based spectroscopic technique is presented with a comprehensive theoretical and experimental basis. This technique demonstrates the untapped potential of helical light beams in investigating various material properties.

This concludes the research I have conducted as part of this dissertation.

Chapter 9

Future scope and potential applications

The helical phase-based spectroscopy technique was demonstrated in solids, liquids, and metasurfaces. A natural extension of this technique is to investigate the ionization of atoms and molecules in the gas phase using asymmetric helical beams. This has already been pursued by our research group, with results demonstrating preferential helical phase-based ionization. These findings highlight the universality of the technique, which exhibits controlled phase-dependent absorption across different material phases within the linear, weak-field, and strong-field interaction regimes. Another promising future extension would be to investigate the response of advanced materials like carbon nanotubes and graphene. Single-walled nanotubes and 2D graphene exhibit promising saturable absorber properties, which have been exploited for passive mode-locking in fiber lasers [1, 2, 3]. Both materials exhibit strong nonlinear response, characterized by an intensity-dependent two-photon absorption coefficient β. Utilizing the helical phase-based spectroscopy in such materials could allow controlled absorption of helical beams, leading to a variable absorption coefficient β. This additional degree of control over β, alongside intensity, could be consequential in enhancing the efficiency of such advanced material-based saturable absorbers for industrial applications.

Another significant aspect of our research is that the developed analytical and experimental methods could serve as a foundation for investigating the effects of asymmetrical phase fronts in other optical phenomena. Various properties and outcomes of the phase-based spectroscopic technique, such as controlled asymmetry in phase, superposition beams, induced dipole forces, and phase-induced coupled quadrupole moments (E1E2), could be employed as tools to explore established optical effects. For example, asymmetry-induced dipole forces can be utilized to orient anisotropic molecules. This could, in principle, impact Rayleigh-wing scattering, which originates due to fluctuations in the orientation of anisotropic molecules[4]. Differential degrees of orientation for left- and right-handed helical beams could enable control over the spectral width.

In conclusion, the research presented in this dissertation constitutes foundational research into the extensive potential of the helical phase-based spectroscopy. Alongside the above-discussed future extensions, I present some of my ideas for potential applications of my research.

9.1 Potential applications

This section presents research ideas utilizing the tools and methods developed for the phase-based spectroscopy technique. Additionally, an extension of my published research on optimizing optical data storage in common plastics is discussed. The data storage work was also conducted during the course of PhD, as part of a collaborative industry project.

9.1.1 Enhancing the resolution of fluorescence-based microscopy

Proposal: To increase the spatial resolution of any fluorescence-based microscopy by a factor of 4X (max. limit).

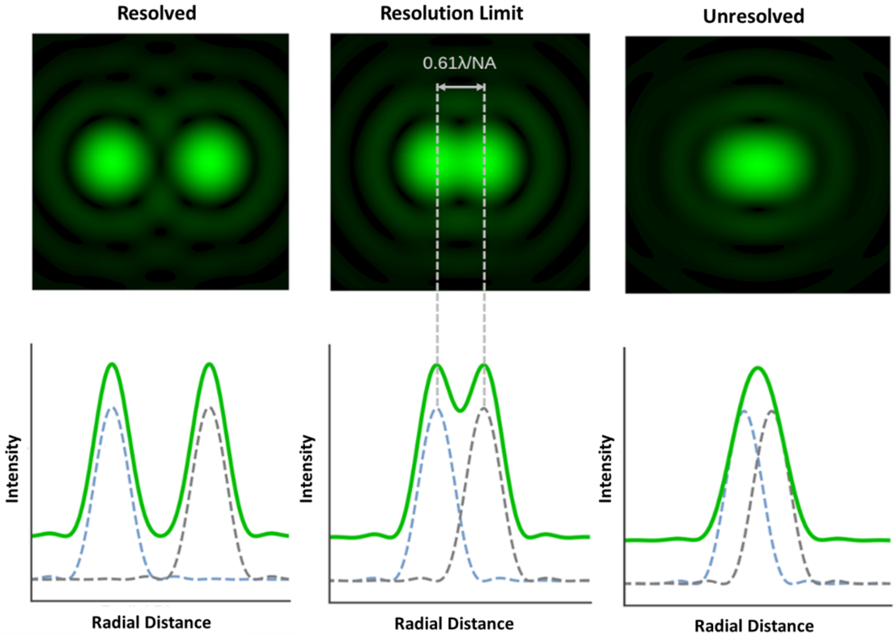

Figure 9.1: 2D point spread functions for resolved, just resolved (Resolution limit), and unresolved point emitters. The corresponding intensity variation over radial distance is also shown with an individual (blue and gray) and combined PSF (green). The image is reproduced from [5]

Background: For any microscopy, the spatial resolution, defined as the minimum separation between two objects corresponding to a certain relative contrast, is given by the diffraction limit. When two objects are brought together, their point spread functions (PSFs) combine, and the combined PSF is imaged by the microscope. The two objects are identified as resolved (Fig.9.1) when the separation between the objects is sufficient, leading to a decrease in the intensity of the combined PSF and an increase in relative contrast. The minimum separation distance - r_l (resolution limit) is usually defined in terms of the Rayleigh criterion defined as :

$$r_l = \frac{0.61\lambda}{\mathrm{NA}}$$

where λ is the wavelength of the incident light, and NA is the numerical aperture of the objective lens. This separation distance defines the minimum feature size discernible in the image. Also, this expression determines the minimum spot size radius achievable by any microscopic lens, known as the *airy disc radius*. A more practical version of the above limit is explained in terms of FWHM size, changing the prefix from 0.61 to 0.51 [5].

In the case of fluorescence-based microscopy, imaging beyond the resolution limit is possible by using advanced techniques like STED (Stimulated Emission Depletion) and multiphoton microscopy. While fluorescence is typically a linear process, these advanced techniques achieve this by utilizing nonlinear processes. For example, STED microscopy uses a depletion laser to effectively shrink the point spread function, and multiphoton microscopy involves nonlinear excitation with multiple photons where the interaction volume is smaller compared to the case of linear interaction. Two-photon fluorescence microscopy (TPFM) is one of the traditional techniques used for imaging biological samples [6]. For TPFM, the modified resolution limit, in terms of the minimum spot size radius, is given by [6]:

$$r_{\mathrm{TP}} = \begin{cases} \frac{0.32\lambda}{\sqrt{2}NA} NA \leq 0.7 \\ \frac{0.325\lambda}{\sqrt{2}NA^{0.91}} NA > 0.7 \end{cases}$$

where r_{xy} represents the $1/e$ radius of the squared intensity profile. The above equation results in a smaller minimum feature size compared to the linear case described by the previous equation. The enhancement in resolution for TPFM can be determined by comparing the two equations as follows ($1/e^2$ radius):

$$\frac{r_{TP}}{r_l} = \frac{\frac{0.32\sqrt{2}\lambda_{TP}}{\sqrt{2}\mathrm{NA}}}{\frac{0.61\lambda}{\mathrm{NA}}} = \frac{0.52\lambda_{TP}}{\lambda} \tag{9.1}$$

Therefore, $r_{TP} = 0.52 * r_l$, resulting in the minimum feature size being halved as compared to what is achieved from single-photon fluorescence microscopy, assuming the wavelength remains the same.

Proposed method

The proposed technique for enhancing the spatial resolution of fluorescence-based microscopy relies on recording the fluorescence of two unresolved objects (see Fig. 9.1) using asymmetric helical beams at different singularity displacements. This concept is illustrated in Fig.9.2.

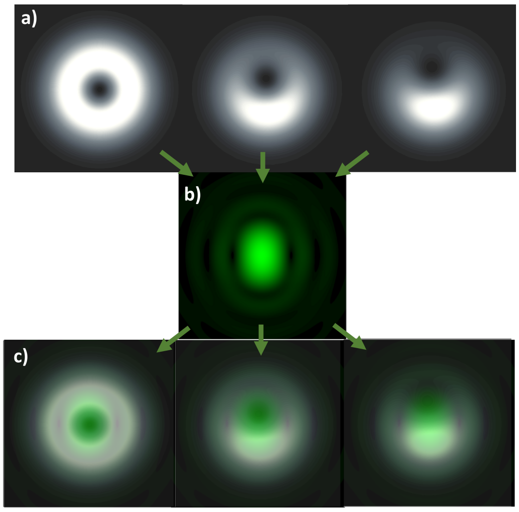

Figure 9.2: **a** 2D beam profile of asymmetric LG beams at different singularity displacements. **b** The fluorescence signal of two unresolved objects aligned vertically. The overlap of images in row a) and the two unresolved objects in b) is shown in **c**

Figure 9.2a illustrates the intensity profile of an asymmetric Laguerre-Gaussian (aLG) beam with an azimuthal index of $l = 1$, at three different displacements of the phase singularity. Additionally, Figure 9.2b shows two unresolved peaks aligned vertically, while Fig.9.2c presents the overlap of the aLG beams at the displacements shown in Fig.9.2a with the unresolved peaks. The overlap depicted in Figure 9.2c demonstrates that, when fluorescence is excited using such asymmetric beams, the majority of the signal originates from the region of peak intensity in the beam. In other words, the fluorescence signal predominantly follows the intensity distribution of the beam.

After recording several fluorescence images at different singularity displacements, the cross-correlation technique can be utilized to find the similarity among them. The cross-correlation technique employs the principles of mathematical linear or cyclic convolution, utilizing Fourier transforms [7], to determine the effective correlation, which represents the optimal overlap between two objects. In the case of image processing, the MATLAB function ‘normxcorr2’[8] can be utilized to perform the above mathematical function. The working principle of this function can be summarized as follows:

$$\boxed{\text{Zero padding} \rightarrow \text{FFT} \rightarrow \text{Frequency domain multiplication} \rightarrow \text{Inverse FFT} \rightarrow \text{Normalization}}$$

In the first step, zero padding is done on the second image to ensure that the convolution operation accounts for all possible overlaps between the source and the second image. In the second step, the Fast Fourier Transform (FFT) is applied to both images, as convolution in the time domain corresponds to multiplication in Fourier space: $\mathcal{F}\{x(t) * h(t)\} = X(f) \cdot H(f)$. The third and fourth steps involve multiplication and the inverse Fourier Transform to obtain the convolution signal in the spatial domain. The last normalization step adjusts the calculated cross-correlation signal to account for local variations in intensity.

The fluorescence signal is modeled in the form of an aLG profile at three different singularity displacements, and the cross-correlation results are shown in Fig.9.3. The rationale for approximating the fluorescence signal in the form of aLG profile is discussed in the description of Fig.9.2. Figure 9.3a shows the fluorescence signal approximated in the same profile as aLG beams for three different displacements of the singularity, labeled as images 1, 2, and 4. In Row 1, the cross-correlation of images 1 (symmetric profile) and 2 (asymmetric profile) is given in the third column. This correlated image is labeled as Image 3 in Row 2, and further cross-correlation is performed with Image 4 (where the singularity is displaced farther). The final cross-correlation is shown in the third column of Row 2, which shows the spatial feature of approx. 1/4 the size of the original structure in image 1.

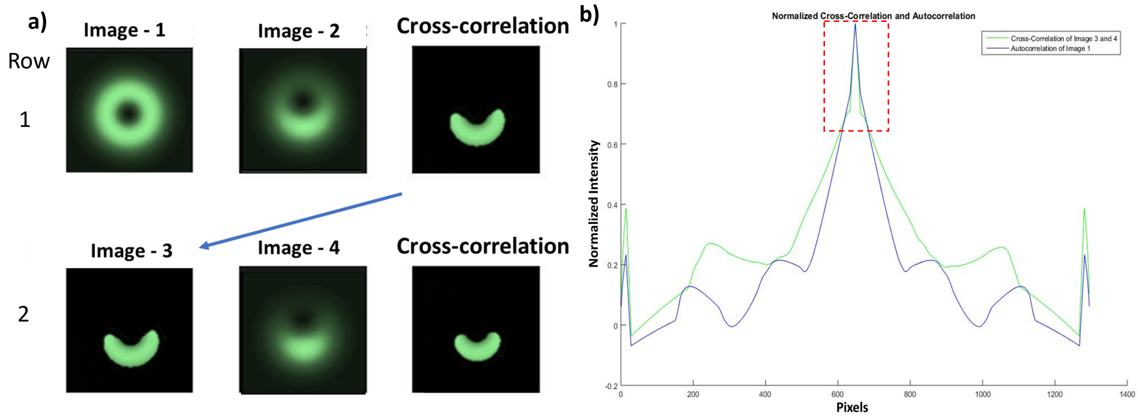

Figure 9.3: **a** The MATLAB simulation results for cross-correlation of the fluorescent signal in images 1 & 2 are shown in row 1 and images 3 & 4 in row 2. **b** The normalized correlation of image 1 with itself (autocorrelation) and cross-correlation of image 3 and 4 in Fourier space. The red box shows the optimal overlap region of the two curves, highlighting their relative widths.

Figure 9.3b also shows the correlation of image 1 with itself (autocorrelation) and the cross-correlation of images 3 and 4 in Fourier space. Inside the red box, the thin peak of the cross-correlation curve (green) relative to the autocorrelation curve (blue) indicates that images 3 and 4 are more sharply aligned compared to the structure of image 1. Therefore, the cross-correlation happens over a smaller region, making it easier to filter the resultant signal. The secondary peaks arise due to the presence of noise and periodic features.

The cross-correlation is shown in Fig.9.3a can also be obtained for the vertically downwards displacement of the singularity (opposite to what is shown) and would result in a similar correlation signal, but in the opposite direction. Combining the two simulations yields the signal shown in Fig. 9.4b. The minimum feature size is reduced, enabling the distinction of point-emitter objects. Thus, the *proposed method results in resolved point emitters* compared to the unresolved state in Fig. 9.4a. Consequently, the spatial resolution is *enhanced, with the minimum feature size reduced to approximately 1/2 to 1/4* of the original size. Moreover, the shape of the resolved signal can be further refined to resemble round point emitters by convolving the fluorescence for azimuthal displacements of the singularity, i.e., across the entire 2D profile. These azimuthal displacements were demonstrated in Chapter 7, where the positional resolution of $\lambda/20$ in displacing the singularity was shown. Also, no further increase in resolution is achieved using the helical beams with higher l values (results not shown).

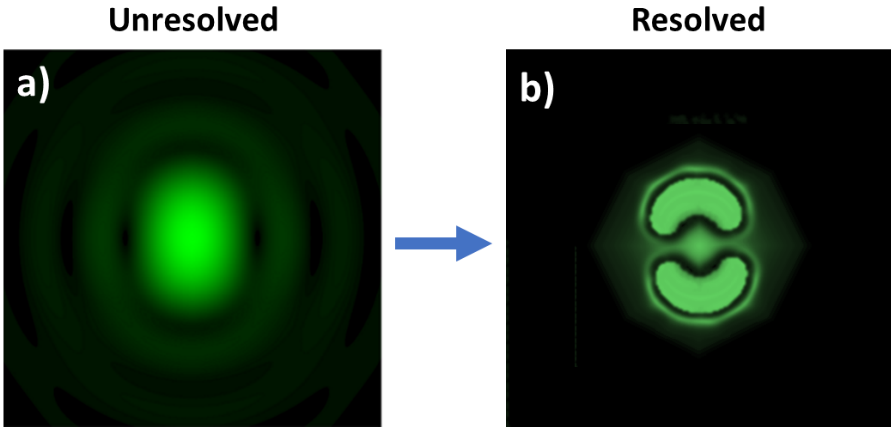

Figure 9.4: **Enhanced resolution**. **a** The fluorescent signal of two unresolved point emitters. **b** The simulated fluorescent signal obtained with the proposed method. Simulation results show a decrease in the minimum feature size, enabling the resolution of the point emitters. The signal around the correlation peaks includes the manually added noise, representing a realistic scenario.

Advantages:

- The proposed method is general and can be employed with any fluorescence-based microscopy to potentially increase its resolution. It can also be implemented with nonlinear microscopy, such as TPFM, as well as with super-resolution techniques, like STED.
- The experimental implementation of this technique is straightforward, requiring only the introduction of an electrically controlled q-plate and HWP into the beam path before the

sample. The proof of principle can be easily demonstrated by fabricating a PMMA cast infused with fluorescent particles, such as carboxyl-based fluorescent polystyrene particles from CD Bioparticles Inc. These particles have a size of 400 nm, an excitation wavelength of 480 nm, and an emission wavelength of 520 nm (DCFG-L005).[9]

Disadvantages:

- Exciting the fluorescence at different singularity displacements may result in the photobleaching or saturation of the sample, particularly with biological specimens. Additionally, computing the cross-correlation of numerous high-definition images would be computationally demanding.
- The proposed technique does not offer any improvement in axial resolution.

9.1.2 Light-driven controlled nano-motor

Proposal: To control the rotational speed of the light-driven plasmonic nanomotor. This can be achieved by utilizing the controlled and tunable absorption of asymmetric helical beams in plasmonic nanostructures based on the research presented in Chapter 6.

Background: The concept of plasmonic nanomotors was demonstrated by Liu et al.[10]. The snippet of the published article with a gammadion-shaped chiral nanostructure sandwiched between two glass slides (fused silica microdisks) and dark-field microscopy images at different time frames demonstrating rotational movement is shown in Fig.9.5.

The nanoscale motors were designed as planar gammadion-shaped gold nanostructures. When illuminated with the linearly polarized light, these chiral structures interacted strongly in terms of resonant plasmonic excitations (resonant wavelength), giving rise to significant photon light absorption and scattering. Consequently, the exchange of angular momentum from the beam resulted in a mechanical force being imparted onto the nanostructures. This force generated the torque, which rotated the larger fused silica microdisks. This was a significant demonstration as a single plasmonic motor rotated a 4,000 times larger (in volume) microdisk (area 2.2x2.2 mm^2) suspended in deionized water. Alternatively, this can be understood as the broken mirror symmetry in gammadion structures gave rise to a chiral distribution of the Poynting vector (Fig.9.6a), which resulted in an optical torque. The rotation direction and speed were controlled by tuning the wavelength of the incident light (Fig.9.6b).

CST Microwave Studio was used by Liu et al. [10] to model the electric and magnetic field distributions around the nanostructure. Parameters for the Drude model of gold permittivity and the boundary conditions were used in simulations. The torque on each point given by $\boldsymbol{\tau} = \mathbf{r} \times \mathbf{F}$ where $\mathbf{r}$ is the displacement and $\mathbf{F}$ is the Lorentz force $\mathbf{F} = q(\mathbf{E} + \mathbf{v} \times \mathbf{B})$, was

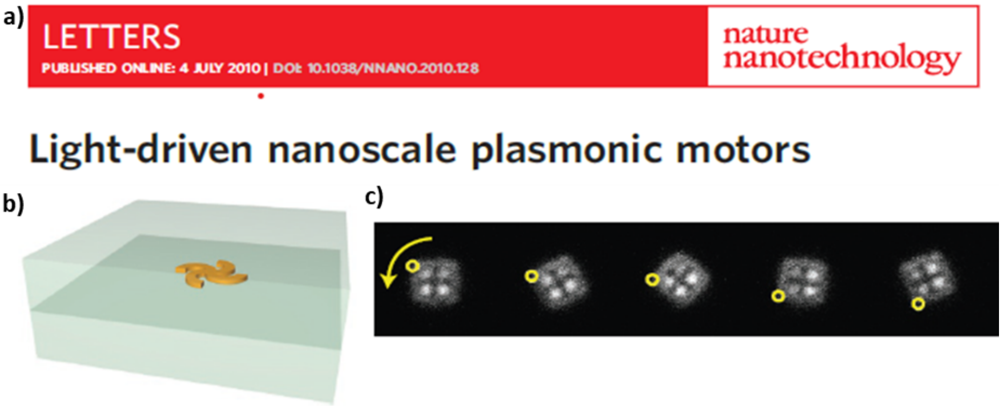

LETTERS

PUBLISHED ONLINE: 4 JULY 2010 | DOI: 10.1038/NNANO.2010.128

nature nanotechnology

Light-driven nanoscale plasmonic motors

Figure 9.5: **a** The snippet of the published article by Liu et al.[10]. **b** Light-driven nanoscale motors in the form of gammadian-shaped plasmonic nanostructure sandwiched between two fused silica microdisks. **c** dark-field microscopy images at different time frames demonstrating the rotation of nanostructure (as shown by markings in yellow)

calculated by inserting the simulated field distributions. For multiple nanomotors, the sum of individual local torques gave the total torque on the system.

Analytically, the force on individual nanomotors can be approximated in terms of electric dipole, magnetic dipole, and recoil forces. The expression for total force can be given as [11]

$$\langle \mathbf{F} \rangle = \frac{1}{2}\,\mathrm{Re}\left[\nabla \mathbf{E}^{*} \cdot \boldsymbol{\mu} + \nabla \mathbf{B}^{*} \cdot \mathbf{m} - \frac{k_0^4}{6\pi\epsilon_0 c}\left(\boldsymbol{\mu} \times \mathbf{m}^{*}\right)\right] \tag{9.2}$$

Here, the $\boldsymbol{\mu}$ and $\mathbf{m}$ represent the induced electric and magnetic dipole. The $\mathbf{E}$ and $\mathbf{B}$ are the incident electric and magnetic fields, and the rest are the standard wave propagation constants. These optical forces for the case of an electric dipole are also derived in Chapter 3 (supplementary file). The total torque can be calculated from the above force equation.

The induced dipoles were further expressed in terms of electric polarizability $\boldsymbol{\alpha}$, magnetic polarizability $\boldsymbol{\chi}$ and mixed electric-magnetic polarizability $\mathbf{G}$ tensors.

$$\boldsymbol{\mu} = \boldsymbol{\alpha} \cdot \mathbf{E} + i\mathbf{G} \cdot \mathbf{B}, \quad \mathbf{m} = \boldsymbol{\chi} \cdot \mathbf{B} - i\mathbf{G} \cdot \mathbf{E}, \tag{9.3}$$

Fabrication Process: The nano-fabrication process employed by Liu et al. [10] is briefly discussed here. The gammadion-shaped plasmonic nanomotor was fabricated using the standard electron beam lithography technique, which was sandwiched between two micro-disks(SiO2 layers). The process involved multiple steps of coating, patterning, etching, and lift-off procedures to achieve the final structure. Further, the micro-disks were placed in deionized water between

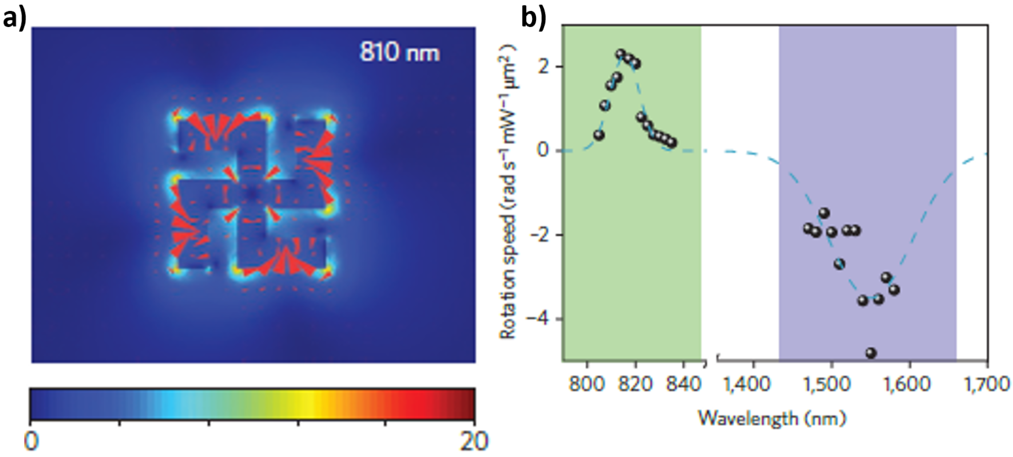

Figure 9.6: **a** Field excitation with intensity distribution shown by the colormap. The red arrows show the distribution of the Poynting vector. **b** Rotational speed vs incident wavelength. The rotation direction and speed were controlled by tuning the wavelength. These results were published by Liu et al.[10] and are reproduced here.

two glass slides. Gravitational force ensured that the microdisks settled at the bottom of the glass slide (not suspended), with the gammadion structures normal to the incident light. This setup minimizes Brownian motion and reduces friction, with viscous drag being the primary limitation of rotation. The surface roughness and fine structure of the microdisks were not consequential due to the laminar flow conditions, as determined by the low Reynolds number (resulting from the low rotational velocity).

Proposed method

The idea of controlling and scaling the rotational speed of the light-driven plasmonic nanomotor is based on the tunable absorption of asymmetric helical beams in plasmonic nanostructures. This was demonstrated in Chapter 7, where a similar plasmonic chiral gammadion-shaped nanostructure exhibited controlled absorption when probed with asymmetric beams. The absorption of light varied with a displacement of the singularity, ellipticity (ϵ), and the azimuthal index l of the beam (see results and transmission curve section in Chapter 7). Hence, a similar plasmonic nanomotor would also exhibit similarly controlled absorption when propelled with asymmetric helical beams. Therefore, in principle, the rotational velocity can be controlled by changing the l-value, ϵ, and singularity displacement. The direction of rotation can be changed by the combination of chiral phase and polarization.

Theoretically, the optical force (Eq.9.2) on induced dipoles can be extended to include the contribution of electric quadrupole, which was demonstrated to be responsible for phased-based preferential absorption. As discussed in Chapter 3 and 7, for asymmetric beams, the coupling of electric dipole and electric quadrupole is responsible for the controlled absorption of light.

Therefore, the optical force and torque equations 9.2 and 9.3 can be extended to include induced multipole. This can be derived by considering the potential energy of induced multipoles as $U = U_{\text{elec. dipole}} + U_{\text{elec. quadrupole}} + U_{\text{mag. dipole}}$:

$$U = -\boldsymbol{\mu} \cdot \mathbf{E} - \frac{1}{3}\theta_{ij}\nabla_i E_j - \boldsymbol{m} \cdot \mathbf{B}$$

The force on induced multipoles in the electromagnetic field can be given as

$$\mathbf{F} = -\nabla U = \nabla(\boldsymbol{\mu} \cdot \mathbf{E}) + \frac{1}{3}\nabla\left(\theta_{ij}\frac{\partial E_i}{\partial x_j}\right) + \nabla(\mathbf{m} \cdot \mathbf{B})$$

where induced dipoles are expanded in terms of electric polarizability $\boldsymbol{\alpha}$, magnetic polarizability $\boldsymbol{\chi}$, mixed electric-magnetic polarizability $\mathbf{G}$ tensors and electric dipole-quadrupole polarizability A_{ijk} (see Chapter 7).

$$\boldsymbol{\mu} = \boldsymbol{\alpha} \cdot \mathbf{E} + i\mathbf{G} \cdot \mathbf{B} + \frac{1}{3}A_{ijk} \cdot \nabla_i E_j; \qquad \theta_{ij} = A_{kij}E_k \quad ; \qquad \mathbf{m} = \boldsymbol{\chi} \cdot \mathbf{B} - i\mathbf{G} \cdot \mathbf{E} \tag{9.4}$$

Additionally, the numerical simulation for the optical force and torque can be performed using the Lumerical FDTD or Comsol software packages. In this software, the input beam source needs to be custom-defined for asymmetric LG beams.

Advantages:

- The proposed technique is straightforward to implement, requiring only the replacement of the incident light mode in the previously demonstrated method. Fabrication and characterization can be easily performed using the approach outlined by Liu et al. [10].
- The proposed method provides several advantages over the approach previously demonstrated by Liu et al. [10], which involved controlling the rotational speed and direction by tuning the wavelength of incident light. The earlier method is limited to broadband sources, where the rotational speed cannot be scaled. Furthermore, its efficiency decreases as the wavelength is varied (see Eq.9.6).

9.1.3 Increasing the 3-D optical data storage density in an optical disc

This application extends our research conducted as part of a collaborative industrial project and is not directly related to phase-based spectroscopy. The research publication is included here for reference.

Proposal: To increase the 3D optical data storage density in a standard compact disc (CD) beyond the previously demonstrated capacity of 275 GB per disc.[12].

Background: With the rise of social media, the majority of globally generated data is now classified as 'cold data.' This type of data is not accessed frequently, but requires long-term archival. This has spurred a critical need for enhanced data storage solutions. Such data storage solutions must not only offer vast capacities but also ensure extended shelf life. Optical data storage (ODS) offers a superior shelf life compared to other existing technologies but lags in storage capacity when compared to conventional magnetic and silicon-based systems. Traditional optical data storage methods, like those used in DVDs and Blu-ray discs, involve data storage on the surface of the disc. This conventional planar technology is constrained by the response and design of materials below 400nm light. This limitation can be addressed by recording data in the 3D volume of the recording medium instead of just the surface. By utilizing the depth of the material, 3D-ODS can significantly increase the amount of data stored in a given volume, offering a promising solution to long-term data storage architectures. Among existing 3D-ODS technologies, ultrafast laser-induced permanent material modification is often used for storing data in binary form (1-on and 0-off). These modifications are in the form of refractive index modifications[13], restructuring of metal nano-clusters[14], or creation of emission centers via nonlinear interaction[15]. Our 3D-ODS technology was based on fluorescence emission from femtosecond laser-modified regions in readily available common plastics, such as polycarbonate and PMMA. A storage capacity of 275 GB per standard 1.2mm thick plastic CD was demonstrated.

The capacity of any ODS technology is determined by the recorded bit size and the spacing between them. In 3D, the number of modified layers scales the storage density. The size of the bit (and the spacing between bits) in any ODS technique is limited by the spherical aberrations introduced by the optical elements in the setup and the storage medium. Aberrations caused by optical setup are determined by the wavefront distortions from the focusing lenses and other refractive optics. The aberrations introduced by the medium increase with depth, causing the laser spot size to enlarge. This typically limits the number of layers that can be efficiently recorded and retrieved. The publication proposed an energy gradient technique to minimize these aberrations. This technique involves precisely determining the nonlinear modification threshold energies at different layers (depths) and adjusting the pulse energy dynamically during the recording process. The threshold energy increases with depth due to the increase in aberrated spot size. By precisely adjusting the laser pulse energy to match nonlinear threshold energies at different depths, the aberrations caused by the medium were minimized.

The publication employed diffraction theory [16, 17] to model the effect of spherical aberration introduced by the medium, as well as finite-difference time-domain (FDTD) simulations to describe light propagation through multi-layered materials. These simulations were used to optimize the data reading and writing processes. The experimental results were in agreement with the simulations.

photonics

MDPI

Communication

Optimization of Multi-Layer Data Recording and Reading in an Optical Disc

Ashish Jain, **Mitra G. Rahimian** and **V. R. Bhardwaj** *

Department of Physics, University of Ottawa, Ottawa, ON K1N 6N5, Canada
* Correspondence: ravi.bhardwaj@uottawa.ca

Abstract: Storage capacity of a conventional optical disc can be enhanced significantly by recording data within the three-dimensional volume. However, spherical aberrations and light-scattering limit the number of layers that can be efficiently recorded and retrieved. In this paper, we show that by optimizing the multi-layer data recording and reading parameters, the number of fabricated layers could be tripled to 60 in commercial grade poly-methyl-methacrylate polycarbonate and reduce the read laser power by a factor of 7 by the 20th layer. Influence of spherical aberration on write laser spot size was studied by using vector diffraction theory and compared with experimental values obtained by monitoring the threshold energy of the write laser with depth. Scattering losses of the read laser were studied by simulating the propagation of light through multi-layered micro-structured material. The main advantage of our technique is its practical implementation, as it refrains from the use of index-matching liquids and specialized optics during the read–write process.

Keywords: optical data storage; nanofabrication

check for updates

Citation: Jain, A.; Rahimian, M.G.; Bhardwaj, V.R. Optimization of Multi-Layer Data Recording and Reading in an Optical Disc. *Photonics* **2022**, *9*, 690. https://doi.org/10.3390/photonics9100690

Received: 17 August 2022
Accepted: 20 September 2022
Published: 26 September 2022

1. Introduction

The majority of the data generated globally every year is the so-called cold data that needs long-term storage for archival purposes and is accessed only occasionally. Consequently, there is an ever-increasing demand for not only higher data storage capacities but also longer shelf life. Among the existing technologies, optical data storage (ODS) has a better shelf life but lags behind magnetic and silicon-based technologies in terms of data storage capacity. This is because in conventional optical discs (DVDs and Blu–ray), data is stored on the surface, and this planar technology cannot be scaled due to the response and design of materials below 400 nm. This limitation can be overcome by encoding multilevel and multiplexed information within the three-dimensional volume of a recording medium.

The 3D ODS often relies on using ultra-fast lasers to induce permanent changes in the medium on a micron scale in the form of refractive index/birefringence [1,2], aggregation/shape alteration of metal nanoclusters/rods [3,4], or emission centers [5]. It was first demonstrated in photopolymers [6] and glass [2] by modifying the refractive index to record data bit by bit. The technique was later extended to demonstrate 4D ODS in silver-doped zinc phosphate glass in which the write laser-induced silver nanoclusters that emitted fluorescence, upon excitation by the read laser, whose intensity represented the fourth dimension [3]. The 5D ODS was recently demonstrated in glass by using laser-induced form birefringence and in stacked gold nanorods mediated by surface plasmon resonances [4,7,8]. In addition to three spatial dimensions, the former exploited two additional dimensions associated with the orientation and retardance of periodic nanostructures, whereas the latter exploited wavelength and polarization of light to multiplex data within the same bit. Recent advances to significantly enhance the storage capacity, in principle, include employing techniques such as multifocal optical nanoscopy [9]. Stimulated emission depletion in specially designed photoresists [10], development of nanocomposites [11], and incorporation of machine learning algorithms [12]. However, their implementation in developing a viable consumer electronic device remains challenging.

Data recorded in a pristine transparent medium with ultra-fast lasers is not erasable and therefore not rewritable. Such ODS, categorized as write once read many times (WORM) type, ensures the highest level of data security and integrity with applications in archival storage. Erasable/rewritable 3D ODS systems require photo-refractive polymers [13] or transparent glasses doped with rare-earth ions [14] or nanocrystals [15]. Alternate technologies, such as holography and two-beam lithography, do not rely on ultra-fast lasers to record bits but require a specially designed photosensitive recording medium [16,17].

The capacity of an ODS is determined by the bit size and spacing, and the number of layers embedded in the recording medium. Smaller bit sizes can be achieved by using a higher numerical aperture (NA) objective in conjunction with index-matching liquids. However, their usage in a practical implementation is restrictive, especially when existing Blu-ray/DVD technology is extended to 3D ODS. Moreover, spherical aberrations and light-scattering generally limit the number of layers that can be efficiently recorded and retrieved. This is true even for the practical and cost-effective 4D ODS technology that we demonstrated in readily available common plastics based on fluorescence emission from femtosecond laser-modified regions [5].

In ODS, the beam emerging from the high-NA objective focuses deeply through an interface between two media of different refractive index leading to spherical aberrations, which increases dynamically at increasing depths. Consequently, the spot size of the write laser increases with depth leading to an increase in the threshold fluence required to record a bit. Spherical aberrations can be compensated by correcting the wavefront by using passive or adaptive optics (such as a spatial light modulator or digital micro-mirror device) to dynamically adjust for different depths [18,19]. Because the practical implementation of such correction techniques is not easy, we adopted a simpler technique of varying the pulse energy with depth during the recording process.

In this letter, we maximize storage capacity without the use of index-matching liquids and employing an energy gradient technique to compensate spherical aberrations of the write laser beam. We optimize the coupling of read laser light by simulating the propagation of light through multi-layered micro-structured material. We effectively tripled the number of layers that can be fabricated in a commercial grade PMMA and also reduced the read laser power requirement by a factor of 7. We measured the threshold fluence required to record bits at different depths to extract the aberrated spot sizes. The write laser power was then accordingly adjusted for each layer to maintain the same fluence while recording the bits. We used vector-diffraction theory to simulate the variation of spot size with depth and compared it with the measured values. To maintain a constant readout signal, we show that the read laser power needs to be adjusted layer to layer to account for scattering losses during propagation through multi-layered nanostructures.

2. Methods

2.1. Data Fabrication

Femtosecond pulses from a Ti:sapphire laser system (800 nm, 1 kHz, 45 fs, 2.5 mJ/pulse) were focused inside clinical quality (CQ grade from Goodfellow, UK), commercial grade (CG) PMMA samples and commercial grade polycarbonate (PC) with a 0.5, 0.83 numerical aperture (NA) aspheric objective. Samples with the thickness of 2 mm were mounted on three-axis translation stages with a resolution of 100 nm (Figure 1a). Pulse energies, measured after the aspheric objective, were varied from ≈ 25–70 nJ by a combination of half-wave plate and polarizer. The pulse duration at the aspheric objective was 70 fs, monitored continuously by using a single-shot auto-correlator. Multiple layers were fabricated in PMMA starting from the bottom with the last layer being at 100 µm depth from the top surface. Each layer consisted of a 25 × 25 array of bits/modified regions, each irradiated with a single laser pulse. Typical bit spacing was 2.0, 0.8 µm, and the layer spacing was 10 µm. Fluorescence emission from bits was recorded by using a Nikon confocal fluorescence microscope with a 40x objective (NA 0.8/1.1, working distance 2 mm, water immersion) at an excitation wavelength of 488 nm, and an emission window in the 500–550 nm range, respectively. Sensitivity of the detector at 488 nm excitation was 140 and the pinhole size for confocal microscope was optimized at 39.6 µm. The CW read laser power measured at the sample was in the range of 1 µW–150 µW.

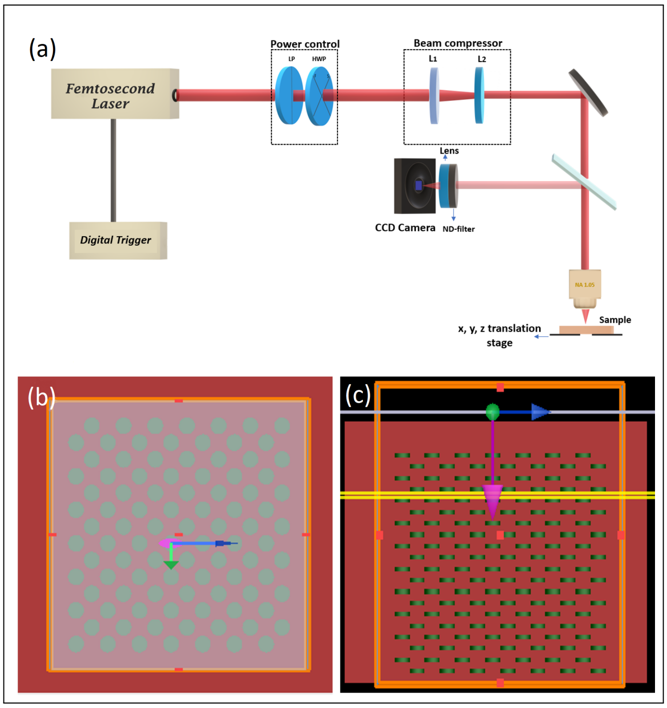

Figure 1. (**a**) Schematic (**b**,**c**) Top and side view of the FDTD grid showing the layout of the modeled nanostructured PMMA. The pink arrow shows the plane wave propagation direction. In addition, the blue (green) arrow represents electric (magnetic) field. Yellow lines, positioned 1 µm above and below each layer, represent the power and field profile monitors.

2.2. Aberration Correction by Energy Gradient

Spherical aberrations increase the laser spot size with depth. Consequently, the threshold energy to induce modification in a medium increases. If the incident pulse energy is not dynamically adjusted with depth to compensate for the change in laser fluence, the number of layers that can be fabricated is limited. This can be overcome by adjusting the incident pulse energy to the threshold value, which ensures a minimum laser spot size and spherical aberration. To determine the variation of threshold pulse energies with depth, a single layer containing an array of bits was fabricated at different depths with an incremental increase in pulse energy between adjacent lines within the array. This information was implemented during the automated fabrication of data in different layers.

2.3. Numerical Simulations

2.3.1. Spherical Aberrations

The effect of aberrations on the spot size was quantified by using the vector diffraction theory developed by Wolf [20] and Torok [21,22]. The focusing lens was assumed to be free of spherical aberration and the wavefront was assumed to be uniform at the focusing plane. The Cartesian components of the electric field at any point p inside the material of refractive index n_2, is given by a linear combination of diffraction integrals:

$$e_x = -iK\left[I_0^{(e)} + I_2^{(e)}\cos(2\theta_p)\right], e_y = -iKI_2^{(e)}\sin(2\theta_p), e_z = -2KI_1^{(e)}\cos\theta_p,$$

where $K = \frac{k_1 f l_0}{2} = \frac{\pi n_1 f l_0}{\lambda}$ and

$$\begin{aligned} I_0^{(e)} &= \int_0^{\alpha} (\cos\phi_1)^{1/2} \sin\phi_1 \exp[ik_0 \Psi(\phi_1, \phi_2, -d)] \\ &\quad \times (\tau_s + \tau_p \cos\phi_2) J_0\left(\frac{v \sin\phi_1}{\sin\alpha}\right) \exp\left(\frac{iu\cos\phi_2}{\sin^2\alpha}\right) d\phi_1 \\ I_1^{(e)} &= \int_0^{\alpha} (\cos\phi_1)^{1/2} \sin\phi_1 \exp[ik_0 \Psi(\phi_1, \phi_2, -d)] \\ &\quad \times \tau_p \sin\phi_2 J_1\left(\frac{v \sin\phi_1}{\sin\alpha}\right) \exp\left(\frac{iu\cos\phi_2}{\sin^2\alpha}\right) d\phi_1 \\ I_2^{(e)} &= \int_0^{\alpha} (\cos\phi_1)^{1/2} \sin\phi_1 \exp[ik_0 \Psi(\phi_1, \phi_2, -d)] \\ &\quad \times (\tau_s - \tau_p \cos\phi_2) J_2\left(\frac{v \sin\phi_1}{\sin\alpha}\right) \exp\left(\frac{iu\cos\phi_2}{\sin^2\alpha}\right) d\phi_1. \end{aligned}$$

Here, ϕ_1 and ϕ_2 are angles of incidence and refraction at the interface between two materials of mismatched refractive indices and the aberration function

$$\Psi(\phi_1, \phi_2, -d) = -d(n_1 \cos\phi_1 - n_2 \cos\phi_2),$$

and the normalized radial and axial coordinates v and u are given by $v = k_1 \left(x^2 + y^2\right)^{1/2} \sin\alpha = k_1 r_p \sin\phi_p \sin\alpha$, $u = k_2 z \sin^2\alpha = k_2 r_p \cos\phi_p \sin^2\alpha$, where α is the solid semi-angle of the lens in the first material, k_0, k_1, and k_2 are the wave numbers in the vacuum, first and second medium (PMMA), respectively, f is the focal length of the lens in the vacuum, l_0 is an electric field amplitude factor, r_p, and ϕ_p and θ_p are spherical polar coordinates to the point p where the fields are being evaluated. The standard expressions were used for the Fresnel transmission coefficients τ_s and τ_p and for the Bessel functions J_n of the first kind. Numerical integration was performed by using the adaptive Gauss-quadrature method and evaluated at the first maximum of energy density in z.

2.3.2. FDTD Simulation

To optimize the coupling of the read laser light, we simulated the absorption of the plane wave (478–498 nm) traversing through 20 layers of laser-modified regions/bits in PMMA by using the FDTD: 3D Electromagnetic Simulator (Lumerical FDTD Solutions, Inc., Vancouver, Canada) Each laser-modified region/bit was assumed to have a cylindrical structure (1 µm diameter and 4 µm length) with 0.15% higher refractive index than the surrounding, unmodified PMMA and an imaginary refractive index of about 8×10^{-5} [23]. A 7 × 7 array with a bit spacing of 2 µm was considered with periodic boundary conditions in the transverse x–y plane. The first layer was positioned 30 µm below the surface and subsequent layers were spaced 10 µm apart. Total simulation dimensions were 15 × 15 µm in the transverse plane and 230 µm along the propagation direction. Power and field profile monitors were positioned 1 µm above and below each layer to study the propagation of light. The side and top view of the FDTD simulation model is shown in Figure 1b,c.

3. Results

Figure 2 shows the variation of fluorescence intensity of an array of bits from different layers fabricated in CQ and CG grade PMMA for different bit spacing (Figure 2a) and layer spacing (Figure 2b). Bits in each layer were fabricated with fixed incident energy. Fluorescence intensity drops significantly as the number of layers increases. Vertical dashed lines represent the layers where the read laser power had to be increased and the fluorescence intensity normalized. CG-PMMA produces a lesser fluorescence signal compared to CQ-PMMA. As a result, only 21 layers could be fabricated in CG-PMMA compared to 35 in CQ-PMMA. This is most likely due to the different chemical compositions of the additives and UV stabilizers. For a fixed layer spacing of 10 µm, the fluorescence signal is lower for smaller bit spacing (Figure 2a). Confocal images of layers 5, 15, 25, and 35 are shown in Figure 2c, d, e, and f respectively, for a bit spacing of 2.0 µm.

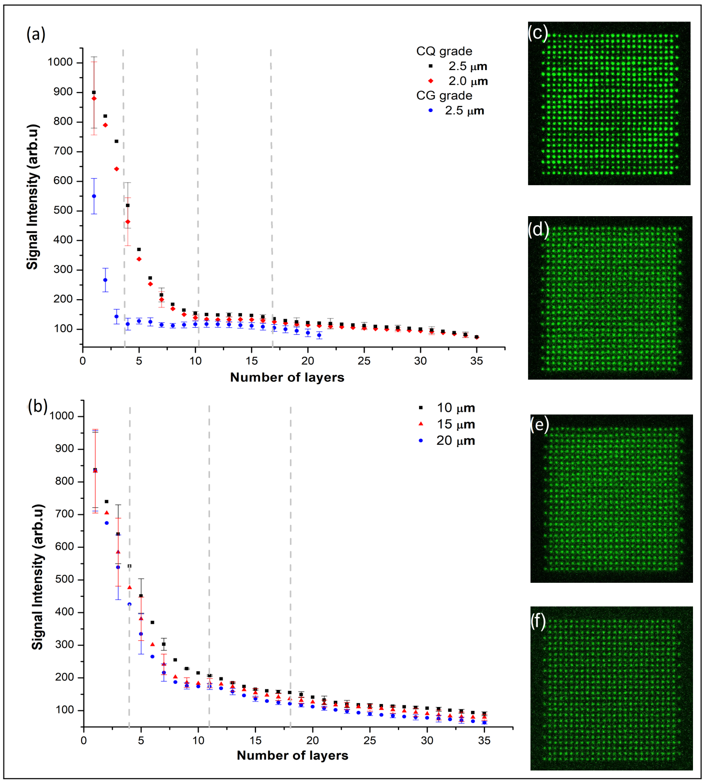

Figure 2. Variation of fluorescence intensity with the number of layers fabricated in PMMA for (**a**) fixed layer spacing of 10 µm and bit spacing of 2.0, 2.5 µm in clinical quality (CQ), and 2.0 µm in commercial grade (CG), and (**b**) fixed bit spacing of 2.0 µm and layer spacing of 10, 15, and 20 µm in CQ grade. Vertical dashed lines represent the layers where the read laser power was adjusted to produce the same fluorescence signal (see text for details). (**c**–**f**) Confocal microscope images of bit arrays, fabricated at a fixed energy of 35 ± 3 nJ energy, for layers 5, 15, 25, and 35, respectively.

There are two major contributions to the rapid change in fluorescence intensity with the number of layers: (1) spherical aberrations influencing the write laser fluence, and (2) coupling losses of the read laser due to scattering from multiple micro-structured layers. For a fixed bit spacing (Figure 2b), the former leads to lower fluorescence intensity with the increase in layer spacing. This is because the depth at which the layers are fabricated increases, causing the spherical aberration to increase the laser spot size and thereby reduce the fluence for a fixed incident pulse energy. The latter requires the use of higher read laser powers. With a 0.5 NA aspheric objective, 10 µm is the optimum layer spacing—a balance between aberrations (that scales with NA of the objective) and cross-talk between layers (that depends on the confocal parameter).

The influence of spherical aberrations on the ability of the write laser to fabricate bits at different depths is shown in Figure 3. For this study, a single layer containing an array of bits was fabricated at different depths with an incremental increase in pulse energy between adjacent lines within the array. As the depth increased the number of lines in the array visible under an optical microscope decreased, as shown in Figure 3b–d. This is due to an increase in the threshold fluence required to modify PMMA as a result of an increase in the spot size from spherical aberrations. Figure 3a shows the threshold energy required to observe fluorescence from bits at different depths. A nearly linear variation of write laser energy with depth makes it easy to implement an energy gradient during the automated fabrication of data in different layers.

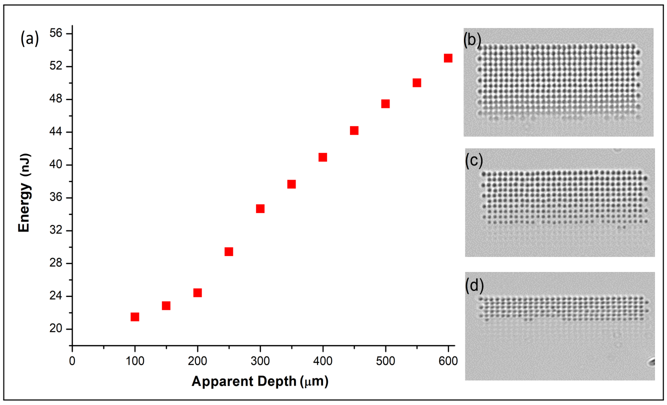

Figure 3. (**a**) Variation of threshold energy required to fabricate bits at different depths in PMMA. (**b**–**d**) Optical microscope images of an array of bits, fabricated with increasing pulse energies from bottom to top, at depths of 100, 150, and 350 µm.

Figure 4 shows the variation of write laser spot size, both experimental and simulated, with depth inside PMMA. Experimentally, the spot size was extracted from Figure 3 by comparing the threshold fluorescence intensity for a given layer with that of the first layer (100 µm below the surface) as a reference. The spot size was obtained by considering bits at different depths (50 µm apart) fabricated with a specific write laser energy that produced fluorescence intensity similar to the reference signal. The effect of aberrations on the spot size was quantified by using the vector diffraction theory developed by Wolf [20] and Torok [21,22] (see Methods).

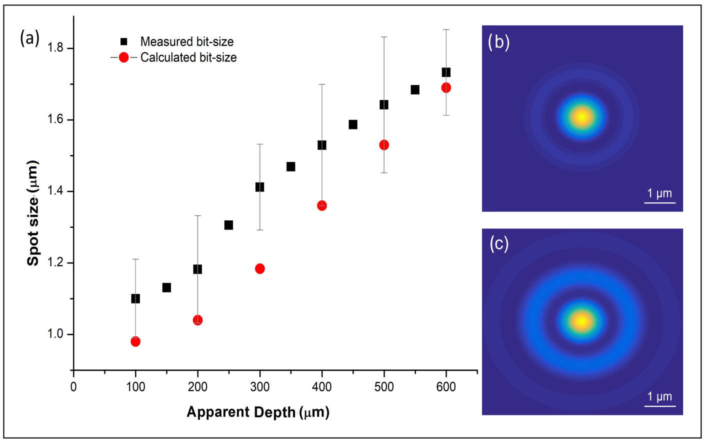

Figure 4. (**a**) Variation of spot size with depth in PMMA extracted from the threshold energies of Figure 3 (black squares) and calculated from the vector diffraction theory (red circles). (**b**,**c**) Spatial profile of the simulated laser spot size at depths of 100 µm and 200 µm focused inside PMMA with a 0.5 NA aspheric objective.

The spatial profile of the simulated focal spot produced by a 0.5 NA aspheric objective at an apparent depth of 100 and 200 µm inside the PMMA is shown in Figure 4b,c. Spherical aberration increases the spot size and energy density in the secondary maxima of the Airy pattern with depth. Simulated bit sizes were obtained by taking 1/e diameter of the central maxima in the diffraction pattern. Agreement with the experimentally obtained spot sizes establishes the fact that non-linear effects such as self-focusing are not dominant at the write laser energies used (up to 60 nJ).

In commercial grade PMMA employing fixed write laser energy, the maximum number of layers that could be recorded and retrieved is limited to only 20 layers, beyond which fluorescence intensity is comparable to background noise (Figure 2a). By employing the energy gradient technique to offset spherical aberration effects and shifting alternate layers in the x–y direction by half the bit spacing, we could fabricate 60 layers with 10 µm layer separation and 2 µm bit spacing in each 25 × 25 array as shown in Figure 5a. Multiple layers were fabricated by incrementally increasing the write laser energy based on the dependence of threshold energy on depth (Figure 3a). Figure 5b shows the dependence of read laser power required to record different layers for the two fabrication methods—fixed write laser energy and energy gradient. For the latter, the read laser power is lower by a factor of 7 for the 20th layer. Lower read laser powers ensure no photo-bleaching of the emission centers induced by the write laser, hence no damage to the recording medium.

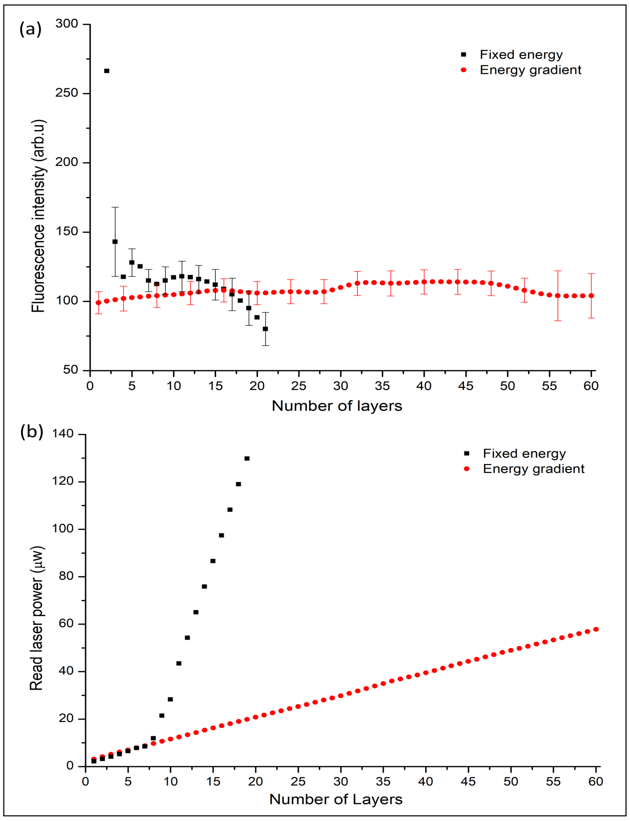

Figure 5. Fabrication of 60 layers in commercial grade PMMA by compensation of spherical aberrations. Fluorescence intensity variation (**a**), and read laser power variation (**b**) as a function of the number of layers fabricated with fixed pulse energy (black squares) and with energy gradient technique (red circles).

The effectiveness of our method is demonstrated by fabricating 50 layers of data with 0.9 µm bit spacing and 10 µm layer spacing in CG grade PC (Figure 6a–c) by using a 0.8 NA objective with no index-matching liquid. The NA of the objective is similar to the one used in Blu-ray disc making it a viable 3D ODS technology. Spherical aberrations are more dominant when using such a higher NA objective. However, our method is effective in minimizing spherical aberrations with higher NA objectives up to depths of ∼400 µm where the bit size increased only by ∼25% (Figure 6f). The read laser power required to obtain nearly constant fluorescence intensity from different layers is shown in Figure 6d,e.

The gradual increase in the read laser power with depth is due to coupling losses arising from scattering and absorption from micro-structured multiple layers. To optimize the coupling of the read laser light, we simulated the absorption of a plane wave (478–498 nm) traversing through 20 layers of laser modified regions/bits in PMMA by using the FDTD: 3D Electromagnetic Simulator (Lumerical FDTD Solutions, Inc., see Methods).

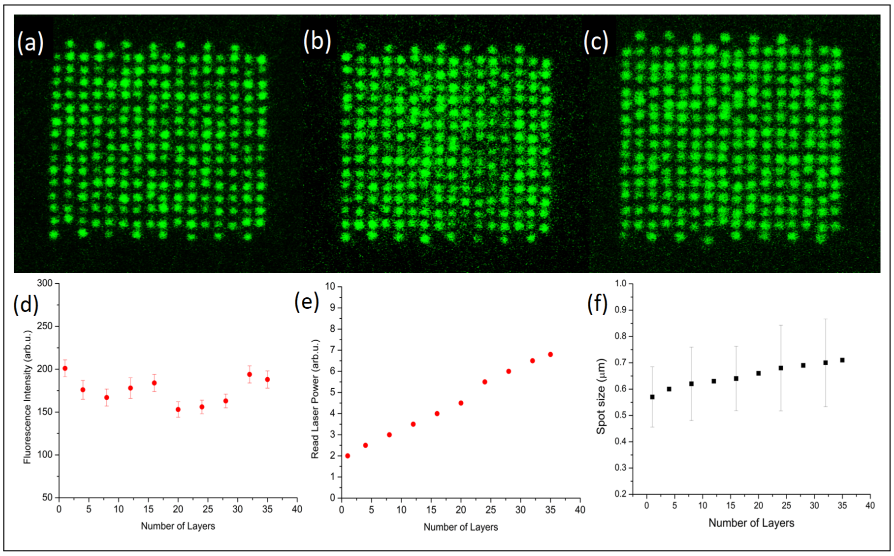

Figure 6. Fabrication of 35 layers in commercial grade PC using a 0.83NA lens. (**a**–**c**) Confocal microscope images of bit arrays with 0.9 µm bit-spacing, for layers 8, 16, and 35, respectively. Fluorescence intensity variation (**d**), and read laser power variation (**e**) as a function of number of layers fabricated with energy gradient technique (red circles), (**f**) Spot size variation as a function of number of layers.

Figure 7a–f shows the field patterns 1 µm below layers 8, 9, and 10, respectively, for two cases in which the bits in alternate layers are either unshifted and lie on top of each other (top row) or shifted in the x–y direction by 1 µm (middle row). In the unshifted case, after propagating through the first few layers, the scattered light localizes near the bits and in the regions between the bits. As the number of layers increases, the scattered light in the regions between the bits increases in magnitude (Figure 7a–c) and less light propagates in the center relative to the edges. Consequently, during imaging, this can reduce the contrast between bits and lead to darkening of the central region of an array of bits as observed previously [24]. When bits are shifted between alternate layers, light is localized near the bits with very little scattering in the surrounding regions (Figure 7d–f). As a result, the bit contrast is enhanced, and coupling losses are reduced.

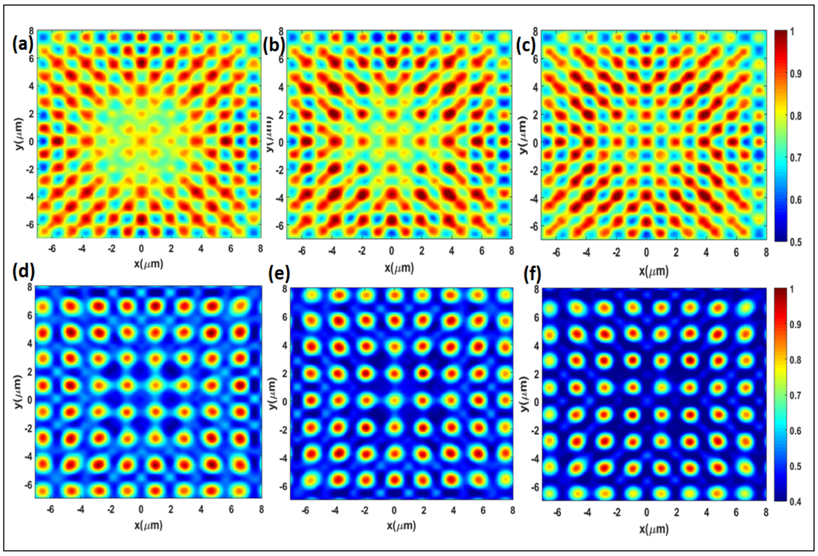

Figure 7. Simulated field patterns of light propagating through an array of unshifted bits between alternate layers, (**a**–**c**) 1 µm below layers 8, 9, and 10, respectively. (**d**–**f**) The same as above for the shifted bits.

Figure 8a,b shows field patterns 1 µm above layer 9 for the unshifted and shifted bits cases, respectively. In the unshifted case, field patterns change drastically while propagating a distance of less than 5 µm. The regions where fields are stronger, just after layer 8 (Figure 7a), become weaker and vice versa. However, in shifted case, light undergoes a simple defocusing effect.

Figure 8c shows the simulated coupling losses of the read laser for shifted (red) and unshifted bits (blue). Relative losses are low for the layers close to the top surface but increase significantly with the number of layers. Assuming coupling losses to be the major contributor for an increase in read laser power, we compare the simulated losses directly with the experimental variation of the read laser power as shown (black). Fabrication and imaging of 60 layers shown in Figure 5 were only feasible by shifting the bits between alternate layers. For the unshifted case, the maximum number of layers that could be imaged was about 25.

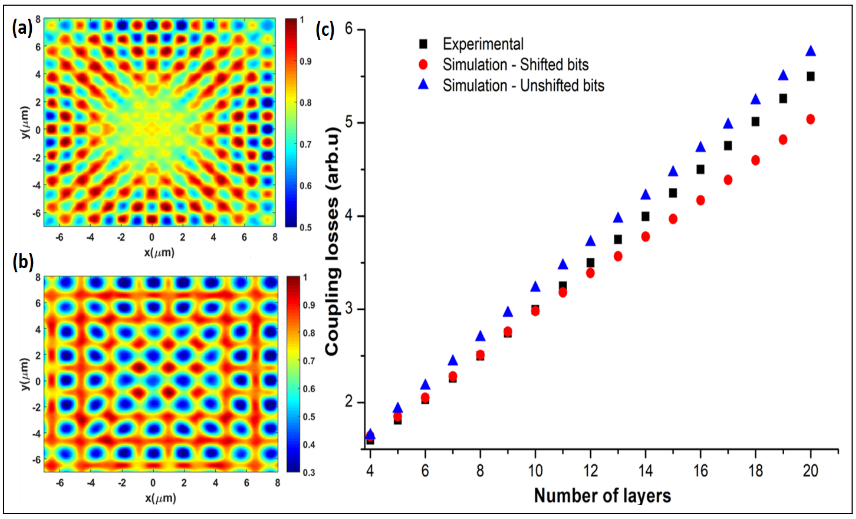

Figure 8. Simulated field patterns of light propagating through an array of unshifted bits between alternate layers, (**a**) 1 µm above layer 9. (**b**) The same in case of the shifted bits. (**c**) Experimental (black) and simulated read laser coupling losses for unshifted (blue) and shifted bits (red).

4. Discussion and Conclusions

Development of 3D ODS technology with enhanced storage capacity relies on simultaneous innovations in two research areas. First, we must find a suitable recording medium capable of storing data in multiple layers with a long shelf life. Secondly, we must spatially localize the data bits and retrieve them from multiple layers.

By using common, inexpensive transparent plastics such as PMMA and PC, we eliminate the need to search for and develop novel composite materials that exhibit photosensitive properties. The embedded data is thermally stable up to the glass transition temperature of the recording medium, thereby offering a long shelf life [5]. PMMA and PC do not fluoresce inherently. Irradiation by an ultra-fast laser results in the localized formation of carbonaceous clusters [25,26] within the focal volume that fluoresces upon excitation. In other words, the ultra-fast laser induces photo-sensitivity.

By refraining from the use of index matching liquids and specialized optics during the read–write process, we demonstrate enhanced storage capacity. This was achieved by minimizing spherical aberrations during the write process and optimizing the light-scattering during the read process. Our method enables practical implementation in developing a viable consumer electronic device. Higher bit density can be achieved with high NA objectives but requires index-matching liquids and is limited by the working distance of the objective. Our method does not use index-matching liquids to compensate for spherical aberrations but exploits the depth variation of threshold pulse energies required for modification. However, it requires an accurate determination of the threshold pulse energies. Any variations in incident pulse energy or determining the threshold energies can lead to either darkening of bottom layers or a low signal-to-noise ratio. In addition, for objectives greater than 1 NA, the method can be ineffective in minimizing aberrations beyond 60 layers (120 layers bi-directional). To simulate spherical aberrations, the focusing lens was assumed to be aberration-free and the wavefront was assumed to be uniform at the focusing plane.

To optimize the coupling of the read laser with different layers in a stack and the scattering of fluorescence signal from the above layers, FDTD simulations assumed each laser-modified region/bit to have a cylindrical structure to mimic the experimental Rayleigh range. Varying the radial bit size changes the scattering regime from Rayleigh to Mie scattering. As a result, the contrast between the modified and unmodified regions is higher when the bit size is greater than the wavelength of the read laser and reduces when the bit size is smaller than the wavelength of light. Varying the axial bit length influences the cross-talk between the adjacent layers and determines the number of layers that can be packed in a standard optical disc. Light coupling is also influenced by the bit spacing. There is an optimum bit spacing that allows a maximum number of layers that can be detected. According to FDTD simulations, a bit spacing of minimum of 1.5λ gives the best contrast and enables the reading of maximum number of layers.

To conclude, we demonstrate the fabrication and imaging of 60 layers of data in CG grade plastics by optimizing the multi-layer data recording and reading parameters. This allows us to stack 120 layers of data in a standard 1.2-mm-thick optical disc by using bidirectional read–write geometry. Optimization using our technique highlights the practical implementation of our method into a fluorescence-based optical data storage technology. A storage capacity of 275-GB disc can be easily realized with the demonstrated bit spacing of 0.9 µm. This can be further enhanced by reducing the bit size (and therefore bit spacing) by using higher NA lenses and shorter wavelengths. Employing adaptive aberration correction and reduced axial bit dimension can potentially lead to recording 150 layers of data in PMMA. Manipulating light propagation by strategically introducing gaps between a set of layers in order for the light to regroup, can further reduce coupling losses of the read laser.

Author Contributions: A.J., M.G.R. and V.R.B. designed and planned the experiments. A.J. and M.G.R. conducted the experiments and analyzed the results. A.J. conducted theoretical simulations. All authors have read and agreed to the published version of the manuscript.

Funding: The authors acknowledge financial support from the Natural Science and Engineering Research Council of Canada, Canadian Foundation for Innovation.

Institutional Review Board Statement: Not applicable.

Informed Consent Statement: Not applicable.

Data Availability Statement: The data that support the findings of this study are available from the corresponding author on request.

Conflicts of Interest: The authors declare no conflict of interest.

Abbreviations

The following abbreviations are used in this manuscript:

PMMA	Poly-methyl-methacrylate
PC	Polycarbonate
ODS	Optical data storage
NA	Numerical aperture
CQ	Clinical quality
CG	Commercial grade

References

1. Glezer, E.N.; Milosavljevic, M.; Huang, L.; Finlay, R.; Her, T.; Callan, J.; Mazur, E. Three-dimensional optical storage inside transparent materials. *Opt. Lett.* **1996**, *21*, 2023–2025. [CrossRef] [PubMed]
2. Zhang, J.; Gecevičius, M.; Beresna, M.; Kazansky, P. Seemingly Unlimited Lifetime Data Storage in Nanostructured Glass. *Phys. Rev. Lett.* **2014**, *112*, 033901. [CrossRef]
3. Royon, A.; Bourhis, K.; Bellec, M.; Papon, G.; Bousquet, B.; Deshayes, Y.; Cardinal, T.; Canioni, L. Silver Clusters Embedded in Glass as a Perennial High Capacity Optical Recording Medium. *Adv. Mater.* **2010**, *22*, 5282–5286. [CrossRef] [PubMed]
4. Zijlstra, P.; Chon, J.; Gu, M. Five-dimensional optical recording mediated by surface plasmons in gold nanorods. *Nature* **2009**, *459*, 410–413. [CrossRef] [PubMed]
5. Kallepalli, D.; Alshehri, A.; Marquez, D.; Andrzejewski, L.; Scaiano, J.; Bhardwaj, R. Ultra-high density optical data storage in common transparent plastics. *Sci. Rep.* **2016**, *25*, 26163. [CrossRef] [PubMed]
6. Strickler, J.; Watt Webb, W. Three-dimensional optical data storage in refractive media by two-photon point excitation. *Opt. Lett.* **1991**, *16*, 1780–1782. [CrossRef]
7. Shimotsuma, Y.; Sakakura, M.; Kazansky, P.; Beresna, M.; Qiu, J.; Miura, K.; Hirao, K. Ultrafast Manipulation of Self-Assembled Form Birefringence in Glass. *Adv. Mater.* **2010**, *22*, 4039–4043. [CrossRef]
8. Gu, M.; Li, X.; Cao, Y. Optical storage arrays: A perspective for future big data storage. *Light. Sci. Appl.* **2014**, *5*, e177. [CrossRef]
9. Li, X.; Cao, Y.; Tian, N.; Fu, L.; Gu, M. Multifocal optical nanoscopy for big data recording at 30 TB capacity and gigabits/second data rate. *Optica* **2015**, *2*, 567–570. [CrossRef]
10. Gan, Z.; Cao, Y.; Evans, R.A.; Gu, M. Three-dimensional deep sub-diffraction optical beam lithography with 9nm feature size. *Nat. Commun.* **2013**, *4*, 2061. [CrossRef]
11. Lamon, S.; Wu, Y.; Zhang, Q.; Liu, X.; Gu, M. Nanoscale optical writing through upconversion resonance energy transfer. *Sci. Adv.* **2021**, *7*, eabe2209. [CrossRef] [PubMed]
12. Lamon, S.; Zhang, Q.; Gu, M. Nanophotonics-enabled optical data storage in the age of machine learning. *APL Photonics* **2021**, *6*, 110902. [CrossRef]
13. Day, D.; Gu, M.; Smallridge, A. Use of two-photon excitation for erasable–rewritable three-dimensional bit optical data storage in a photorefractive polymer. *APL Opt. Lett.* **1999**, *24*, 948–950. [CrossRef]
14. Hu, Z.; Huang, X.; Yang, Z.; Qiu, J.; Song, Z.; Zhang, J.; Dong, G. Reversible 3D optical data storage and information encryption in photo-modulated transparent glass medium. *Light Sci. Appl.* **2021**, *10*, 140. [CrossRef]
15. Lin, S.; Lin, H.; Ma, C.; Cheng, Y.; Ye, S.; Lin, F.; Wang, Y. High-security-level multi-dimensional optical storage medium: Nanostructured glass embedded with $LiGa_5O_8$: Mn^{2+} with photostimulated luminescence. *Light Sci. App.* **2020**, *9*, 22. [CrossRef] [PubMed]
16. Ashley, J.; Bernal, M.; Burr, G.; Coufal, H.; Guenther, H.; Hoffnagle, J.; Jefferson, C.; Marcus, B.; Macfarlane, R.; Shelby, R.; et al. Holographic data storage technology. *IBM J. Res. Dev.* **2000**, *14*, 341–368. [CrossRef]
17. Li, X.; Ren, H.; Chen, X.; Liu, J.; Li, C.; Xue, G.; Jia, J.; Cao, L.; Sahu, A.; Hu, B.; et al. Athermally photoreduced graphene oxides for three-dimensional holographic images. *Nat. Commun.* **2015**, *6*, 6984. [CrossRef]
18. Simmonds, R.; Salter, P.; Jesacher, A.; Booth, M. Three dimensional laser microfabrication in diamond using a dual adaptive optics system. *Opt. Express* **2011**, *19*, 24122–24128. [CrossRef]
19. Kontenis, G.; Gailevičius, D.; Jonušauskas, L.; Purlys, V. Dynamic aberration correction via spatial light modulator (SLM) for femtosecond direct laser writing: Towards spherical voxels. *Opt. Express* **2020**, *28*, 27850–27864. [CrossRef]
20. Wolf, E. Electromagnetic diffraction in optical systems-I. An integral representation of the image field. *Proc. R. Soc. Lond. A* **1959**, *253*, 349–357.
21. Török, P.; Varga, P.; Laczik, Z.; Booker, G. Electromagnetic diffraction of light focused through a planar interface between materials of mismatched refractive indices: An integral representation. *J. Opt. Soc. Am. A* **1995**, *12*, 325–332. [CrossRef]
22. Török, P.; Varga, P.; Booker, G. Electromagnetic diffraction of light focused through a planar interface between materials of mismatched refractive indices: Structure of the electromagnetic field. I. *J. Opt. Soc. Am. A* **1995**, *12*, 2136–2144. [CrossRef]
23. Baum, B.; Scully, P.; Basanta, M.; Thomas, P.; Fielden, P.; Goddard, N.; Perrie, W.; Chalker, P. Photochemistry of refractive index structures in polymethyl methacrylate by femtosecond laser irradiation. *Opt. Lett.* **2007**, *32*, 190–192. [CrossRef] [PubMed]
24. Gao, L.; Zhang, Q.; Evans, R.; Gu, M. 4D Ultra-High-Density Long Data Storage Supported by a Solid-State Optically Active Polymeric Material with High Thermal Stability. *Adv. Opt. Mater.* **2021**, *9*, 2100487. [CrossRef]
25. Alshehri, A.M.; Deepak, K.L.N.; Marquez, D.T.; Desgreniers, S.; Bhardwaj, V.R. Localized nanoclusters formation in PDMS upon the irradiation with femtosecond laser. *Opt. Mater. Express* **2015**, *5*, 858–869. [CrossRef]
26. Nie, Z.; Lee, H.; Yoo, H.; Lee, Y.; Kim, Y.; Lim, K.S.; Lee, M. Multilayered optical bit memory with a high signal-to-noise ratio in fluorescent polymethylmethacrylate. *Appl. Phys. Lett.* **2009**, *94*, 111912. [CrossRef]

Proposed extension:

The most straightforward way to increase the 3D-ODS capacity is to decrease the spot size by using a high NA oil immersion objective lens. However, the use of high NA oil immersion objectives is not practically feasible in any type of disc reader due to the intricacies of oil immersion systems.

Another way to decrease bit size is by wavefront correction using phase-modulated spatial light modulators to dynamically adjust for different depths. Although diffraction-limited spot size can be achieved[18], the phase-modulated spatial light modulators (SLMs) are not an economical industry-relevant solution (consumer product applications). The following methods are proposed to decrease the bit size by minimizing spherical aberrations resulting from the optical elements in the setup and enhancing axial resolution through a combination of spatial and temporal focusing. These methods are experimentally feasible and relatively cost-effective compared to the techniques discussed above.

Minimizing aberrations

The spot size can be decreased by minimizing spherical aberrations arising from the optical elements in the setup. The focusing lens contributes to the majority of these aberrations. One effective approach is to use aspheric lenses, which are specifically designed to minimize these aberrations. The aspheric lens (0.83 NA- Edmund optics) was used in the publication. However, these lenses are commercially produced for a specific design wavelength, i.e., the aberrations are minimized for the specific wavelength. The design wavelength for the 0.83 NA lens used in the publication was 587 nm. For any other wavelength, even within the working range specified by the supplier, the aberrations would result in the spot size larger than the diffraction limit. This was observed in our experiments, where the average fluorescent spot size was $\sim 0.7\ \mu m$ (or $\sim 1\ \mu m$ for $1/e^2$). Considering the nonlinear two-photon interaction, as the bandgap of commercial polycarbonate is 3 - 3.5ev [19], this corresponds to the focused spot size of $\approx 2\ \mu m$ for linear interaction (see Eq.9.1), which is not the diffraction-limited spot size for 0.83 NA lens.

Such aberrations from the focusing lens can be minimized by using optical design software such as Zemax. In Zemax software, most of the commercially available lenses can be imported, with all of the design parameters, from the inbuilt library. Through the variation of design parameters like length, width, and conic surface shapes, a diffraction-limited spot size can be obtained at any specific design wavelength. Figure 9.7 shows the snippet of the simulations performed in Zemax. The non-paraxial 0.83 NA lens (designed for a wavelength of 587 nm) was optimized to achieve diffraction-limited spot size at 800 nm.

The diffraction-limited spot size for 0.83NA lens with 800 nm light, calculated in terms of airy disc (black circle) radius, was 757 nm, as highlighted by the red underline in Fig.9.7a. Without optimization, the root mean square (RMS) radius was approximately 1.41 μm (not shown). The RMS value in Zemax measures the average spread of rays around the centroid of a spot, providing a quantifiable measure of the achievable spot size by considering various aberrations. After optimization of the lens, the RMS radius decreased to 886 nm, as shown by

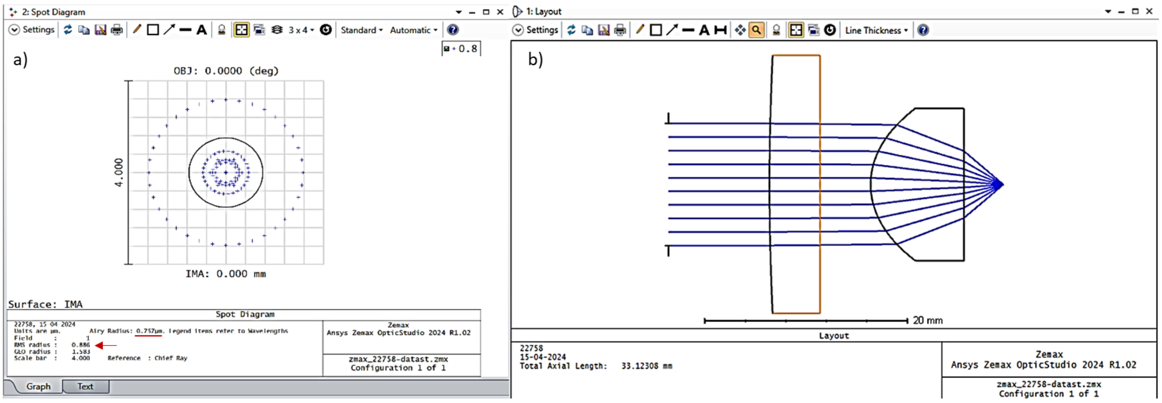

Surface: IMA

Spot Diagram

22758, 15-04-2024
Units are µm.   Airy Radius: 0.757µm. Legend items refer to Wavelengths
Field : 1
RMS radius : 0.886
GEO radius : 1.583
Scale bar : 4.000   Reference : Chief Ray

Zemax
Ansys Zemax OpticStudio 2024 R1.02

zmax_22758-datast.zmx
Configuration 1 of 1

Layout

22758
15-04-2024
Total Axial Length: 33.12308 mm

Zemax
Ansys Zemax OpticStudio 2024 R1.02

zmax_22758-datast.zmx
Configuration 1 of 1

Figure 9.7: **Zemax simulations** performed for minimizing the spherical aberrations introduced by the lens for the 800nm input wavelength. **a** The diffraction-limited spot size in terms of airy disc radius (757 nm), highlighted by the red underline and by the black circle in the image. Also, the RMS radius was achieved at 886 nm after optimization. **b** The combination of plano-convex and aspheric lens utilized for optimization of the spot size

the red arrow in Fig.9.7a. This was achieved by reducing the thickness of the objective lens from 9.71 mm to 9.21 mm and adding an additional plano-convex lens with a focal length of 300mm (Fig.9.7b). The conic surface and length of the lens were not adjusted, as altering these parameters is not practically (or economically) feasible given the manufacturing constraints of commercial manufacturing. Therefore, an approximate *35% reduction in spot size* is achieved by optimizing the focusing lens of the designed system.

Temporal Focusing

The temporal focusing technique can be utilized to enhance the axial resolution, thus allowing for a higher density of recorded data layers in 3D-ODS. This technique operates on principles similar to chirped pulse applications. Light pulses are stretched (or spectrally separated) and then compressed only at the focal plane of the lens. As a result, the pulse duration is shortest (high peak power) at the focal plane, leading to a strong intensity gradient at the spatial focal plane. These high-intensity gradients ensure that the energy required to induce two-photon absorption or nonlinear interaction, which initiates material modification, is only achieved at the focal plane. This creates a highly localized modification, avoiding unwanted modifications above or below the focal plane, thus achieving enhanced axial resolution. This technique was recently employed by Saha et al. [20] in the two-photon lithography (TPL) method and demonstrated high axial resolution $2\omega_z \sim 1\ \mu m$ with 1.2 NA lens and 800nm laser wavelength. This is near the modified diffraction limit in the case of a two-photon process [6] (refer to Eq.9.5). Therefore, using temporal focusing, Saha et al. [20] achieved diffraction-limited axial spot size.

Figure 9.8 shows the schematic of the temporal focusing technique, which can be easily integrated into the existing setup. The step-by-step process is discussed below:

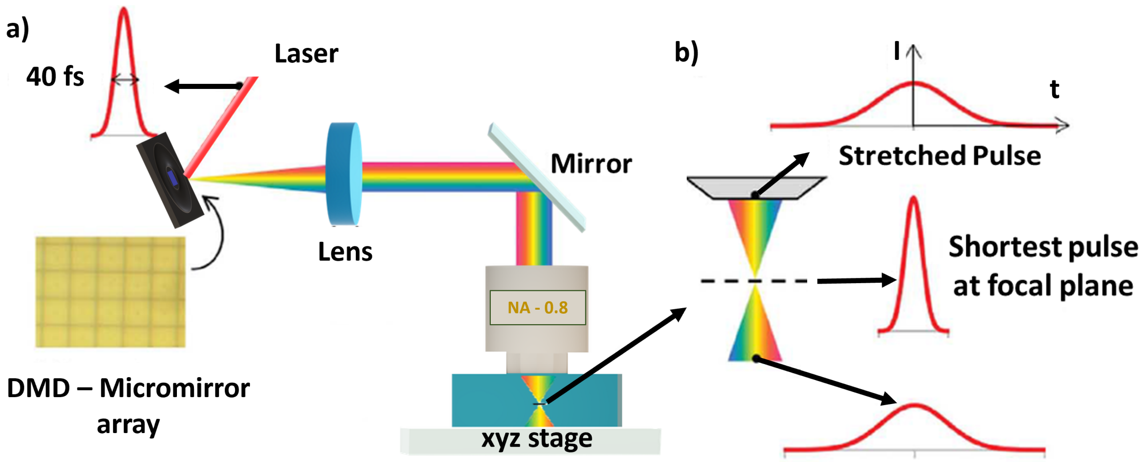

Figure 9.8: **Schematic of the temporal focusing technique. a**Femtosecond pulses are stretched and compressed as they pass through the optical system to implement temporal focusing. The micromirror array spectrally separates the different wavelengths of the femtosecond pulse and stretches it, whereas the objective lens focuses the pulse in the time domain. **b** A 4f-like optical arrangement to ensure that the optical path lengths for all wavelengths are equal between the micromirror array and the focal plane of the objective lens but unequal everywhere else, leading to the shortest pulse at the focal plane. Part of this schematic is reproduced from Saha et al.[20]

- Temporal focusing begins with the stretching of the femtosecond pulse by passing it through a dispersive digital micromirror array (DMD), optimized to achieve efficient diffraction for the central wavelength of 800 nm, as shown in Fig. 9.8a. This DMD causes different wavelengths of the pulse to spatially separate and to travel at slightly different speeds, effectively elongating the pulse duration.

- The stretched pulse is then directed through an optical setup designed to recompress the pulse specifically at the focal plane. A 4f-like optical arrangement (Fig. 9.8a) can be used to ensure that the optical path lengths for all wavelengths are equal between the micro-mirror array and the focal plane of the objective lens, while remaining unequal at all other points. Consequently, at the focal plane, the various wavelength components realign temporally, and the laser spectrum spatially overlaps, resulting in the shortest pulse duration, as illustrated in Fig. 9.8b.

- Material dispersion also stretches the pulse as it propagates through the sample. However, for $\sim 50fs$ pulse widths, the pulse broadening introduced by 1.2mm thick PMMA with GVD of 81.808fs^2/mm is 0.295fs, which can be neglected. However, if only a few cycle pulses were employed, pulse broadening would be significant and would need to be dynamically compensated.

Therefore, temporal focusing avoids any modification above or below the point where the pulse duration is shortest, leading to a highly localized modification. Thus, high axial resolution, near the modified diffraction limit for two-photon microscopy, can be achieved. The diffraction-limited axial spot size in the case of TPM is given as [6]

$$\omega_{\mathrm{z}} = \frac{0.532\lambda}{\sqrt{2}} \left[\frac{1}{n - \sqrt{n^2 - \mathrm{NA}^2}} \right] \tag{9.5}$$

Substituting $\lambda = 800$nm, NA = 0.83 and n = 1.57 for polycabonate, the axial spot size $2\omega_{\mathrm{z}}$ = 2.54 μm. In the publication, a maximum of 120 layers were recorded in a 1.2 mm disc due to a layer spacing constraint of 10 µm, determined by the axial spot size of approximately 7 µm of the fluorescent spot. Thus, in principle, by employing the temporal focusing technique, the layer spacing can be effectively reduced by half - nearly doubling the storage capacity.

Advantages:

- The proposed method can be easily integrated with the existing data writing setup.
- Temporal focusing combined with optical design optimizations in Zemax can lead to at least a twofold increase in 3D-ODS capacity.
- Compared to oil immersion high NA objectives and phase-modulated SLMs, the proposed method is both practically feasible and cost-effective for consumer applications.

Disadvantages: There is an inherent complexity in optical alignment to ensure the path length of different wavelengths is the same at the focal plane. If not properly compensated, this pulse stretching can result in a loss of intensity gradient at the lens's focal plane, thereby decreasing resolution.

References

[1] Amos Martinez and Zhipei Sun. Nanotube and graphene saturable absorbers for fibre lasers. *Nature Photonics*, 7(304):842–845, 2013.

[2] Xiaohui Li, Kan Wu, Zhipei Sun, Bo Meng, Yonggang Wang, Yishan Wang, Xuechao Yu, Xia Yu, Ying Zhang, Perry Ping Shum, and Qi Jie Wang. Single-wall carbon nanotubes and graphene oxide-based saturable absorbers for low phase noise mode-locked fiber lasers. *Scientific Reports*, 6:25266, 2016.

[3] Alexander A. Balandin, Suchismita Ghosh, Wenzhong Bao, Irene Calizo, Desalegne Teweldebrhan, Feng Miao, and Chun Ning Lau. Superior thermal conductivity of single-layer graphene. *Nano Letters*, 8(3):902–907, 2008.

[4] Robert W. Boyd. *Nonlinear Optics*. Academic Press, Inc., third edition, 2008.

[5] Edinburgh Instruments. Rayleigh criterion for microscope resolution, 2020.

[6] Warren R Zipfel, Rebecca M Williams, and Watt W Webb. Nonlinear magic: multiphoton microscopy in the biosciences. *Nature Biotechnology*, 21(11), 2003.

[7] R.N. Bracewell. *The Fourier Transform and Its Applications*. McGraw-Hill Kogakusha, Ltd., Tokyo, second edition edition, 1978.

[8] MathWorks. 2-d normalized cross-correlation. https://www.mathworks.com/help/images/ref/normxcorr2.html.

[9] CD Bioparticles. Diagpoly carboxyl fluorescent polystyrene particles, green, 0.4 m (item: Dcfg-l005). https://www.cd-bioparticles.com/product.html.

[10] Ming Liu, Thomas Zentgraf, Yongmin Liu, Guy Bartal, and Xiang Zhang. Light-driven nanoscale plasmonic motors. *Nature Nanotechnology*, 5(8):570–573, 2010.

[11] Jungho Mun, Minkyung Kim, Younghwan Yang, Trevon Badloe, Jincheng Ni, Yang Chen, Cheng-Wei Qiu, and Junsuk Rho. Electromagnetic chirality: from fundamentals to non-traditional chiroptical phenomena. *Light: Science & Applications*, 9:139, 2020.

[12] Ashish Jain, Mitra G. Rahimian, and V. R. Bhardwaj. Optimization of multi-layer data recording and reading in an optical disc. *Photonics*, 9:690, 2022.

[13] J. Zhang, M. Gecevičius, M. Beresna, and P. Kazansky. Seemingly unlimited lifetime data storage in nanostructured glass. *Physical Review Letters*, 112(3):033901, 2014.

[14] Peter Zijlstra, James WM Chon, and Min Gu. Five-dimensional optical recording mediated by surface plasmons in gold nanorods. *Nature*, 459(7245):410–413, 2009.

[15] Dheeraj Kallepalli, Abdulaziz Alshehri, Daniel Marquez, Luke Andrzejewski, Juan C Scaiano, and Rajesh Bhardwaj. Ultra-high density optical data storage in common transparent plastics. *Scientific Reports*, 6:26163, 2016.

[16] E. Wolf. Electromagnetic diffraction in optical systems - i. an integral representation of the image field. *Proc. R. Soc. Lond. A*, 253:349–357, 1959.

[17] P. T or ok, P. Varga, Z. Laczik, and G.R. Booker. Electromagnetic diffraction of light focused through a planar interface between materials of mismatched refractive indices: an integral representation. *J. Opt. Soc. Am. A*, 12(2):325–332, 1995.

[18] Gabrielius Kontenis, Darius Gailevičius, Linas Jonušauskas, and Vytautas Purlys. Dynamic aberration correction via spatial light modulator (slm) for femtosecond direct laser writing: towards spherical voxels. *Optics Express*, 28:27850–27864, 2020.

[19] D. P. Gupta, Shyam Kumar, P. C. Kalsi, V. K. Manchanda, and V. K. Mittal. -ray modifications of optical/chemical properties of polycarbonate polymer. *World Journal of Condensed Matter Physics*, 5:129–137, 2015.

[20] Sourabh K. Saha, David Wang, Vu Nguyen, Young-Wook Chang, James S. Oakdale, and Steve C. Chen. Scalable submicrometer additive manufacturing. *Science*, 366(6461):105–109, 2019.

Appendix A

Energy absorption rate via induced dipoles

The energy absorption rate for a single-photon transition is attributed to induced higher-order multipoles. When a monochromatic electromagnetic field interacts with a molecule, it generates oscillating charge and current distributions, which are described through a multipole expansion. As outlined by Barron et al. [1], the induced electric dipole, $\tilde{\mu}$, electric quadrupole, $\tilde{\theta}$, and magnetic dipole, $\tilde{m}$ are expressed through a limited series expansion, representing a linear combination of dynamic molecular tensors [2, 1].

$$\tilde{\mu}_\alpha = \sum_\beta \tilde{\alpha}_{\alpha\beta}\tilde{E}_\beta + \sum_\beta \tilde{G}_{\alpha\beta}\tilde{B}_\beta + \frac{1}{3}\sum_{\beta\gamma}\tilde{A}_{\alpha\beta\gamma}\tilde{E}_{\beta\gamma};\quad \tilde{\theta}_{\alpha\beta} = \sum_\gamma \tilde{a}_{\gamma\alpha\beta}\tilde{E}_\gamma;\quad \tilde{m}_\alpha = \sum_\beta \tilde{\chi}_{\alpha\beta}\tilde{B}_\beta + \sum_\beta \tilde{g}_{\alpha\beta}\tilde{E}_\beta \tag{A.1}$$

where the cartesian indices are represented by Greek letters. The electric dipole polarizability is given by complex dynamic tensor $\tilde{\alpha}_{\alpha\beta}$, the magnetic susceptibility is given by $\tilde{\chi}_{\alpha\beta}$, electric dipole-quadrupole polarizability is given by $\tilde{A}_{\alpha\beta\gamma}$, where $\tilde{A}_{\alpha\beta\gamma} = \tilde{a}_{\gamma\alpha\beta}$, and the electric-magnetic dipole polarizability is given by $\tilde{G}_{\alpha\beta}$ where $\tilde{G}_{\alpha\beta} = -\tilde{g}_{\alpha\beta}$. The double subscript notation $\tilde{E}_{\beta\gamma}$ is used to represent field gradients $\nabla_\beta \tilde{E}_\gamma$ [2, 1]. The electric and magnetic fields are defined with time dependence expressed separately as $\tilde{E}(t) = \tilde{E}_0 e^{-i\omega t}$ and $\tilde{B}(t) = \tilde{B}_0 e^{-i\omega t}$, where $\tilde{E}_0$ and $\tilde{B}_0$ are the field magnitude represented in terms of complex vectors and ω is the frequency of the incident light. All the terms represented with tilde in the above equation are complex quantities $\tilde{\alpha}_{\alpha\beta} = \alpha'_{\alpha\beta} + i\alpha''_{\alpha\beta} = \tilde{\alpha}^*_{\beta\alpha}$, $\tilde{A}_{\alpha\beta\gamma} = A'_{\alpha\beta\gamma} + iA''_{\alpha\beta\gamma} = \tilde{A}_{\gamma\alpha\beta}$, $\tilde{G}_{\alpha\beta} = G'_{\alpha\beta} + iG''_{\alpha\beta}$.

The rate of change in the multipole interaction Hamiltonian reflects the time-averaged rate at which energy is absorbed from the electromagnetic fields by the induced multipoles [2, 1].

$$\Gamma = \langle \dot{\mu}_\alpha E_\alpha + \dot{m}_\alpha B_\alpha + \frac{1}{3}\dot{\theta}_{\alpha\beta} E_{\alpha\beta} \rangle_t \tag{A.2}$$

where $\dot{\mu}, \dot{m}, \dot{\theta}$, $E_\alpha = \frac{1}{2}\left(\tilde{E}_\alpha e^{-i\omega t} + \tilde{E}^*_\alpha e^{i\omega t}\right)$ and $B_\alpha = \frac{1}{2}\left(\tilde{B}_\alpha e^{-i\omega t} + \tilde{B}^*_\alpha e^{i\omega t}\right)$ are real quantities. By examining the component of the dipole moment in the direction of the electric field, β is replaced with α to derive the following expression,

$$\Gamma_{E1-E1} = \frac{\omega}{4}\alpha''_{\alpha\beta}\left(\tilde{E}^*_\beta \tilde{E}_\alpha + \tilde{E}_\beta \tilde{E}^*_\alpha\right) \rightarrow \Gamma_{E1-E1} = \frac{\omega}{2}\alpha''_{\alpha\alpha}\left[\tilde{E}_\alpha \tilde{E}^*_\alpha\right] \tag{A.3}$$

Magnetic dipole-dipole excitation (M1-M1) is given by

$$\Gamma_{M1-M1} = \frac{\omega}{4}\chi''_{\alpha\beta}\left(\tilde{B}_\beta \tilde{B}^*_\alpha + \tilde{B}^*_\beta \tilde{B}_\alpha\right) \rightarrow \Gamma_{M1-M1} = \frac{\omega}{2}\chi''_{\alpha\alpha}\left[\tilde{B}_\alpha \tilde{B}^*_\alpha\right] \tag{A.4}$$

The electric-magnetic dipole excitation (E1-M1) arises from the interaction between the electric field and the electric dipole moment induced by the magnetic field, and vice versa. The corresponding expression is given by

$$\Gamma_{E1-M1} = \frac{i\omega}{4}\langle G'_{\alpha\beta}\rangle_\rho \left(\tilde{B}_\beta \tilde{E}^*_\alpha - \tilde{E}_\alpha \tilde{B}^*_\beta\right) \rightarrow \Gamma_{E1-M1} = \frac{\omega}{2}\rho G'_{\alpha\alpha}\mathrm{Im}\left[\tilde{E}^*_\alpha \tilde{B}_\alpha\right] \tag{A.5}$$

To accurately model the bulk response of the material, it is essential to average the tensor quantity $G'_{\alpha\beta}$ over all possible molecular orientations. However, when molecules exhibit partial alignment due to laser-induced dipole forces, the assumption of isotropic orientation no longer holds. In such cases, an anisotropic averaging method must be employed. This approach modifies the averaging process to $\langle G'_{\alpha\beta}\rangle_\rho \rightarrow \rho G'_{\alpha\alpha}$, where ρ is an orientation-dependent weighting factor that reflects the extent of molecular alignment within the system [3].

Electric dipole-quadrupole excitation (E1-E2) arises from two distinct contributions. The first is the interaction between the field gradient and the quadrupole moment induced by the electric field. The second involves the interaction between the electric field and the induced electric dipole moment. The corresponding expression is given by

$$\Gamma_{E1-E2} = \frac{\omega}{6}\langle A''_{\alpha\beta\gamma}\rangle_\rho \left[\nabla_\beta \tilde{E}_\gamma \tilde{E}^*_\alpha + \tilde{E}_\alpha \left(\nabla_\beta \tilde{E}_\gamma\right)^*\right] \rightarrow \Gamma_{E1-E2} = \frac{\omega}{3}\rho A''_{\alpha\alpha\gamma}\mathrm{Re}\left[\nabla \tilde{E}^{\pm}_\delta \cdot \left(\tilde{E}^{\pm}_\delta\right)^*\right] \tag{A.6}$$

here we applied anisotropic averaging to the tensor $\langle A''_{\alpha\beta\gamma}\rangle_\rho \rightarrow \rho A''_{\alpha\alpha\gamma}$, where ρ is a weighting factor that depends on the degree of molecular alignment. When complete molecular alignment is achieved ($\rho = 1$) and the principal molecular axis is aligned with the propagation axis (γ), the tensor simplifies to $\langle A''_{\alpha\beta\gamma}\rangle_\rho \rightarrow \left(A''_{\alpha\alpha\gamma} + A''_{\beta\beta\gamma}\right)$ [2]. Since the primary contribution to the dipole moment is along the electric field direction (α), we focus on the term $A''_{\alpha\alpha\gamma}$. This tensor component vanishes for randomly oriented molecules, representing isotropic averaging. Higher-order multipole transitions, such as E1M2, E2M1, and E2E2, are excluded from consideration, as their corresponding molecular response tensors for these transitions are negligibly small.

The total rate of excitation is a sum of all four absorption rates given below for an asymmetric Laguerre-Gaussian (LG) beam

$$\Gamma_\delta^\pm = \frac{\omega}{2}\{\underbrace{\alpha''|\tilde{E}_\delta^\pm|^2}_{\text{E1E1}} + \underbrace{\chi''|\tilde{B}_\delta^\pm|^2}_{\text{M1M1}} + \underbrace{\rho G'\mathrm{Im}\left[\left(\tilde{E}_\delta^\pm\right)^* \cdot \tilde{B}_\delta^\pm\right]}_{\text{E1M1}} + \underbrace{\frac{2}{3}\rho A''\mathrm{Re}\left[\nabla\tilde{E}_\delta^\pm \cdot \left(\tilde{E}_\delta^\pm\right)^*\right]}_{\text{E1E2}}\} \tag{A.7}$$

here δ represents the asymmetry parameter, where $\delta = 0$ indicates a symmetric LG beam, and $\delta \neq 0$ indicates an asymmetric LG beam. The sign in $\Gamma^\pm$ represents the sign of OAM.

References

[1] Laurence D. Barron. *Molecular Light Scattering and Optical Activity.* Cambridge University Press, Cambridge, United Kingdom, 2 edition, 2004.

[2] Nan Yang and Adam E. Cohen. Local geometry of electromagnetic fields and its role in molecular multipole transitions. *Journal of Physical Chemistry B*, 115:5304–5311, 2011.

[3] D. L. Andrews, L. D. Romero, and M. Babiker. On optical vortex interactions with chiral matter. *Opt. Commun.*, 237:133–139, 2004.